Development of a Freehand Three-Dimensional Radial Endoscopic Ultrasonography System

Scott Inglis

A thesis submitted for the degree of Doctor of Philosophy

The University of Edinburgh

2009

Declaration of Originality

I hereby declare that the research recorded in this thesis, and the thesis itself, was composed and originated entirely by myself in the Departments of Medical Physics, and Gastroenterology & Hepatology, at the University of Edinburgh.

Scott Inglis

Abstract

Oesophageal cancer is an aggressive malignancy with an overall five-year survival of 5-10% and two-thirds of patients have irresectable disease at diagnosis. Accurate staging of oesophageal cancer is important as survival closely correlates with the stage of the tumour, nodal involvement and presence of metastases (TNM staging). Endoscopic ultrasonography (EUS) is currently the most reliable modality for providing accurate T and N staging. Depending on findings of the staging, various treatment options including endoscopic, oncological, and surgical treatments may be performed.

It was theorised that the development of three-dimensional radial endoscopic ultrasonography would reduce the operator dependence of EUS and provide accurate dimensional and volume measurements to aid planning and monitoring of treatment. This thesis investigates the development of a three dimensional endoscopic ultrasound technique that can be used with the radial echoendoscopes.

Various agar-based tissue mimicking material (TMM) recipes were characterised using a scanning acoustic macroscope to obtain the acoustic properties of attenuation, backscatter and speed of sound. Using these results, a number of endoscopic ultrasound phantoms were developed for the in-vitro investigation and evaluation of 3D-EUS techniques.

To increase my understanding of EUS equipment, the imaging and acoustic properties of the EUS endoscopes were characterised using a pipe phantom and a hydrophone. The dual 'single element' mechanical and 'multi-element' electronic echoendoscopes were investigated. Measured imaging properties included dead space, low contrast penetration, and pipe length. The measured acoustic properties included transmitted beam plots, active working frequency and peak pressures.

Three-dimensional ultrasound techniques were developed for specific application to EUS. This included the study of positional monitoring systems, reconstruction algorithms and measurement techniques. A 3D-EUS system was developed using a Microscribe positional arm and frame grabber card, to acquire the 3D dataset. A Matlab 3D-EUS toolbox was written to reconstruct and analyse the volumes. The 3D-EUS systems were evaluated on the EUS phantom and in clinical cases.

The usefulness of the 3D-EUS systems was evaluated in a cohort of patients, who were routinely investigated by conventional EUS for a variety of upper gastrointestinal pathology. 3D-EUS accurately staged early tumours and provided the necessary anatomical information to facilitate treatment. With regards to more advanced tumours, 3D-EUS was more accurate than EUS in T and N staging. 3D-EUS gave useful anatomical details in a variety of benign conditions such as varicies and GISTs.

Table of Content

Acknowledgements

I would like to acknowledge the following individuals:

- Professor W. Norman McDicken for his supervision and aid during the project.
- Dr. Harry Brash for his support, supervision and aid during the project.
- Dr. John N. Plevris for his guidance, supervision and support during the clinical segments of the project and his enthusiasm for the project.
- Dr. Jim Hannan for his support during the project.
- Dr. Stephen Pye for his support, understanding and aid during the project.
- Dr. Kumar Ramnarine for his passing on his expertise in TMM manufacture and SAM measurements.
- Mr Derek Christie for the development of the IC3D program and the numerous times I have used him to brain storm.
- Mr Stan Lowenski, for the manufacture of numerous mechanical engineering projects and devices that have been the backbone of the project.
- Sister Helen Chisholm and the endoscopy nursing staff for having been so helpful and even tolerated me during the most hectic times.
- Mrs Karne McBride for training me in the use of hydrophones.
- Miss Anna Janeczko for her aid with the EUS equipment and assistance in performing measurements.
- Dr. Robin Watson, for the use of the 3DScan program and assistance in performing comparative volume measurements.
- My mother, father and sister for their support and understanding through the good and bad times experienced during the project.

Abbreviations

2D	Two Dimensional
3D	Three Dimensional
3D-EUS	Three-Dimensional Endoscopic Ultrasound
AA	Aortic Arch
AD	Adventitia
ADBAC	Benzalkonium Chloride
AFI	Auto Fluorescence Imaging
AWF	Acoustic Working Frequency
B	Breadth
Ca	Cancer
CLE	Confocal Laser Endomicroscopy
CT	Computed Tomography
E3DI	Endoscope 3 Dimensional Imager
EBUS	Endo-Bronchial Ultrasound
ECG	Electrocardiogram
ER	Endoscopic Resection
EUS	Endoscopic Ultrasonography
EUS-FNA	Endoscopic Ultrasound – Fine Needle Aspiration
FICE	Fujinon Intelligent Colour Enhancement
FF	Far Field Measurement
FFT	Fast Fourier Transform
fps	Frames Per Second
Gb	Giga Byte
GIST	gastrointestinal stromal tumour
GI	Gastrointestinal
GUI	Graphical User Interface
H	Height
Hyper	Hyperechoic
Hypo	Hypoechoic
L	Length
LCP	Low Contrast Penetration
M	Metastases (can have the suffix 0 to 1, signify presence or absence of metastases)
Mal	Malignant nodes found in resection.
Mb	Mega Byte
MDCT	Multi-detector Computed Tomography

MI	Mechanical Index
MPC	Mucularis Propria Circular
MPL	Mucularis Propria Longitudinal
Mrk	Mark
MRI	Magnetic Resonance Imaging
MS	Mucosa
N	Node (can have the suffix 0 to 1, signify presence or absence of metastases)
NACR	Neo-Adjuvant Chemotherapy
NBI	Narrow Band Imaging
NF	Near Field Measurement
NPL	National Physics Laboratory
NR	No Reconstruction
Oes	Oesophagus
OGJ	Oesophago-Gastric Junction.
PVA	Polyvinyl acetate
PACS	Picture Archiving and Communications System
PBM	Pixel based methods
PC	Personal Computer
PET	Positron Emission Tomography
PSE	Power Spectral Estimate
PVC	Polyvinyl chloride
PVDF	polyvinylidine difluoride
PVR	Personal video recorder
QA	Quality Assurance
RF	Radio Frequency
RMS	Root Mean Square
RT	Radiotherapy.
SAM	Scanning Acoustic Macroscope
SDK	Software Development Kit
SM	Submucosa
SML	Sub-mucosal lesion
STC	Sensitivity Time Control
T	Tumour (can have the suffix 0 to 4, signify stage of the disease)
TMM	Tissue Mimicking Material
TOE	trans-oesophageal echo
Tot	Total number of Nodes resected.
TPC0	Tissue Particle Concentration of TMM recipe with a particle concentration of 0%
TPC5	Tissue Particle Concentration of TMM recipe with a particle concentration of 5%

TPC10	Tissue Particle Concentration of TMM recipe with a particle concentration of 10%
TPC20	Tissue Particle Concentration of TMM recipe with a particle concentration of 20%
TPC30	Tissue Particle Concentration of TMM recipe with a particle concentration of 30%
TPC40	Tissue Particle Concentration of TMM recipe with a particle concentration of 40%
TPC50	Tissue Particle Concentration of TMM recipe with a particle concentration of 50%
TPC60	Tissue Particle Concentration of TMM recipe with a particle concentration of 60%
TPC75	Tissue Particle Concentration of TMM recipe with a particle concentration of 75%
TPC100	Tissue Particle Concentration of TMM recipe with a particle concentration of 100%
UK	United Kingdom
US	Ultrasound
USB	Universal Serial Bus
VB6	Visual Basic 6
VBM	Voxel Based Methods
WB	Water Balloon

Nomenclature

a_p	The angle of the pipe [50˚].
A_{p2p}	The angle travelled per 2 points (due to splitting to positive and negative peaks) [˚]
A_{pp}	Where is the angle travelled per point [˚]
ave_d	The average sample thickness (mm),
ave_fft(data)	The results of the average FFT of the data
ave_fft(ref)	The results of the average FFT of the reference frame
ave_α	The calculated average attenuation, and.
c	Medium specific speed of sound in soft tissue (e.g. 1540m/s) [m/s]
c_o	the offset from the centre
c_r	Reference speed [m/s]
c_s	the speed of sound through the sample [m/s]
c_w	the speed of sound in water [m/s]
d	thickness of the sample [mm]
dH	Step factor for y direction (normally 1).
$dist_{arm}$	Distance between each image calculated from the arm [mm].
$dist_{basic}$	Distance between each image [mm].
d_{pp}	the distance travelled per point [mm]
ΔT	time-shift [s, ms or μs].
Δtp	The time difference between the data pulse and the reference pulse
dW	Step factor for x direction (normally 1).
d_x	The distance travelled for each angle increment [mm]
f	Ultrasound frequency [MHz]
f_f	The far-field measurement [mm]
F_{awf}	acoustic working frequency [Hz or MHz]
fft(data)	The results of the FFT of the data, and.
fft(ref)	The results of the FFT of the reference frame
f_s	The sampling frequency of the SAM system [Hz]
G_{Amp}	the gain of the amplifier
HS	The distance step between transducer and the hydrophone [mm]
I (x, y, f)	the power spectrum intensity at frequency f and position x, y through the sample
I_o(x, y, f)	the power spectrum intensity at position x, y and frequency f of the reference signal with no sample in the path
m	the gradient of the line
M	the hydrophone sensitivity [μV/Pa]
n_f	The near field measurement [mm]

nF	Number of individual images within the image stack.
nPx	Number of pixels within the cropped image corresponding to the x dimensions.
nPy	Number of pixels within the cropped image corresponding to the y dimensions.
p	Pressure [Pa or MPa]
pbd	Pull back distance [mm or cm].
pl	Pipe Length (mm)
ppsi	pulse-pressure-squared integral [Pa^2s]
r	the radius of the transducer [mm]
sf	Arbitrary scaling factor of window selection
si	Step Index for z direction (normally 1).
$t_{10\%}$	Time taken to reach 10% of the maximum value [s, ms or μs].
$t_{90\%}$	Time taken to reach 90% of the maximum value [s, ms or μs].
t_{dur}	Pulse duration [s, ms or μs].
T1	Time taken from Tx to the reflected pulse maximum from steel plate through water
T2	Time taken from Tx to the reflected pulse maximum from steel plate through water & TMM sample
T3	Time taken from Tx to the maximum of the TMM sample surface reflection pulse
Tx	Time from the excitation pulse to start of pulse recordings
V	The RF pulse voltage [V]
X or x	X Dimension in Cartesian Coordinates
x_tot	Distance moved at each image acquisition in x direction from the origin.
Xd	The dimensions of ultrasound imaging window in the x direction [mm].
Y or y	Y Dimension in Cartesian Coordinates
y_tot	Distance moved at each image acquisition in y direction from the origin.
Yd	The dimensions of ultrasound imaging window in the y direction [mm].
Z or z	Z Dimension in Cartesian Coordinates
z_tot	Distance moved at each image acquisition in z direction from the origin
Z_{ai}	Acoustic Impedance [$kg \cdot m^{-2}s^{-1}$]
Zd	The pullback distance of the 3D acquisition [mm].
α	Attenuation [dB/cm or dB/cm.MHz]
λ	Wavelength in soft tissue [μm]
ρ	Specific density of the medium [kg/m^3]
μ	Backscatter Power [dB]

Figures

Tables

Chapter 1 – Introduction

1.1. Endoscopy

Endoscopy is a minimally invasive diagnostic medical procedure that is used to assess the interior surfaces of an organ by the insertion of a flexible or rigid tube into the body. Endoscopy is a broad term that may be subdivided into numerous specialties, e.g. gastro-intestinal (GI) Tract, respiratory tract, urinary tract, female reproductive system. However, when using the term endoscopy within this thesis it will be associated with the GI tract. The main advantages of GI endoscopy are that the endoscopist has the ability to observe the anatomy in real-time and under direct vision, and can apply therapy if something abnormal is identified or to examine further by taking tissue samples. The therapeutic options made available to the endoscopist have increased dramatically over the years. At present new techniques allow the endoscopist to treat disorders, e.g. early cancer, or pre-cancerous disorders, which normally could only be successfully treated via surgery or radiotherapy. Some of those include endoscopic mucosal resection and photodynamic therapy.

Currently there are a number of techniques within GI endoscopy to visualise structures below the surface. The depths of penetration for these techniques are illustrated in Figure 1.1. These are:

- Endocytoscopy. (Curvers et al. 2008, Kiesslich & Neurath 2005, Buchner & Wallace 2008).
- Confocal Laser Endomicroscopy. (Polglase et al. 2005, Curvers et al. 2008, Gossner 2008, Buchner & Wallace 2008, Delaney et al. 2008, Wallace et al. 2006).
- Narrow Band Imaging (N.B.I). (ASGE Technology Committee 2008. Wong Kee Song & Wilson 2005, Curvers et al. 2008, Gossner 2008 Buchner & Wallace 2008, Wallace et al. 2006).
- Fujinon Intelligent Colour Enhancement (FICE). (ASGE Technology Committee 2008, Osawa et al. 2008, Fujinon Corporation 2007, Buchner & Wallace 2008).
- Auto Fluorescence Imaging (AFI). (Wong Kee Song & Wilson 2005, Curvers et al. 2008, Buchner & Wallace 2008, Wallace et al. 2006).
- Endoscopic Ultrasound (EUS): Endoscopic ultrasound is a highly useful technique that can investigate a wide variety of diseases. The primary uses of EUS includes the staging of GI cancers and associated lymph nodes (Brugge et al. 1997), investigation of deeper GI wall abnormalities and pathology that impinge on the GI tract (e.g. GIST, varicies) not accessible to standard endoscopic examination and biopsies (ASGE Standards of Practice Committee 2007). Endoscopic ultrasound equipment comes in many different endoscope configurations to enable the endoscopist to perform a wide range of procedures, both diagnostic and therapeutic. (Yusuf et al. 2007, McLean & Fairclough 1996, Wallace et al. 2006).

1.2. The Anatomy

In its simplest terms the GI system is composed of a series of tubular organs. These main organs of the GI tract consist of the oesophagus, stomach, small intestine and large intestine. The main focus of this project will be the components of the upper GI tract, which consist of the oesophagus, oesophagogastric junction (OGJ), stomach, and duodenum. There are a number of other organs associated with the GI tract, which are the liver, gallbladder, pancreas and appendix. Any disruption of this process, via disease, can be detrimental to the health of the patient. Typical symptoms of GI disorders include vomiting, nausea, GI bleeding, dysphasia, dyspepsia, abdominal pain, constipation and diarrhoea. The manifestation of these symptoms can indicate any number of GI disorders (e.g. cancer, varicies, polyps, Gastrointestinal Stromal Tumours (GIST)).

The wall of the oesophagus is made up of a number of layers of different cellular consistencies. The inner most layer, or lumen, of the oesophagus is the mucosa and is approximately 500μm thick (Darlas & Couard 1999). The lumen is normally collapsed and only opens during swallowing. The mucosa is made up of a number of sub-layers that include the Epithelium, Lamina Propria and Muscularis mucosae, approximate thickness = 100μm (Darlas & Couard 1999). The submucosa is composed of dense connective tissue and its approximate thickness is 400μm in a normal oesophagus (Darlas & Couard 1999). The muscularis propria of the oesophagus is composed of both skeletal and smooth muscle and is arranged into two layers, the inner circumferential fibres and outer longitudinal fibres. The upper third of the oesophagus is mostly composed of skeletal muscle; the middle third has both skeletal and smooth muscle; and the lowest third is only composed of smooth muscle fibres. This configuration of the muscularis propria corresponds with the conscious control over swallowing reflex in the upper portions and the autonomic control in the lower portions. The approximate thicknesses of the muscularis propria circular and longitudinal fibre layers are 500μm and 300μm respectively. The oesophagus is covered by an adventitia until it pierces the diaphragm, after which it is covered by a serosa. A detailed cross section of the anatomy of the wall of the oesophagus is shown in Figure 1.2.

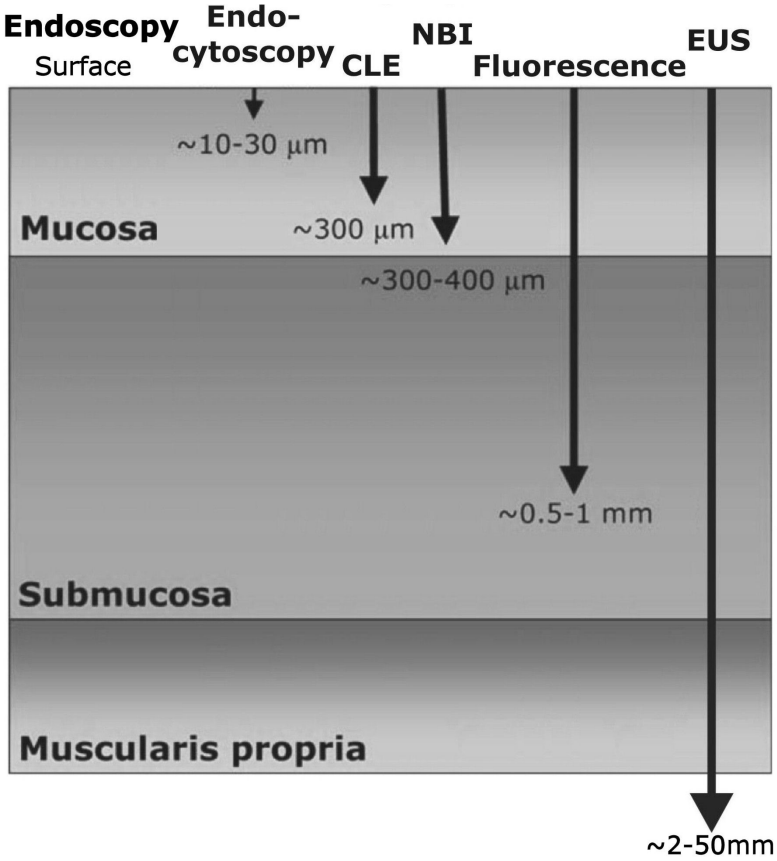

Figure 1.1– Endoscopic imaging techniques used in the diagnosis of GI diseases their use for imaging deep structures and pathology.

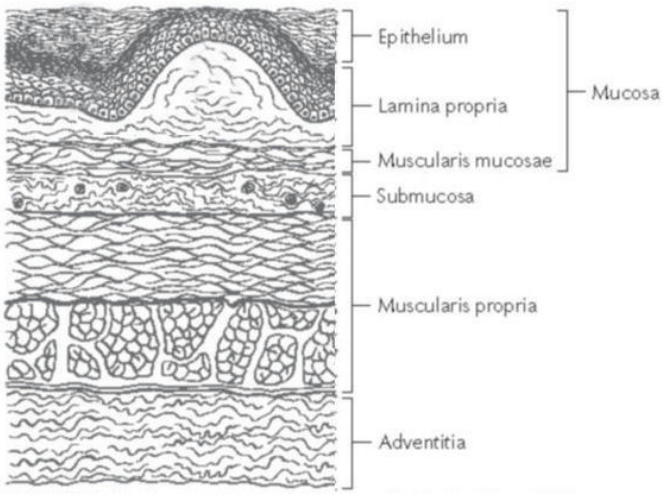

Figure 1.2 – The histological images of the wall of the oesophagus, modified from AJCC Cancer Staging Atlas (Greene et al. 2006).

1.2.1. Study of the 3D Anatomy

Figure 1.3 details the study of the idealised three-dimensional anatomy of the GI tract and surrounding structures, obtained from the educational DVD, Endoscopic Ultrasound in the diagnosis of thoracic diseases (Olympus Europa GMBH, Hamburg, Germany). The anatomy was reconstructed from CT scans. Using the tools provided, the anatomy was visualised and the structures studied, to enable the creation of the Mark 3 EUS phantom. The anatomy included in figure 1.3 was the aorta, bronchus, and stomach. The anatomy was rotated, in both X and Y axes, to determine its shape and path. The oesophagus was found to curve around the bronchus and aortic arch, and then maintain a constant path till it reached the OGJ, where it curved into the stomach. The endoscopic ultrasound examination of the oesophagus normally starts at the OGJ and terminates at the bronchus. However, there is no literature available that details the effects on the anatomy when the echoendoscope is introduced into the GI tract and as it is withdrawn.

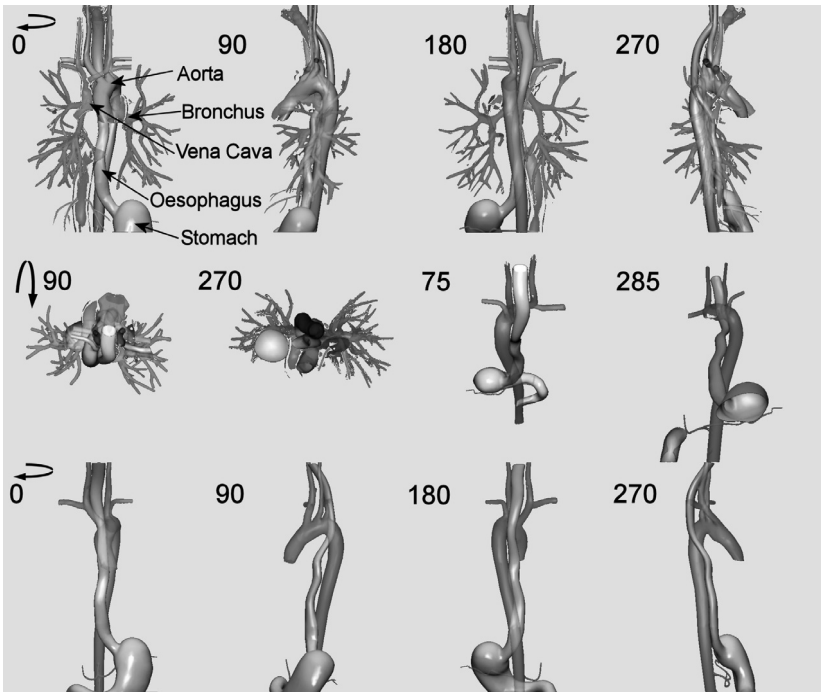

Figure 1.3 - The idealised 3D anatomy of the upper GI tract and aorta. Also included was the bronchus and vena cava. The anatomy was rotated around the axes to visualise the shape of the aorta and oesophagus. Certain organs had transparency applied to them for improved visualisation. The images were captured from the educational DVD, Endoscopic Ultrasound in the diagnosis of thoracic diseases (Olympus Europa GMBH, Hamburg, Germany)

1.2.2. Ultrasound appearance of the oesophageal wall

From the basics of ultrasound (McDicken 1976, Darlas & Couard 1999, Martin & Ramnarine 2003), if the transmitted pulse interacts with an interface or boundary that is wider than the wavelength of the transmitted pulse, a reflection is produced, where a proportion of the pulse intensity will return to the transmitter / receiver, and the remaining pulse intensity will continue to meet its next interaction and so on. If the ultrasound wave interacts with an object that is smaller than the ultrasound wavelength, scattering will occur, where the resultant pulses will radiate in many different directions. The ultrasound wavelength may be approximated using equation 1.1.

$$\lambda = \frac{c}{f} \qquad \text{Eq. 1.1}$$

Where λ is the wavelength in soft tissue (μm), c is the speed of sound in soft tissue (e.g. 1540m/s) and f is the ultrasound frequency (MHz).

As the main operating frequencies of the echoendoscopes are 5, 7.5, 10, 12 and 20 MHz, the resultant wavelengths would be 308, 205, 154, 128 and 77 μm respectively. If the transmitted ultrasound wave strikes a tissue layer that is wider than the wavelength and has different acoustic impedance to the preceding layers then a reflection of the beam will occur and return a bright echo within the constructed image. Depending on the acoustic impedance of the various mediums, a proportion of the pulse intensity will continue to the next boundary (McDicken 1976, Darlas & Couard 1999, Martin & Ramnarine 2003). The acoustic impedance is determined by equation 1.2.

$$Z_{ai} = \rho \times c \qquad \text{Eq. 1.2}$$

Where Z_{ai} is the acoustic impedance, ρ is the specific density of the medium, and c is the medium specific velocity of ultrasound beam.

If the target is smaller than the wavelength of the ultrasound pulse or strikes a rough surface then the scattering phenomenon will occur. This is where the beam will be reflected from the structure in many different directions and is dependant on the frequency and the volume concentration of scatterers (McDicken 1976, Darlas & Couard 1999, Martin & Ramnarine 2003). Structures that cause the scattering phenomenon include the liver, debris within the gallbladder and is visible within the thicker layers made up from various fibres and cells. The resultant ultrasound image will produce a gray scale speckle effect.

When imaging the GI tract with the ultrasound probe of the EUS scope, an image consisting of a number of bright (hyperechoic) and dark (hypoechoic) rings is obtained. Figure 1.4 illustrates an idealised ultrasound image relating to the anatomical layers of the oesophagus. A water filled latex balloon is used to maintain contact with the wall of the oesophagus. The balloon is normally filled to

the extent where good contact is obtained around the circumference of the oesophagus, and not to the point where the layers are compressed. When the ultrasound pulse is transmitted from the transducer, it will strike the latex balloon and mucosa. Due to the change in acoustical impedance from water to the latex / mucosa, a reflection will occur producing the first hyperechoic boundary or layer. The thickness of the 'layer' or boundary will depend upon the ultrasound frequency and its corresponding wavelength. As the mucosa is approximately 500μm, the remainder of the mucosa will appear hypoechoic and form the second layer. When the pulse reaches the mucosa / submucosa interface, there is a difference in the tissue types and a reflection will occur, producing a hyperechoic boundary and the third layer. This layer can merge with the reflection obtained from the submucosa / muscularis propria interface, resulting in a wide, prominent hyperechoic layer. The remainder of the muscularis propria will form the hypoechoic fourth layer. As the muscularis propria changes consistency in the upper, mid and lower segments of the oesophagus, a hyperechoic layer may be visualised during the mid segment, as it consists of separate layers of circular and longitudinal muscular fibres. The interface between these muscle layers can produce the hyperechoic layer, depending upon the imaging frequency and pathology of the wall. Therefore, the number of visualised layers can change from 5 to 7 layers depending upon location and frequency of the transducer. The hyperechoic fifth layer is produced by the ultrasound pulse striking the boundary between the muscularis propria and the adventitia / serosa. However, during clinical EUS investigations, it is often found that the actual number of visible layers can vary from patient to patient. This would be dependant upon:

- the type of EUS device / transducer used,
- ultrasound imaging frequency used,
- orientation of the transducer (e.g. tangential placement),
- actual thicknesses of the wall layers,
- presence of abnormal pathology,
- fat content and
- location of the transducer within the oesophagus.

Darlas & Couard (1999) studied the generation of the ultrasound image as the ultrasound beam traverses the GI wall and discussed a number of artefacts. They also described why the clinicians have the misconception that the hyperechoic and hypoechoic rings represent the layers of the oesophagus. Within the explanation they described the imaging process of a tissue layer, effects of frequency, amplification and reflection coefficients. They also created a model that simulated the walls of the various organs of the GI tract and generated the resultant ultrasound images. They modelled the effects of axial resolution and frequency and concluded that the number of visible layers varied with frequency and the thickness of the hyperechoic boundaries diminished with increasing frequencies (Darlas & Couard 1999). Figure 1.5 shows the reproduced results obtained from the model simulation of the oesophageal wall by Darlas & Couard (1999). Their model simulated a simplified anatomy and resulted in an increase in the wall layers from 7 at 5MHz, to 9 layers at 10MHz. The difference

between the simulated results and the image normally seen during clinical scanning was the submucosa. The model did not simulate the complex nature of this layer, as it contained a number of glands and dense connective tissue.

Figure 1.6 a and b illustrate the layers of the oesophageal wall at 20MHz and 12 MHz. The ultrasound images were acquired when the transducer was located in the mid oesophagus from different patients and in both cases 7 layers of the oesophagus were observed. Figure 1.6a illustrates normal, mid, oesophageal wall layers imaged at 20MHz. The anatomical image corresponds to the 7 layers of the standard EUS image detailed in Figure 1.4.

Figure 1.6b illustrates the effects of abnormal pathology on the oesophageal wall layers. On the left side of the oesophagus, the wall layers were normal, and not visible due to compression by the balloon. However, on the right side of the oesophagus seven layers were visualised. This effect was due to its proximity to abnormal pathology that caused the wall thickness to expand. The first hyperechoic layer observed at 12MHz was due to the interface of the latex balloon and the mucosa of the oesophageal wall.

Figure 1.6 a and b clearly shows the ring artefact generated by the mechanical radial echoendoscope. The transducer is housed within a polythene dome, filled with oil. As the RF pulse strikes this transducer housing and due to the dome thickness and change in acoustical impedance from the oil to dome to water, a ring artefact is generated.

Figure 1.4 – Correlation between the standard five EUS layers and histological layers of the normal oesophageal wall. 1st = interface between balloon, fluid in the lumen and the superficial mucosa; 2nd = lamina propria and muscularis mucosae, 3rd = the interfaces between the submucosa and mucosa and muscularis propria; 4th = muscularis propria; (4a) circular, (4c) longitudinal and (4b) thin connective tissue layer, only seen at high frequencies; 5th = interface between Muscularis Propria and the adventitia. (The histological images were modified from AJCC Cancer Staging Atlas (Greene et al. 2006)).

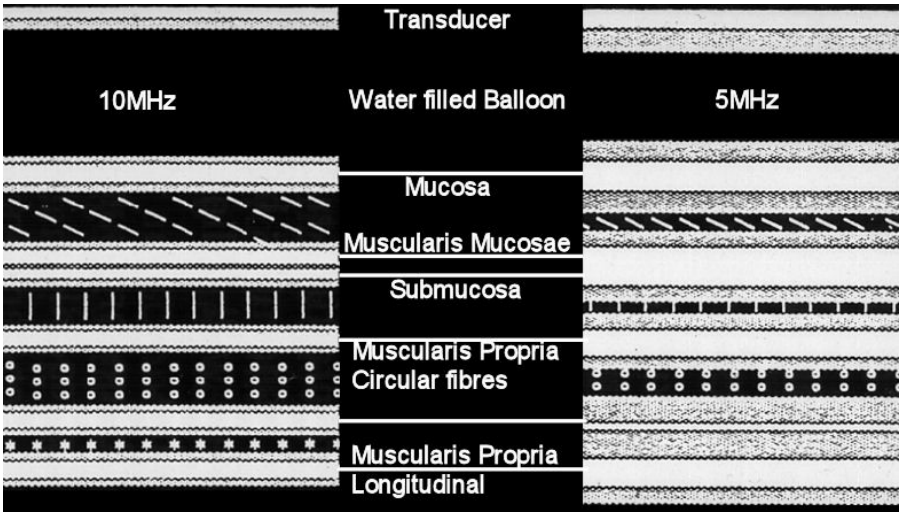

Figure 1.5 – The results obtained from the model simulation oesophageal wall created by Darlas & Couard (1999). The model simulated various layers and the effects of changing frequency. (The image was modified from the Darlas & Couard (1999) mathematical model of the oesophageal wall.).

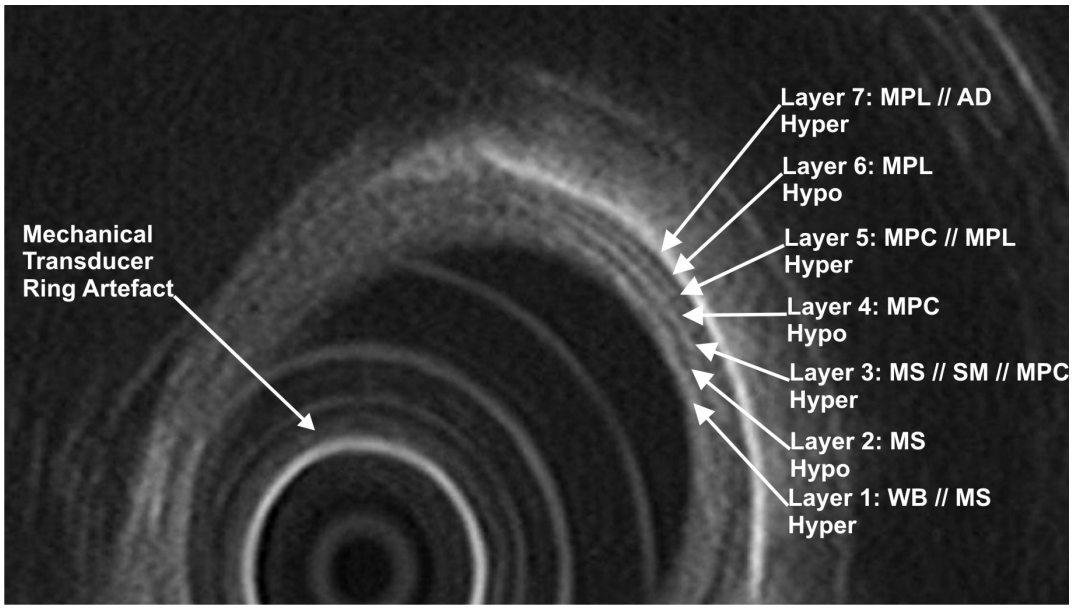

Figure 1.6.a – Normal oesophageal wall layers imaged at 20MHz. (7 layers were observed). The image was acquired in the mid oesophagus. The wall layers were most prominent when the wall was perpendicular to the transducer. The GF-UM2000 echoendoscope and EU-M2000 processor was used to acquire the image.

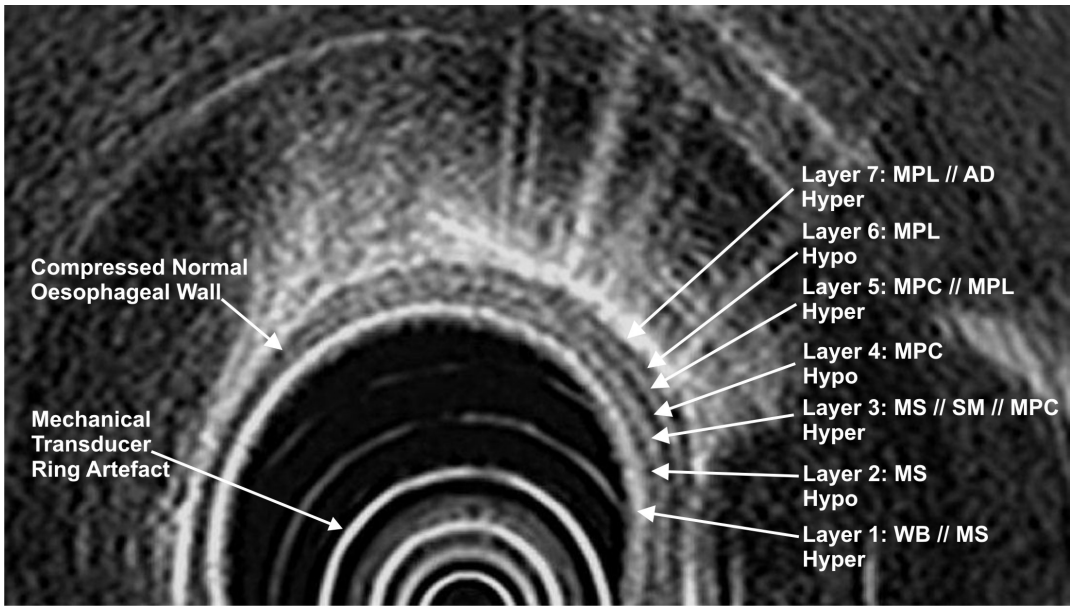

Figure 1.6.b – Expanded oesophageal wall layers, preceding an area of abnormal pathology, acquired at 12MHz (7 layers were observed). The image was acquired in the area of the mid oesophagus. The GF-UM2000 echoendoscope and EU-M2000 processor was used to acquire the image.

Where WB - Water Balloon; MS – Mucosa; SM – Submucosa; MPC – Mucularis Propria Circular; MPL – Mucularis Propria Longitudinal; AD – Adventitia; Hyper – Hyperechoic layer; Hypo – Hypoechoic layer; // - Interface, for Figures 1.6 a & b.

1.3. Endoscopic Ultrasound Equipment

Endoscopic ultrasonography (EUS) is a technique that combines endoscopy and ultrasonography. Yusuf et al. (2007) reviewed the available EUS technology and equipment. Technologies have changed since the clinical introduction of radial EUS in the mid-80's (Yusuf et al. 2007, Tio 1988, Tio et al. 1989, McLean & Fairclough 1996). The first flexible EUS scopes incorporated a rotating single element piezoelectric crystal transducer attached to the tip of the endoscope, to produce a 360º ultrasound B-mode cross-sectional image of the wall of the GI tract. Acoustic contact with the wall of the GI tract was obtained by a water filled balloon (Yusuf et al., 2007).

Echoendoscopes are classified by the orientation of the transducer, and are the radial and curvilinear orientated echoendoscopes (Yusuf et al. 2007, Fukuda 2000). The curvilinear echoendoscope was introduced clinically in the early 90s (Erickson 2000, Raj & Chen 2006) and produced an image that was longitudinally orientated in relation to the endoscope, and is frequently used as an interventional or therapeutic device (Raj & Chen 2006, Yusuf et al. 2007, Yong & Roberts 2003, Yamao et al. 2007). The introduction of the endobronchial ultrasound scope (EBUS) by Olympus has seen a significant reduction of the diameter of the linear EUS scope (14.6mm) to the EBUS scope (6.9mm) so that it can fit into the bronchus (Sheski & Mathur 2008).

In comparison, the radial echoendoscope is used for diagnosis, to produce a 360º image of the anatomy. The ultrasound image obtained is easily related to the anatomy of the GI tract and reduces the complexity of its interpretation (Yusuf et al. 2007). The recent advent of solid state electronic radial echoendoscopes has meant that Doppler and flow imaging are now available (Yusuf et al. 2007). A comparative study of Olympus mechanical and Pentax electronic radial echoendoscopes was performed in 2004. This highlighted the improvements in image quality and reduction of the artefacts that were inherent in the mechanical systems (Niwa et al. 2004), specifically the ring artefact that is present on all mechanical rotational transducer. This is generated as the transducer is housed within a plastic oil filled container. The acoustic impedance mis-match between the oil and plastic produced the artefact that masks the near field of the image (Niwa et al. 2004). In 2003 – 2004, Olympus introduced their prototype 360º solid state electronic radial echoendoscope (Yasuda et al. 2004, Hawes 2004, Hashimoto et al. 2004, Culliford et al. 2004). A study performed by Ogawa et al. (2006) comparing the Olympus GF-UM 2000 mechanical radial and Olympus GF-UE 260 electronic radial echoendoscopes (Olympus Medical systems corp. Tokyo, Japan.) stated that both systems had equivalent image quality, however the GF-UE260 suffered from noticeable grating lobes. Where the electronic radial surpassed its mechanical counterpart was the removal of the ring artefact and the inclusion of flow imaging (Ogawa et al. 2006). Hwang and Kimmey (2006) and Martin (2003) summarised a number of errors and artefacts that can occur during ultrasound imaging and specifically EUS (Hwang and Kimmey 2006); included were acoustic & imaging artefacts.

The most common artefacts observed during the imaging include:

- the ring or reverberation artefact (e.g. dominant rings present in the mechanical transducers),
- multiple reflections (e.g. when the ultrasound beam strikes air at the bronchus),
- acoustic shadowing (e.g. when the ultrasound beam encounters a large impedance mismatch and the beam is completely reflected as in gall stones),
- through transmission (e.g. a structure is enhanced that is posterior to a fluid filled object),
- Tangential scanning (e.g. when the transducer is not placed at right angles to the object, it can appear thicker than it actually is),
- Side or grating lobes, (e.g. the off axis projection of the ultrasound beam that can produce image artefacts that can be mi- interpreted as abnormal structures).

Other errors arise from the calibration of the equipment and callipers, and, during measurements, the inaccurate use of the callipers.

The echoendoscopes and ultrasound scanners / processor units available for use within this project are detailed in tables A1.1 and A.1.2. Figure 1.7 illustrates the schematic and connection diagram of the Olympus GF-UE260 echoendoscope. Figures 1.8 a to e shows the transducers of a number of different echoendoscopes and a mini-probe. The main difference between the Olympus and Fujinon electronic radial echoendoscopes is that the video component and working channels are in a different position. The Olympus system has oblique view optics, where as the Fujinon system is a front view echoendoscope.

EUS mini-probes have been developed by Fujinon and Olympus that are designed to be used within areas that are normally inaccessible to normal echoendoscopes (e.g. pancreatic and biliary ducts, stenotic lumen) or in the high frequency study of the gastric wall (Okamura et al. 1999, Wu et al. 2003, Cysewska-Sobusiak et al. 2006, Stergiou et al. 2003, May et al. 2004). These devices use a small mechanical rotating single element piezoelectric ultrasound transducer. These devices suffer from limited penetration and, when measuring deep structures, the accuracy was shown to decrease (Okamura et al. 2004).

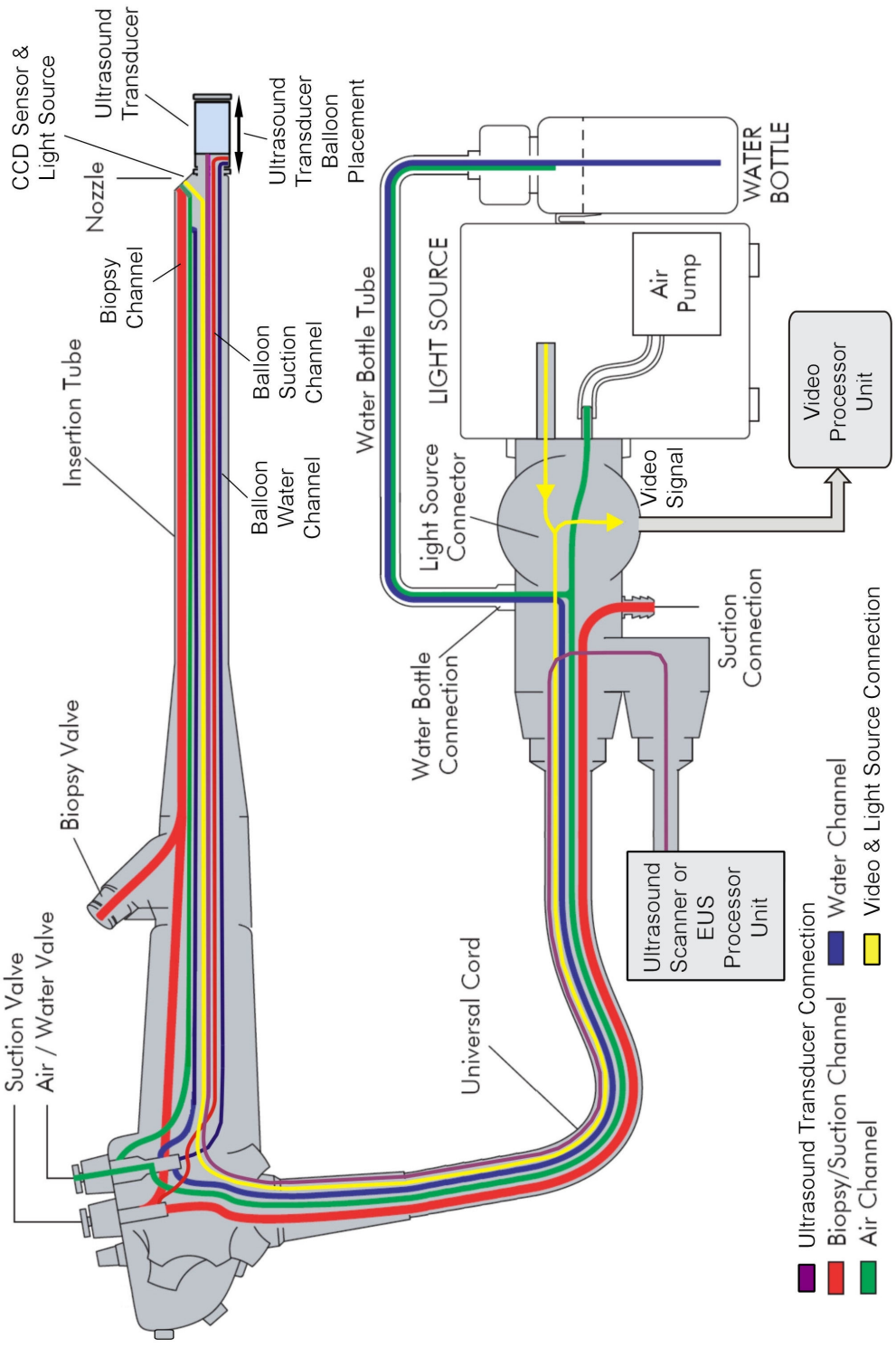

Figure 1.7 – The basic construction of the Olympus GF-UE260 echoendoscope. Included within the diagram are the air an.d water channels, the video connection to the light source and video processor units and connection to the Ultrasound scanner.

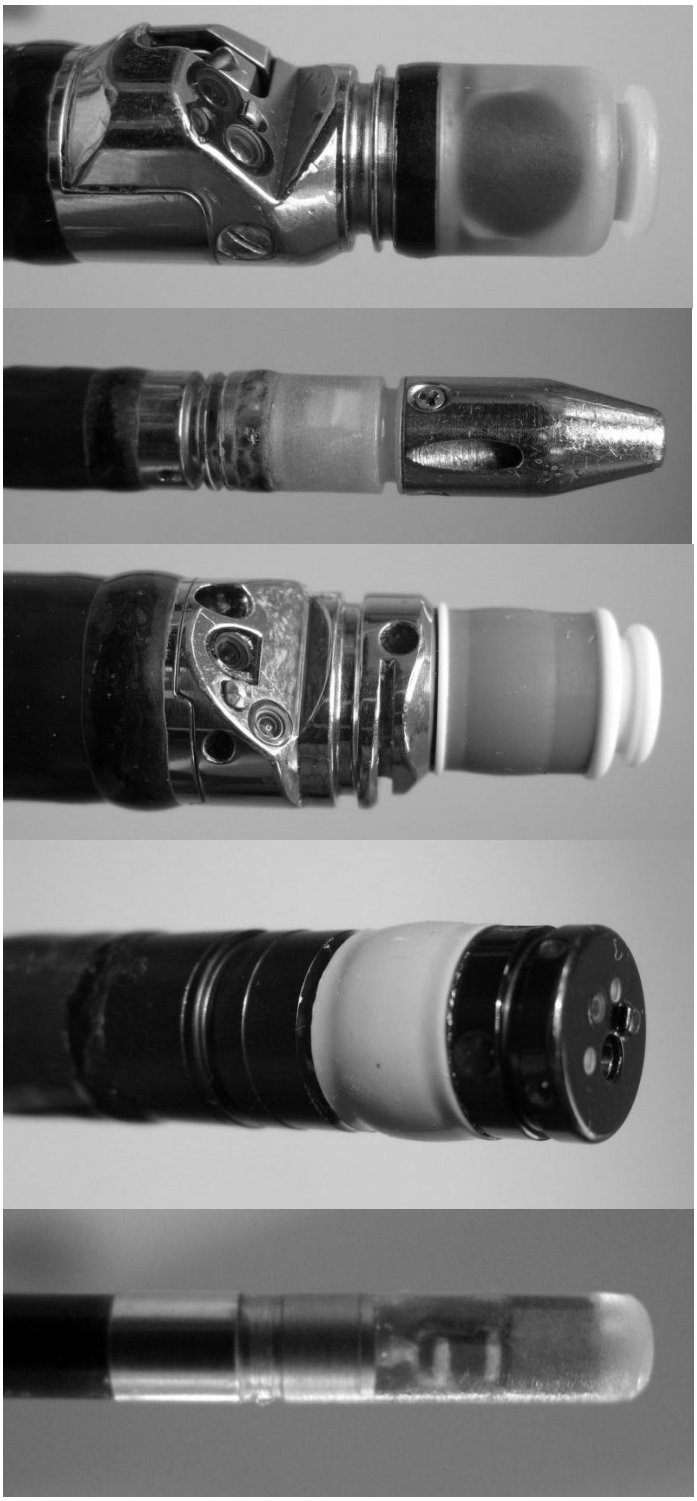

(a) The tip of the Olympus GF-UM series radial echoendoscope

(b) The tip of the Olympus MH-908 radial echoendoscope

(c) The tip of the Olympus GF-UE 260 electronic radial echoendoscope

(d) The tip of the Fujinon electronic EG-530UR radial echoendoscope

(e) The tip of the Fujinon 26-12 mini-probe.

Figure 1.8 - Examples of the Olympus and Fujinon echoendoscopes that are currently available and an example of a mini-probe transducer.

1.4. Endoscopic Ultrasound Technique

Conventional Endoscopic Ultrasound (EUS) is a technique that is used to diagnose a variety of gastro-intestinal diseases that cannot be reliably imaged by other modalities (CT, MRI) or diagnosed with conventional endoscopy and biopsies. Endoscopic Ultrasound is used to investigate (a) luminal GI malignancies (ASGE Standards of Practice Committee 2007, Rahul et al. 2007, Kelly et al. 2001, Tio et al. 1989, Kwee & Kwee, 2007, Lennon & Penman 2007, Lightdale & Kulikarni 2005 McGlave et al. 2005, Zhang et al. 2005, McLean & Fairclough 1996, ESGE 1996, Ødegaard 1995); (b) submucosal abnormalities (e.g. lipoma, leiomyoma, GIST), (McLean & Fairclough 1996, ASGE Standards of Practice Committee 2007, Kameyama et al. 1997); (c) vascular structures (e.g. varicies portal hypertensions) (Tio et al. 1995, Fusaroli & Caletti 2003, Irisawa et al. 2002, Irisawa et al. 1999, Miller 2005) (d) pancreatico-biliary disease (e.g. gall stones, cancers, and pancreatitis) (McLean & Fairclough 1996, Buscarini & Buscarini 1999, Ødegaard 1995); (e) mediastinal disease (e.g. lymph node, lung cancer) (Barawi & Gress, 2000, Wallace et al. 2004, Fritscher-Ravens 2003); (f) peri-anal disease (e.g. fistula, cancer, inflammation) (Schwartz et al. 2001, McLean & Fairclough 1996); (g) extraluminal abnormalities identified on other imaging studies (e.g. cyst, normal anatomy imprint) (McLean & Fairclough 1996); and (h) therapeutic applications (e.g. EUS-FNA, cyst drainage, core biopsies) (Raj & Chen 2006, Yong & Roberts 2003, Hawes 2002, Giovannini 2004, Yamao et al. 2007). However, as this equipment is relatively expensive, compared with standard endoscopy equipment, and requires an extensive period of training to become proficient at performing the procedure and interpreting the images, it is often limited to large acute hospitals.

An endoscopic ultrasound procedure is regarded as one of the most difficult procedures performed by an endoscopist (ASGE Standards of Practice Committee 2007, Plukker & van Westreenen 2006). As conventional EUS is operator dependent (Bergele & Giovannini 2004, Lennon & Penman 2007), it is possible for even the most experienced endoscopist to miss important pathological structures, and as the markings on the insertion tube of the echoendoscope are every 1cm, it is not possible to obtain reliable, accurate dimensional measurements in the longitudinal (Z) direction. Although it may provide adequate information on extent of tumour invasion (X-Y direction), it has reduced accuracy in the estimation of the length of the lesion.

1.4.1. Oesophageal Cancer staging.

The most important use of radial EUS is the staging of cancer. Cancer is classified in the T N M staging (Tumour Node Metastasis). T (Tumour) is the extent of the tumour and is detailed from T0, to T4. Each classification provides the clinician with the extent of the disease. Figure 1.9 illustrates the differences between the tumour staging (T1 to 3) histological oesophageal wall with cancer and corresponding idealised EUS images. N (Node) is the presence or absence of Lymph node metastasis and are classified as N0 or N1 (Greene et al. 2006, ASGE Standards of Practice Committee 2007, Rahul et al. 2007, Kelly et al. 2001, Tio et al. 1989, Kwee & Kwee 2007, Lennon & Penman 2007, Lightdale & Kulikarni 2005). To distinguish between malignant and benign nodes, via radial EUS frequencies above 7MHz, the criteria in table 1.1 were used (McLean & Fairclough 1996). A single matching factor signifies a low possible presence of malignancy. However, as the number of matching factors increases, the possibility of the node being malignant also increases.

Table 1.1 - Criteria to differentiate malignant and benign lymph nodes.

Characteristics	**Malignant**	**Benign**
Boundaries	Well defined	Indistinct
Echogenicity	Hypoechoic Homogeneous	Hyperechoic Non-homogeneous
Shape	Round	Irregular
Size	≥10mm	

M (Metastasis) is the presence or absence of metastasis and is classified as either M0 or M1 (Greene et al. 2006, ASGE Standards of Practice Committee 2007, Rahul et al. 2007, Kelly et al. 2001, Tio et al. 1989, Kwee & Kwee 2007, Lennon & Penman 2007). However, EUS only provides loco regional M classification of the disease (e.g. left lobe of the liver, celiac axis lymph nodes). Computed Tomography (CT) or Positron Emission Tomography (PET) is used to provide distal metastatic disease staging.

Oesophageal cancer is an aggressive malignancy with an overall five-year survival of 5-10%; two-thirds of patients have irresectable disease at diagnosis (Harewood & Kumar 2004). Accurate staging of oesophageal cancer is important because survival is closely correlated with tumour, nodal and the presence of metastases (TNM stage) (Harewood & Kumar 2004). Computed Tomography (CT) is the first staging investigation once the histological diagnosis is made, and it is used for the detection of distal and nodal metastases (McLean & Fairclough 1996, Plukker & van Westeernan 2006, Blackshaw et al. 2008, Pfau et al. 2007). Its ability to accurately determine T-stage is limited

(sensitivity 40% to 60%) (Schrager et al. 2005, Wakelin et al. 2002), as it was unable too accurately delineate the component layers of the oesophageal wall. Furthermore, it was recognized that helical CT scanning cannot define accurately the proximal and distal margins of oesophageal tumours and has limited accuracy in the detection of lymph nodes measuring less than 1 cm (Wakelin et al. 2002). Particularly in early disease the value of helical CT in diagnosis and staging of the disease is limited to the exclusion of obvious lymphadenopathy and distal metastases (Berger &Walter 2004, Kienle et al. 2002).

The advent of multi-detector computed tomography (MDCT) has seen an increase in the image resolution and a decrease in the acquisition time compared with helical CT. A recent comparative study of MDCT, EUS and PET have reported correct oesophageal T stage accuracies of 42% for MDCT and PET and between 71% and 80% EUS (Lowe et al. 2005, Sandha et al. 2008), compared with FNA & surgical histology. The accuracy of loco regional nodal staging, reported by Sandha et al. (2008) was 68% for MDCT, 56% for PET and 81% for EUS.

There are two main sub-divisions for oesophageal cancer staging, where correct EUS diagnosis could have a significant impact on the planning of treatment. These are early tumours (T1, N0 or T2, N0) and advanced tumours (T3, N0 or T3, N1). In early tumours the treatment possibilities include (i) endoscopic mucosal resection, (ii) radio-frequency ablation, (iii) radiotherapy, and (iv) surgery (Veuillez et al. 2007). In advanced tumours, T3 can refer to a wide spectrum of 'advanced' tumours. The available treatment options are limited to surgery. However, it may be necessary to pre-treat the area of the tumour with radiotherapy or neo-adjuvant chemo-radiotherapy to reduce the size of the tumour and destroy cancerous cells within malignant nodes (Veuillez et al. 2007). Therefore, it is imperative that, during the EUS examination, the endoscopist accurately determines the progression of the disease.

However, a preliminary study comparing the lengths and locations of upper GI cancers obtained from CT and EUS indicated that there could be differences in the reported lengths of tumour invasion that leading to insufficient treatment and tumour reoccurrence (Thomas et al. 2004).

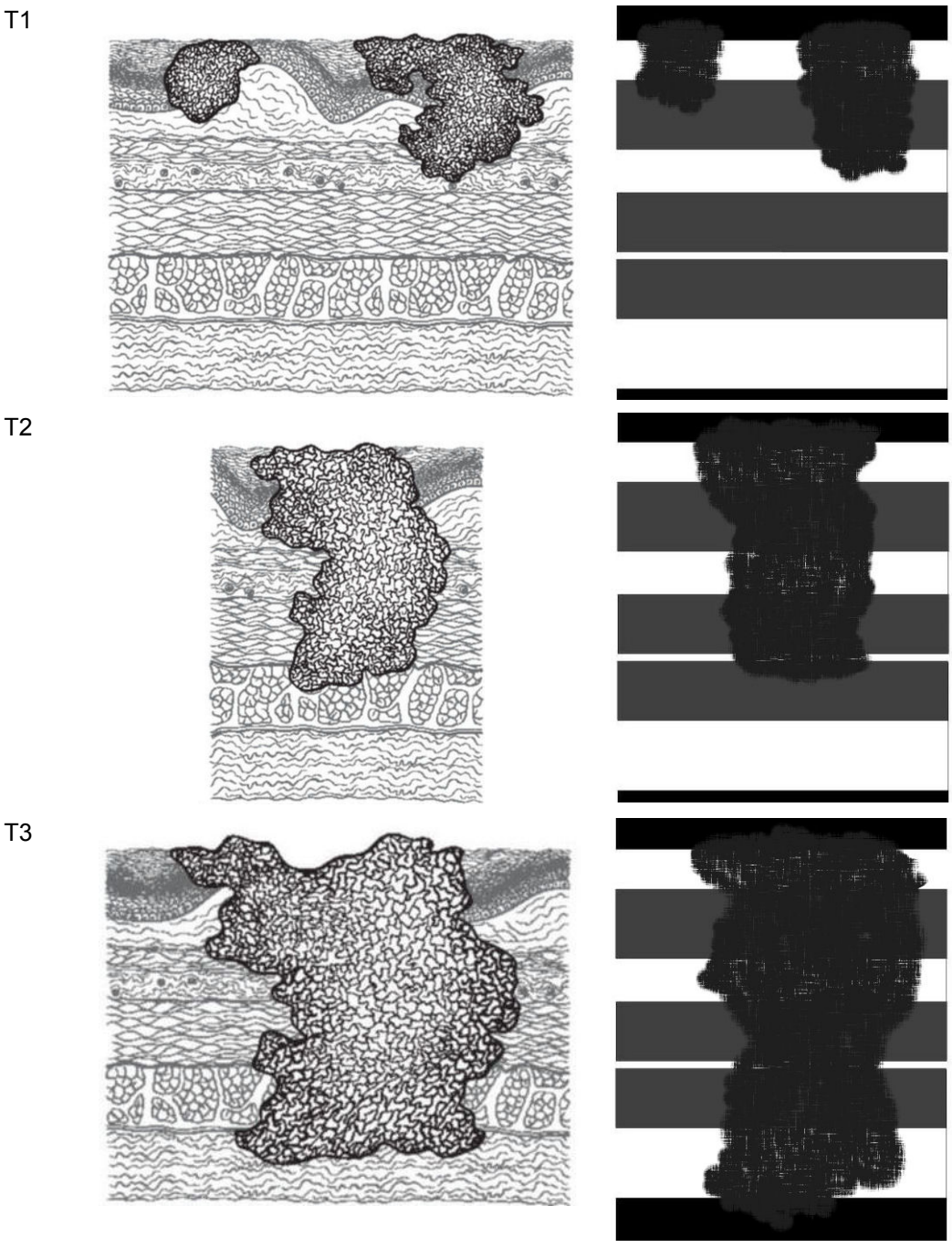

Figure 1.9 – The histological T staging of oesophageal cancer and the idealised corresponding EUS image. (The histological images were modified from AJCC Cancer Staging Atlas (Greene et al. 2006)).

1.5. Three-Dimensional Endoscopic Ultrasound

1.5.1. Basic Principles of three-dimensional Ultrasound

The basic principles of three-dimensional (3D) ultrasound are the acquisition of a series of images that may be reconstructed into a volume for display. At present there are three ways to acquire the images; either by the design and manufacture of specialised transducers (Gee et al. 2003, Akhnak et al. 2002, Smith et al. 2004), the freehand acquisition of a series of images with known positional information (Gee et al. 2003, Gilja 2007, Nelson & Pretorius 1998) as the ultrasound transducer is moved or by a controlled mechanical pullback (Gee et al. 2003, Gilja 2007). These techniques are the most common methods implemented for research systems (Koizumi et al. 2002, Hünerbein et al. 1997, 1999, Tokiyama et al. 1999 Sumiyama et al. 2002, 2005, Molin et al. 1999, 1998, 1998, 1998, Andreassen et al. 2005). The steps required to obtain the volume are:

- **Acquisition & digitisation** – Currently most ultrasound scanners provide analogue video outputs and network connections to PACS systems for the exporting of data. RF outputs are not standard on ultrasound scanners, usually only included in top of the range research scanners. The digitisation of the analogue ultrasound video output can be performed by the use of a frame grabber, or video capture cards. A second process may be required to capture positional data and synchronise with physiological data (ECG) (Gee et al. 2003, Nelson & Pretorius 1998).
- **Storage** – The digitised images and positional information are normally stored locally on the hard drive of the computer for reconstruction.
- **Processing / Reconstruction** - Solberg et al. (2007) reviewed the freehand algorithms used within 3D ultrasound. There are a number of different algorithm based methods that can be used to reconstruct volumes, and can be subdivided into Voxel, Pixel and Function based methods (Solberg et al. 2007). The Voxel Based Method traverses the target volume and gathers information with regards to each voxel. These are the most common techniques used to reconstruct freehand volumes. The Pixel-Based method (PBM) traverses the 2D input images and distributes the information to the target volume and may consist of additional steps. Solberg et al. (2007) concluded that the PBM can be used as a fast real-time reconstruction algorithm. The basic principles of the reconstruction algorithm are the conversion of each image into Cartesian coordinates that will correspond to a point within the volume array. The Function Based method used mathematical interpolation techniques to generate values to fill the gaps between each slice and create a voxel (Gee et al. 2003, Gilja 2007).
- **Visualisation** – The visualisation of the volume data may occur in a number of ways. The most common method for displaying the volume information is slice projection. This is where a planar image is extracted from the volume, with an arbitrary orientation (e.g. Coronal, Sagittal and transverse or axial planes) at a specified location (Gee et al. 2003, Nelson & Pretorius 1998). The volume may be visualised, in three-dimensions using surface or volume rendering techniques to aid manipulation and segmentation of the volume (Gee et al. 2003, Nelson & Pretorius 1998).

- **Analysis** – The basic measurements that can be performed on the volume include dimensional, area and volume. The dimensional measurements are often performed by user interactive calibrated lines placed on the planer images. The area and volume measurements require the user to interactively define the area and by stepping through each plane, the volume may be selected (Gee et al. 2003, Nelson & Pretorius 1998).

1.5.2. Positional Monitoring Techniques

Three-dimensional endoscopic ultrasound transducer research has not progressed to the development of 3D transducers. Therefore this technique is limited to either the controlled withdrawal of the EUS equipment by a mechanical linear stepping motor device (Molin et al. 1998, 1998, Gilja 2007) or the use of a positional monitoring device to monitor the transducers position within three-dimensional space (Mercier et al. 2005). The main advantage of the transducer and positional sensor system is that theoretically, it has an unlimited field of view (Nelson & Pretorius 1998). The technologies applied to positional monitoring devices include:

- Mechanical positional arms with optical or potentiometer sensors within the joints to monitor the location (e.g. Microscribe Positional Digitising arm X to G2X [Immersion Corporation, San Jose, California USA]). These devices are capable of accuracies between 0.04 to 0.23mm RMS and can operate in confined spaces.
- Optical infra-red tracking systems use an active transmitter and either active or passive markers to monitor the location of the transducer within 3D space (e.g. Polaris system [NDI Waterloo, Ontario, Canada]). The optical infra-red devices are capable of accuracies to 0.3mm RMS. However, they require a clear field of view to obtain accurate positional information.
- Optical shape tape uses the properties of the optical fibre and its ability to change its reflection and refraction properties as it is manipulated. A number of fibres are included within the tape at different points to determine the position and shape of the tape (e.g. Shape Tape [Measurand Inc. Fredericton, New Brunswick, Canada]). The accuracy of the system was approximately 1 to 3% of the length of the tape (e.g. 1m tape would have a 10-30mm error at the tip).
- Electromagnetic positional systems generate a shaped electromagnetic field from transmitter coils. As the passive sensor cuts the field, the position is determined (e.g. Aurora system [NDI Waterloo, Ontario, Canada], Ascension Mini-Bird and Micro-Bird [Ascension Technology Corporation, Milton, VT 05468, USA]) (Gee et al. 2003). These systems have an approximate accuracy ranging between 0.9 to 1.8mm RMS.

1.5.3. Three-Dimensional EUS Systems

The concept of three-dimensional EUS (3D-EUS) was first reported in 1989 for the study of gastric tumours (Molin et al. 1999). Since then a number of research groups, worldwide, have been developing various 3D-EUS techniques (e.g. Koizumi et al. 2002, Hünerbein et al. 1997, 1999, Tokiyama et al. 1999 Sumiyama et al. 2002, 2005, Molin et al. 1999, 1998, 1998, and Andreassen et al. 2005). Many groups have specialised on specific EUS systems (e.g. radial, linear echoendoscopes or mini-probes) and positional tracking systems (e.g. mechanical, optical, or electromagnetic). The EUS transducers are inaccessible to standard positional tracking systems, that have been used for 3D medical ultrasound systems (Gilja et al. 1997, 2007, Mercier et al. 2005) and the EUS transducer is constrained in size as it must pass into the GI tract, whereas new 3D US transducers have been developed for the real time display of volumes (Akhnak et al. 2002, Smith et al. 2004).

The benefits of 3D-EUS have not been proven clinically due to the lack of research and commercial systems. However, they have been used within a number of organs of the GI tract, including the oesophagus (Hünerbein et al. 1997, 1999, Tokiyama et al. 1999), stomach (Tsutsui et al. 2005, Sabet et al. 2002), pancreas (Fritscher-Ravens et al. 2005), colon and anus (Kim et al. 2002, Cho et al. 1997). At present there are two systems available:

1. Olympus dual planner mini-probe (UM-DP12-25R and UM-DP20-25R) and 3D upgrade kit (MAJ-1330) for the EU-M2000 (or EU-M60) ultrasound processor unit (Cho et al. 1997, Sabet et al. 2002, Vegesna et al. 2006).
2. Hitachi 6500 or 8500 ultrasound scanners with 3D reconstruction module and the Pentax- Hitachi EG36 series radial or EG 38 UT series linear echoendoscopes (Giovannini, 2008 Kawashima et al. 2006).

Hawes (2004) reported preliminary work being performed by Olympus in the development of a linear scope based 3D EUS system incorporating the Olympus electromagnetic position sensor. However, to date, no other reports have been published documenting this system, which will have a limited field of view. Each of the commercial systems are not without faults, the Hitachi system can be used with both radial and linear echoendoscopes. However it does not monitor the location of the echoendoscope, therefore dimensional and volume measurements will be subject to significant errors. In general, mini-probes have limited penetration due to the frequency and size of the transducer (Okamura et al. 1999). The Olympus Mini-Probe system has a number of limitations:

- Small transducer which has limited penetration.
- Limited travel distance (Z direction max = 40mm).
- Captures between 40 and 120 frames.

The technology to obtain scope positional data has been available within a commercial package since 2002 (Saunders & Shah 2003). In 1993, a scope imager (prototype scope guide) was first reported by Bladen et al. (1993) and Williams et al. (1993) and the first trials were reported by Saunders et al. (1995) and Bell et al. (1999). The Scope Guide system by Olympus (Olympus Medical systems corp. Tokyo, Japan.) uses magnetic positional sensors at discrete points along the length of the insertion tube of the colonoscope. This device was developed as a tool for monitoring the shape and relative position of a colonoscope during abnormal or complex anatomy (e.g. colonic loops or diverticula disease), and its accuracy has not been investigated. However, this technology has not currently been integrated into the EUS scopes possibly due to the increase in the physical diameter of the endoscopes insertion tube making it unsuitable for use within the upper GI tract.

There are three main EUS equipment configurations, the radial echoendoscope, the linear echoendoscope and the EUS mini-probe. Most 3D-EUS systems have been designed around the mini-probe (Cysewska-Sobusiak et al. 2006, Vegesna et al. 2006, Nishimura et al. 1995, Cho et al. 1997, Sabet et al. 2002, Lui et al. 2000, Wallace et al. 2000, Hünerbein et al. 1997, 1998, Tsutsui et al. 2005, and Tokiyama et al. 1999). These systems either have used the commercial Olympus dual planner mini-probe system (Sabet et al. 2002, Cho et al. 1997) or have used linear mechanical, stepper motor controlled pullback systems (Gilja 2007, Molin et al. 1998, 1998, 1998, 1999, Andreassen et al. 2005). These systems have been used to study a variety of GI conditions (e.g. cancer, vascular, GIST) within the oesophagus (Tokiyama et al. 1999, Hünerbein et al. 1997, 1998, Molin et al. 1998), stomach (Sabet et al. 2002, Tokiyama et al. 1999, Tsutsui et al. 2004, Hünerbein et al. 1998, Molin et al. 1998), duodenum (Molin et al. 1998, Tokiyama et al. 1999), bronchus (Andreassen et al. 2005) and colon (Kim et al. 2006, Hünerbein et al. 1998). However, all of these studies have been preliminary, and no definitive data has been published on the advantages and disadvantages of 3D-EUS using the mini-probes. The reported errors with these studies have been ‘fuzzy’ volumes due to motion artefact from the surrounding vascular structure (Kallimanis et al. 1995). Molin et al. (1998) and Hünerbein et al. (1997) showed it was possible to minimise this effect by ECG gating the acquisition of frames by pausing the capture and mechanical withdrawal system during the cardiac cycle.

There has been limited investigation in the use of the radial echoendoscope for the application of 3D-EUS. The first reported study into the clinical use of the radial echoendoscope was performed by Kallimanis et al. (1995), where they investigated a number of GI conditions within the oesophagus. The technique used to withdraw the echoendoscope was to perform a slow manual ‘stabilised’ pullback. Fried et al. (1997) and Molin et al. (1997, 1998, 1999) used mechanical stepper motor controlled pullback systems to withdraw the echoendoscope at a controlled rate. Molin et al. (1998) and Fried et al. (1997) used ECG gating to minimise the motion artefacts observed due to aortic pulsation. Fried et al. (1997) only captured images during the diastolic phase of the cardiac cycle. With the inclusion of 3D reconstruction packages on modern scanners, electronic radial

echoendoscopes have been used to produce volumes (Giovannini 2008, Kawashima et al. 2006). This technique will not be able to produce accurate Z-dimensional and volume measurements due to the lack of positional correction.

The linear echoendoscopes provide a different challenge to the mini-probe and radial systems. Instead of scope withdrawals, the linear system would require a rotational movement to generate a volume. Sumiyama et al. (2002, 2005), Koizumi et al. (2002) and Fritscher-Ravens et al. (2005) have reported the development of linear 3D-EUS systems. The systems developed by Sumiyama et al. (2002) and Fritscher-Ravens et al. (2005) used an electromagnetic sensor attached to the handle of the echoendoscope to monitor its 3D position and rotation as it is manipulated. Where as Koizumi et al. (2002) added an optical shape tape, attached to the insertion tube of the echoendoscope. Each system has shown promise, however there have been few clinical trials reported (Fritscher-Ravens et al. 2005).

There have been several studies of endoluminal volume measurements using the 3D mini-probe based technique, withdrawn by a computer controlled mechanical stepper motor system. The study by Vegesna et al. (2006) created pseudo tumours with known volumes, within an animal model. The 3D pullback was performed using the commercial Olympus 3D-EUS system. The calculated average error between the calculated volume and actual volume was 3.25%. The largest errors within the volume measurements were obtained with the smallest objects and sampling every 10^{th} slice (12.6%). A similar study by Liu et al. (2000), obtained an average error of 8.7%, using an IVUS system to acquire the data. Duplicate CT volume measurements on the pseudo tumours obtained an average volume error of 11.9%. A comparative study of 2D and 3D-EUS, using ridged probes showed an increased accuracy with 2D to 3D staging of 84.8% to 90.9% respectively for early tumours and 75.8% to 84.8% respectively for advanced tumours (Kim et al. 2002). This was performed in a small cohort of patients.

1.6. Ultrasound Phantoms

Ultrasound phantoms are used in ultrasound quality assurance programmes, to compare and evaluate system and transducer performance (Hoskins & Ramnarine 1999, Pye et al. 2004). In addition to specific test objects, there is a growing need for realistic anthropomorphic phantoms for different ultrasound applications. These are required for teaching and training, machine calibration, and assessment of new imaging modalities. Anthropomorphic phantoms have been developed to simulate features of the breast (Madsen et al. 1982), abdomen (Zagzebski et al. 1991), and arteries (Dineley et al. 2006, Ryan and Foster 1997, Brunette et al. 2001, Gatzoulis et al. 2003, Chu & Rutt 1997 Teirlinck et al. 1998, Meagher et al. 2007).

It is important that the various simulated tissue types in an anthropomorphic phantom have appropriate and well characterised acoustic properties: speed of sound, frequency dependence of attenuation, backscatter and reflection. Data on the acoustic properties of different tissue types is scarce (Duck 1990) and published values differ due to a wide variety of factors concerned with measurement technique, tissue type (e.g. muscle, skin, liver) and tissue preparation. International standards and professional bodies have made recommendations with regard to the acoustic properties of Tissue Mimicking Materials (TMM): speed of sound of 1540m/s, as assumed by ultrasound machines, and attenuation coefficient of 0.3-0.7 dB/cm.MHz (AIUM Technical Standards Committee: 1990, AIUM: 1992, IEC 61390: 1997) and 0.5 dB/cm.MHz (IEC 61685 standard 2001).

A variety of materials have been suggested and used in TMM phantoms and test objects (Browne et al. 2003). Many of the materials have poor or inappropriate acoustic properties, particularly with regard to frequency dependence of attenuation and/or speed of sound (Browne et al. 2003). Fluids mixtures (e.g. ethanol and water) are capable of obtaining appropriate speeds of sound (Martin & Spinks 2001).

Tissue mimicking materials with good acoustic properties typically consist of appropriate scattering particles suspended in a water based gelatine or agar material (Teirlinck et al. 1998, Browne et al. 2003, Blechinger et al. 1988, Burlew et al. 1980, Madsen et al. 1978, Madsen 1986, Zagzebski 1991, Ryan and Foster 1997, Ramnarine et al. 2001, Bush & Hill 1983). The use of cellulose scattering particles has been suggested (Rickey et al. 1995), and used to develop an intravascular artery phantom (Brunette et al. 2001) and flow phantom (Rickey et al. 1995, Poepping et al. 2002) although this TMM suffers from poor frequency dependence of attenuation.

A well characterised, agar based tissue mimicking material with good acoustic properties, was used to construct a number of flow, test and QA phantom within Medical Physics, RIE and UoE (Browne et

al. 2003, Ramnarine et al. 2001, Inglis et al. 2006). The TMM's chemical components contribute to specific acoustic characteristics, which are detailed in table 1.2.

Table 1.2 - A breakdown of the chemical components of the TMM and the characteristics that they affect.

TMM Component	**Main Characteristics**
Water / glycerol ratio	Speed of sound within the material. (1540m/s)
Agar	Provides mechanical strength to the material for handling, shaping and use.
Al_2O_3 (3 and 0.3μm)	Attenuation of 0.5dB/cm.MHz.
SiC	Backscatter, or brightness, of the material.
Benzalkonium chloride	An anti-fungal agent that is used to reduce the possibility of fungi growing on to the TMM and deteriorating the surface.

1.7. Characterisation of Ultrasound Equipment

Two standard acoustic measurement methods used to analyse the imaging and beam properties of the ultrasound scanners are hydrophones (Preston et al. 1983, Martin 1988, Harris 1988) and QA or custom phantoms (Pye et al. 2004, Ramnarine et al. 2001). Phantoms are often used to determine imaging properties such as calliper accuracy, spatial and axial resolution, low contrast penetration, near and far field, and transducer dead space (Pye et al. 2004). The hydrophone has the ability to measure the acoustic properties and field characteristics of the ultrasound beam (e.g. positive and negative peak pressures, pulse duration and acoustic working frequency) (Preston 1986, 1986, 1991). By performing specific measurements, it is possible to reconstruct the beam shape (Martin & Fernandez, 1997).

The hydrophone produces an electrical signal that is related to the applied acoustic field (Preston 1986). There are a number of different types of hydrophones available including, needle, membrane, multi-element and fibre optic (Robinson 1991, Hill 2004). There are three types of membrane hydrophones, the coplanar shielded, bilaminar and differential (Preston et al. 1982). There are many advantages and disadvantages to the different types of membrane hydrophone, however, the bilaminar membrane hydrophone provided the best environmental and noise immunity capabilities of the three (Preston 1986). The available acoustic measurement device available within the laboratory was a bilaminar membrane hydrophone that could measure signals up to 20MHz.

The articles by Preston (1986), Harris (1988), Martin (1988) and Bacon (1991) discussed a number of problems faced during hydrophone measurements and the uncertainties. Potential problems that can be faced during the hydrophone measurements include conditions of the water (e.g. temperature changes, bubbles adherent on the surface of the hydrophone, source of the water), distortions due to high amplitude signals, and triggering and sampling rate of the oscilloscope. This can result in a deviation of the average pressures by a few percent. Other stated maximum systematic uncertainties include calibration (±10%), hydrophone electrical loading and hydrophone measurement of the signal (±4%), spatial averaging (±4%), and random uncertainties (±10%) (Preston 1986).

As there has been no hydrophone study of the beam characteristics of the mechanical and electronic radial echoendoscopes, it was difficult to know what to expect from the hydrophone measurements. The GF-UM20 mechanical radial echoendoscope contained two single element transducers at 7.5 to 12 MHz, and changing the image brightness and contrast or the STC (image sector gain) did not alter the transmitted beam. The electronic radial transducer of the GF-UE260 echoendoscope was capable of transmitting frequencies at values of 5, 6, 7.5 and 10MHz and changing the focal depth to 6 individual settings. The difficulty with performing hydrophone measurements on the radial echoendoscopes were that the transducer rotated or was configured as a cylinder.

1.8. Aims and Structure of the Thesis

Having reviewed the literature regarding the application of EUS, and other imaging modalities, to the staging of oesophageal cancer, it was evident that EUS had potential to improve the accuracy of locoregional staging by the application of three-dimensional ultrasound techniques. Various positional monitoring techniques have been used to produce 3D-EUS systems, including mechanical withdrawal. However, no freehand technique has been developed for use with radial echoendoscopes. Studies of mechanical based 3D-EUS systems have shown that it was possible to obtain accurate dimensional and volume measurements, but this is unknown for a freehand system. Also there have been few clinical studies evaluating the usefulness of 3D-EUS. This thesis addresses these three issues. As such, the aims of the thesis are:

- To develop a suitable test object to aid in the development and analysis of three-dimensional EUS techniques;
- To gain an understanding of the echoendoscope and obtain various imaging and acoustic properties of the mechanical and electronic transducer echoendoscopes;
- The develop and evaluate a freehand three-dimensional endoscopic ultrasound technique for use in the oesophagus;
- To clinically evaluate the usefulness of the 3D-EUS technique by the study of early and advanced oesophageal cancer and a number of benign conditions.

Structure of the Thesis

Chapter 1 introduces the fields of endoscopic ultrasound, three-dimensional endoscopic ultrasound and the basic principles of 3D ultrasound imaging. An overview of current EUS equipment and applied technologies is described within this chapter. The clinical applications of EUS and its importance to the investigation of upper GI abnormalities, concentrating on the staging of oesophageal cancer are discussed. The anatomical structures of the oesophagus, important adjacent structures and the ultrasound appearance of the GI are described. The development of ultrasound phantoms, their applications, and the materials used in their construction are discussed. The hydrophone and measurement techniques are also described.

Chapter 2 describes the development of an anthropomorphic endoscopic ultrasound phantom that has known acoustic properties and can be used for the evaluation of the 3D-EUS systems. A recipe for an agar based tissue mimicking material will be modified to vary the acoustic properties. These properties will be measured by a scanning acoustic macroscope, and will be used in the construction of a simple EUS phantom. A number of TMM variants will be manufactured and scanned using an EUS system to assess their suitability for use as the objects and oesophageal wall layers of the phantom. From the development of the simple phantom, various moulding techniques will be

investigated for the manufacture of complex anthropomorphic shapes with known dimensions. Using the results obtained from the characterisation and visualisation of the TMM variants and the development of suitable moulding techniques, a complex anthropomorphic phantom will be constructed for the evaluation of standard and 3D endoscopic ultrasound systems.

Chapter 3 details the characterisation of the GF-UM20 (oldest) and GF-UE260 (newest) echoendoscopes, by a pipe phantom and hydrophone. Various imaging parameters will be measured using the phantom, including near and far field, dead space, and low contrast penetration. The hydrophone will be used to visualise and characterise specific components of the transmitted ultrasound beam.

Chapter 4 describes the development and evaluation of a prototype and version 2 3D-EUS systems. The systems will be evaluated using various EUS phantoms and in the case of the version 2 system, will be used within one clinical case. A comparison of the basic and full positional information will be performed. Various dimension and volume measurements will be performed on the phantoms to determine the accuracy of the developed techniques.

Chapter 5 describes the clinical application of the 3D-EUS systems, developed within this project, for the investigation of early and advanced tumours, and a number of benign conditions. A number of clinical cases of cancerous and benign conditions will be highlighted and reviewed within the chapter. The clinical advantages of 3D-EUS, over existing practices, will be investigated.

Chapter 6 discusses the results from the experimental chapters of the thesis and provides concluding remarks from the thesis. Future work will also be discussed.

Chapter 2 - Development of an Endoscopic Ultrasound Phantom

2.1. Characterisation of Tissue Mimicking Material.

Background

Ultrasound test phantoms have an important role in performing quality assurance and acceptance tests on ultrasound scanners and transducers. Specialist medical ultrasound phantoms, that simulate idealised anatomical and pathological situations, are often used in teaching and within research and development projects. Most ultrasound phantoms have been manufactured to evaluate standard ultrasound transducers. However a small number of phantoms have been manufactured for trans-vaginal or rectal probes.

Ultrasound test phantoms are often manufactured from tissue mimicking materials, so that their measurement results will simulate the clinical performance. Tissue-mimicking materials are manufactured to be equivalent of soft tissues (e.g. liver), and have similar acoustic properties to the tissue being mimicked over the range of diagnostic scanning frequencies. These materials are often designed to mimic the acoustic velocity, attenuation coefficient and scattering coefficient of soft tissue. The recommended acoustic properties for TMM are 0.5dB/cm.MHz for the attenuation coefficient and 1540m/s for the speed of sound (AIUM 1990, IEC 61390: 1997 & IEC 61685: 2001).

There are a number of commercially available tissue-mimicking phantoms. The materials most commonly used are Zerdine™ from CIRS Inc. (Norfolk, VA), urethane rubber from ATS Labs (Bridgeport, CT), and condensed milk gel from Gammex-RMI (Middleton, WI). However, these are often proprietary and their recipes are not available to research groups. Also, the acoustic properties of these materials are often stated at only one frequency and at room temperature. As most endoscopic ultrasound equipment operates between 5 and 12MHz, the frequency range over which the acoustic properties would have to be measured would have to include these frequencies. A number of TMMs have been developed by research groups for the manufacture of ultrasound phantoms and include water based gelatine or agar material with a suspension of appropriate scattering particles, cellulose scattering particles and evaporated milk.

Medical Physics has a wealth of experience in the manufacture of various ultrasound phantoms and in the use of the agar based tissue mimicking material (Teirlinck et al. 1998). To mimic various organs and pathology of the oesophagus (e.g. Aorta and blood, heart, liver, oesophagus wall layers, tumour

and nodes) it would be necessary to alter the acoustic properties of the TMM. Due to the TMM's construction, it would be possible to modify the volume of scattering particles within the recipe and alter its acoustic properties from the recommended properties.

The ingredients of the agar based TMM includes water, glycerol, agar, aluminium oxide, silicon carbide, and benzalkonium chloride. The ratio of the water to glycerol produced the recommended acoustic speed of sound of 1540m/s. Altering this ratio would make it possible to modify the speed of sound from 1480m/s (no glycerol, just water). The benzalkonium chloride was used as an anti-fungal agent to reduce the possibility of fungal growth on the TMM from deteriorating the material surface. The agar provided both the baseline attenuation of approximately 0.12dB/cm.MHz, and the mechanical properties of strength for handling, moulding and scanning and solidity to hold the scattering and attenuating particles in a heterogeneous suspension. The aluminium oxide (3 and 0.3μm) increased the attenuation to the recommended value of 0.5dB/cm.MHz over the desired frequency range (5 to 15MHz). It also minimised the attenuation gradient, observed in pure agar TMM, over the desired frequency range. The silicon carbide particles were used to increase the materials background brightness, or backscatter, to mimic healthy liver parenchyma. Reducing the amount of silicon carbide increases the hypoechoic nature of the material.

This chapter details the manufacture of the agar based tissue mimicking material. The acoustic properties of the TMM with various quantities of scatterer (expressed as a % of the standard TMM scatterer particle content or as the material recipe abbreviation TCP**), were evaluated by a Scanning Acoustic Macroscope. For each of the manufactured tissue mimicking materials, the attenuation, speed of sound and backscatter power was calculated.

Aims

1. To manufacture tissue mimicking material.
2. To modify the recipe of the TMM, using various quantities of scatterer particles, to obtain different acoustic properties.
3. To characterise the attenuation, speed of sound and backscatter of the variants of the TMM using a Scanning Acoustic Microscope.

Materials

Table 2.1 contains the ingredients of the tissue mimicking material used to manufacture the phantoms used to evaluate and test the 3D-EUS systems and where it could be obtained. Table 2.2 details the weights for each component of the TMM material when the particle levels were varied from 0 to 100% for a volume of 500ml. The standard Tissue Mimicking Material relates to the 100% particle concentration recipe and has the acoustic properties of 0.5dB/cm.MHz for the attenuation and 1540m/s for the speed of sound.

Table 2.1- A list of the ingredients of the standard agar based tissue mimicking material.

Ingredients	**% weight concentration**	**Order Code and Manufacturer / Distributor Details**
Water	82.97%	
Glycerol 99% (pure)	11.21%	(G7757) Sigma-Aldrich Company Ltd. The Old Brickyard, New Road, Gillingham, Dorset, UK.
Merck Agar – Agar technical (111925)	3%	(53648 5K) VWR International Ltd. Hunter Boulevard, Magna Park, Lutterworth, Leics, UK.
Al_2O_3 Powder 3µm	0.95%	Logitech Ltd. Erskine Road, Old Kilpatrick, Glasgow, Scotland.
Al_2O_3 Powder 0.3µm	0.88%	
SiC Powder 400 grain	0.53%	
10% Benzalkonium chloride (ADBAC) ($C_6H_5CH_2N(CH_3)_2RCl$)	0.46 %	(09621) (50% solution, diluted to 10%) Sigma-Aldrich Company Ltd. The Old Brickyard, New Road, Gillingham, Dorset, UK.

Table 2.2 – The ingredient weights for each component of the manufactured TMM variant materials for a 500ml volume.

Material	**Particle levels (%)**	**Water (g)**	**Glycerol 99% (g)**	**10% ADBAC (g)**	**SiC 400grain (g)**	**Al_2O_3 3µm (g)**	**Al_2O_3 0.3µm (g)**	**Agar (g)**
TPC0	0	416.47	59.93	24.45	0	0	0	15.9
TPC5	5				0.14	0.25	0.2325	
TPC10	10				0.28	0.5	0.465	
TPC15	15				0.42	0.75	0.6975	
TPC20	20				0.56	1	0.93	
TPC30	30				0.84	1.5	1.395	
TPC40	40				1.12	2	1.86	
TPC50	50				1.4	2.5	2.325	
TPC60	60				1.68	3	2.79	
TPC75	75				2.1	3.75	3.4875	
TPC100	100				2.8	5	4.65	

2.1.1. Tissue Mimicking Material manufacture

The agar-based tissue mimicking material, used to construct the phantom, had the ingredients detailed in Table 2.1. During the development of the phantoms, the stirrer paddle was modified as per Appendix 8. The following steps were followed in the manufacture of the material:

1. The water was measured out into the stainless steel mixing beaker use to manufacture the material. Approximately half of the water was separated into another container. A second small volume of water was separated into a beaker and set aside. Tap water was used as the water source and was degassed during the cooking process. An Ohaus Scout Pro 6kg weighing balance (Ohaus Corp. Pine Brook NJ. USA) was used to measure the fluids.
2. The glycerol and benzalkonium chloride were poured into the mixing beaker, to their desired weights. The tare was activated after each addition.
3. The mixing beaker, with fluids was placed within the water bath. The stirrer paddle was placed into the fluids, as close to the bottom of the beaker as possible, and set at 50 revolutions per minute (rpm). A KIKA EUROSTAR power control-visc overhead stirrer (KIKA Werke GmbH & Co. KG, Staufen Germany) was used to mix the fluids.
4. The water bath was filled with tap water to a level that would deactivate the cut-off of the Techne TE-10D thermo regulator (Techne Ltd. Duxford, Cambridge UK.), but would not float the mixing beaker. The thermo regulator was set to 96°C and allowed to heat the water bath. This is the melting point of the agar.
5. The necessary weights of Aluminium Oxide (Al_2O_3) (0.3μm and 3μm) and Silicon Carbide (SiC) (400 grain) were measured out, depending on the desired acoustic properties (section 2.1.3.) ,using a Sartorius 1202 MP 300g weighing balance (Sartorius AG Goettingen, Germany) and placed in separate containers. Table 2.2 detail the weights for materials TPC0, TPC10, TPC20 and TPC100 materials using particle concentrations of 0, 10, 20 and 100% respectively. For illustration material TPC100, with a recipe for the standard or 100% particle concentration material, is assumed to be manufactured. To cast the surrounding material of the phantom between 3 and 4 litres of TMM was manufactured.
6. After each particle concentration was measured out, the particles were poured into water that had been set aside earlier. The particle / water suspension was stirred to breakup any lumps.
7. The agar was measured out using the Sartorius 1202MP weighing balance and slowly poured into the beaker containing the water and particles. After each addition of agar, the contents was stirred to break up any agar lumps and to maintain the suspension.
8. Once all the agar was introduced and thoroughly stirred, the fluid was slowly poured into the main mixing beaker (already in the water bath). The stirrer speed was set to approximately 90 - 100 rpm. The second volume of water was poured back into the mixing beaker and swilled around to collect any leftover particles.

9. The combined lid for the bath and beaker was lowered into place to ensure that water loss due to evaporation was kept to a minimum. Care was taken to secure the beaker within the guides on the lid so that it would not move during the mixing.
10. The stirrer speed was altered to maintain good particle dispersion, whilst avoiding the creation of air bubbles or a vortex on the surface. Typically the speed was set at 80 rpm.
11. Once a temperature of 96°C was reached within the mixing beaker, it was maintained for one hour. This allowed the agar to dissolve and any air removed from the fluid.
12. After one hour the thermo-regulator was set to 42°C and the mixture allowed cooling to that temperature. Due to the insulation surrounding the tank, it was necessary to substitute quantities of hot water in the tank for cold to aid the cooling process. The water bath and mixing beaker was left to equalise for approximately 30 minutes after each substitution and then repeated. When the material reached 42°C it was poured into a mould. For large batches of TMM, it was placed into a refrigerator to aid the cooling and minimise particle settling.

The TMM manufacturing setup is illustrated in figure 2.1. This consisted of a custom designed tank and stand. The IKA EUROSTAR power control-visc overhead stirrer was attached to the stand and could be raised and lowered. The Techne TE-10D thermo regulator was incorporated into the water bath design.

The acoustic effect of changing the particle concentration of the tissue mimicking material was measured using a scanning acoustic microscope. A series of materials, with recipes denoted by TPC0 to TPC100, were manufactured with the differing concentrations of the Al_2O_3 (3 and 0.3μm) and SiC (400 grain) particles. Table 2.2 details the weights of the components for the varying particle levels used to manufacture the corresponding particle level. A small series of TMM was manufactured to try and obtain an echogenic material. To obtain a noticeably brighter object, under ultrasound, it required significant amounts of particles specifically SiC, approximately 4 times the standard weight, to be included into the mix.

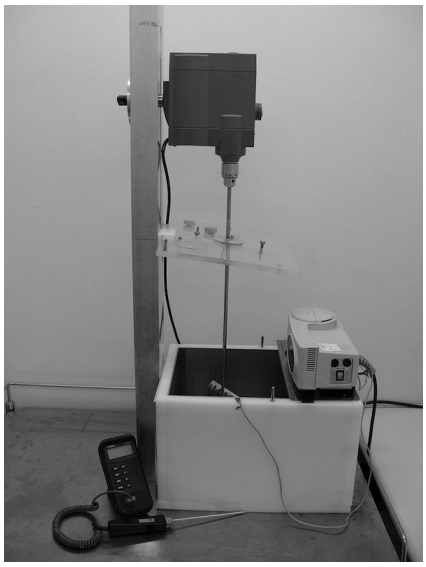

Figure 2.1 - The TMM Manufacturing setup

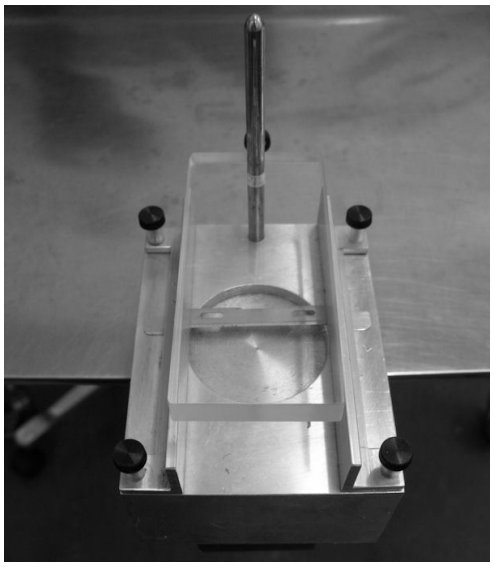

Figure 2.2 - Modified Bench Microtome and sectioning blade, used to obtain accurate TMM samples for analysis in the SAM system. The Perspex top was used to minimise the effects of material lifting while the cut is performed.

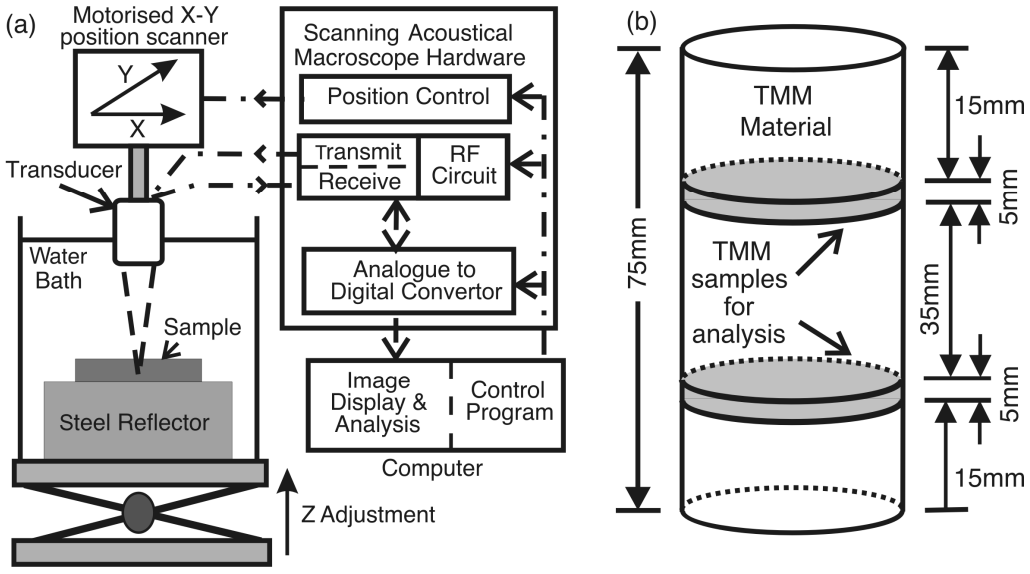

Figure 2.3 - (a) Block diagram of the scanning acoustic micro-scope and acoustic measurement setup. (b) Diagram detailing the positional setup for the sample extraction from each of the manufactured tissue mimicking materials, for acoustic analysis.

2.1.2. Acoustic Measurement Methodology

The acoustic properties were measured using a PC based scanning acoustic macroscope [SAM] (Ultrasonic Sciences Limited, Fleet, UK). The basic SAM hardware consisted of a Master System Controller analogue to digital input/output board allowing software control of the system, a 20MHz pulser receiver and an 8-bit 100MHz analogue to digital converter. The transducer was attached to an X-Y raster scan rig and consisted of computer controlled dual stepper motors with attached screw shafts. This controlled the position of the transducer and enabled a scan area of the sample to be defined. The scan rig was initially positioned over the material using a manual control joystick. The excitation and reflected RF pulses were visualised and acquired using the SAM digital storage oscilloscope display. To increase the sampling rate of the digitiser to 100MHz, the capture window was reduced to a size of approximately 20μs and set to only acquire the reflected RF pulse.

Samples of each of the manufactured materials were cut, using a modified bench microtome and sectioning razor (figure 2.2), into 25mm diameter by 5mm thick cylinders and each of the acoustic properties (attenuation, backscatter and speed of sound) was measured using the scanning acoustic microscope.

The acoustic properties were measured using the pulse echo substitution technique, in which the reference echo signal from a 20mm thick plane steel reflector was compared with the signal after insertion of the sample in the water path (see Fig. 2.3a). A wideband, 7 MHz centre frequency, focused transducer was used as a transmitter and receiver and was aligned perpendicular to the plane reflector. The transducer had a diameter of 1.4cm, a focal length of 5.4cm and a –6dB beam width of 0.5 mm at the focus. The active element of the transducer was a concave single element, with a focal length defined by the distance from the transducer face to the axial pressure maximum. The water bath was filled with tap water and left for four hours to ensure no bubbles generated due to the filling process were present and that the temperature of the water had stabilised to room temperature (nominally 20 ± 0.4ºC). Boiled water was also used within the water bath and allowed to cool before proceeding with the acoustic measurements.

Two samples were cut at different depths from the same batch of material, as per fig. 2.3b. The test sample was placed into the water bath for approximately 5 minutes, during which diffusion of the glycerol was assumed to be negligible.

To perform the attenuation and speed of sound measurements, the steel reflector was positioned at the transducer's focus point. Figure 2.4 waveform 1 shows the location of the excitation pulse transmitted by the SAM transmitter. The attenuation measurement excitation pulse was set at 100V and the SAM digitiser attenuation set between 10 to 55dB. Three separate measurements were performed:

1. The acquisition of the reference waveform, where the echo RF signal from only water and the steel reflector was acquired (Figure 2.4 waveform 2). The reference waveform was also used to split and align the sample waveforms.
2. The acquisition of the sample waveform, where the TMM sample was placed on the surface of the steel reflector and the echo signal, obtained from the steel reflector, was acquired. This echo signal waveform would have been altered, in speed and amplitude, as it passed through the sample (Figure 2.4 waveform 3).
3. To calculate the thickness of the sample, a third waveform was acquired where the amplitude of the excitation pulse was increased to 400V and the SAM digitiser attenuation set between 10 to 55dB. With the TMM sample still in place from measurement (2), the echo signal was obtained from the steel reflector and sample, was acquired (Figure 2.4 waveform 5). It was necessary to ensure that the signal received from the TMM surface was maximised and that all other measurement parameters were constant from the previous measurements.

The transducer was made to perform a 16 by 16mm raster scan over the sample of tissue mimicking material, at a step size of 1mm. At each step, the reflected RF signal from the steel reflector was digitised at a sampling rate of 100 MHz and stored. Custom designed analysis software developed using Matlab ™ (The Mathworks Inc, Massachusetts, USA) was used to calculate the acoustic properties from the raw RF data and display an image of attenuation, speed of sound and backscatter power at specified frequencies of the FFT. The mean results were obtained by analysing the RF signals received from a 16 by 16mm sample area, with two hundred and fifty six RF signal pairs. The attenuation was calculated from the log difference between the FFT of the sample spectrum and the reference spectrum, using equation 2.1 (Bamber, 2004).

$$\alpha(x, y, f) = -\frac{10}{2d}\log_{10}\frac{I(x, y, f)}{I_o(x, y, f)} \qquad \text{Eq. 2.1}$$

Where α(x, y, f) is the attenuation in dB/cm at frequency f and position x, y of the sample, d was the sample thickness, I (x, y, f) was the power spectrum intensity at frequency f and position x, y through the sample, I_o(x, y, f) was the power spectrum intensity at position x, y and frequency f of the reference signal with no sample in the path. The calculation was performed on each of the two hundred and fifty-six RF signals.

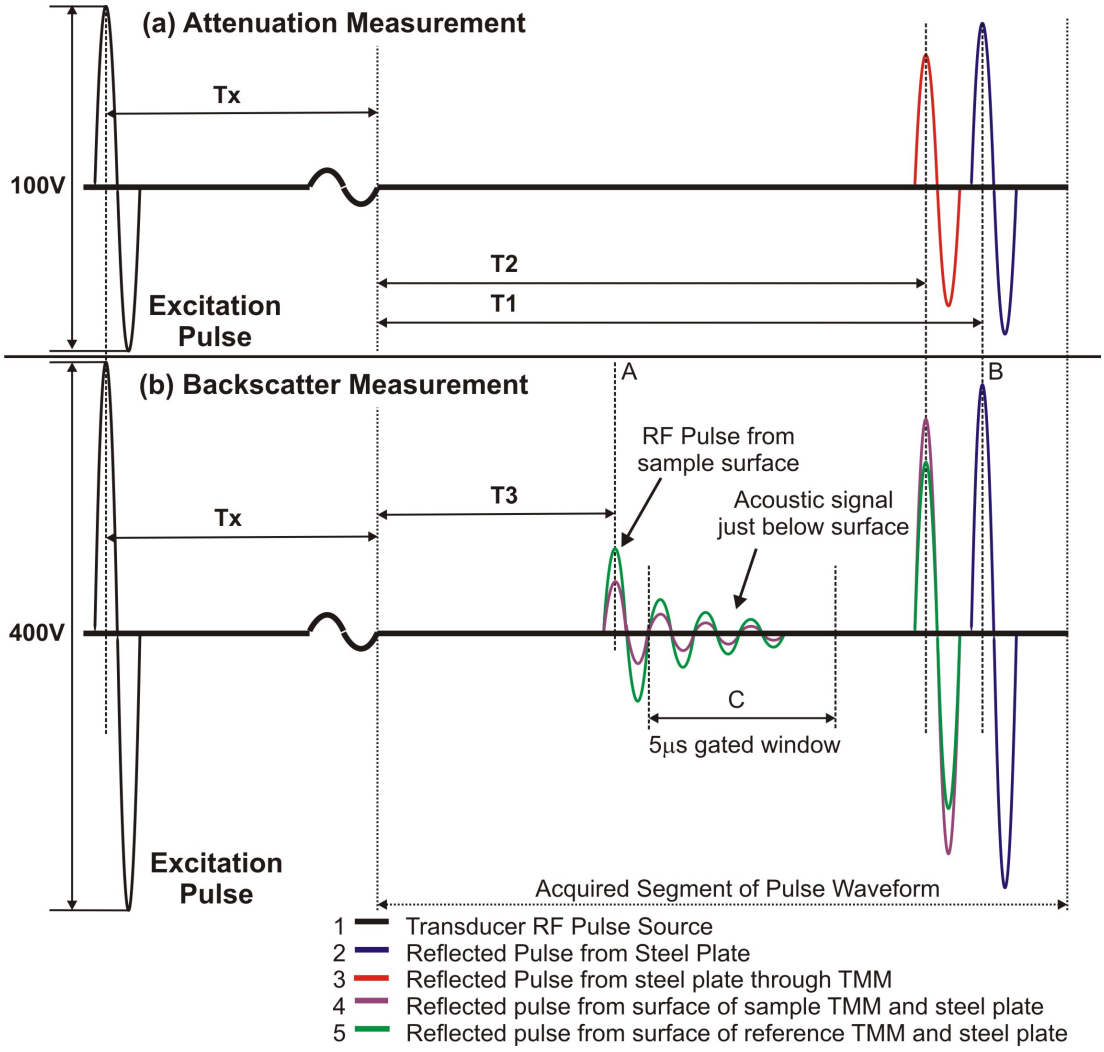

Figure 2.4 Example of idealised waveforms obtained from the SAM system during the (a) Attenuation measurements and (b) the backscatter power measurements. Where T1 is the time taken from Tx to the reflected pulse maximum from steel plate through water, T2 is the time taken from Tx to the reflected pulse maximum from steel plate through water & TMM sample, T3 is the time taken from Tx to the maximum of the TMM sample surface reflection pulse and Tx is the time from the excitation pulse to start of pulse recordings and is constant throughout the measurements.

To perform backscatter power measurement, the steel reflector was positioned at the transducer's focus point for the reference alignment frame and altered to just below the sample surfaces for all other backscatter measurements. The minimum sample thickness of each material was used to guide the focusing of the SAM system and was obtained from the previous thickness measurements (measurement 3). The backscatter measurement amplitude of the excitation pulse was increased to 400V and the SAM digitiser attenuation set between 10 to 55dB, to increase the signal to noise ratio of the received signal and ensure that the surface signal was distinguishable from the noise. Three separate measurements were performed:

1. The acquisition of the reference alignment waveform was a duplicate measurement of attenuation reference signal, where the echo signal from only water and the steel reflector was acquired (Figure 2.4 waveform 2). This data set was used to split and align the backscatter reference and sample datasets within the analysis software.
2. The acquisition of the sample reference waveform, where a sample of the TPC100 material was used as the reference object and the focus was shifted to below the TMM surface. With the reference TMM sample in place, the echo signal acquired was from the steel reflector and sample (Figure 2.4 waveform 5).
3. The acquisition of the test sample waveform, where each of the cut TMM samples were placed on the steel reflector and the transducer focus altered to just below the TMM surface With the TMM sample in place, the echo signal acquired was from the steel reflector and sample (Figure 2.4 waveform 4).

During the acquisition of all waveforms, the SAM capture settings for timebase remained constant and water, at room temperature (20°C), was used as the measurement transmission medium.

For the backscatter power measurements, the focus was altered to just below the surface of each sample. The reference backscatter power signal was obtained from the TCP100 TMM recipe. The three separate waveforms were loaded into the analysis software. The alignment waveform was used to split and align the two backscatter waveforms. A 5µs gate window was applied to the split RF signals just after the TMM surface reflection and at the transducer focal point (Figure 2.4 point (C)). This avoided interference due to the reflection from the TMM sample surface and minimised sample attenuation affecting the backscatter power measurement. A 2048 point Fast-Fourier Transform (FFT) was calculated on the windowed data, at each SAM measurement point on the 16 x 16 mm scan. The backscatter power was calculated using equation 2.2, where I was the FFT calculated from the test samples and I_o was the FFT calculated from the reference TMM material (TCP100 or 100% particle scatterer particles). To improve the signal to noise ratio, the calculated waveform was averaged over the 16 x 16 mm scan, and the backscatter power was determined as the value at the transducer centre frequency of 7MHz, expressed in dB.

The backscatter power was calculated from the log difference between the FFT of the sample spectrum and the reference spectrum, using equation 2.2 (Bamber 2004).

$$\mu(x,y,f) = -10\log_{10}\frac{I(x,y,f)}{I_o(x,y,f)} \qquad \text{Eq. 2.2}$$

Where μ(x, y, f) is the backscatter power at frequency f and position x, y of the sample, I (x, y, f) was the power spectrum intensity at frequency f and position x, y through the TMM sample, I_o(x, y, f) was the power spectrum intensity at position x, y and frequency f of the reference TMM sample (TCP100). The calculation was performed on each of the two hundred and fifty-six RF signals.

Inglis et al. (2006) described the uncertainties expected for the attenuation and speed of sound measurements. A previous study of the SAM system performed within the Department to determine the random uncertainty from repeat measurements of the attenuation was less than ± 0.03 dB over the frequency range 3-10 MHz and included the errors in sample thickness measurement, reflection, diffraction, nonlinear propagation, alignment, and temperature (Bamber 2004). Estimated systematic uncertainty due to equipment was <0.2dB (e.g. noise, transducer stability). The estimated systematic uncertainty within homogeneous samples was <1dB (e.g. temperature, sample thickness, reflection, nonlinear propagation).

From a study performed on standard silicone oil reference cells supplied by the UK National Physical Laboratory (NPL, Teddington, UK), the measured attenuation was within 5% of the NPL reference cell. It was estimated that the overall uncertainty in attenuation measurement was ± 5%. Nonlinear propagation of the RF pulse became apparent at high acoustic pressures and was estimated to be less than 2% of the maximum acoustic pressure of the pulse and the nonlinear loss was restricted to the fundamental frequency, at the distances used for the SAM measurements. Nonlinear propagation manifested as distortions to the shape of the RF pulse, which increased with increasing distance. To minimise the nonlinear propagation a lower power excitation pulse was applied to the SAM system's transducer crystal.

To determine the thickness at each measuring point upon the sample, the third waveform was captured at a higher excitation pulse voltage of 400V. Within the analysis software, a mask was created to determine the surface position of the sample, at each point. A second mask was created to determine the surface position of the steel reflector. The thickness was determined from the time difference between the position of the sample surface (A) and the surface of the steel reflector (B) (Figure 2.4) and calculated by equation 2.3. The maximum variation in the thickness obtained from the analysis of 22 samples was 10%. The average variation in the sample thickness, over all samples, was 4.5% ± 2%.

$$d = c_w * (T1 - T3) \quad \text{Eq. 2.3}$$

where d was the thickness of the sample (mm), c_w was the speed of sound in water (speed of sound in water is 1481 m/s at nominally 20 ± 0.4 ^{o}C), T1 is the time taken from Tx to the reflected pulse maximum from steel plate through water and T3 is the time taken from Tx to the maximum of the TMM sample surface reflection pulse . Two hundred and fifty-six RF signals were stored and analysed.

The speed of sound in the material was calculated from the difference between the time taken for the RF pulse to travel to and from the plane reflector with and without the sample in the path using equation 2.4:

$$\frac{1}{c_s} = \frac{1}{c_w} - \frac{\Delta T}{2d} \quad \text{Eq. 2.4}$$

where c_s was the speed of sound through the sample (m/s), c_w was the speed of sound in water (speed of sound in water is 1481 m/s at nominally 20 ± 0.4 ^{o}C), ΔT is the time-shift and calculated by equation 2.5 and d was the thickness of the sample (mm). Two hundred and fifty-six RF signals were stored and analysed.

$$\Delta T = T1 - T2 \quad \text{Eq. 2.5}$$

Where T1 is the time taken from Tx to the reflected pulse maximum from steel plate through water, T2 is the time taken from Tx to the reflected pulse maximum from steel plate through water & TMM sample.

A previous study of the random uncertainty in the measurement of speed of sound was ± 0.2 m/s. The estimated systematic uncertainty was ± 0.15%. Examples of the estimated systematic uncertainties were temperature, water speed accuracy, alignment, digitisation, noise, time base accuracy, sample thickness. The SAM system measurements of speed of sound were validated using liquid reference cells (5,10 and 15mm thickness) containing Dow Corning 710 silicone fluid supplied by the UK National Physical Laboratory (Zeqiri 1991, 1989). The NPL stated values for speed of sound within the 5mm reference cell at 7MHz was 1378m/s, measured at 21.5^{o}C. It was estimated that the overall uncertainty in speed of sound measurement was ± 0.15%.

It must be noted that due to the lack of a national standard backscatter reference cell, and the wide differences, across laboratories, in the measurement of backscatter, it was not possible to characterise the uncertainties involved with the backscatter measurements.

2.1.2.1. SAM analysis program

The SAM analysis program was written to provide a tool capable of analysing the data exported from the SAM system. The main components of the SAM analysis program are listed within Appendix A.5.1 to A.5.3. The exported data '*.vol' file was a binary file and required the removal of header information and conversion into the Matlab workspace. As all of the data was stored in a single stream of data, it was necessary to select and split the data into an array for each pulse from the SAM pulser for the 16 x 16mm scan. This was done by low pass filtering the data and obtaining a logical mask using a comparative routine that compared the filtered reference signal with a set level that was above the noise level of the measurement. The RF signal peaks of the reference frame were detected and an index was created detailing their position in the data file. This index was used to split each of the reference and data frames into individual measurements, all stored into one reference and data arrays. For each pulse, the speed of sound and thickness of the sample was calculated and stored in separate arrays. The thickness was calculated using equation 2.3.

A routine was created to initially calculate the fast Fourier transform (FFT) of both the reference and data pulse arrays. The FFT was calculated as a 2048 point discrete FFT and only the first 512 points were saved as this corresponded to the frequencies of interest. The 2048 point FFT was performed to obtain sufficient sampling points in the frequency region of interest for different SAM transducers (up to 20MHz). Once the FFT was stored within corresponding arrays, the attenuation was calculated as in equation 2.6:

$$\alpha = -\frac{10}{(2 \times d)} \times \log_{10}\left(fft(data) \Big/ fft(ref) \right) \qquad \text{Eq. 2.6}$$

Where α is the calculated attenuation (dB/cm), d is the sample thickness (cm), fft(data) is the results of the FFT of the data, and fft(ref) is the results of the FFT of the reference frame. A mean FFT for both the reference and sample data was calculated and the average attenuation was calculated as in equation 2.7:

$$Ave\_\alpha = -\frac{10}{(2 \times Ave\_d)} \times \log_{10}\left(Ave\_fft(data) \Big/ Ave\_fft(ref) \right) \qquad \text{Eq. 2.7}$$

Where ave_α is the calculated average attenuation, ave_d is the average sample thickness (mm), ave_fft(data) is the results of the average FFT of the data, and ave_fft(ref) is the results of the average FFT of the reference frame.

The backscatter power was calculated by modifying the Matlab code from the attenuation equations 2.6 and 2.7 to equations 2.8 and 2.9. Using a window selection tool, a user defined region of interest (Figure 2.4 C) was selected and the FFT calculated as a 2048 point discrete FFT. Only the first 512

points of the FFT were saved, corresponding to the frequencies of interest. Once the FFT was stored within corresponding arrays, the backscatter power was calculated using equation 2.8:

$$\mu = -10 \times \log_{10}\left({fft(data)}/{fft(ref)} \right) \qquad \text{Eq. 2.8}$$

Where μ is the calculated backscatter power, fft(data) are the results of the FFT of the data, and fft(ref) are the results of the FFT of the reference sample frame. A mean FFT for both the reference and sample data was calculated and the average attenuation was calculated as in equation 2.9:

$$Ave\_\mu = -10 \times \log_{10}\left({Ave\_fft(data)}/{Ave\_fft(ref)} \right) \qquad \text{Eq. 2.9}$$

Where ave_μ is the calculated average attenuation, ave_fft(data) are the results of the average FFT of the data, and ave_fft(ref) are the results of the average FFT of the reference sample frame. The power value at the 7 MHz centre frequency of the focused transducer was the calculated backscatter power for the material, with reference to the reference sample.

The speed was obtained by calculating the difference between the peaks of the RF reference frame and the data frame, and then using equation 2.10, the speed of sound in the sample was calculated:

$$\frac{1}{c_s} = \left(\frac{1}{c_r} \right) - \left({\left(\frac{\Delta tp}{f_s} \right)}/{(2 \times d)} \right) \qquad \text{Eq. 2.10}$$

Where c_s is the calculated speed of sound in the material, c_r is the speed of sound in the reference medium (m/s), Δtp is the number of samples separating the peak of the data and reference pulses, f_s is the sampling frequency of the SAM system, and d is the sample thickness (mm).

The results were displayed in two forms. The first graphical display is displayed in figure 2.5a which illustrates the data in graph plot form. Using this visualisation toolset enabled the analysis of calculated attenuation and FFTs, pixel by pixel from the constructed surface plot, as well as display the average values for the calculated acoustic parameters. To visualise and analyse the backscatter power, the graph plot was used. The second method for display was the surface plot of each of the calculated parameters (e.g. attenuation, speed of sound, and thickness). A 3D array of attenuation surfaces corresponding to each step of the FFT's frequency components was constructed. Basic axis and colour controls enabled the alteration of the scaling of the data to optimise the views. A 3D surface plot was used to display the data, examples of attenuation, speed of sound and thickness plots are shown in figures 2.5 b to d. Within the software it was possible to select a region of interest to remove faulty data that may be due to misalignment of the sample. The data shown was captured from a sample of TCP100 TMM.

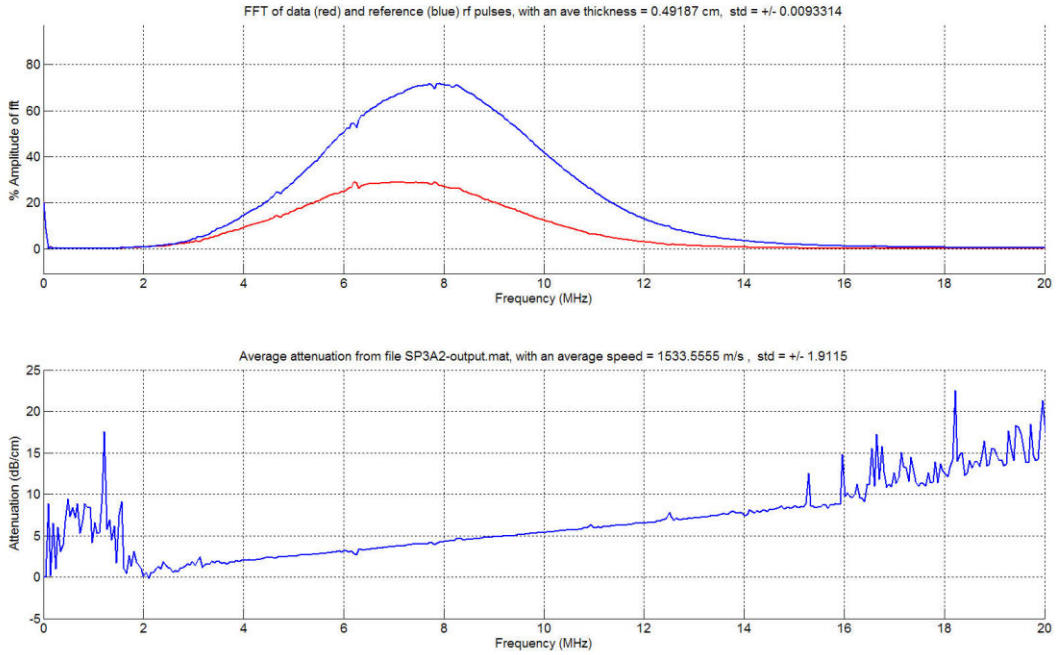

2.5 (a) X-Y graph plots of the average FFTs of Data (red) and reference (blue) RF pulses and the average attenuation (dB/cm) plotted against frequency (MHz).

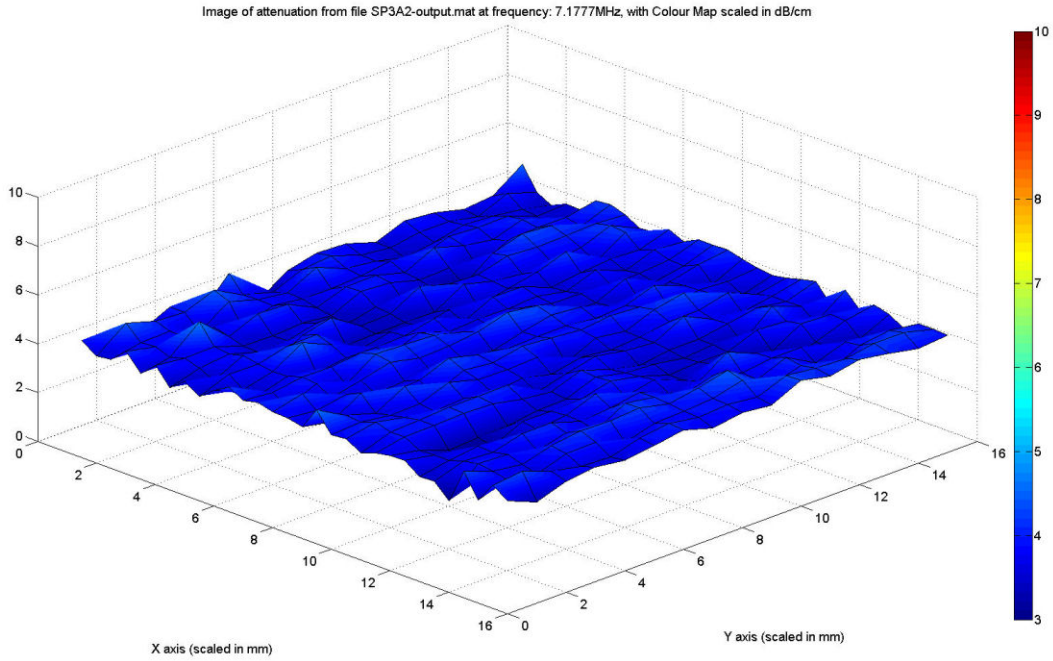

2.5 (b) A 3D surface plot of attenuation at a frequency of 7MHz of the FFT (centre frequency of the wideband transducers was 7MHz).

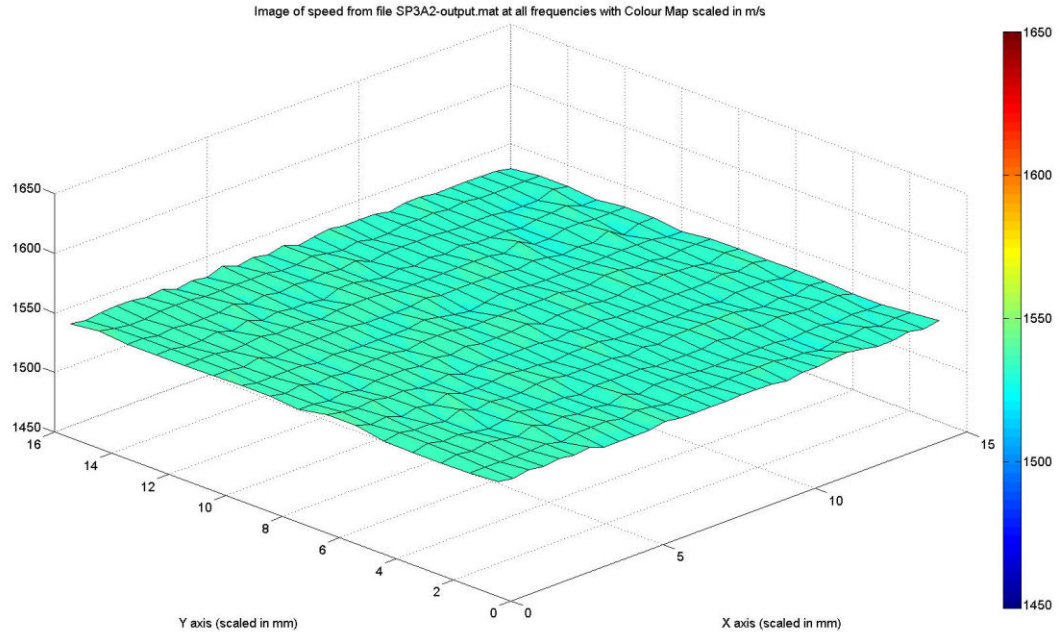

2.5 (c) A 3D surface plot of the distribution of speed of sound in the material

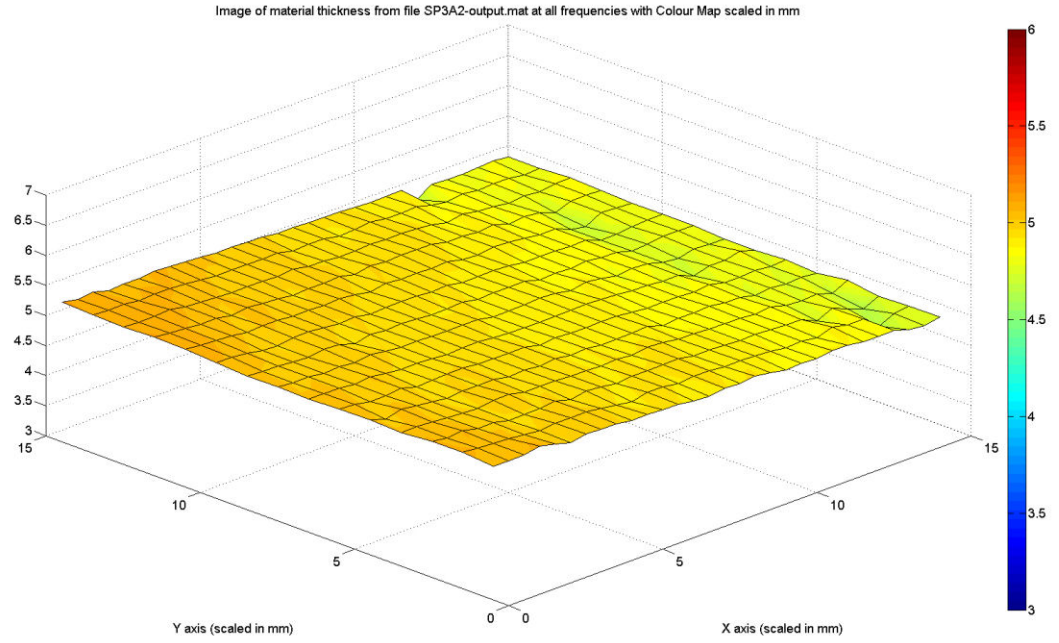

2.5 (d) A 3D surface plot of the distribution of TMM sample thickness over the scan plane of the SAM system.

Figure 2.5 - Example plots obtained from the SAM analysis toolbox written in Matlab.

2.1.3. Acoustic Measurement Results

Eleven different particle concentration TMM samples were manufactured and the acoustic properties (attenuation, speed of sound and backscatter power) were measured. The TMM samples of different particulate concentrations had attenuation coefficients which varied between 0.12 to 0.5 dB/cm.MHz, backscatter power between 0 to -12.2 dB relative to the TCP100 TMM recipe (or 'normal' TMM) and an average speed of sound of 1537 ± 1.9 m/s (mean ± 1 standard deviation). Table 2.3 summarises the averages of the acoustic properties of attenuation, backscatter power (both at 7.5MHz), and the average speed of sound of the material. The acoustic properties of attenuation and backscatter at 7.5MHz were displayed as this is the frequency most common to all existing echoendoscopes. The gradient was obtained from the calculated equation of the line of linear best fit to the attenuation data, for each particle concentration, between 4 and 18MHz.

A graph showing the relationship of the average attenuation coefficient (n = 2) plotted as a function of the frequency for the eleven TMM particulate concentration samples is shown in figure 2.6. The graph was displayed as the attenuation coefficient as a function of frequency, versus frequency and indicated the frequency dependence of the attenuation for each of the materials. To obtained the gradient of the attenuation a linear line of best fit ($Y = mX+c_o$, where m is the gradient of the line and c_0 is the offset from the centre) was applied to each of the plots of attenuation (dB/cm.MHz) of each particle concentration. Table 2.3 illustrates that the gradient decreased as the particle concentration increased. The reduction in gradient of the linear line of best fit with increased particle concentration illustrates the reduction of the frequency dependence of the attenuation.

Single attenuation readings were taken at 7.5MHz, 10MHz & 12MHz. The frequencies were chosen as they correspond to the implemented frequencies of the transducers in most diagnostic and therapeutic EUS systems. Figure 2.7 illustrates the linear relationship between averaged attenuation and particle concentration over the set frequencies. The mean attenuation was obtained by averaging the calculated attenuation at chosen frequencies of the two samples taken at different depths (35mm separation) (n = 6). The graph is displayed as an average of the two samples at three different frequencies to enable the selection of a particle concentration for a set attenuation over the operating frequency range of the EUS system (7.5 to 12 MHz). The error bars are +/- two standard deviations from the mean. The plot illustrates that the attenuation has a linear trend between 0.15 and 0.5 dB/cm.MHz with increasing scatterer particle concentration.

Table 2.3 - Summary of the properties obtained from the Scanning Acoustic Microscope. The attenuation and backscatter were displayed as an average at a frequency of 7.5MHz on the attenuation plot (figure 2.6) and of two mean values calculated from the 16 x 16 mm sample scan. The speed of sound was the mean value, calculated same scan dimensions. The gradient was obtained from the linear line of best fit of each of the plotted attenuation data (figure 2.7).

Material Recipe	Particle Concentration (%)	Average Attenuation (dB/cm.MHz) or [(dB/cm)]	Average Backscatter Power (dB)	Average Speed of Sound (m/s)	Gradient
TCP100	100	0.501 [3.79]	0	1538.1	$4x10^{-6}$
TCP75	75	0.420 [3.10]	-1.05	1538.3	0.0003
TCP60	60	0.376 [2.83]	-1.85	1534.4	0.0006
TCP50	50	0.337 [2.53]	-2.8	1536	0.0015
TCP40	40	0.294 [2.20]	-3.75	1535	0.0025
TCP30	30	0.264 [1.98]	-5.07	1535	0.0032
TCP20	20	0.228 [1.73]	-6.85	1535.3	0.0036
TCP15	15	0.202 [1.50]	-8.35	1536.5	0.0045
TCP10	10	0.173 [1.30]	-9.55	1536.5	0.0047
TCP5	5	0.159 [1.17]	-10.6	1538.2	0.0054
TCP0	0	0.124 [0.93]	-11.85	1540.4	0.0055

Figure 2.8 shows the logarithmic relationship between the backscatter powers with increasing particle concentration at 7.5MHz from 2 samples of the same material (as per fig. 1B). Reducing scatterer concentration by 50% and 75% reduced backscatter power by 50% (-3dB) and 75% (-6dB). Between 100% and 10%, the results show good agreement with the ideal logarithmic trend of the backscatter power. Due to this logarithmic nature of the backscatter with this TMM recipe, it would be difficult to obtain a significant increase in the brightness of the TMM without using different scattering particles or the addition of large quantities of SiC particles.

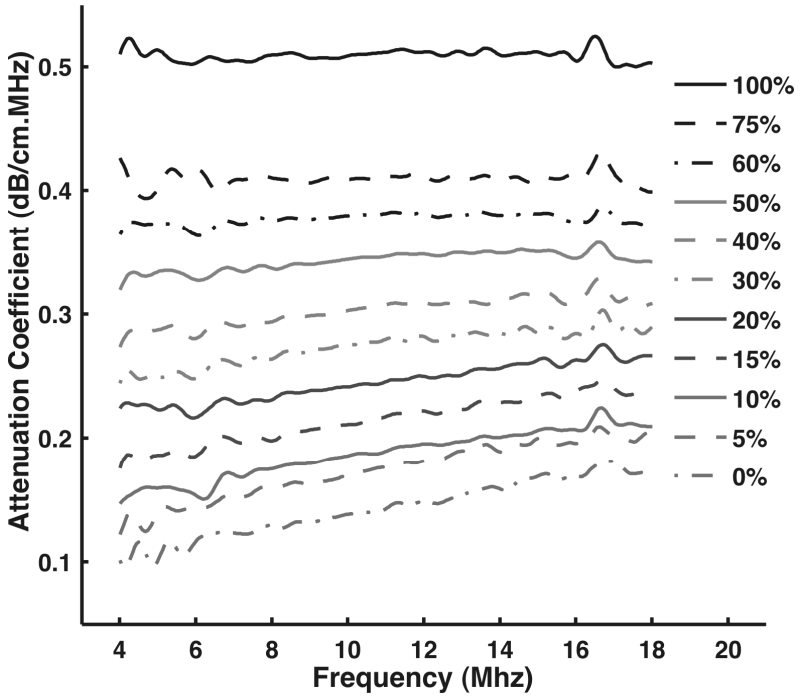

Figure 2.6 - The average attenuation coefficient of the extracted sample (n=2), plotted as a function of the frequency for a range of TMM particulate concentrations. X-Axis was frequency of the calculated FFT (MHz) and Y-Axis was the Attenuation calculated as a function of frequency (dB/cm • MHz).

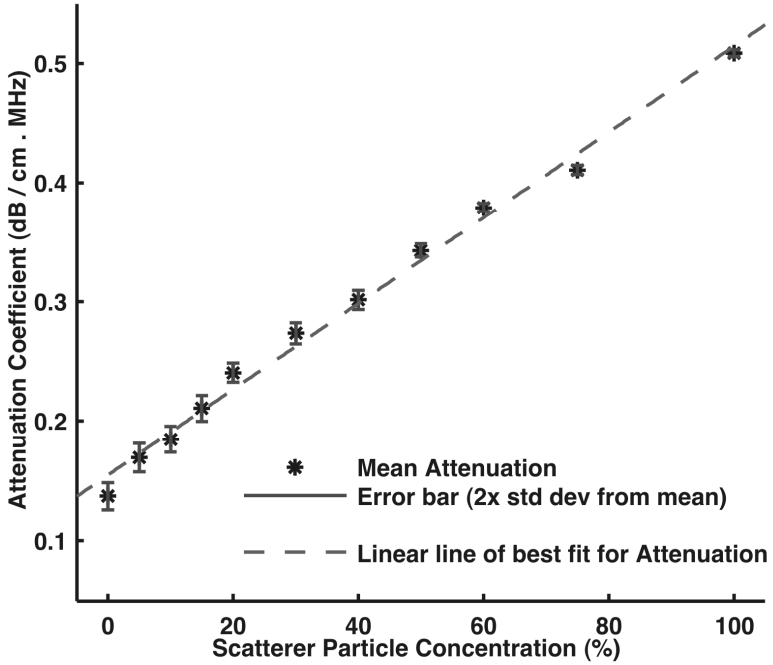

Figure 2.7 - The mean attenuation against the particle concentration obtained from measurements of two samples at frequencies of 7.5, 10 and 12MHz of the FFT. The error bars indicate +/- two standard deviations. X-Axis was Scatter particle concentration (%) and Y-Axis was the Attenuation calculated as a function of frequency (dB/cm • MHz).

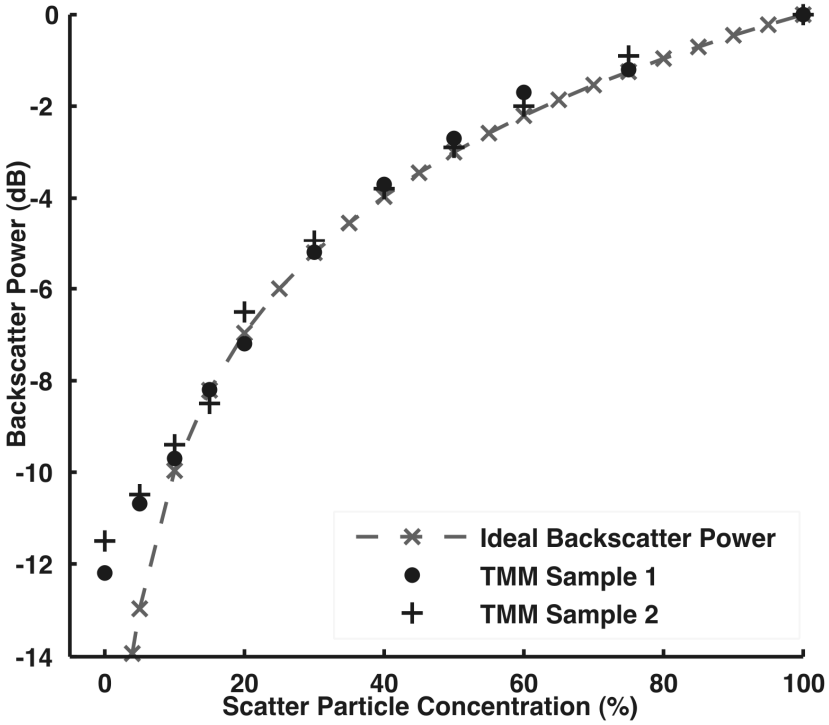

Figure 2.8 - The backscatter power relative to 100% particle concentration of the standard TMM measured at 7.5MHz. The particle concentration was plotted as a function of the backscatter power. X-Axis was Scatterer particle concentration (%) and Y-Axis was the backscatter power (dB).

2.1.4. Discussion

The agar based tissue mimicking material was successfully modified and manufactured using the recipes in table 2.1 and the protocol detailed in section 2.1.1. The TMM was characterised using the scanning acoustic microscope for eleven different recipes. The attenuation, speed of sound and backscatter was measured to obtain the relationship for each acoustic parameter (attenuation, speed of sound and backscatter) with decreasing particle concentration. It was possible to vary the attenuation from 0.12 to 0.5dB/cm.MHz and the backscatter power from -12 to 0dB (referenced to normal or the TCP100 TMM recipe). By maintaining the ratio of water to glycerol, the speed of sound was maintained at approximately 1540m/s. Using figures 2.7 and 2.8 it would be possible to select different TMM recipes to obtain chosen acoustic properties over the normal operating frequencies of the EUS equipment (e.g. 7.5, 10 and 12MHz).

These results would enable an individual to design a phantom containing variants of the normal tissue mimicking material (TCP100) which would mimic the ultrasound features of the GI tract and pathological structures associated to disease (e.g. cancer). The desired acoustic properties of the normal agar based tissue mimicking material were the speed of sound of 1540m/s, and an attenuation coefficient of 0.5 dB/cm.MHz.

2.2. Mark 1 Phantom development.

Background

Ultrasound test phantoms are commonly used in quality assurance and performance testing of ultrasound equipment. Most QA phantoms are used to test axial resolution, lateral response width, uniformity, dead zone measurements, depth of visualisation, high and low contrast mass imaging, and spatial calibration. Specialised teaching ultrasound phantoms have been developed to simulate anatomical, pathological and physiological situations to train medical staff in measurements, image guided biopsy and treatment therapies (e.g. Doppler, vascular flow, brachytherapy). Endosonography is a specialised field that requires significant training and expensive equipment, often limiting it to large acute hospitals that perform upper GI surgery. Few centres perform QA on these devices. They rely on the clinician to diagnose faults with their ultrasound equipment. To date, there are very few commercially available endoscopic ultrasound phantoms, and none suitable for use in the development and evaluation of a 3D-EUS system.

From the measurement of the acoustic properties, the modification of the TMM recipe, and the selection of complex moulds, it would be possible to manufacture a complex phantom for use with endoscopic ultrasound equipment. The development of the mark 1 phantom would allow for the visual inspection of variants of tissue mimicking material recipes to obtain the most suitable materials for the construction of an EUS phantom and simulate the anatomy and pathology of the oesophagus.

This chapter details the initial development of an endoscopic ultrasound phantom to be used for the visual evaluation of the TMM variants and employed construction techniques. Everyday objects were selected for their suitability for use as moulds for the phantom. Objects were chosen to show changes in shape and dimension within a 3D reconstruction to indicate movement of the echoendoscope (e.g. measuring flasks, candle mould, measuring spoons, egg holders) and accuracy of the 3D reconstruction techniques and measurements.

Aims

1. To investigate a series of everyday objects to be used as object moulds.
2. To use the characterised materials to construct a phantom.
3. To modify the construction to obtain the best combination of particles for the phantom.

Materials

A number of everyday objects were chosen to act as moulds for the embedded objects and consisted of small measuring flasks, candle mould, measuring spoons, egg holders, and plasticine concave shapes (examples shown in figure 2.9). A mould created to manufacture the layer is illustrated in figure 2.10a, and the water tight container shown in figure 2.10c was purchased. The Olympus EU-M30 processor and the GF-UM20 and 200 echoendoscopes were used to scan the phantom.

2.2.1. Methods

The following procedure was used to manufacture the mark 1 phantom:

1. The manufacture of Layer 1:
    a. The layer mould shown in figures 2.10a and 2.11(i) was prepared for pouring. A 30mm Perspex bar was placed in the centre of a cylinder with an inner diameter of 40mm, as shown in figure 2.11(i).
    b. Using the protocol detailed in section 2.1.1, a 500ml batch of agar only TMM (TCP0 recipe) was manufactured. This was poured into the cavity of the layer mould and allowed to set. Once solid, the layer was removed (figure 2.11(ii) and set aside.
2. The production of the test object blocks:
    a. Using the manufacturing protocol detailed in section 2.1.1, 500ml volumes of TMM recipes TCP0, TCP10 and TCP20 were manufactured and poured into the object moulds and allowed to set (figures 2.9 and 2.10b).
    b. The TMM recipe was modified to contain 4 times the silicon carbide in TCP100 TMM. This produced the very dark grey object shown in figure 2.10b.
    c. Once the TMM objects were removed from the moulds, a batch of normal TMM was manufactured. The objects were positioned within a flat bottom waterproof storage container and the normal TMM was slowly poured over the objects until they were fully covered.
    d. The TMM was allowed to set and a mixture of water / glycerol / ADBAC poured on top. A small amount of the normal TMM was poured into the phantom container to level off any deformities on the base.
3. The manufacture of layer 2 and the final phantom:
    a. A 3l batch of normal TMM was manufactured as per protocol 2.1.1.
    b. The agar cylinder was glued to the TMM covered bottom of the phantom container, using Cyanoacrylate glue.
    c. A 20mm Perspex tube (Figure 2.11(iii)) was introduced into centre of the agar cylinder and held in place with a clamp and retort stand.

d. Three object blocks were placed close to the agar TMM cylinder. The normal TMM was carefully poured into the container over an object block and into the space between the tube and the agar cylinder.
e. The TMM was allowed to set and then the supporting central tube was removed and the container filled with the mixture of water / glycerol / ADBAC. The final assembled phantom is displayed in figures 2.10 (c) and 2.11(iv), and a cross section of one of the mark 1 phantoms is displayed in figure 2.10 (e).

A number of 'Mark 1' phantoms were manufactured to test different TMM recipes and objects. The echoendoscope was positioned at various points within the core of various 'Mark 1' phantoms and images acquired using a Meteor II or Morphis image acquisition card (Matrox Electronic Systems Ltd, Québec, Canada) and are shown in the results section. Rudimentary three-dimensional reconstructions were performed using a constant pullback and in-house 3D reconstruction software. Each Mark 1 phantom was scanned using the GF-UM20 and GF-UM200 echoendoscope and the EU-M30 ultrasound processor. A series of b-mode images were captured as the echoendoscope was withdrawn using a custom developed image capture system incorporating the Matrox Meteor II capture card and custom developed software.

Figure 2.9 - Examples of moulds used to create the embedded objects.

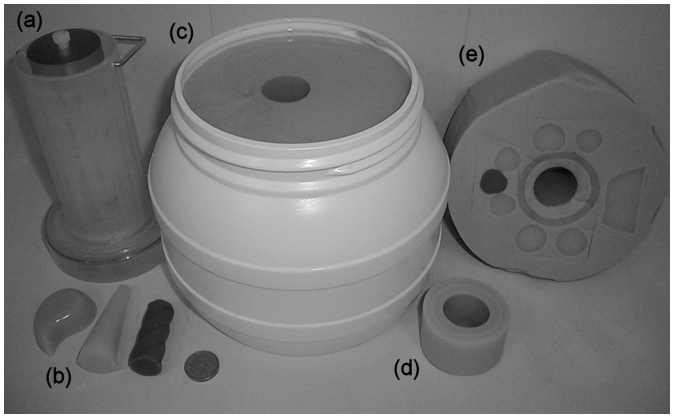

Figure 2.10 - (a) The layer mould used to create the hypoechoic layer within the Mark 1 Phantom. (b) Example s of the objects created with different particle concentrations. (c) The assembled phantom within the container. (d) A segment of the central core 2 layers (outer layer is hypoechoic and inner layer is hyperechoic. (e) A cross section of a mark 1 phantom showing the embedded objects.

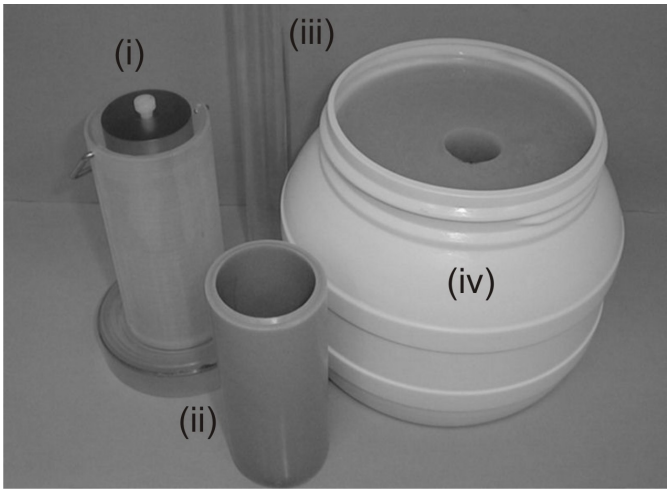

Figure 2.11 – Stages of the layer manufacture, (i) is the mould used to create the layer, (ii) the manufactured layer, (iii) the cylinder used to produce the inner layer of the phantom and the core of the phantom, & (iv) the final mark 1 phantom.

2.2.2. Results

Large quantities of additional SiC particles (4 times the value in the recipe for TCP100) were found to increase the brightness however the material was found to be attenuating when imaged and produced a dark shadow behind the surface of the cast object. This value could be used to mimic stones or plaque within the GI tract. Images of the phantom created to test the increased silicon carbide content in objects are shown in figure 2.12 (a) and (b). The ultrasound image showed a shadow artefact where the ultrasound beam was significantly attenuated and unsuitable for inclusion within the phantom. Therefore, batches of TMM samples of various % particle concentrations were manufactured, between 0 and 100% of the weights of particles (e.g. TMM recipes TCP0 to TCP100).

Figures 2.13 and 2.14 show a number of ultrasound images captured at various levels of two of the manufactured 'Mark 1' phantoms as well as a reconstructed 3D view. Figure 2.13 details a Mark 1 phantom where the main body of the phantom consisted of normal, or TCP100, TMM. The embedded objects were constructed from three different TMM recipes (TCO0, TCP10 and TCP20). The images in figure 2.14 (a) to (c) were obtained from the GF-UM20 echoendoscope at a frequency of 12MHz. The main bulk of the TMM was manufactured from the TCP40 TMM recipe (e.g. scatterer particle concentration of 40%). The bright objects were manufactured using the TCP100 recipe (e.g. 100% scatterer particle concentration) and hypo echoic objects from the TCP0 and TCP10 TMM recipes.

(a) 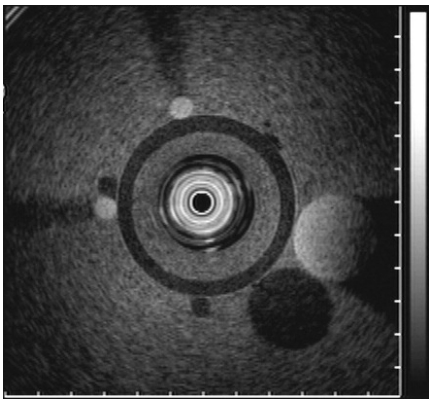 (b) 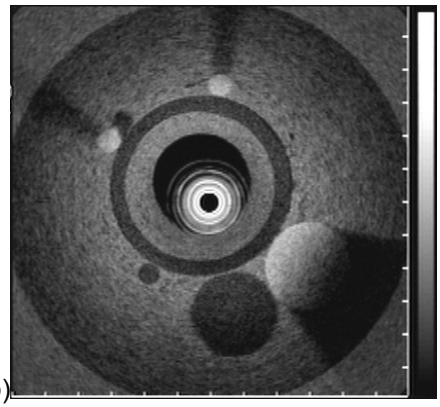

Figure 2.12 - Sample images captured from a mark 1 phantom created to test the increased content of SiC. The image captured at the mid point of the phantom at (a) 7.5MHz and (b) 12MHz.

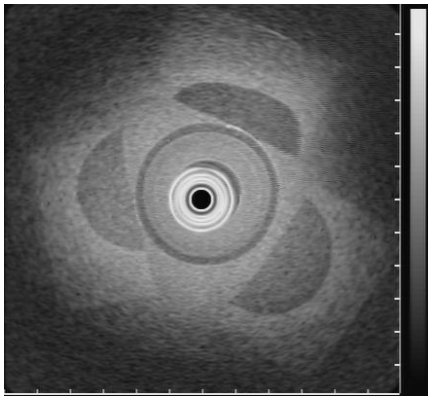

(a) Mrk. 1 Phantom at lower third

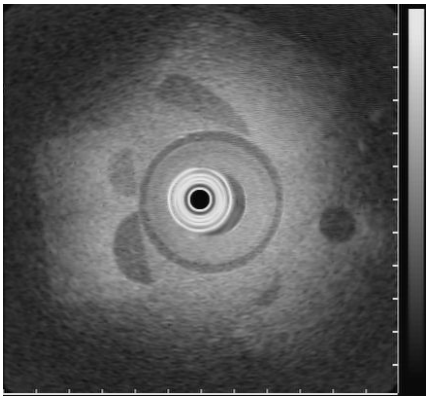

(b) Mrk. 1 Phantom at mid third

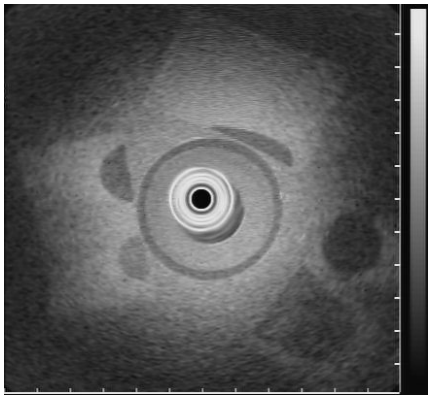

(c) Mrk. 1 Phantom at upper third

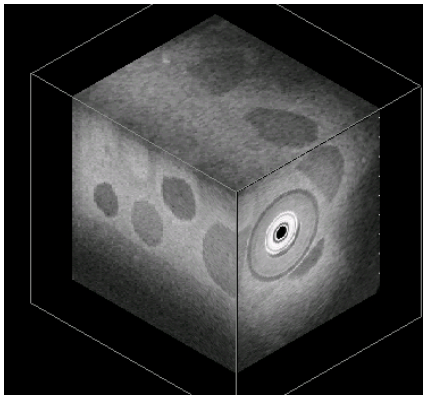

(d) 3D reconstruction of the phantom

Figure 2.13 - (a) to (c) show the ultrasound images at 7.5MHz of a second mark 1 phantom at various levels. (d) A cut away view of the reconstructed volume of the Mrk. 1 phantom.

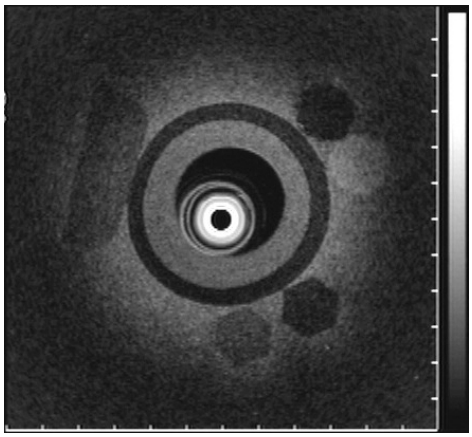

(a) Mrk 1 Phantom at lower third

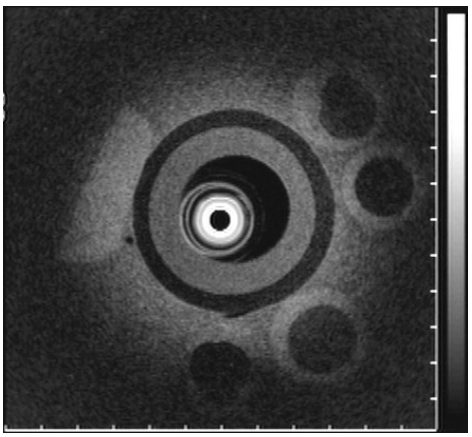

(b) Mrk 1 Phantom at mid third

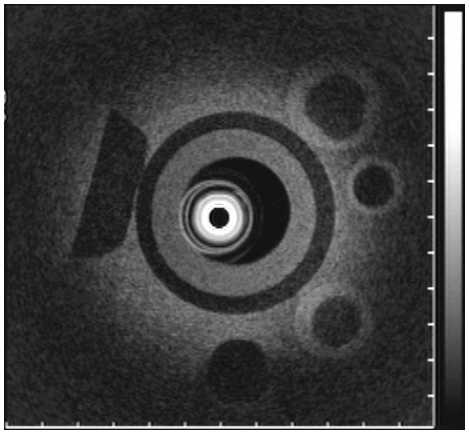

(c) Mrk 1 Phantom at upper third

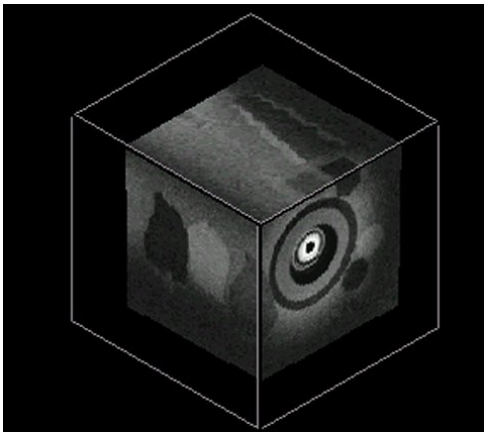

(d) Boxview visualisation of the 3D reconstruction of the phantom

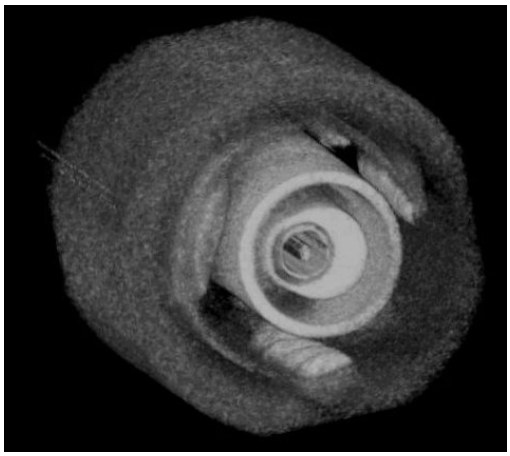

(e) An inverse display of the 3D reconstruction in (d) with transparency applied to visualise the embedded objects. reconstructed volume with an applied inverted grey scale

Figure 2.14 - (a) to (c) show the ultrasound images at 12MHz of the phantom at various levels. The main body of the phantom was manufactured using the recipe for TCP40 TMM. (d) A cut-out view of the reconstructed volume of the Mrk 1 phantom. (e) An inverted gray scale colour map and transparency processing applied to the volume.

2.2.3. Discussion

A prototype, or Mark 1, EUS phantom was successfully produced that allowed for the scanning by the radial echoendoscopes. A number of everyday objects were identified and used as moulds for the production of the objects at various particle concentrations. A technique was developed to allow for the manufacture of an EUS phantom with layers and embedded TMM structures with different acoustic properties.

Various phantoms were constructed to evaluate different material recipes and combinations, via the echoendoscope, for the identification of the most suitable concentrations to simulate both malignant and benign structures. The TMM recipes of TCP0, TCP10, TCP20, TCP40 and TCP100 were chosen as the most suitable recipes to be used within the phantom. The regular shapes of the phantom were suitable for the evaluation of the materials, but did not produce a challenging test object for the development and testing of the 3D-EUS system.

It was found that, if care was not taken during the manufacture of the TMM, it was possible to alter the visual appearance of the TMM (figure 2.13). This produced TMM blocks that were visibly different to the surrounding material, under EUS examination. This may be due to inconsistencies in the manufacturing process (e.g. different stirrer speeds between TMM batches, increased particle residue left after the mixing process, or the introduction of small air bubbles during the cooking process). As the TMM manufacturing process was refined, these possible errors were minimised and not reproduced in subsequent phantoms.

2.3. The Mark 2 Phantom Development.

Background

The Mark 1 phantom was used to develop the manufacturing techniques necessary to construct an EUS phantom and test the imaging characteristics associated with varying the scatterer particle concentration of the TMM material. The Mark 2 phantom will expand on these techniques to construct a phantom with anthropomorphic features of the oesophagus. An anthropomorphic EUS phantom would be useful in quality assurance of equipment, training and in reseach and development.

The oesophagus and surrounding structures (aorta, tumour, nodes, heart etc.) make up a complex arrangement of organs to simulate. The oesophageal wall, under ultrasound, is made up of 5 to 7 concentric layers with consecutive dark and bright echo properties and different thicknesses. The vascular structures surrounding the oesophagus are dark under ultrasound as they contain fluid (blood). Tumours and nodes appear to be dark structures under ultrasound. Bright areas observed within the region of the oesophagus were normally plaque within the vascular structures or a lipoma that was normally situated within the oesophageal wall.

This chapter details the development of a phantom with increased anthropomorphic features. Using the results obtained from the acoustic measurements and expanding on the techniques developed with the Mark 1 phantom, a more challenging phantom was constructed. The embedded objects, that were both complex and irregular in shape, would have a visual relation to the anatomical structures surrounding the oesophagus, for assessment of the 3D EUS reconstruction techniques. An engineering diagram of the proposed phantom design is illustrated in figure 2.15. A phantom would need to be created with more than ‘2 layers’ for the ‘oesophageal wall’ and anatomical shapes.

To manufacture the phantom it was necessary to design and have manufactured a custom mould to allow for the production of the oesophageal wall layers. A container was also manufactured to house the final phantom.. The technique developed in the production of the mark 1 phantom layers was modified to produce at least 4 TMM cylinders of different acoustic properties. The wall layers of the phantom were produced by interchanging a series of Perspex rods with decreasing diameters and filling the resultant cavity with TMM with different acoustic properties.

The method used to manufacture the objects and test blocks in the mark 1 phantom was altered to allow for the manufacture of complex shapes, to represent the anatomical and pathological structures surrounding the GI tract. For ease of manufacture, plasticine was used to shape the anatomical structures. Various complex TMM objects were embedded into a block of normal TMM to produce an

anatomical scenario block, and each block was designed to simulate a different 'anatomical scenario'. For example one block would simulate the aorta and adjacent nodes. The other anatomical scenario blocks would contain various vascular, nodal and tumour mimicking structures of various sizes and shapes (figure 2.16).

Aims

1. To design a new phantom enclosure and mould for the central core layers.
2. To construct a phantom that contained a 'wall' with more than 2 layers.
3. To develop a technique that would enable complex objects with anatomical shape to be manufactured.

Materials

A phantom mould was constructed and is shown within figure 2.15. The tissue mimicking materials detailed in 2.1.1 were used to construct the phantom. Different TMM's were manufactured using the TMM recipes TCP0, TCP10, TCP20, TCP40 and TCP100. Liquid latex and plasticine were used to construct the master objects for the moulds.

2.3.1. Methods

A new central core was manufactured to enable the manufacture of 4 cylinder layers with thicknesses between 2 and 4mm. The fifth layer would be the interface between the core and the main body of the phantom and would be the final layer. Modelling plasticine was used to construct custom anatomical shapes to act as the aorta, tumours, cysts, vascular structures and lymph nodes. The shapes were fashioned to be similar to anatomical structures observed during EUS scanning of patients, and were secured onto a flat plate that would have TMM poured on to the surface to create a mould (figure 2.16).

When the objects were suitably shaped, four different anatomical scenarios were prepared with different objects. To protect the TMM from the plasticine, a barrier layer of liquid latex was applied to the surface of the modelled plasticine objects and allowed to dry for 24 hours. The anatomical scenario plates were placed into suitable containers for filling with TMM. A batch of normal TMM (TCP100) was manufactured as per the TMM protocol detailed within chapter 2.1.1 and poured into the container and allowed to set. After removing the TMM block, the indented shapes were carefully cleaned of any surplus materials using a soft brush.

From the characterised acoustic properties of attenuation and backscatter, specific values were chosen to construct the various layers of the phantom and embedded objects. Four different TMM recipes, TCP0, TCP10, TCP20 and TCP40 were manufactured and carefully poured into chosen cavities within the TMM block. For complex structures, where different objects came into contact, one of the latex covered objects would be placed and the cavity filled with the appropriate TMM.

As the four anatomical scenario blocks were filled with different particle concentration TMM's, the 'oesophageal' layer mould was also filled. The mould used to produce the 'oesophageal' layers of the phantom consisted of a plastic tube and a series of reducing diameter plastic rods. The tube and largest rod was placed together to produce a layer of 2mm thickness. The TCP0 TMM mix was poured and allowed to solidify, the rod was then removed and a second rod inserted into the mould. This procedure was repeated to produce four different layers with different acoustic properties and varying thicknesses. The layers from outer to inner (closest to the central core) were manufactured using the TMM recipes TCP0, TCP40, TCP10 and TCP100 respectively. Once the 'wall' layers and the four anatomical scenarios were manufactured, the phantom was assembled and filled with 100% TMM material. The innermost rod of the core was kept in position until the TMM had solidified. Figure 2.15 a to c illustrates the construction of the phantom via an engineering drawing, where the shapes shown embedded within the phantom are examples only. Figure 2.15d is an example of the mould, phantom and embedded shapes.

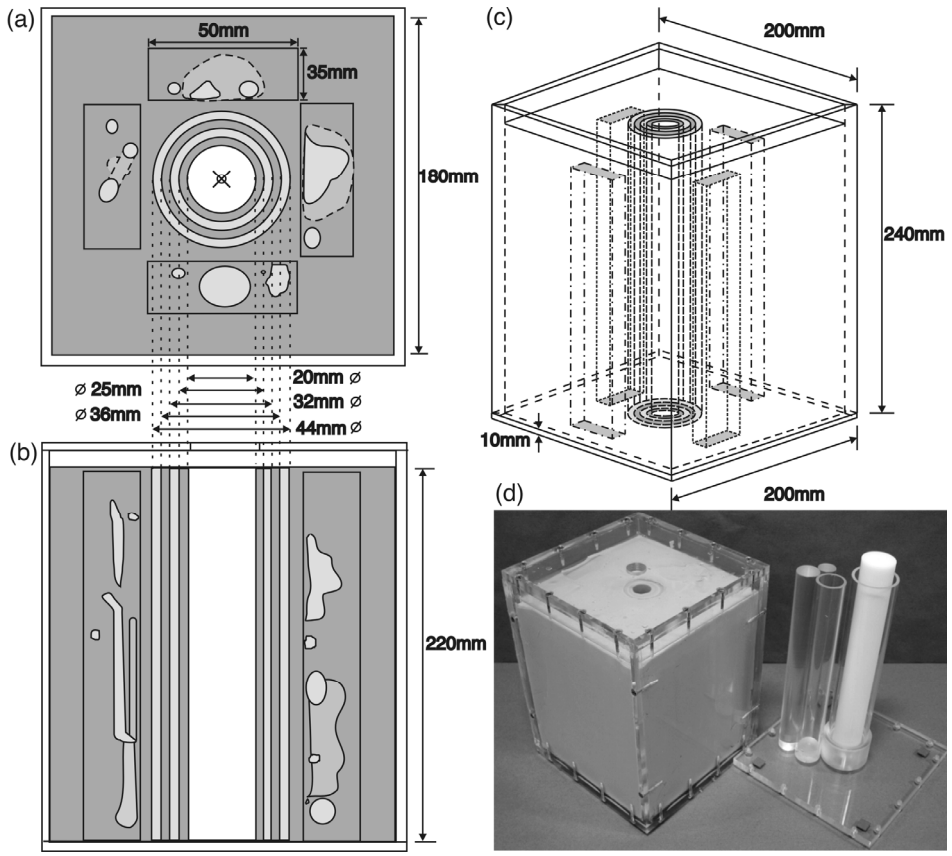

Figure 2.15. - Example engineering drawing of the construction of the phantom and picture of the manufactured phantom and mould. (a) Transverse view of the phantom, (b) example view of the coronal view through the phantom, (c) 3D engineering view of the construction of the phantom, & (d) picture of the constructed phantom and mould

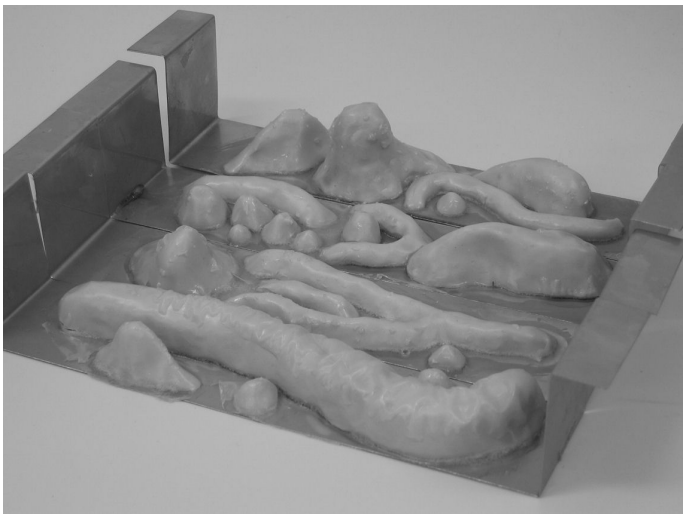

Figure 2.16 - Stainless steel plates with the plasticine shapes secured onto the surface and coated with liquid latex.

2.3.1.1. Phantom Scanning

A study to investigate the endoscopist's ability to accurately estimate the length of a simulated cancer lesion within the phantom using conventional (2D) EUS and compare it with three-dimensional endoscopic ultrasound (3D-EUS) was performed to visualise and validate the phantom. The phantom was scanned at 7.5 and 12MHz. Each endoscopist performed examinations of the phantom, mimicking a normal diagnostic patient procedure where they identified an object, and dimensions were measured using the tools provided, and the position and dimensional measurements were recorded. Five distinct objects were chosen, with different shape and dimensional characteristics, to compare the endoscopic and 3D-EUS measurements. Figure 2.17 illustrates the 3D-EUS measurement and acquisition setup. The echoendoscope was positioned at the base of the central core of the phantom and then withdrawn at a relatively constant rate as the images were captured at 12.5 frames / second (fps), using the Meteor II or Morphis image acquisition card (Matrox Electronic Systems Ltd, Québec, Canada). The positional information was captured using a Microscribe G2X positional digitising arm. The tip of the digitising arm was attached to the back of the endoscopist's hand controlling the withdrawal of the echoendoscope, using a custom designed strap and holder. Positional data was acquired simultaneously with EUS images, over the entire length of the phantom. Volumes were reconstructed, using a custom developed reconstruction and analysis program developed within Matlab™ (The Mathworks Inc, Massachusetts, USA), from the series of parallel B-mode images and the positional information. A comparison was made between the dimensions obtained during the scan and those obtained from the 3D reconstruction and analysis software.

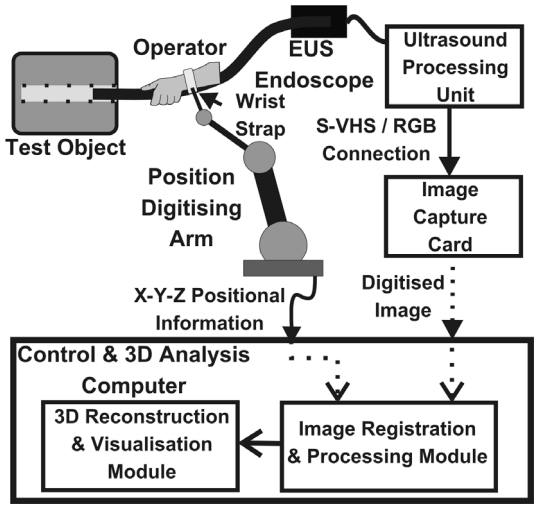

Figure 2.17 - Block diagram of the 3D Acquisition and Measurement setup.

2.3.2. Results

Figure 2.18 displays sections of the Mark 2 phantom, where (a) to (d) are transverse selections at various levels. The embedded objects show different particle concentrations and different shapes included within the phantom. Figures 2.19 a to d shows the 3D reconstruction of the phantom with transverse, coronal and sagittal views and a cut out segment of the volume.

Repeated dimensional measurements were performed on the phantom shown in figures 2.18 & 2.19 by two experienced endoscopists. It was found that the endoscopists had a maximum error in the X-Y plane of 5% and average of 3%. The 2D measurements performed by the endoscopists, in the Z plane, produced an average error of 8% with a maximum error of 23%. Identical measurements in the Z plane performed on the 3D dataset, illustrated in Figure 2.19, obtained an average error of 2.2% and a maximum of 3.7%.

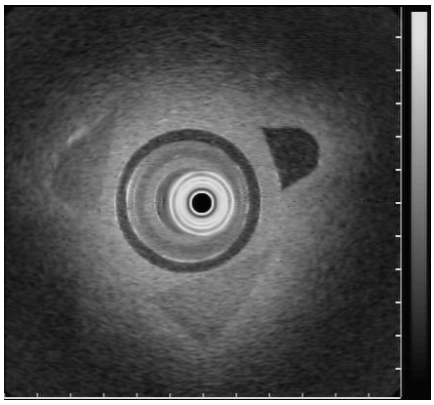

(a) Mrk. 2 phantom 1st quarter

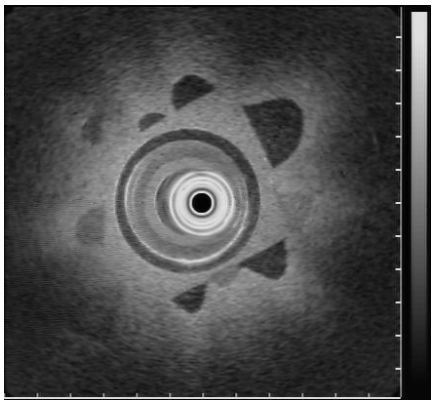

(b) Mrk. 2 phantom 2nd quarter

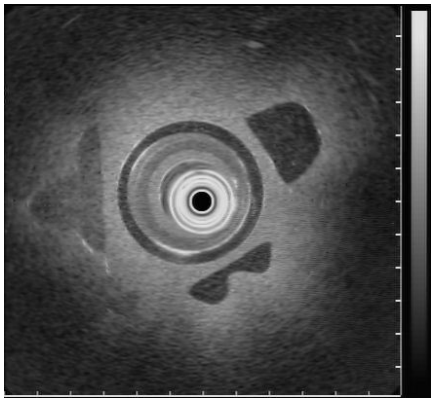

(c) Mrk. 2 phantom 3rd quarter

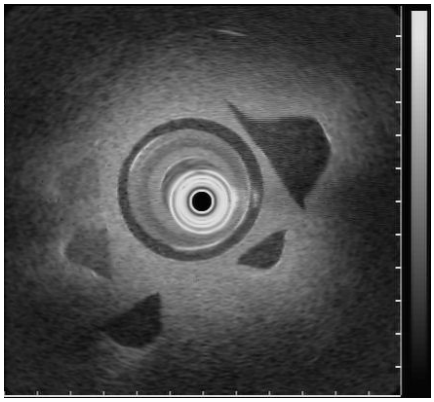

(d) Mrk. 2 phantom 4th quarter.

Figure 2.18 - Ultrasound images captured at 7.5MHz from various levels of the Mark 2 phantom. The surrounding TMM was manufactured using the TCP100 recipe and the embedded objects were from the TCP0, TCP10, TCP20 and TCP40 recipes.

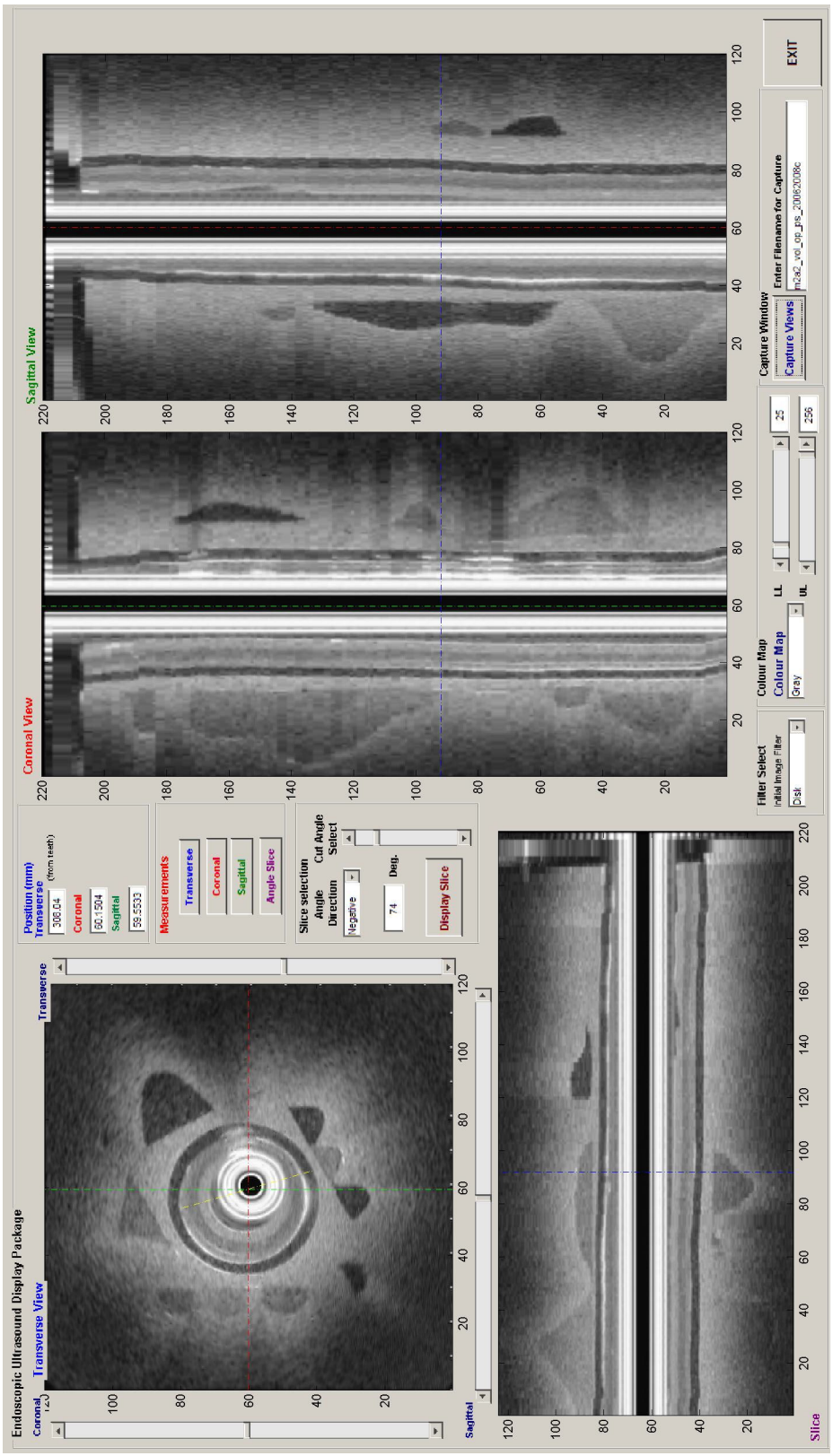

Figure 2.19a - 3D reconstruction of the Mark 2 phantom used to assess the accuracy of the measurements performed by endoscopists.

(b)

(c)

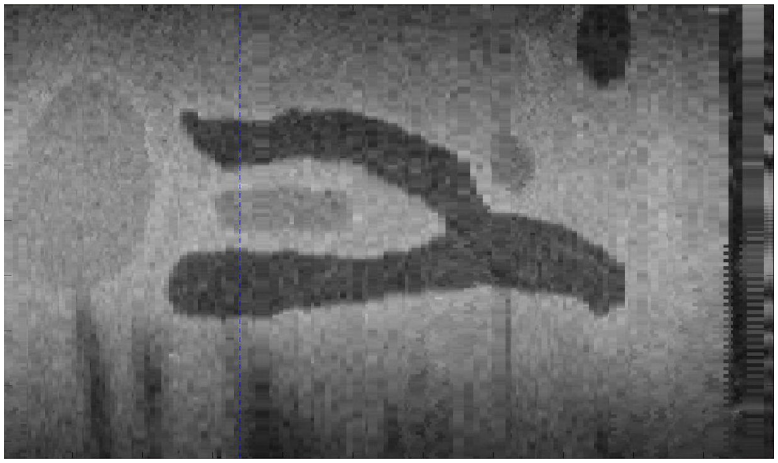

(d)

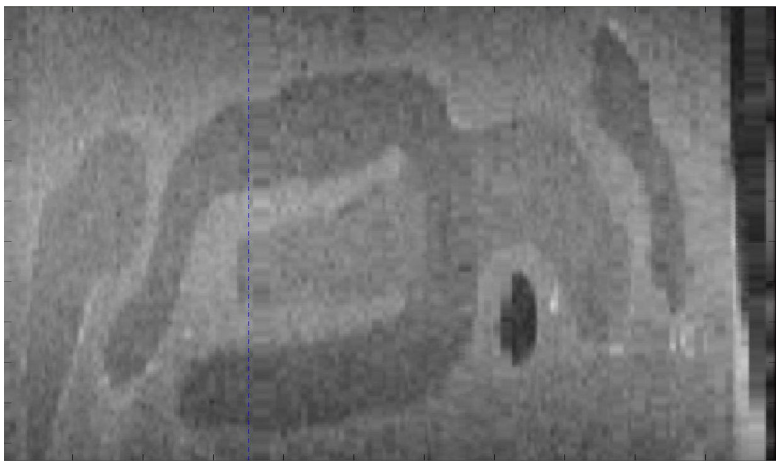

Figure 2.19 - (b to d) example slices captured from the reconstructed volume. Each of the embedded TMM object blocks were visualised using a segmenting tool written into the reconstruction software. The images are displayed from left to right is from the phantom bottom to top respectively.

2.3.3. Discussion

A phantom was created that had four layers of different acoustic properties. The technique used to manufacture the oesophageal layers was limited to a minimum layer thickness of 2mm. If the layer thickness was reduced below 2mm, the wall became fragile and could be easily broken. Therefore the minimum oesophageal wall thickness would be 8 to 10mm for 4 to 5 layers respectively.

The methodology used to construct the moulds increased the complexity and irregularity of the embedded objects. These techniques resulted in a phantom with increased complexity for the evaluation of the 3D-EUS system. However, the technique used to produce the embedded objects had drawbacks. These were:

- The objects would have a flat segment due to the surface that was in contact with the plate.
- The objects would only arise from one plane.
- It was difficult to obtain accurate volume measurements of the objects.

To obtain the volume, it would require either (1) the volume measurement of the plasticine object or (2) the cavity within the TMM block. Errors were introduced into method 1 as the coating of latex was often destroyed during object removal and its thickness unknown. Also, as the objects were often adjacent, or in continuity with other structures, the latex would smooth all sharp boundaries increasing the errors between the actual and the calculated volume. When filling this cavity with TMM, often it would mould around the adjacent plasticine object and change the actual volume. Method 2, measuring the cavity volume, required the adjacent cavities to be filled with the plasticine objects. However, as the cavity would be filled with water, it could escape to the adjacent cavities. Also, due to the latex coating, the top was often not flat and water would not completely fill the cavity, introducing errors in the measured volume.

2.4. The Mark 3 Phantom Development.

Background

To develop an anthropomorphic EUS phantom of the oesophagus, a number of anatomical and pathological features of the oesophagus would have to be simulated. The main features that would have to be included were:

1. The aorta rotated around the length of the oesophagus by approximately 90°.
2. The aortic arch is an important landmark for localisation of pathological features.
3. Tumours may invade either a portion or the entire circumference of the oesophagus.
4. Anatomical and pathological structures may originate from multiple planes.
5. The embedded objects must have complex three-dimensional shape, no flat surfaces and have known volumes.
6. The oesophageal wall consists of 5 to 7 concentric layers with consecutive hypo and hyperechoic properties, and different thicknesses.

This chapter details the design of the Mark 3 phantom mould, the investigation of materials that may be used for the hyperechoic layers, and the development of techniques for the creation oesophageal wall layers of different thicknesses and the production of complex anatomical structures with measureable volumes. From the visual study of the 3D anatomy of the GI tract, and ultrasound studies of the anatomy during clinical scanning, a design for the new mould was created. An engineering diagram of the Mark 3 phantom is illustrated in figure 2.20. The previous methods employed in the creation of the phantom wall layers and objects were limited. The oesophageal wall of the Mark 2 phantom could manufacture four TMM cylinders of different acoustic properties. However, the minimum obtainable wall thickness was 2mm. The method used to produce the object relied on the plasticine objects situated on a plate and placed within a box, being covered with TMM. The indents within the resultant block of TMM were filled with differing particle concentration TMM mixtures. This meant that the objects inherently had a flat edge and were all situated on one plane. By designing a technique that would create truly 3D objects that could be embedded into a TMM block it was possible to situate them at different depths.

Aims

1. To investigate different everyday materials that may be used to visually simulate the hyperechoic layers of the oesophagus.
2. To develop a technique that would enable complex objects with anatomical shape to be manufactured.
3. To construct and visually evaluate the phantom using conventional and 3D EUS.

Materials

A new phantom container, housing the 'aorta' and 'oesophageal' moulds were manufactured within the mechanical workshop. A number of moulding materials, plaster of Paris, latex, re-meltable PVC and plasticine was used to construct the objects. Potting boxes and Perspex sheets were used to house the object moulds. The objects to be embedded into the phantom were manufactured using TCP0, TCP10 or TCP20 recipes. The wall (central core) of the phantom and the 'aorta' were manufactured with agar only and no particles. The rest of the phantom was manufactured using the 100% particle concentration recipe. The moulding materials investigated for the construction of the object moulds were:

- Latex
- Re-meltable PVC compound
- Plaster of Paris

To try and reduce the total thickness, a number of different materials were investigated to simulate the layers of the oesophagus and included:

- Latex 700μm thick bicycle inner tube.
- Latex TOE probe sheath with thickness of 300 μm
- Condom of 60 μm latex rubber.
- Cling film of 10 μm polythene.
- Packing stretch film made of high tactile 25 μm polythene.
- Polythene lay flat tubing of 130μm thickness.
- Tin foil of thickness 25 μm.

2.4.1. Methods

The requirements for this phantom were that it would have 5 layers of different thicknesses between the echo bright and dark layers, an aortic structure and complex objects that could be identified visually as anatomical and pathological structures were embedded within the phantom.

A flexible silicone tube of diameter 31mm was incorporated into the design of the phantom to simulate as the aorta and a 20mm flexible silicone tube acted as the oesophagus. Figure 2.20 details the design of the new mould. Examples of the shapes embedded within the phantom were included in the figures 2.20 a and b. It was possible to partially embed objects and have a section protruding from the block. This enabled the objects to be positioned in close proximity to other structures (e.g. the oesophageal wall). Figure 2.21 is a photograph of the actual phantom and the moulds used to construct it. The mould was manufactured within our mechanical workshop.

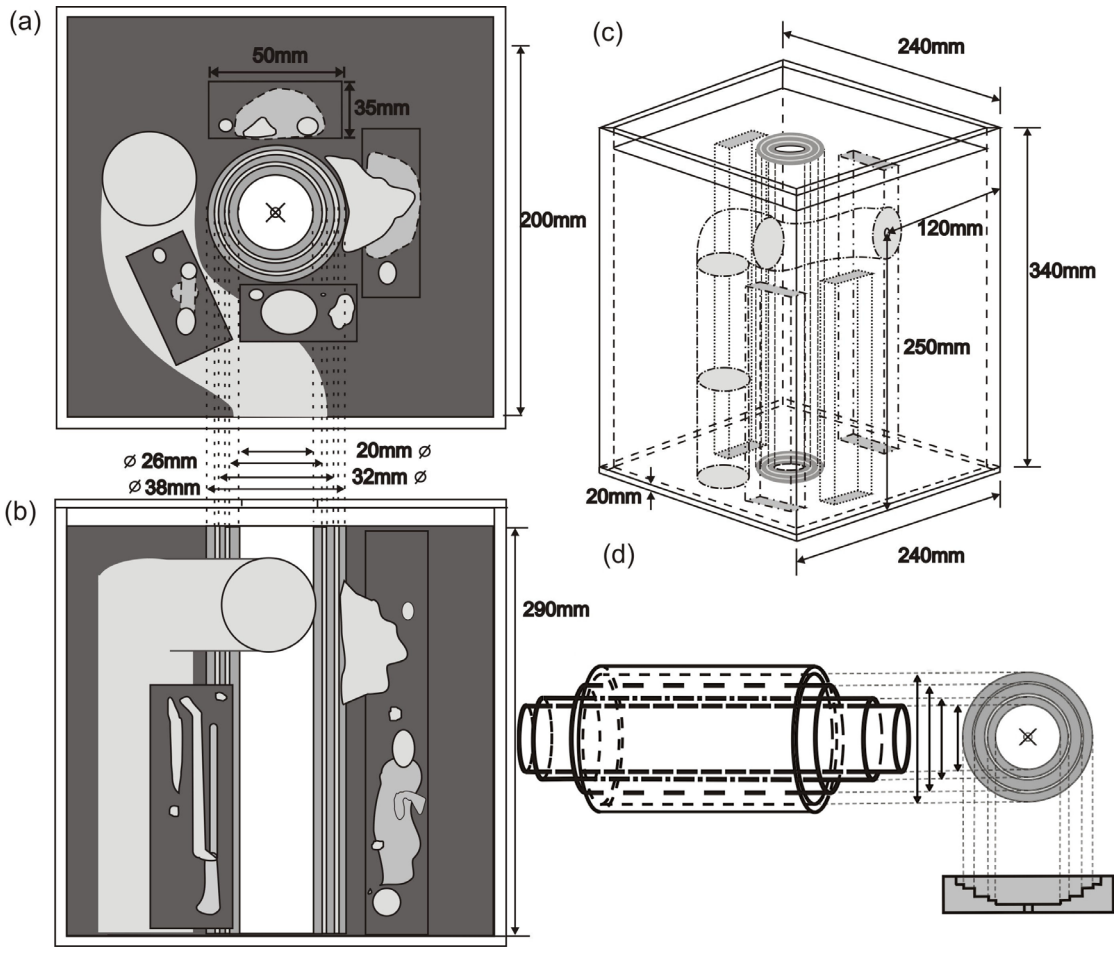

Figure 2.20 - A Schematic diagram of the mark 3 endoscopic phantom mould.

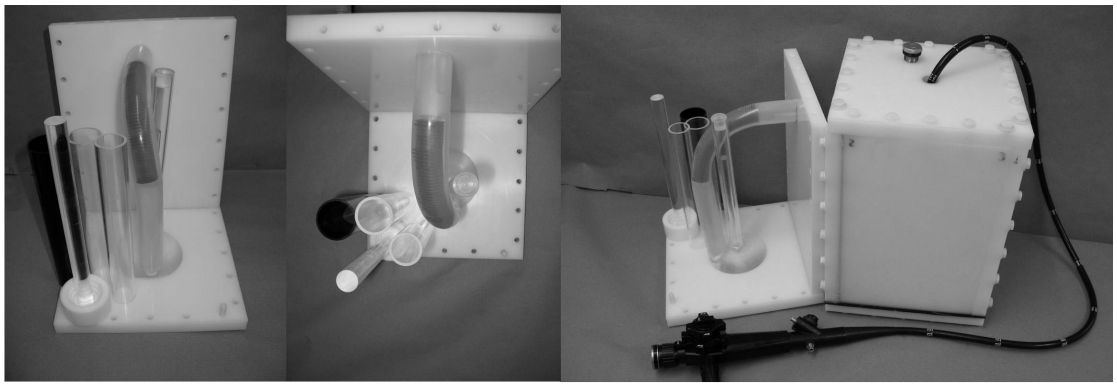

Figure 2.21 - The basic mould of the mark 3 phantom that incorporated the 'Aorta', mould for the layers and the final phantom.

2.4.1.1. Mould Design

To design a suitable moulding technique, it was necessary to investigate different materials used for moulding and which could be easily manufactured within a laboratory setting. These were latex, Plaster of Paris and PVC compound.

A basic mould enclosure was manufactured from two plastic potting boxes that were attached together at the base using industrial packing tape. Two large holes were drilled into the top of the enclosure to allow for pouring the moulding material and TMM. A Perspex sheet was used to separate each of the potting boxes into two separate compartments, as it allowed the objects to be aligned with greater accuracy. The object masters were designed to mimic vascularity, nodal, and tumour structures. Plasticine was chosen to create these shapes as it was a very flexible mouldable medium, when slightly heated to approximately 30°C. The objects were then shaped and cooled, either air cooled or placed into a fridge, to reduce the flexibility. The material could be easily cut and placed into the mould enclosure.

The objects were 'halved' along a suitable axis (coronal, sagittal or transverse planes). The axis was chosen depending on the how easy it would be to extract from the mould. Examples of manufactured shapes and where they would be cut was shown in figure 2.22 (a) to (d). To minimise the deformation of the object during the cutting, a very fine blade was used, e.g. a microtome blade. The objects were placed on the central Perspex sheet of the enclosure and secured using the adherent properties of plasticine.

Mould material manufacture

- **Latex –** The method used to create the mould was to dip the master object repeatedly into liquid latex. The latex would dry on the master and was removed once a suitable thickness had been achieved. However, a non-porous master object, e.g. plasticine, could not be used as the moisture would not be drawn from the latex and the drying would be hindered.
- **Re-meltable PVC -** Re-meltable PVC was found to be a useful material for the manufacture of flexible moulds. TMM could be poured into the mould and could be removed easily. However, as plasticine melts at temperature greater than 65°C (Liechty & Webb 2006), it could not be used as the object master.
- **Plaster of Paris -** As plaster of Paris needed to be poured into the mould enclosure, it was necessary to obtain a watery consistency. The recommended consistencies can vary depending on the type of plaster used. With the typical ratios of 2:1 or 1:0.7 (plaster: water) the plaster was too thick to ensure an even distribution around the object and often set before the mould was completely filled. A mixture ratio of 1:1 of plaster to water was sufficiently runny to ensure an even distribution within the mould.

The plaster was accurately weighted using a balance and placed into a clean dry beaker and any clumps in the powder were broken up. The volume of plaster was modified depending on the number of required moulds. The corresponding amount of water was measured using the balance. Cold tap water was used to prolong the time before hardening took place. The plaster was sprinkled into the water and allowed to sink; the mixing did not start for a few minutes to allow the powder to properly soak. The powder was slowly mixed into the water to limit any air entrainment. Water was added at this point if the resultant mixture was too thick. Care was taken to remove air bubbles by tapping of the beaker to free any trapped air and bring it to the surface. The plaster was poured into the moulds taking care to avoid splashing and air entrainment. Once again the mould was gently tapped to release trapped air from some of the complex shapes of the master objects. During the setting process the plaster became warm (~35ºC). The plaster was allowed to set for approximately 15 to 20 minutes and then the enclosure was split and the master objects removed. As plaster of Paris is a porous medium which would draw the fluids from the TMM, it was necessary to seal the surface. After investigating a number of sealing materials Marvin Medium (Berol Adhesives, Sanford UK) was chosen to coat the inside of the mould. When the TMM was poured into the mould and set, the Marin Medium became slippery to the touch and aided the removal of the objects.

2.4.1.2. Investigation of the Layer materials

The previous technique to create the 'bright layers' of the phantom consisted of pouring 'normal' TMM into the layer mould. This produced a layer 2 to 3 mm thick. The entire 'wall' consisted of 5 layers that could result in a total thickness of between 10 to 15mm. It was not practical to reduce the thickness of the TMM layer as the material would be too fragile.

Each of the layer materials was chosen to be suitable for scanning with an ultrasound beam without significant beam attenuation. A sample of each material was cut and placed between 2 layers of TMM as per figure 2.23. The removable central core had a thickness of 3mm. Each layer material was placed around the outside of the central core and placed within the central cavity, filled with TMM fluid suspension and scanned with an Olympus GF-UM 20 echoendoscope and the EU-M30 processor at frequencies of 7.5 and 12 MHz. (Figure 2.23). The transducer was angled using the guiding controls of the endoscope and the effects of tangential cutting of the beam were observed. Images were captured using the image capture system as previously described.

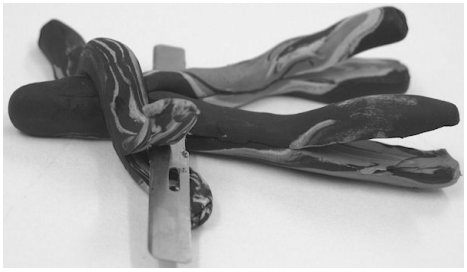

(a) Vascular or fragile structures were sectioned along the coronal plane (the long axis of the object).

(b) Tumour or similar structures that were complex or that conformed to the central core were cut along a suitable plane for easiest extraction.

(c) Complex irregular objects that could not be easily removed, (e.g. a dumbbell shape) were cut along the sagittal plane.

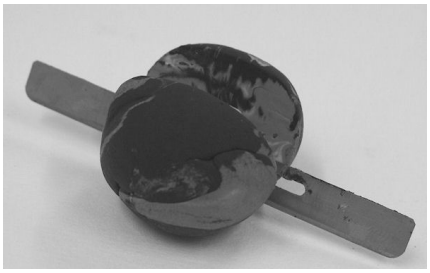

(d) Regular objects that could be easily removed (e.g. spheres, diamond base pyramid) and simulate nodal structures were cut along any axis.

Figure 2.22 - Examples of the plasticine objects designed for inclusion in the phantom and how they would be split.

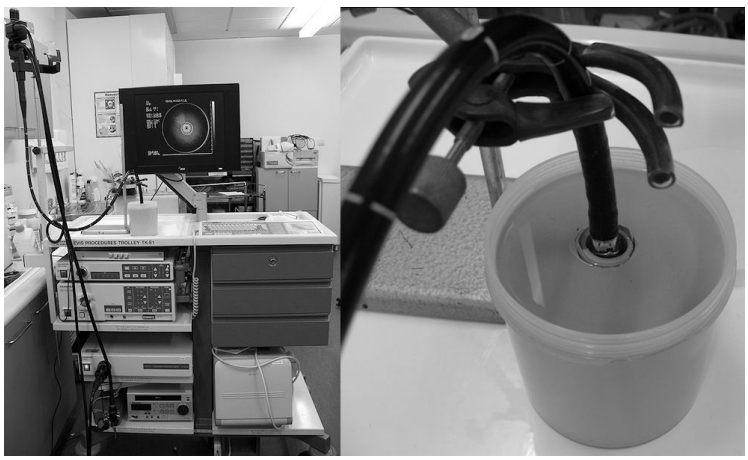

Figure 2.23 - The test setup for the Layer material samples. A GF-UM 20 echo endoscope imaged the core material phantom at 7.5MHz and 12MHz. The tip of the echoendoscope was centralised and placed in contact with the wall.

2.4.1.3. Phantom Manufacture

The phantom was manufactured in three stages:

Stage 1. - Manufacture of embedded objects.

The moulds and objects were manufactured using the plaster of Paris and Marvin medium combination as detailed below:

1. 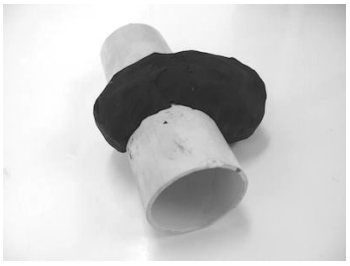

The plasticine was warmed to 30ºC for pliability and moulded into the desired shape. Example shown was a tumour that conforms to approximately 2/3's of the circumference of the outer layer.

2. 

The plasticine object was cut through the centre and using the adhering properties of plasticine, was attached to the Perspex central divider. The clear Perspex sheet allowed for greater accuracy in the alignment of each half. Additional pieces of plasticine were added to the top of the object, close to the pouring holes to ensure access into the cavity. Care was taken to ensure that space was left for pouring the plaster. The mould was then closed and sealed along the sides using packing tape.

3. 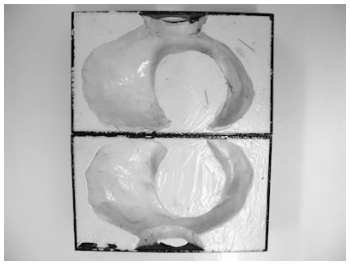

The mould was filled with a 'watery' plaster and allowed to set as detailed above. The exposed surfaces of plaster was coated with Marvin medium, a PVA based adhesive. This was allowed to dry overnight.

4. 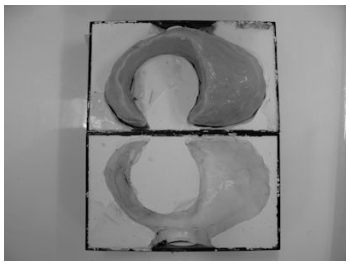

The enclosure was then resealed with packing tape and filled with TMM. The TMM was manufactured using the above protocol, however it was poured at 48 ºC to ensure that it would fill the entire mould and any trapped air could be tapped out. The mould was placed into the fridge to assist in the cooling. The objects were cast using 0, 10 and 20% particle concentrations. The TMM filled pouring holes were carefully trimmed and removed using a scalpel.

5. Once the objects were set and removed from the moulds, they were arranged within containers. If different depths of object placement were desired, slices of 'normal' (100% particle concentration) were cut using the bench microtome and placed underneath the objects. The containers were then filled with 'normal' TMM and left to set. Complex shaped objects like the one above were partially encased within the TMM block. The segment that fitted around the central core of the phantom was left uncovered. The blocks were carefully removed from the containers and stored for stage 3 of the phantom manufacture.

Stage 2. - Manufacture of the 5 layer 'oesophageal wall' of the phantom.

The mould used to produce the 'oesophageal' layers of the mark 3 phantom consisted of a plastic rod as the central core and a series of increasing diameter plastic tubes (figure 2.20d). A batch of agar only TMM was manufactured, as per the protocol, but left within the water bath at a temperature of 48 ºC. The 20mm diameter rod was placed into the base with the 26mm inner diameter tube. The beaker containing the TMM was removed and the cavity between the rod and tube filled. The beaker was then replaced into the water bath and the stirrer reintroduced.

After the TMM layer had set, the outer tube was removed and a layer of stretch film was applied to the TMM layer surface. To ensure that no air was left between the TMM and stretch film, a water based lubricant was generously applied to the surface of the TMM. The core was then 'rolled' onto a carefully cut and sized sheet of stretch film. Sufficient pressure was applied to the core to remove any excess lubricant and air, while maintaining the adhesion of the stretch film on to the TMM and lubricant.

The central core with TMM and film layer was then placed back onto the base and the next tube (32mm inner diameter) was fitted into its recess. The TMM was again removed from the water bath and poured slowly into the cavity. Care was taken to ensure that the stretch film did not become dislodged. This process was repeated for the remaining layers. When all the layers were produced, the assembled 'oesophagus wall' was stored in TMM preserving fluid, with the core and final tube in place.

Stage 3 - The assembly and filling of the phantom.

The mark 3 phantom mould shown in figures 2.20 and 2.21 was assembled and prepared for filling. As the base of the phantom had a shallow conical platform that housed the 'aorta' and 'oesophageal' wall, it was necessary to add a small quantity of TMM into the bottom of the mould to level off the base. This allowed the object blocks to be placed at any position within the mould. The agar based TMM used to manufacture the 'oesophageal wall' was also used to level the base.

The Mark 3 phantom container had a capacity of 8 litres of TMM. The object blocks and 'oesophageal wall' were positioned within the mould. As the maximum capacity of normal TMM that could be manufactured was 3.5l, between 2 to 3 batches were manufactured and carefully poured into the mould. After each addition of TMM the mould was placed into a fridge to assist in the setting process. When the mould was completely filled with TMM, the mould, top and side holding the 'aorta' and 'oesophageal wall' were exchanged with a plain side and mould top. The mould was rotated so that the base became the top. The silicone tube supporting the 'oesophageal wall' and the one acting as the 'aorta' were removed. An agar only batch of TMM was manufactured and poured into the cavity of the 'aorta' and allowed to set. A plain base was attached to the phantom enclosure, sealed and righted. The phantom was filled with TMM preserving fluid and allowed to settle before scanning. After the phantom was fully assembled, it was scanned as per the phantom scanning methods detailed in section 2.3.1.1.

2.4.2. Results

Moulding materials

- Latex - was found to be a flexible moulding material, however it required a significant number of layers to provide sufficient strength in the mould to maintain its shape during pouring of the TMM. If the latex was left on the plasticine for long periods of time it became more susceptible to cracking and splitting. For complex shaped objects, the latex moulding technique was not suitable as the object could be difficult to extract without damaging it.
- PVC Compound - Re-meltable PVC mould was found to produce a strong flexible mould that was very suitable for the manufacture of the objects. However, the construction of the moulds required heat treatment within the lab area. It was necessary to heat the PVC to 135°C to melt it. As our laboratory did not include these facilities, it was not possible to manufacture phantom using this material.
- Plaster of Paris - proved to be a versatile moulding material. It was easy to manufacture within a limited laboratory environment. Care had to be taken when preparing the plaster, to obtain a watery consistency. If the mixture was not watery enough, it was possible that the plaster would start to solidify while pouring.

Layer materials

Table 2.4 details the results of the investigation of the layer materials. Figure 2.24 (a) to (i) illustrates layer properties of each of the materials while being scanned using the GF-UM20 echoendoscope. The thicknesses of the layer materials were measured with a Microstat MS-25 digital micrometer (Moore & Wright Microsystems Ltd. Sheffield, UK). Images captured with the transducer placed firmly up against the wall are shown in figure A.2 of appendix 2.

Phantom Imaging

When the Mark 3 phantom was fully assembled, it was visualised with the GF-UM20 fibre echoendoscope and EU-M30 ultrasound processor. The images in figure 2.25 are of the constructed phantom at various levels at 7.5 and 12MHz. Each of the images shows examples of the embedded objects. Figure 2.26a shows the transverse, coronal and sagittal views of the mark 3 phantom and the software tools available to perform measurements and visualise the volume at different levels. Figure 2.26b shows each of the four embedded objects blocks along the coronal and sagittal planes.

Slice 1 simulated a series of vessels, a tumour and a number of nodes. The tumour was situated close to an S shaped vessel and then continuing out of plane to a bifurcating vessel and with adjacent nodes.

Slice 2 contained two vessels coming close together and then separating. These were surrounded by a number of nodal structures and a tumour that encompassed half of the circumference of the oesophageal wall. Slice 3 contained the simulated aorta showing the path of the aorta and the arch. Trapped air pockets can be seen in the 'aortic arch' of the phantom. The final slice (4) held a number of different nodal shapes both benign and malignant looking.

Ring artefacts were visible on the ultrasound image of the EUS phantom, at 7.5MHz. This was due to the ultrasound beam passing through a number of stretch film layers. To minimise this artefact it may be necessary to use the cling film.

Table 2.4. - Results of the study of different layer materials for the inclusion within the phantom.

Type of Material	Material	Thickness (µm)	Visible at: (F <75%, P>75% & <25%, N >25%)				Beam Attenuation Visible	Artefact Visible Type
			Perpendicular		Angled			
			7.5 MHz	12 MHz	7.5 MHz	12 MHz		
None	/	/	/	/	/	/	/	/
Polythene	Cling Film	11µm	F	F	P	P	None Detectable	None Detectable
	Stretch Film	25µm	F	F	F	P	None Detectable	None Detectable
	Lay flat polythene	130µm	F	F	F	F	None Detectable	Ring artefact detectable at 7.5MHz.
Latex	Condom	80µm	F	F	P	N	Detectable at 12MHz	None Detectable
	Latex TOE Probe Sheath	300µm	F	F	P	P	Detectable at 7.5 and 12MHz. Most noticeable at 12MHz.	None Detectable
	Racing bicycle inner tube	300µm	F	F	P	N	Clearly visible on image at 7.5 and 12MHz. Significant at 12MHz.	None Detectable
Tin Foil	Kitchen Foil	25 µm	F	F	F	F	None Detectable	Significant artefact at all frequencies and conditions

	EUS : 7.5mhz & scale depth : 12cm	EUS : 12mhz & scale depth : 12cm
(a) Normal Image without layer material	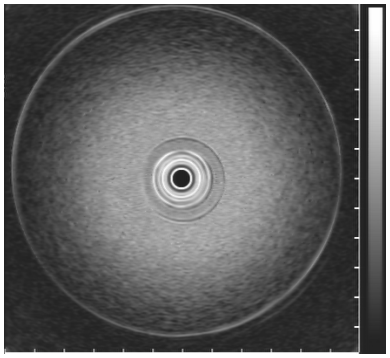	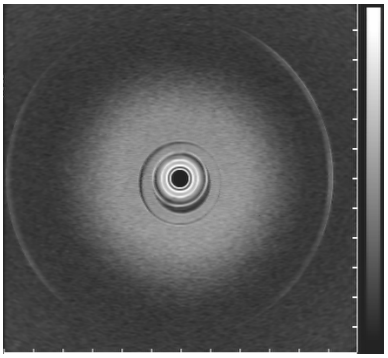
(b) Cling Film (Polythene) with a thickness of 11 μm	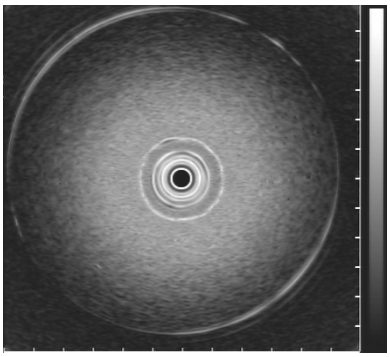	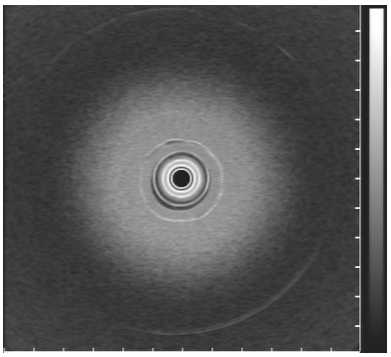
(c) Stretch Film (Polythene) with a thickness of 25 μm	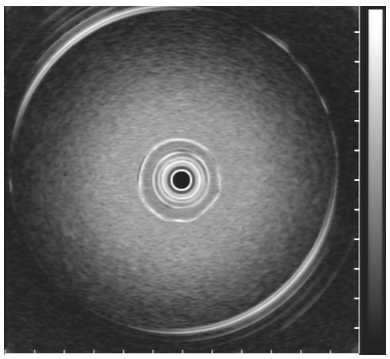	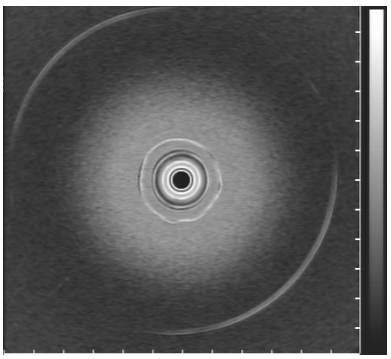
(d) Polythene with a thickness of 130 μm	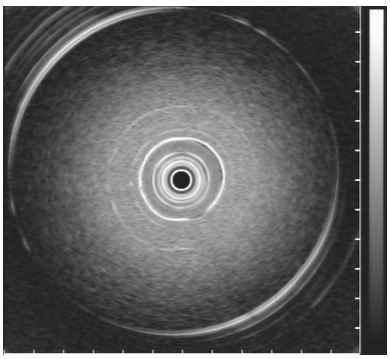	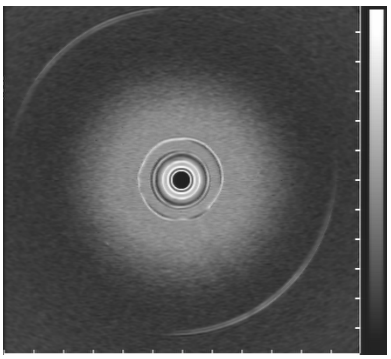

Figure 2.24 - Images obtained from the GF-UM20 echoendoscope when placed into the test phantom, with the endoscope perpendicular to the wall of the phantom.

(e) Latex Condom with a thickness of 80 μm

(f) Latex TOE Probe sheath with a thickness of 300 μm

(g) Latex Tyre Inner with a thickness of 700 μm

(h) Tin Foil with a thickness of 25 μm

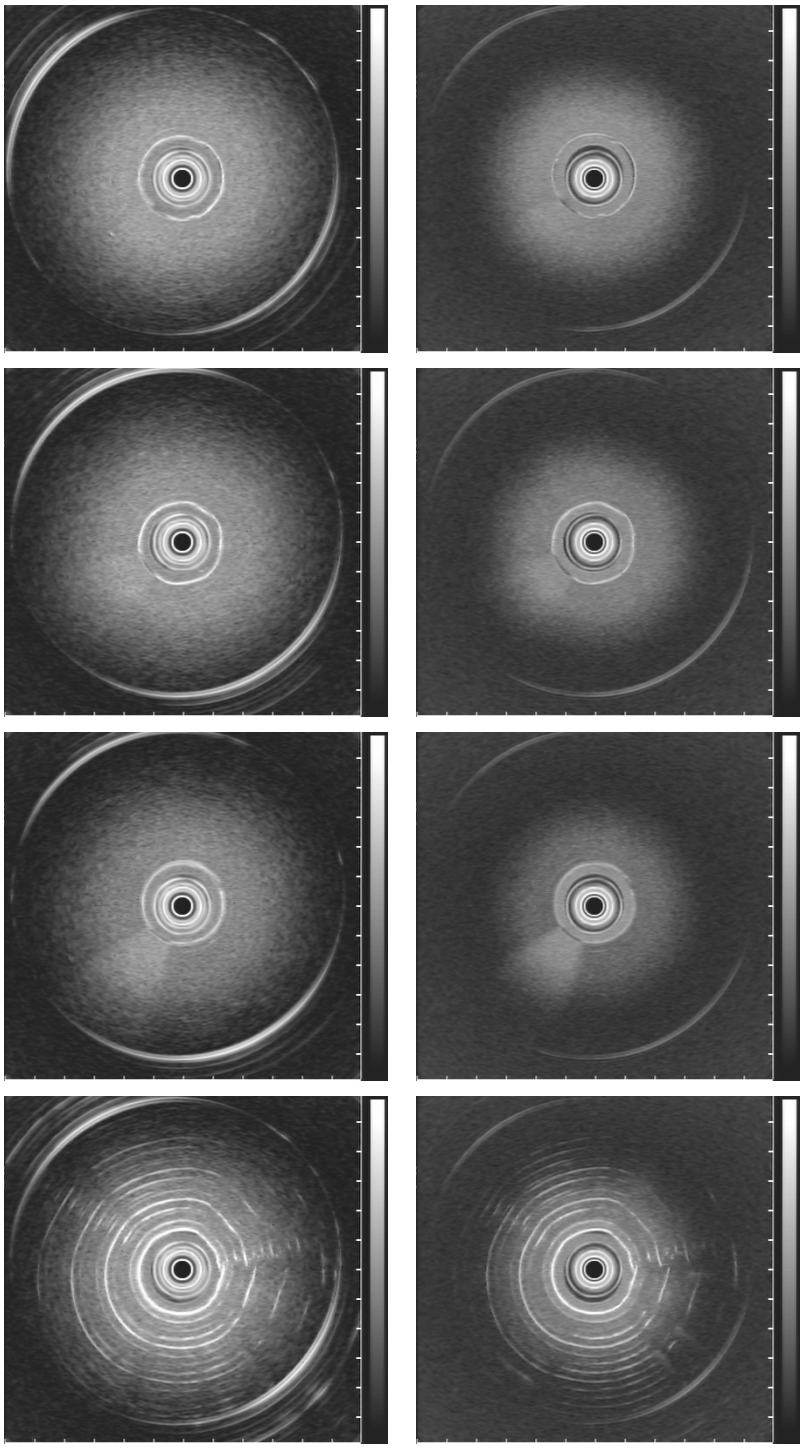

Figure 2.24 - Images obtained from the GF-UM20 echoendoscope when placed into the test phantom, with the endoscope perpendicular to the wall of the phantom.

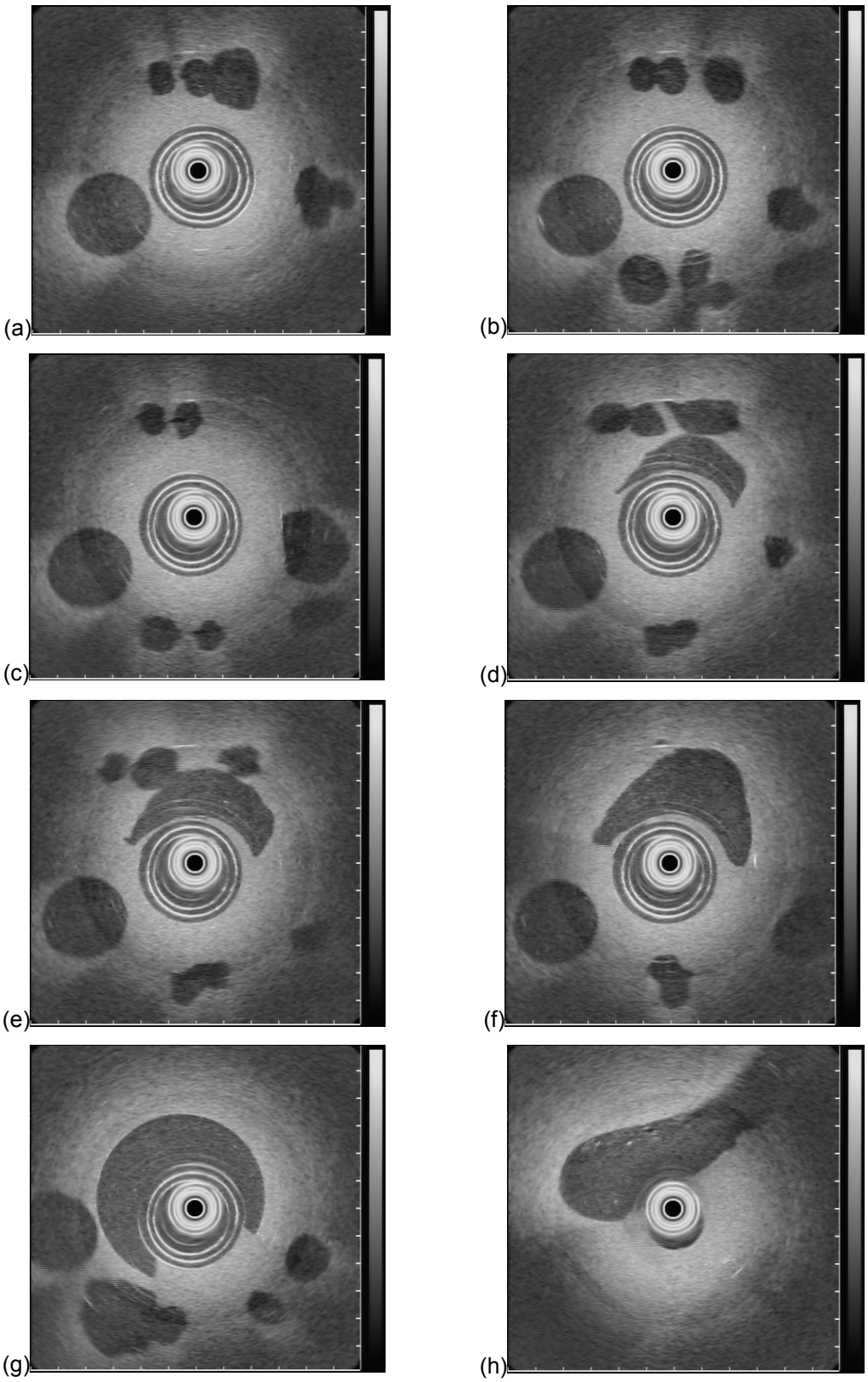

Figure 2.25 - Images of the phantom captured at different levels illustrating the embedded objects. From (a) which is close to the bottom, to (h) which was acquired close to the top of the phantom.

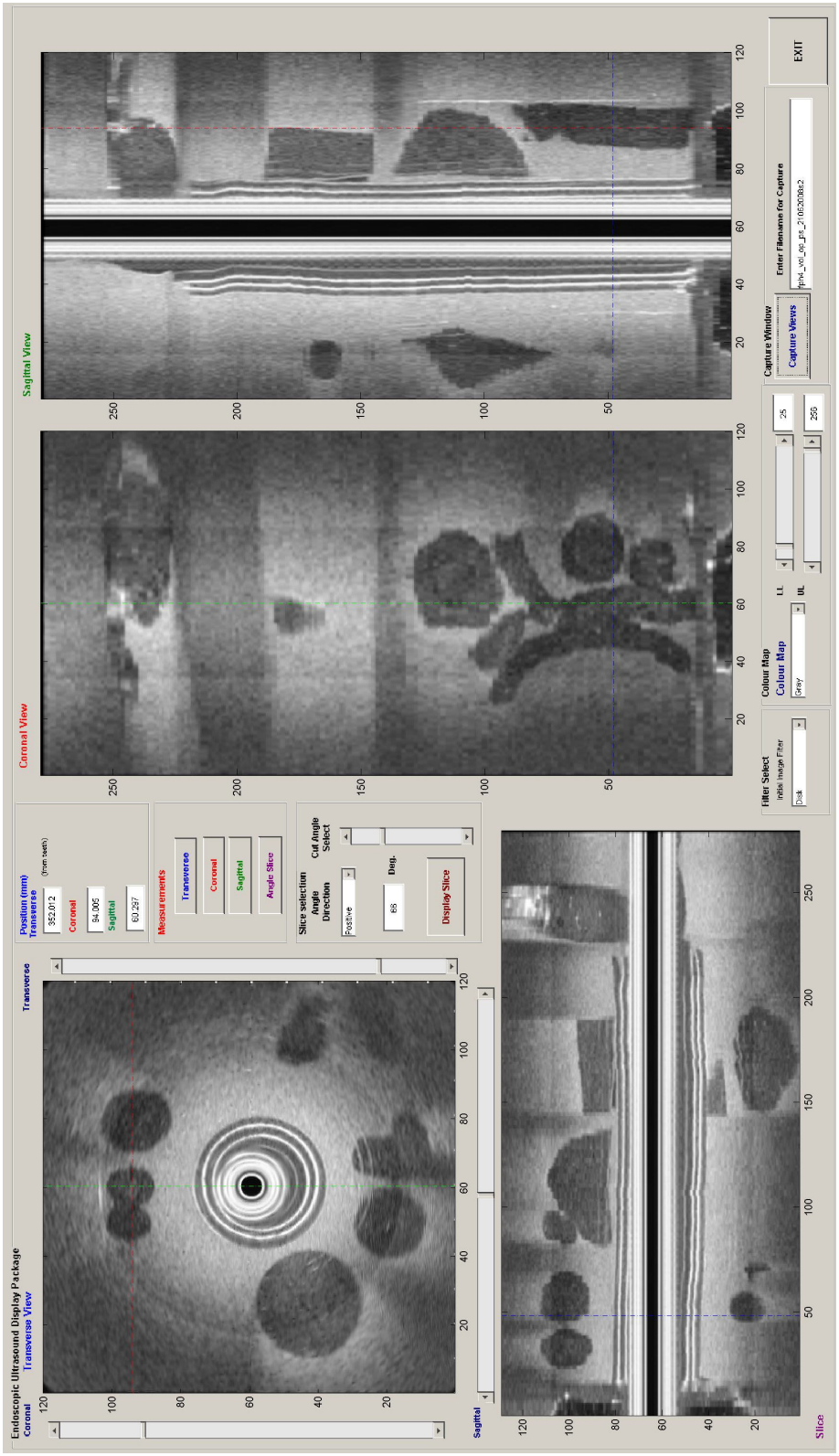

Figure 2.26a - The 3D reconstruction of the phantom. Shown are the Transverse, Coronal and sagittal views of the phantom.

Slice 1- Contained a node close to a vessel and then continuing out of plane to a bifurcating vessel and nodes

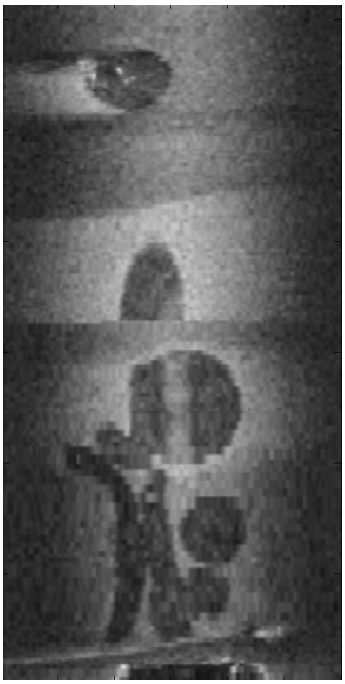

Slice 2 - Contained two vessels surrounded by nodal and tumour

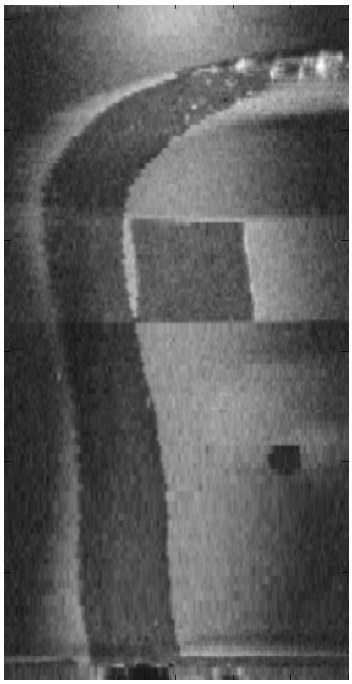

Slice 3 – The Aorta tube contained within the phantom. Slice shows the path of the aorta and the aortic arch.

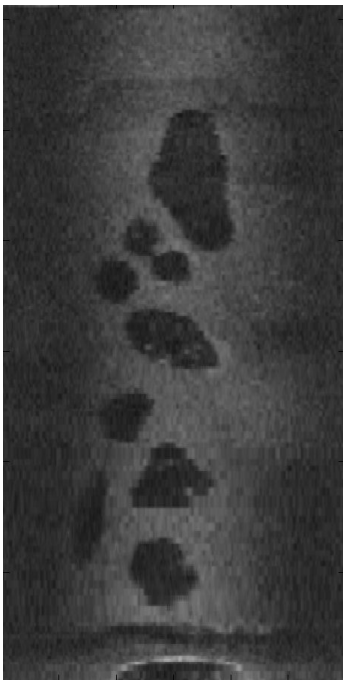

Slice 4 – A number of different nodal shapes both benign and malignant looking.

Figure 2.26b - A series of reconstructed slices from the coronal and sagittal views, through the phantom along the axis of the embedded objects

2.4.3. Discussion

A complex phantom was constructed that consisted of a number of identifiable landmarks that simulated the aorta and oesophago-gastric junction. Moulds were created to produce complex, irregular, three-dimensional objects that could be used to simulate a variety of anatomical structures. The creation of solid moulds allowed for the accurate dimension and volume measurements of the object. The dimensions were measured using the positional digitising arm and standard vernier callipers, to an accuracy of 0.2mm or 0.05mm respectively. The chosen method of dimensional measurement was dependant upon the physical size of the object. Volumes were measured by filling each mould with calibrated volumes of water, dispensed by 1ml syringe, and confirmed by measuring the weight of the mould with and without the additional water, using the Sartorius 1202 MP 300g weighing balance, and varied from approximately 1ml to 325ml. These measurements would be used for the analysis of the 3D-EUS system and measurement toolbox.

The design of the phantom made it possible to replace the object blocks with alternate anatomical scenarios. The only embedded objects that could not be change were the aorta and circumferential tumour blocks. Depending upon the acoustic matching of the TMM making up the phantom body and scenario blocks, there was no interface visible during EUS examination. The resultant phantom gave the appearance that it was constructed from a single block of normal TMM with embedded objects.

A number of everyday materials were investigated to simulate the hyperechoic layers of the ‘oesophageal wall’. Latex was found to attenuate the ultrasound beam and was dependant on the thickness of the latex layer. Adding additional layers of latex, to produce the oesophageal layers, would increase the attenuation of the ultrasound beam. Tin foil produced significant ring artefacts that were prevalent over the entire image and all EUS frequencies. Polythene sheeting of different thicknesses (11µm to 130µm) was examined within the layer test phantom. The 130µm sheet was found to have visible ring artefacts at 7.5MHz. The 11µm and 25µm polythene sheets were found to produce no ring artefacts and no attenuation at the frequencies of interest (7.5 to 12MHz). Angling the transducer reduced the visibility of the 11µm sheet. It was also difficult to maintain the adhesion of the cling film sheet on the surface of the TMM cylinder during the manufacture of the oesophageal wall. Polythene stretch film was chosen as it did not noticeably affect the ultrasound beam of the echoendoscopes, but was still visible when the transducer was angled. As the stretch film was thicker and had improved surface adhesion, it was found to be easier to manipulate and integrate within the oesophageal wall layers. With the production of object moulds, it was possible to obtain accurate volume measurements of the embedded objects for the evaluation of 3D-EUS systems.

2.5. Conclusion

The agar based tissue mimicking material had the desired acoustic properties of speed of sound of 1540m/s, and an attenuation coefficient of 0.5 dB/cm.MHz (IEC 61685 standard 2001). The attenuation, speed of sound and backscatter was successfully characterised using the scanning acoustic microscope for TMM materials with a variety of particle concentrations. The speed of sound did not significantly change with changing particle concentrations, as the particles did not contribute to the speed of sound in the material. The attenuation was found to have an increasing linear relationship with increasing particle concentration. The backscatter was found to have a logarithmic relationship with increasing particle concentration. Therefore it was difficult to increase the brightness of the tissue mimicking material above the normal TMM recipe or 100% particle concentration without significantly altering the recipe (e.g. increasing the SiC particle to 4 times the 100% value).

A prototype, or Mark 1, EUS phantom was successfully produced that allowed for the scanning by the radial echoendoscopes. A number of regular objects were identified and used as moulds for the production of the objects at various particle concentrations. It was difficult to obtain materials that were noticeably brighter than the normal TMM recipe, without significantly changing the acoustic properties. A phantom was investigated that was constructed using the TCP40 TMM recipe for the main body of the phantom and with embedded objects manufactured with the TCP100 recipe, therefore bright objects were successfully obtained. However, this was at the cost of the acoustic properties and resultant image. It was decided that for future phantoms, the TCP0 recipe would be used for vascular and malignant (e.g. nodes and tumour) structures and the hypoechoic layers of the wall. The TCP10, TCP20 and TCP40 recipes would be used for various other benign structures and some of the hyperechoic layers of the central core walls. The TCP100 recipe would be used for the main body of the phantom and hyperechoic layers of the central core walls. This would provide objects that differed visually from each another.

The deficiencies of the Mark 1 phantom were that it housed a very simple anatomy with regular shapes that were easy to reconstruct and analyse using the preliminary 3D-EUS system. It had no relation to what was visualised during patient scanning and the conventional EUS examination of the phantom was not challenging, as none of the objects were complex or irregular in shape.

The design and manufacture of the mark 2 phantom used the methods and techniques developed during the production of the mark 1 phantom and the characterisation of the materials. Suitable custom moulds and enclosure were manufactured from Perspex. The wall mould consisted of 4 tubes, of reducing sizes, to produce four layers, with a thickness between 2 and 4mm. The objects were produced by the techniques described within 2.3.1. However, this technique had drawbacks, which

meant that the objects had a flat segment and arose from one plane. It was also difficult to obtain accurate volume measurements of the objects.

A final phantom was produced to overcome many of the deficiencies of the previous phantoms. The production of a new mould and the introduction of layer materials allowed for an increase in anatomical similarities, with the inclusion of a prominent aorta and OGJ which could be used as reference points for measurements. The techniques used to manufacture the object moulds allowed for accurate volumes to be ascertained by filling the resultant depressions with water and comparing the differences in weight. Complex, three-dimensional TMM shapes could be manufactured by the techniques detailed within section 2.4.1.3. The limiting factor to the phantom was the size of the container used to house the object moulds.

Chapter 3 – Characterisation of echoendoscopes, by Phantom and Hydrophone.

3.1. Pipe Phantom Measurements.

Background

Endoscopic Ultrasound is a well established technique for the investigation of abnormal pathology within the GI tract. However, endoscopists, who only have cursory knowledge of the mechanics and the intricacies of medical ultrasound, often perform this technique. Due to this, abnormal structures may be masked by artefact or not fully visualised due to the performance of the echoendoscope. Ultrasound phantoms are one way of obtaining useful information with regards to the performance and imaging capabilities of the echoendoscope and ultrasound processor.

A number of ultrasound QA phantoms can be used for the performance testing of ultrasound equipment. Quality Assurance phantoms are predominately used to test axial resolution, lateral response width, uniformity, dead zone, depth of visualisation, high and low contrast mass imaging, and spatial calibration of callipers. However, few ultrasound phantoms have been designed for performance testing of EUS or other radial equipment and most are designed for teaching application. The only QA phantom that can be used with EUS and similar equipment is the Model 570 Multipurpose Endoscopic Phantom by ATS Laboratories (ATS Laboratories, Inc. Bridgeport, CT). However, this phantom is constructed from urethane rubber and is only suitable between 2.5 to 7.5MHz. Examples of other QA phantoms include models 40, 42, 44, 50 and 54 QA phantoms from CIRS Inc. (Norfolk, VA) and the Gammex 408LE, 406LE, 405GSX, 404/3 LE phantoms from Gammex-RMI (Middleton, WI). These phantoms can be used to evaluate one or more of the above tests.

Most commercial phantoms are manufactured from Zerdine™ (CIRS Inc. (Norfolk, VA)), urethane rubber (ATS Labs (Bridgeport, CT)), or condensed milk gel (Gammex-RMI (Middleton, WI)). However, the acoustic characteristics of these materials, over the operating frequency of the EUS equipment, are often unknown.

A phantom that has been developed internally was the ‘Edinburgh pipe phantom’, designed by Pye et al. (2004). This phantom is capable of measuring many of the typical performance attributes mentioned above. It has been used to characterise a number of radiological ultrasound scanners within Edinburgh and in some UK Medical Physics Departments. The main advantages of this phantom are that it is constructed from the agar based TMM, that has been extensively characterised, and that it is

possible to modify the phantom for use with EUS or high frequency equipment. The construction of the phantom, the series of wall-less, fluid filled, pipes of various diameters made it a challenging phantom to scan and tested the capabilities of the EUS equipment and the user simultaneously.

The phantom can be used to assess the resolution and penetration of an ultrasound imaging system by imaging each pipe in turn, longitudinally with the pipe aligned within the scan plane. The length of each pipe imaged between the near field and far field limits, gives a measure of these performance parameters.

This chapter details (1) the modification of the 'Edinburgh pipe phantom' so that it could be used to evaluate radial echoendoscopes, and (2) the evaluation of the Olympus GF-UM20 mechanical and Olympus GF-UE260 electronic radial echoendoscopes, using the Olympus EU-M30 processor and Aloka α5 scanner respectively. The imaging parameters, including resolution, near and far fields, low contrast penetration (LCP), dead space and the length of pipes / per pipe diameter will be determined to gain a better understanding of the EUS system and the technology driving it. This will aid the clinician to select suitable equipment for the examination of specific diseases (e.g. the examination of superficial vascular lesions and early cancers, of the staging of advanced tumours that extensively invade into the thoracic and abdominal cavity).

When evaluating EUS equipment, the clinician will often try to answer the following questions using patient examinations:

1. What is the smallest object that can be visualised and how crisp is the image?
2. What is the deepest structure that can be resolved during the examination?
3. What is the closest structure that can be resolved during the examination and how close can the EUS transducer be placed to the GI wall before they are no longer visualised?

Aims

1. To modify the 'Edinburgh pipe phantom' for use with radial echoendoscopes.
2. To measure the imaging parameters of the GF-UM20 / EU-M30 processor combination using the pipe phantom.
3. To determine the imaging capabilities of the of the GF-UE260 / SSD-α5 combination using the pipe phantom.

Materials

Table 3.1 - The echoendoscopes and ultrasound processors evaluated by the pipe phantom.

Type	Manufacturer	Serial no.	Comments
GF-UM20	Olympus	1700949	7.5 and 12 MHz Mechanical radial echoendoscope
EU-M30	Olympus	1700522	EUS processor unit with basic functions of gain, TGC and measurements
GF-UE260	Olympus	1700064	5, 6 7.5 and 10 MHz capable electronic solid state radial echoendoscope
SSD-α5	Aloka	M01916	Aloka ultrasound scanner

To create the pipe phantom, the materials required included the TMM materials detailed within section 2.1.1, the pipe phantom mould, shown in figures 3.1 and 3.2, and a suitable container to house the complete phantom.

3.1.1. Methods

To assess the image performance of the GF-UM20 / EU-M30 and GF-UE260 / Aloka SSD-α5 EUS system combinations, a modified 'Edinburgh pipe phantom' and analysis program, designed and developed by Pye et al. (2004) was used to assess the near and far fields, depth of penetration etc.

The pipe phantom design is based on a series of fluid filled wall-less pipes of decreasing diameters embedded within the phantom. The mould used to create the 'Edinburgh Pipe Phantom' was used to manufacture this TMM test object. Using the recipe and procedure detailed in chapter 2.1.1 for the manufacture of a 100% particle concentration tissue mimicking material, the mould was filled and allowed to set within the refrigerator to aid in the setting of the TMM around the pipes and minimise any artefacts due to the flow around the pipes.

Figure 3.1a demonstrates the mould used in the manufacture of this pipe phantom and figure 3.1b was the completed phantom filled with 3.6 litres of TMM. The schematic diagram of the pipe phantom, detailing the placement and dimensions of the pipes is illustrated in figure 3.2. When the phantom was set and the pipes were removed, the phantom was taken out of the moulding case and placed on its side within a suitable sealable container. The bottom 5 cm was cut off using a fine blade knife. The phantom was submerged into a solution of water / glycerol / ADBAC. The container was sealed and placed on its side to allow any air introduced into the pipes to diffuse out. After 2 hours the container was placed back on its base.

The following experimental procedure was used to asses the parameters of the echoendoscopes:

1. Absorber was cut to appropriate sizes to fit the walls of the container that would be situated close to the transducer and exposed to the ultrasound beam and secured into position.
2. The echoendoscope was securely held in position by a retort stand and clamp, via the handle. A second retort stand and clamp was securely attached to the lab-jack to hold the insertion tube in place (Figure 3.3).
3. The phantom was placed on the bench close to the lab-jack. The distal end and tip of the echoendoscope was carefully secured within the jaws of the attached retort clamp and lowered into the container.
4. The transducer was placed into the tank and the processor activated. The transducer was placed at a part of the phantom that did not contain any pipes and an image was acquired. The gain, STC and contrast were altered to obtain a uniform mid grey over the image.
5. By changing the height and the location of the lab-jack, individual pipes were identified and analysed. Using fine manual adjustments to the tip of the echoendoscope, by hand, the proximal and distal points of the pipes were determined and the image frozen.
6. When a pipe was located, specific measurements of the low contrast penetration, dead space, near and far field were performed. The smallest pipe observed by the transducer was recorded.
7. The focal point was changed to a single level. The focal point was also set at the maximum point for the scanner.
8. The depth of the image was increased so that the entire pipe could be imaged.
9. Where necessary the STC was altered to regain the image grey scale uniformity.
10. Using Equation 3.1, a rule of thumb scaling factor was calculated to obtain a ‘slot’ or ‘window’ size for ascertaining a desired region of interest. The cursors were placed to the exact dimensions and then using a ruler, the dimensions were measured. The value in centimetres related to a slot size in mm (e.g. an 8cm length on the ruler related to an 8mm window size). This remained constant throughout the measurements as long as the image scale remained constant. When the image depth was changed, the window size was re-evaluated.
11. To obtain the transducer ‘dead space’, it was placed in contact with the surface of the phantom at the start of a large bore pipe. The dead space was defined as the area that no structure could be imaged due to artefacts.
12. The low contrast penetration (LCP) was measured by increasing the depth of the image to the point where machine noise was evident. Then using the measurement callipers, the distance to the point where the speckle of the TMM became indistinct from the machine noise.
13. To determine the nearest measurable object depending on the pipe size. The ultrasound image was set to upper quadrant imaging and placed over the start of a pipe. The tip of the endoscope was manipulated till the shallowest depth of pipe was obtained and the image frozen.
14. The window was placed over the pipe. To determine that the pipe was discernable using peripheral vision, the eye was focused at 12, 3, 6 and 9 o’clock. If the pipe was prevalent in at

least 3 out of 4 cases, the pipe was deemed worthy of 'scoring'. If only 2 out of 4 focus points were distinctive then the window was repositioned. The measurement callipers were positioned between the lowest point on the pipe within the scan window and the transducer. (Near field measurement)

15. The tip of the endoscope was repositioned to obtain the deepest point where the pipe could no longer be imaged. The tip was manoeuvred to the point where the transducer face was perpendicular to this point and the image was frozen. The scanning window was placed over the pipe and step 15 was repeated. In this case the callipers were placed between the upper limit of the window and the transducer (Far field measurement). To remain consistent, the transducer was placed in contact with the surface of the phantom in all cases.
16. The measurements were repeated to obtain a total of 3 independent measurements of both the near and far fields and the average was calculated. For each case the tip was repositioned on the pipe under study.
17. The tip of the echoendoscope was located on the next greatest pipe and steps 13 to 17 were repeated.
18. For the GF-UM20 echoendoscope, measurements were performed at 7.5 and 12 MHz.
19. The GF-UE260 echoendoscope was set at the maximum focal point and not altered and then the frequency was changed to each of the frequency settings of 5, 6, 7.5 and 12MHz.
20. Each of the EUS systems was connected to the 3D image capture and analysis system via an SVHS cable. Images were captured for each of the systems and measurement combination.
21. From the Near and Far field measurements and the known angle of the pipes (50º), the pipe lengths were calculated using equation 3.2.

$$sf = \frac{c}{f} \times 15 \qquad \text{Eq. 3.1}$$

Where sf is the scaling factor for window, c is the speed of sound in the material and f is the ultrasound frequency.

$$pl = \frac{f\_f - n\_f}{Sin(a\_p)} \qquad \text{Eq. 3.2}$$

Where pl is the pipe length, f_f is the far-field measurement, n_f is the near field measurement and a_p is the angle of the pipe (50˚).

When the pipe phantom was set and disassembled, it was placed into a container filled with a mixture of water / glycerol / ADBAC. Air was displaced from the pipes by capillary action. A series of pipe measurements were performed on the oldest (GF-UM20 / EU-M30) and newest (GF-UE260 / Aloka SSD-α5) EUS systems available as per the methods.

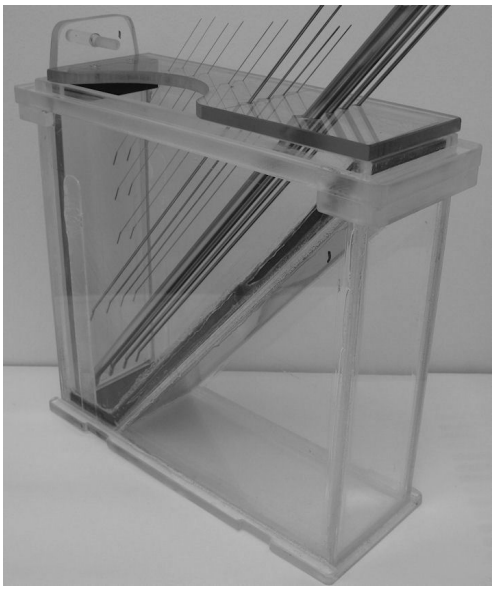

Figure 3.1a – Mould used in the manufacture of the 'modified Edinburgh pipe phantom'.

Figure 3.1b – The manufactured 'modified Edinburgh pipe phantom before removal from the moulding tank.

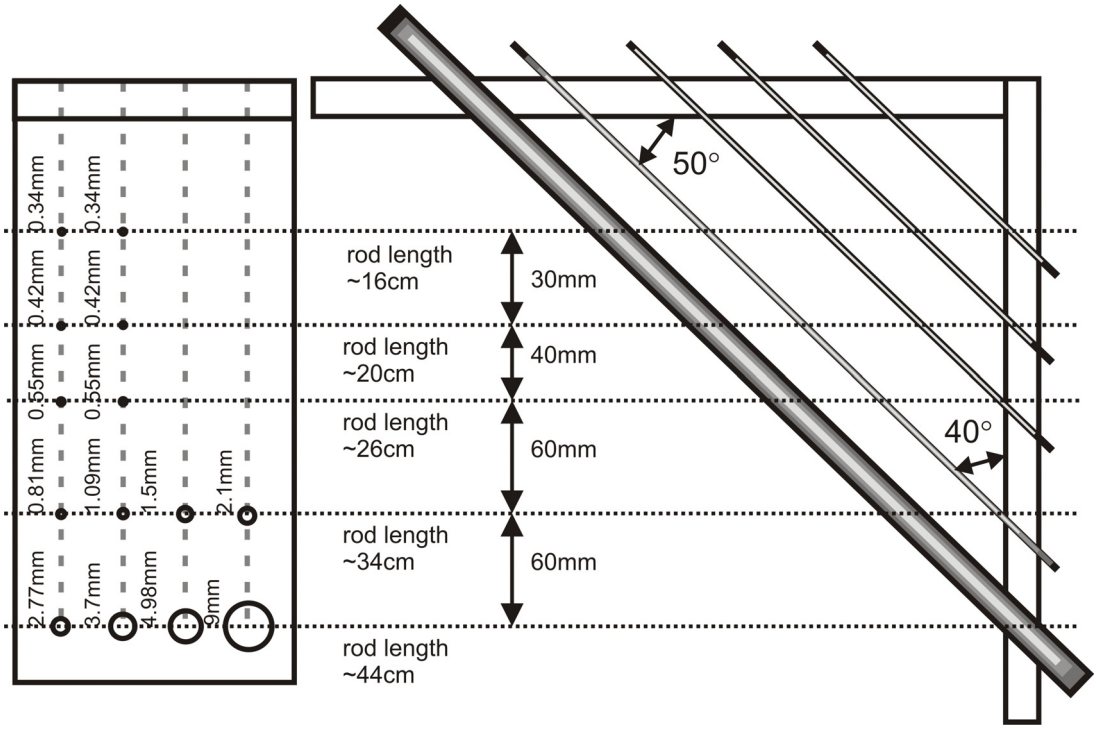

Figure 3.2 - Schematic diagram of the pipe phantom and the placement of the pipes with dimensions.

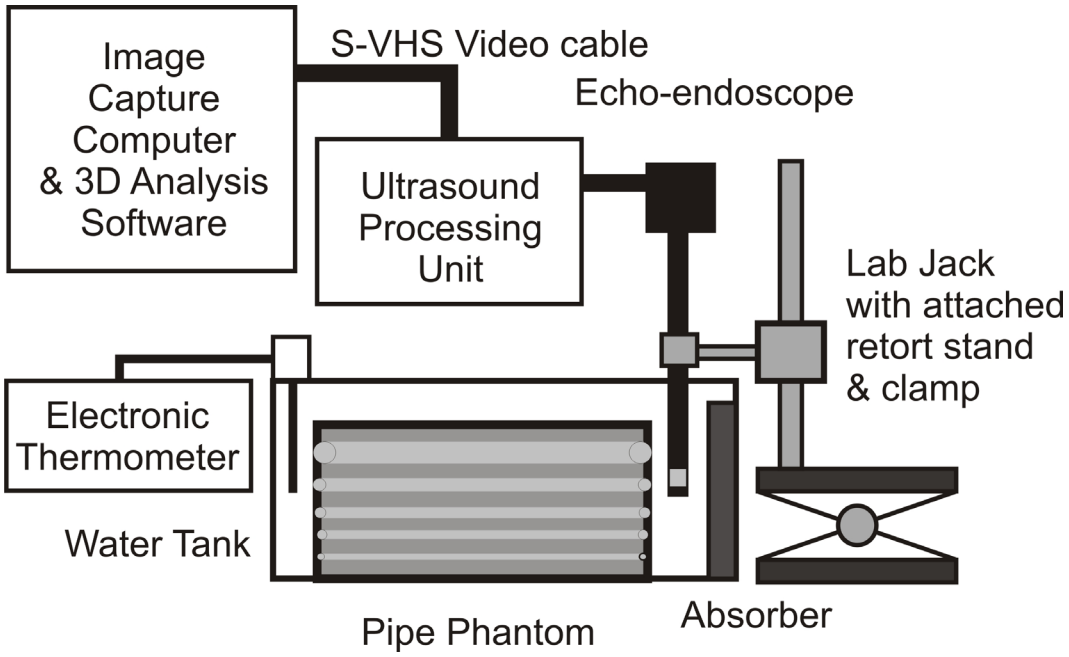

Figure 3.3 – Experimental setup for the pipe phantom measurements.

3.1.2. Results

Tables 3.2 & 3.3 detail the results obtained from the GF-UM20 / EU-M30 (i) & GF-UE260 / Aloka SSD-α5 (ii) EUS systems. The table 3.3 was of the results obtained from the basic measurements of transducer artefact dead space and low contrast penetration. As was expected, the GF-UM20 / EU-M30 system was inferior to the GF-UE260 / Aloka SSD-α5 in both dead space and low contrast penetration. The dead space values of (i) was between 4 to 5 times the depths of system (ii) depending on the frequency of system (i). EUS system (ii) was consistent with changing frequencies and focal depths. The low contrast penetration (LCP) was measured as the deepest point from the transducer in which tissue speckle was visible over the machine noise. As was expected the EUS system (ii) had greater LCP, with values of 1.3 to 1.5 times the LCP of system (i) at frequencies between 5 to 7.5MHz. At higher frequencies of 10 to 12 MHz, the LCP of system (ii) was nearly 2 times the depth of system (i).

Figures 3.4 a to d show example images obtained from both EUS systems when visualising the 2.1mm pipe with the GF-UM20 and 4.98mm with the GF-UE260. From figures 3.4 a and b, the mechanical radial's large transducer artefact clearly masks the area close to the transducer (5mm, at 7.5MHz and 3.6mm at 12MHz) and the penetration of the beam was noticeably diminished when compared to the performance of the GF-UE260 and α5 (Scale of image on the EU-M30 was 6cm, compared with 12cm on the α5).

The series of pipe measurements were performed as per the pipe phantom protocol detailed above. The results of the pipe measurements are shown in Table 3.2 and illustrated in figures 3.5 and 3.6. On average, at 7.5MHz, the GF-UM20 scope / EU-M30 processor combination could only resolve 58% of the pipe lengths observed by the GF-UE260 scope / Aloka SSD-α5 EUS system for pipe diameters between 1.09 and 4.98mm. At the highest operating frequencies of the echoendoscopes (10 / 12MHz), the GF-UM20 could only observe 60.5% of the pipe lengths resolved by the GF-UE260 scope, at the same diameters.

Figures 3.4 c and d, show that the electronic radial's artefact has been significantly improved when compared with its mechanical counterparts, as the transducer artefact dead space was ≤ 1mm at all frequencies. However, there was a 10mm darkened area close to the transducer that could not be brightened to obtain a uniform grey over the image and could mask small superficial objects.

Table 3.2 – Averaged results obtained from the measurements of the Near field, Far field and pipe length as per echoendoscope and the frequency (NF – Near Field Measurement, FF – Far Field Measurement, & L – Length of Pipe calculated using Equation 3.2, Pipe angle is 50º. The / symbol indicated that the results from the 4.98mm pipe to the 9mm pipe did not significantly change the measurements).

	Frequency (MHz)	**Pipe diameters (mm)**							
		0.81	1.09	1.5	2.1	2.77	3.7	4.98	9
GF - UM20 (i)									
NF	7.5	17.57	15.47	13.17	12.17	8.93	6.20	5.80	5.00
FF		23.30	25.03	26.73	28.97	37.13	41.10	46.60	49.57
L		7.48	12.49	17.71	21.93	36.81	45.56	53.26	58.18
NF	12	13.37	12.57	11.10	8.27	6.80	4.87	5.00	/
FF		23.77	27.53	29.77	29.87	29.70	31.73	35.03	/
L		13.58	19.54	24.37	28.20	29.90	35.07	39.21	/
GF - UE260 (ii)									
NF	5	0	11.57	9.07	5.03	3.40	2.57	1.13	/
FF		0	23.90	27.70	33.23	46.93	54.77	69.33	/
L		0	16.10	24.33	36.81	56.83	68.15	89.03	/
NF	6	0	9.77	7.93	6.20	2.83	2.57	1.40	/
FF		0	26.33	29.13	36.60	45.83	56.07	68.33	/
L		0	21.63	27.68	39.69	56.14	69.84	87.38	/
NF	7.5	0	8.73	6.80	5.63	2.87	2.50	1.00	/
FF		0	24.57	34.27	40.10	48.83	56.47	64.67	/
L		0	20.67	35.86	45.00	60.01	70.45	83.12	/
NF	10	0	8.67	4.60	3.23	2.50	2.50	1.00	/
FF		0	28.80	34.32	40.13	44.02	48.81	56.67	/
L		0	26.28	38.80	48.17	54.21	60.46	72.67	/

Table 3.3 - Measurements of the dead space and low contrast penetration as per echoendoscope and the frequency.

Echoendoscope	Frequency (MHz)	Dead space (mm)	LCP (mm)
(i) GF-UM20	7.5	5	55
	12	3.8	36.5
(ii) GF-UE260	5	0.8	80
	6	0.8	80
	7.5	0.8	74
	10	0.8	70

Figure 3.5 graphically displays the near and far field measurements in relation to the pipe diameter. The near field measurements from the GF-UM20 echoendoscope, at 12MHz, were closer to the transducer when compared with the measurements at 7.5MHz, at all pipe diameters.

The near field measurements obtained from the GF-UE260 were a significant improvement over the GF-UM20, with an average decrease of 59.3% in the near field measurements (range: 43.5 to 83%) at7.5MHz and 57% at 10 / 12MHz (range: 31 to 80%). The deepest scoring points of the pipe obtained from the GF-UE260 were also significantly improved over the GF-UM20, with an average increase of 21.2% (range: -2% to 27.9%) in the penetration depth when compared with the GF-UM20 at 7.5MHz and 24.8% at 10 / 12MHz (range: 4.4 to 38.2%).

Figure 3.6 displays the calculated pipe lengths, using equation 3.2, measured at different frequencies in relation to the pipe diameter. At pipe diameters below 2.1mm, the higher frequency settings of the EUS systems see greater length of pipes. The GF-UM20 echoendoscope at 12 MHz will see, on average, a 32.6% increase in the length of pipe when compared with 7.5MHz (range: 45% to 22.2%). When comparing the GF-UE260 pipe lengths, (diameters between 1.09 to 2.1 mm), measured at 10MHz with the other frequency settings, the average increase in the pipe lengths observed at 10MHz were 33.2% at 5MHz (range: 38.7% to 23.6%), 21.3% at 6MHz (range: 17.6% to 28.6%), and 11.8% at 7.5MHz (range: 21.3% to 6.6%).

When measuring the pipes at a diameter above 2.1mm, the calculated pipe lengths were greater at the lower frequencies. The average calculated pipe length increased by 29.6% when the frequency was dropped from 12MHz to 7.5MHz, with the GF-UM20 echoendoscope (range: 23.1% to 35.8%). When using the GF-UE260 scope and the Aloka SSD-α5 scanner, the average calculated pipe length was shown to increase by 13.9% when the frequency was dropped from 10MHz to 7.5MHz (range: 10.7% to 16.5%). When the signal was dropped from 10MHz to 6MHz, the average calculated pipe length increased by 13.1% (range: 3.6% to 20.2%) and when again drop from 10MHz to 5MHz, the average calculated pipe length increased by 13.4% (range: 4.8% to 22.5%)

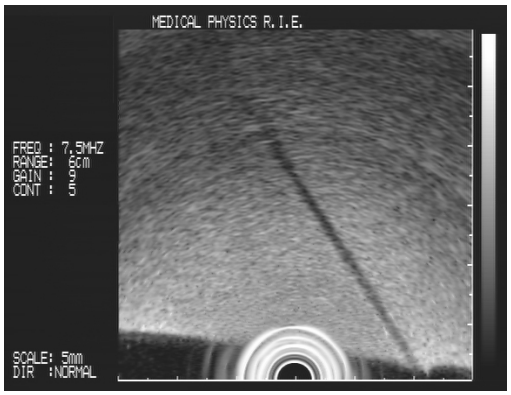

Figure 3.4a – The 2.1mm diameter pipe imaged by the GF-UM20 and EU-M30 EUS system at 7.5MHz. This shows both the dead space and deepest point that the pipe was visualised.

Figure 3.4b – The 2.1mm diameter pipe imaged by the GF-UM20 and EU-M30 EUS system at 12MHz. This shows both the dead space and deepest point that the pipe was visualised.

Figure 3.4c – The 4.98mm diameter pipes imaged by the GF-UE260 and Aloka SSD-α5 EUS system at 5MHz and a depth of 12cm. This image shows an example of the dead space, the relatively course speckle, and a darkened area close to the transducer that can mask fine detail.

Figure 3.4d – The 4.98mm diameter pipes imaged by the GF-UE260 and Aloka SSD-α5 EUS system at 10MHz and a depth of 12cm. This image shows an example of the dead space, the smooth speckle, and a darkened area close to the transducer that can mask fine detail.

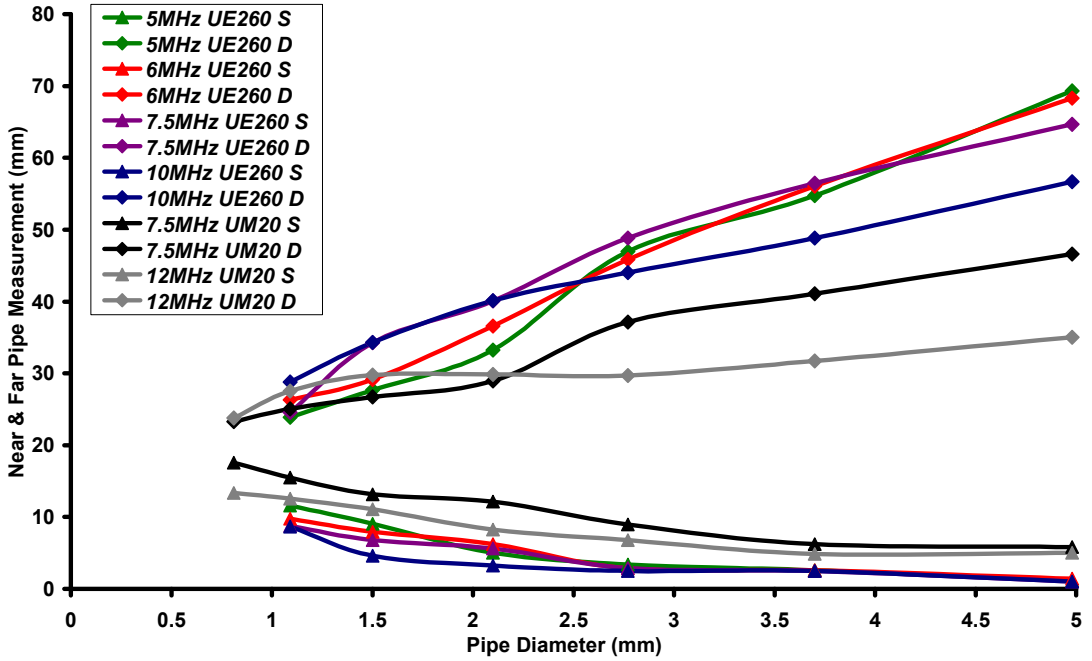

Figure 3.5 - The near and far pipe locations as measured on the pipe phantom with the GF-UM20 and GF-UE260 echoendoscopes, in relation to the pipe diameter (x-axis was pipe diameter (mm) and y-axis was near and far field measurements (mm)).

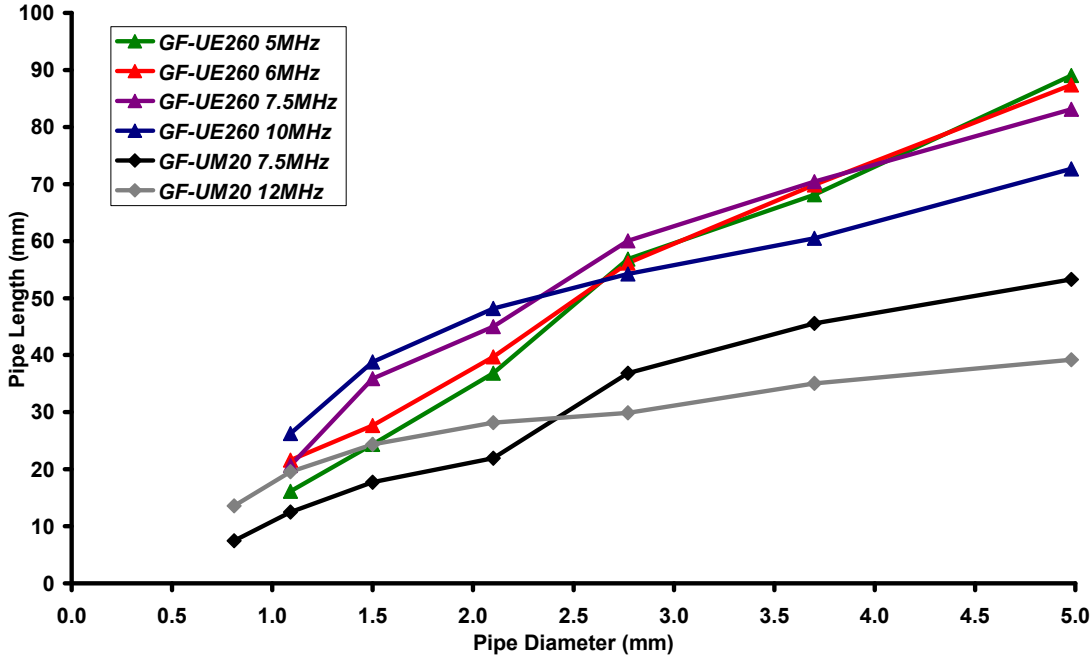

Figure 3.6 - The calculated pipe lengths obtained from the near and far field measurements. These were calculated for the different echoendoscopes and frequencies in relation to the pipe diameter (x-axis was pipe diameter (mm) and y-axis was pipe length (mm)).

3.1.3. Discussion

The examination of the Olympus GF-UM20 / EU-M30 mechanical and Olympus GF-UE260 / Aloka α5 electronic radial EUS systems using the modified 'Edinburgh Pipe Phantom' allowed for the characterisation of a number of imaging parameters. These parameters included resolution, near field depth, far field depth, low contrast penetration, and dead space. The phantom analysis highlighted that there were advantages and disadvantages with both mechanical and electronic EUS systems.

Using the Edinburgh Pipe Phantom, it was possible to characterise the imaging properties of the oldest and newest available EUS systems and pass this information to the clinicians to aid in the selection of equipment for clinical studies. This information would also aid the clinicians in answering their typical clinical questions.

Question 1: What is the smallest object that can be visualised and how crisp is the image?
This question related to the resolution of EUS system under examination. From the imaging of the phantom, the GF-UM20 mechanical radial echoendoscope could clearly see the 0.81mm pipe with both the 7.5 and 12MHz frequencies. However, the GF-UE260 could not resolve a pipe below the 1.09mm diameter pipe, at any frequency. At pipe diameters below 2.77mm, the longest lengths of pipes were visualised at the higher frequencies of the GF-UM20 (12MHz) and the GF-UE260 (10MHz) (Figure 3.6). Above pipe diameters of 2.77mm, the lower frequencies resolved the longest pipe lengths. As most of the structures of interest are in close proximity to the GI tract (within 3 to 6cm), using the GF-UE260 scope at frequencies below 7.5MHz provided no advantage over the 7.5 and 10MHz. In addition, the resolution dropped off when imaging the small pipes, at the lower frequencies (<7.5MHz). The image crispness was due to the operating frequency and, in the case of the electronic radial echoendoscope, the transducer element density and processing of the image by the scanner. The GF-UM20 / EU-M30 combination would produce a crisp image that could visualise small pipes, especially at 12MHz (figure 3.4b). The GF-UE260 / Aloka α5 combination was a softer image that had difficulty resolving small diameter pipes (e.g. < 1.09mm). This was, in part, due to the transducer only having approximately 128 elements. In comparison, other manufacturers (e.g. Fujinon [Fujinon Corp., Saitama, Japan] and Hitachi / Pentax [Hitachi, Tokyo, Japan]) have transducers with over 200 elements in their electronic radial echoendoscopes, but were not examined during this study.

Question 2: What is the deepest structure that can be resolved during the examination?
Question 2 refers to the LCP and the far field depth for each EUS system. From the imaging of the phantom, the GF-UM20 mechanical radial echoendoscope had a LCP of 55mm and 36.5mm for frequencies 7.5 and 12MHz respectively. This was significantly improved with the GF-UE260 echoendoscope and Aloka α5 scanner. It was possible to obtain an LCP ranging between 70 to 80mm

for frequencies of 10 MHz to 5 MHz respectively. The additional penetration allowed for the visualisation of deeper structures and could provide a complete staging of advanced cancers, where the boundaries would be at the fringes of the mechanical scopes capabilities. At pipe diameters below 2.77mm, the deepest visible pipe boundaries were at the higher frequencies of the GF-UM20 (12MHz) and the GF-UE260 (10MHz) (Figure 3.5). As the pipe diameter reduced, the improvement in the depth margin between the electronic and mechanical echoendoscope reduced significantly, to the point where the deepest boundary of the 1.09mm diameter pipe was only 2mm deeper with the electronic radial system. Above pipe diameters of 2.77mm, the lower frequencies resolved the deepest pipe boundary. For the 1.5 and 2.1 mm diameter pipes, the GF-UE260 could visualise an additional 5 and 10 mm depths, respectively, over the depths visualised by the GF-UM20. This depth improvement increased to 20mm as the pipes became larger and the frequency dropped.

Question 3: What is the closest structure that can be resolved during the examination and how close can the EUS transducer be placed to the GI wall before they are no longer visualised?
Question 3 related to the measurement of dead space and the depth of the near field for each of the EUS systems. Using the phantom, the dead space of the GF-UM20 mechanical radial echoendoscope was 5mm and 3.8mm for frequencies 7.5 and 12MHz respectively. This was attributed to the ring artefact generated by the ultrasound beam passing through the thick polythene transducer enclosure. The GF-UE260 had a measured dead space of approximately 0.8 mm. The reduction in dead space was due to the change in technology removing the need for the polythene transducer housing. The reduction in the dead space saw an improvement in the near field depth of the GF-UE260.

In comparison with the GF-UM20, the GF-UE260 was superior in the areas of dead space, low contrast penetration, near and far field measurements. However the GF-UM20 mechanical radial echoendoscope had better resolution. Due to the improved image performance of the electronic radial echoendoscope, the visualised pipe lengths were significantly greater with the larger diameter pipes. However, where the mechanical echoendoscope out shone the electronic radial echoendoscope, was the resolution, as it was capable of visualising the pipe with a diameter of 0.81mm.

From the phantom measurements, it would be recommended that the clinician should use the operating frequency of 10MHz as standard for the GF-UE260 echoendoscope. This scope could be used for the majority of clinical EUS examinations. However, the detailed studies of the GI tract wall layers (e.g. early tumours of the mucosa) would require increased resolution. For this purpose the mechanical radial echoendoscope operating at 12MHz should be used with care, to minimise the possibilities of masking the tumour in the ring artefact.

3.2. Hydrophone Measurements.

Background

Endoscopic ultrasound is a well established technique for the study of GI conditions. Until recently, the majority of available echoendoscopes were based on two, user selectable, single crystals, tuned to either a 7.5 or 12MHz operating frequency, which were mechanically rotated to obtain a 360º ultrasound image. The transducers were attached to the tip of the echoendoscope with a separation of 180º. With the manufacture of small solid state transducers into a cylindrical configuration has seen the advent of electronic radial echoendoscopes. The wide technological difference of these echoendoscopes suggested that the transmitted RF pulse and resultant beam would differ dramatically from the mechanical to electronic radial systems. Also, during the evaluation of the EUS equipment by the 'Edinburgh Pipe Phantom', it was unexpected that the mechanical radial echoendoscope and analogue electronic EU-M30 ultrasound processor unit produced a higher resolution, when compared with the electronic radial echoendoscope and digital Aloka α5 ultrasound scanner.

Needle and membrane hydrophones have been extensively used for the measurement of the acoustic fields of both single and multi element diagnostic and therapeutic ultrasound transducers in the medical field (Hill, 2004). There are many advantages and disadvantages in the use of each hydrophone type. The hydrophone available for this project was the GEC-Marconi bi-laminar PVDF membrane hydrophone. The bi-laminar membrane design provided the best environmental and noise immunity capabilities and good, stable spatial and frequency responses. The available needle hydrophones were optimal for lower operating frequency therapeutic ultrasound devices, and not suitable for measurements of EUS operating frequencies.

The oldest available EUS scope processing unit combination was the Olympus GF-UM20 scope and EU-M30 processor unit. The newest available scope / processor were the GF-UE260 scope and Aloka SSD-α5 scanner. The use of acoustic hydrophones allowed for the visualisation and measurement of ultrasound pressure waves that were transmitted from the transducer. This allowed for the calculation of a number of acoustic parameters and the reconstruction of the transmit beam.

This chapter details the modification of the standard hydrophone measurement to allow for the characterisation of the mechanical and electronic radial echoendoscopes, and the evaluation of a number of beam characteristics for the Olympus GF-UM20 mechanical and Olympus GF-UE260 electronic radial echoendoscopes, using the Olympus EU-M30 processor and Aloka α5 scanner respectively. The evaluation of the endoscopic ultrasound equipment by the hydrophone would allow for the assessment of the characteristics of scope and ultrasound processor combination, and aid the clinician to select suitable EUS equipment to optimise the imaging for specific outcomes. The

calculated acoustic parameters included positive and negative peak pressures, pulse duration, acoustic working frequency, focus, pulse-pressure-squared integral (ppsi), and the beam profile as the hydrophone was moved away from the transducer face.

Combining the results from the pipe phantom analysis and the hydrophone results would allow for the detailed characterisation of the Olympus GF-UM20 mechanical and Olympus GF-UE260 electronic radial echoendoscopes, and the Olympus EU-M30 processor unit and Aloka α5 scanner respectively. The hydrophone analysis may be able to explain the difference in the phantom results obtained for resolution. It can also provide useful information to the endoscopist for obtaining optimal imaging during clinical examinations.

Aims

1. To measure the acoustic properties of a single pulse of the transmit beam and determine the beam shape by the acquisition of a pulse train of the transmit beam of the GF-UM20 / EU-M30 processor combination.
2. To measure the acoustic properties of a single pulse of the transmit beam and determine the beam shape by the acquisition of a pulse train of the transmit beam of the of the GF-UE260 / SSD-α5 combination.
3. To determine the rotational speed of the GF-UM20 echoendoscope.

Materials

The table below (table 3.4) lists the instruments and apparatus used to perform the hydrophone measurements.

Table 3.4 - The systems and echoendoscopes tested and equipment required to perform the hydrophone measurements.

Type	**Manufacturer**	**Serial No. / Model No.**	**Comments**
GF-UM20	Olympus	1700949	7.5 and 12 MHz Mechanical radial echoendoscope
EU-M30	Olympus	1700522	EUS processor unit for the GF-UM20 scope.
GF-UE260	Olympus	1700064	5, 6 7.5 and 10 MHz solid state radial echoendoscope
SSD-α5	Aloka	M01916	Ultrasound scanner to drive GF-UE260 scope.
Stabilised power supply	Farnell	FAO603	±15V variable power supply to drive the pre-amplifier.
Hydrophone	GEC-Marconi	IP089	Bi-laminar PVDF membrane hydrophone.
Pre-amplifier	GEC-Marconi	IP146	20MHz bandwidth
Micro-manipulator	Prior	83319	3 axis manual mechanical
Digital storage Oscilloscope	HP	HP 54615B	500MHz with serial connection for PC download.
BenchLink	HP	HP 34810A	HP Bench link oscilloscope interface software
Laptop computer	Mesh	8888E	Laptop with serial port and capable of running the Benchlink software
Thermocouple temperature probe.	Tenma	02034700	Model: 72-2060 k-type temperature probe.

3.2.1. Methods

A PVDF membrane hydrophone was used to carry out the ultrasound transmit beam captures as the membrane hydrophone as a receiver has the following advantages, when compared with a needle hydrophone. It has a broader, flatter frequency response, good directional characteristics, a reasonably high signal-to-noise ratio and has an impedance value very close to water and therefore introduces little acoustic disturbance.

The following setup was used to perform the hydrophone measurements:

1. A Perspex water tank with dimensions of 40 x 30 x 30 cm was filled with a mixture of tap water and boiling water, 12 hrs before the hydrophone measurements were performed and allowed to settle overnight. The tank was covered with cling film to minimise any dust and particles being introduced into the tank.
2. Before the hydrophone was introduced into the tank, any air bubbles on the surface of the tank were dislodged using a soft fine paint brush and allowed to come to the surface.
3. The GEC-Marconi Y-34-3598 bilaminar shielded membrane hydrophone consisted of two thin PVDF membranes stretched across a 10cm diameter ring with a central active area of 0.5 mm diameter. (Figure 3.7)
4. A retort clamp was attached to the support ring of the hydrophone membrane and clamped into position. Lead weights were placed on the base of the micro-manipulator to ensure that it did not move accidentally and misalign the hydrophone.
5. The membrane was submerged within the water of the tank and secured to the micro-manipulator. The micro-manipulator was placed on a bench lab jack to provide gross alignment changes. The hydrophone was wetted for at least one hour before measurements and any air bubbles were dislodged using a very soft fine paint brush. The water tank with the hydrophone in place and secured to the micro-manipulator is shown in figure 3.8.
6. The echoendoscope was secured onto a long retort stand, via two clamps, where one held the handle in place and the second held the lower portion of the insertion tube and tip close to the hydrophone membrane. The tip of the echoendoscope was roughly positioned close to the active element of the hydrophone and lead weights were placed on the base of the retort stand to ensure that it did not move or tip during the measurements, preventing the EUS scope transducer becoming misaligned.
7. At the back corner of the tank, a k-type thermocouple probe was secured to monitor the temperature of the tank during the experiments.
8. The block diagram illustrating the experimental setup and connection diagram is illustrated in figure 3.9. A photograph of the setup of the electronic radial system is shown in figure 3.10.

9. The power rails of the pre-amplifier were connected to the stabilised variable voltage outputs of the ± 15V power supply.
10. The BNC output from the hydrophone was connected to the pre-amplifier, whose output was connected to channel one of the oscilloscope. A T-piece BNC connector was attached to the BNC cable and connected to the oscilloscope and a 50 Ω BNC terminator was attached to the T-piece connector to ensure to impedance matching.
11. The oscilloscope was connected to the serial port of a laptop computer by a RS-232 cable.
12. The echoendoscope and hydrophone were carefully aligned. The hydrophone was placed parallel to the surfaces to the tank and at right angles to the tank's bottom. The transducer was manoeuvred in front of the active element of the membrane hydrophone using the echoendoscope's control levers. The tip was deemed to be partially aligned to the hydrophone when it visually appeared to be parallel to the hydrophone. For each movement of the hydrophone and scope tip, the voltage reading on the oscilloscope was monitored. When a maximum signal was obtained, small adjustments to the position of the hydrophone were performed using the 3 axes micro-manipulator. By independently altering the position of the hydrophone in each of the axes it was possible to fine tune the alignment of the hydrophone to obtain the maximum signal strength on the oscilloscope. Fine adjustments were performed and the hydrophone was deemed to be aligned.
13. The transducer was positioned 5mm away from the hydrophone. This was determined by measuring the reflection from the hydrophone using the callipers available on the ultrasound processor or scanner.
14. Two independent measurements were performed at each of the chosen distance interval. The first measurement performed was to obtain a single RF pulse. A manual DC trigger level was used to determine the largest peak and triggered from the rising edge of the pulse. If necessary a time delay was added onto the time base of the oscilloscope to centralise the RF pulse waveform. The oscilloscope time base was set at 200ns/division. Using the BenchLink software, the waveform containing 1000 points was acquired from the oscilloscope and saved as a .csv or comma separated values file format.
15. The second measurement was to obtain the series of pulses as the transducer rotated and came into the range of the active element of the hydrophone. The trigger level of the oscilloscope was once again set to trigger on the rising edge of the largest positive RF peak. The oscilloscope time base was set at 0.2ms / div depending on the breadth of the near field pulse spread. The waveform was once again downloaded to the laptop computer.
16. The temperature was monitored at the beginning, middle and end of the measurements to ensure that the water temperature did not vary.
17. For the first 10mm, both measurements were performed every 1mm, from 10mm to the 30 / 40mm (the travel distance of the micro-manipulator) a step size of 2mm was chosen. Both the single pulse and pulse stream measurements were performed at each distance step.

It was necessary to perform measurements at 7.5MHz and 12MHz on the Olympus GF-UM20 echoendoscope. The EU-M30 processor used to drive the scope did not provide any additional functions to modify or alter the transmitted ultrasound beam. The STC and gain functions only altered the reconstructed and processed B-mode image. This was determined by altering a number of the settings on the EU-M30 processor and monitoring the RF signal on the oscilloscope for any changes in amplitude or beam shape.

The GF-UE260 electronic radial echoendoscope and Aloka SSD-α5 scanner was able to be driven at 5, 6, 7.5 and 10 MHz. The scanner was also able to change the focal depth of the transmitted beam. All of the above mentioned scanner options changed the transmitted beam shape, amplitude and / or duration. Hydrophone measurements were performed at 5, 6, 7.5 and 10MHz frequencies at the first deepest focal point and at a set frequency of 7.5MHz and at all of the six different MI settings.

To determine the rotational speed of the mechanical transducer a simple variable strobe light system was manufactured. Using a variable resistor to vary the time base of the LED pulses it was possible to vary the strobes until the rotating transducer became stationary. Figure 3.11 details the circuit used to strobe 2 LED's at a variable speed from 1 to 60 Hz. Once the transducer became visually stationary the pulse waveform was displayed on an oscilloscope and the duration between pulses was measured.

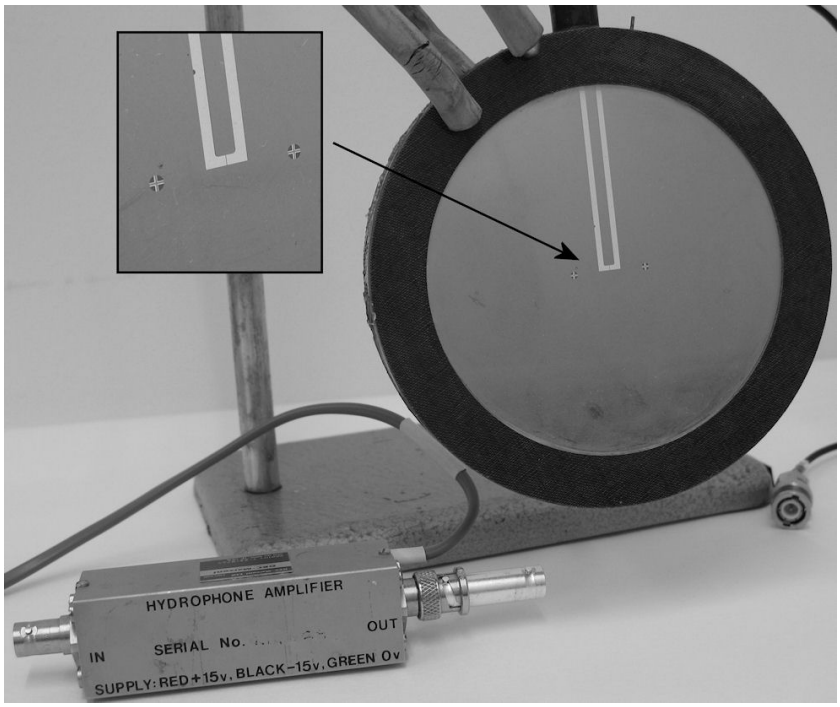

Figure 3.7 - Membrane hydrophone before submersion in the tank and signal amplifier. The insert is a close up of the active segment of the membrane hydrophone.

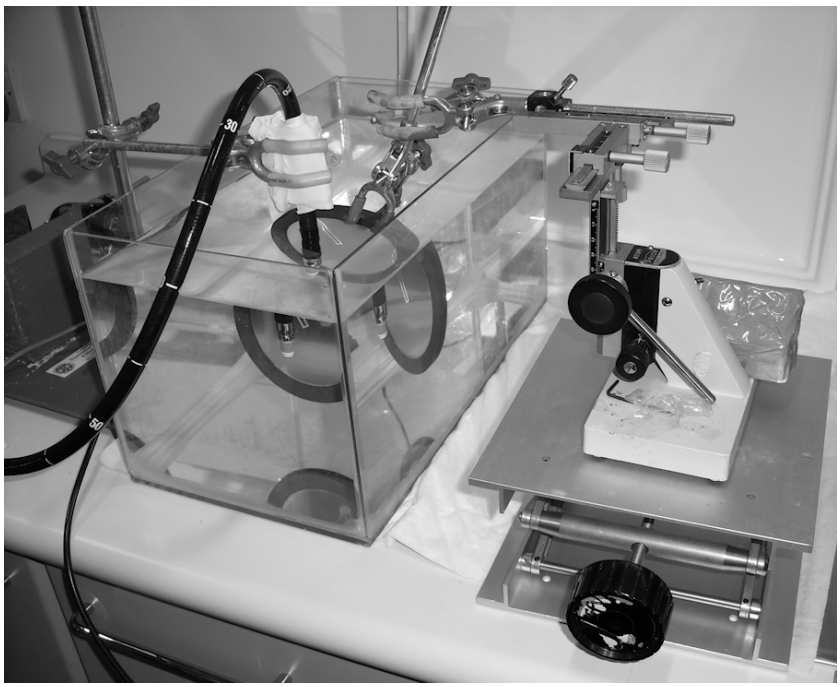

Figure 3.8 - The GEC-Marconi Y-34-3598 bilaminar shielded membrane hydrophone with the GF-UE260 echoendoscope placed in front of the active part of the hydrophone.

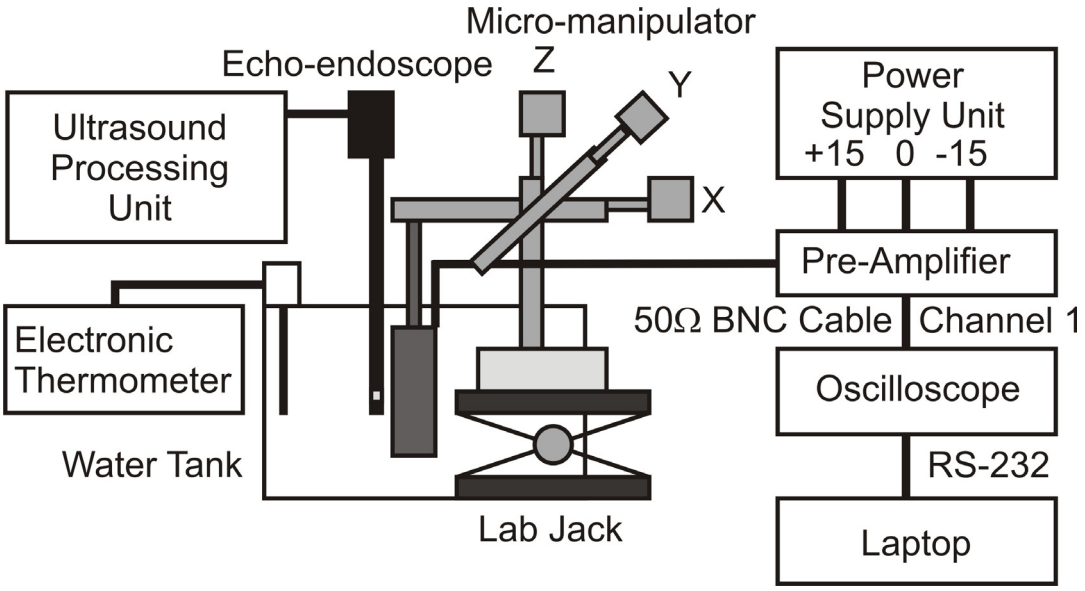

Figure 3.9 – Block diagram illustrating the experimental setup for the hydrophone measurements and the connections between each system.

Figure 3.10 - The measurement setup including the tank, GF-UE260 echoendoscope secured onto a retort stand and the Aloka scanner. The pre-amplifier was placed behind the tank.

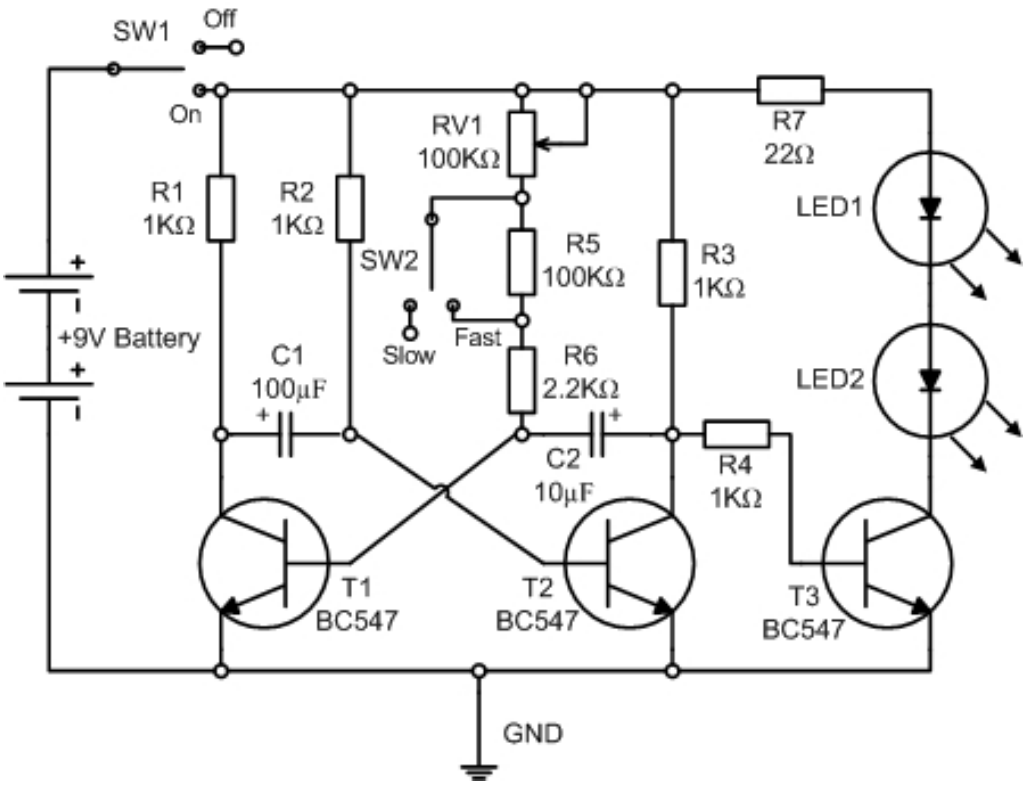

Figure 3.11 – A simple variable strobe light used to determine the rotational speed of the transducer. The circuit was purchased as a kit (MK147) for assembly (Produced by Velleman Components (Belgium, Europe).

3.2.1.1. Analysis Program

A Matlab program was written to analyse and display the results of the hydrophone measurements. The program was written with the assumption that the beam originated from the centre of the of the transducer cylinder. The single 'csv' file contained the results for each hydrophone measurement performed. Each series of 'csv' files that corresponded to a series of measurements for a single protocol setup were individually loaded into the Matlab workspace and stored into separate arrays. Each column contained a single hydrophone measurement acquired at each increasing distance step of the hydrophone from the transducer. One array contained the single RF pulses and the second, separate, array contained the pulse envelope. The data was stored within two MATLAB variable binary files (.mat), one per analysed echoendoscope. The full routines used within the program are listed in Appendix 4 A.5.4 and A.5.5.

The first MATLAB program written was designed to analyse and display the data acquired from the hydrophone. The RF data was scaled to take into consideration the hydrophone sensitivity and the gain of the amplifier at the acoustic working frequency. The RF data was converted from voltage to acoustic pressure using equation 3.3 (Hurrell 2004).

$$p(t) = \frac{V(t)}{M(F_{awf}) \times G_{Amp}(F_{awf})} \qquad \text{Eq. 3.3}$$

Where p is the pressure, V was the RF pulse voltage, M (F_{awf}) was the hydrophone sensitivity at the acoustic working frequency (Figure 3.12 B), and G_{Amp} (F_{awf}) was the gain of the amplifier at the acoustic working frequency. The values of the hydrophone sensitivity and amplifier gain were obtained from the calibration sheet. The acoustic working frequency (AWF) was determined from the mid point of the bandwidth of the PSE at the -3dB point. The acoustic pressure pulse was squared and the integral calculated over the duration of the captured RF pulses, to obtain the pulse-pressure-squared integral (ppsi). The maximum positive and negative peaks and peak to peak pressures were calculated at the focal point of the beam. The pulse duration was calculated from the ppsi plot, where the time was calculated from the time taken for the signal to go from 10% to 90% of the final value. Equation 3.4 was used to determine the pulse duration (t_{dur}):

$$t_{dur} = 1.25(t_{90\%} - t_{10\%}) \qquad \text{Eq. 3.4}$$

Where t_{dur} is the pulse duration, $t_{10\%}$ is the time taken to reach 10% of the amplitude and $t_{90\%}$ is the time taken to reach 90% of the amplitude.

From each of the individual scaled RF pulses at different distances from the transducer, an FFT was calculated. This returned a vector value, with real and imaginary components, for each of the frequency components. A power spectral estimation was performed for each of the components using the complex conjugate command, on the FFT data and then multiplying it with the calculated FFT data, in MATLAB (see Appendix 3: Code example A.3.1).

To analyse and display the lateral hydrophone measurements the program, illustrated by the flow chart in figure 3.12A was used. The program initially loads up the data from the relevant echoendoscope and sets up a number of constants (e.g. sampling frequency, rotational frequency & rotational speed (RPM), time for a single rotation, radius and circumference of transducer). The first segment of the program calculated the angle travelled for each 'sample' point, using the speed of rotation and the sampling frequency, the distance per point was calculated (Appendix 3: Code Example A.3.2). From this, the angle for each point was calculated using equation 3.5 where the adjacent was the radius and opposite was the calculated distance travelled per point.

$$A_{pp} = \tan^{-1}\left(\frac{d_{pp}}{r}\right) \qquad \text{Eq. 3.5}$$

Where A_{pp} is the angle travelled per point, d_{pp} is the distance travelled per point and r is the radius.

The distance travelled by each angle increment was calculated using equation 3.6. To calculate the total distance of the d_x variable was multiplied by the total number of points in the series of separated positive and negative peaks.

$$d_x = \tan\left(A_{p2p}\right) \times \left(HS + r\right) \qquad \text{Eq. 3.6}$$

Where d_x is the distance travelled for each angle increment, A_{p2p} is the angle travelled per 2 points, HS is the distance between the transducer and the hydrophone, and r is the radius.

The next step of the program was to split the data into positive and negative peaks for each distance increment as the hydrophone was moved away from the transducer. The command 'findpeaks' was used to determine the amplitude and location of each of the positive peaks and was stored into an expanding array. To obtain the negative peaks, the signal was inverted and then the 'findpeaks' command was implemented for a second time. Two arrays were constructed, one containing the positive peaks and a second containing the negative peaks (Appendix 3: Code example A.3.3).

To remove the artefacts and superfluous peaks obtained due to noise the positive and negative peak arrays were compared with constant levels to obtain a logical mask. Each column of the mask was multiplied with the corresponding column of the data arrays to remove the noise signals (Appendix 3: Code example A.3.4).

To obtain the envelope of the lateral measurements as the hydrophone was moved away from the transducer (Appendix 3: Code example A.3.5), the 'findpeaks' routine was used on the threshold data. As the number of peaks would change as the distance changed it was necessary to resample the data, while maintaining the position of the peaks. An interpolation routine was used to generate additional points between each of the peaks to obtain a smooth signal with defined number of points.

To scale the data from time to distance, a loop was constructed that would resample the data to the largest distance calculated. This scaling factor changed as the hydrophone was positioned with increasing distance from the transducer and changed the sampling rate of a 'resample' routine. An array was constructed using the maximum number of points that corresponded to the maximum calculated beam travel distance and a number of columns that corresponded to the steps of the hydrophone. For all other hydrophone steps, the re-sampled data was transposed into a corresponding column of the array, at an appropriate point to centralise each waveform.

The data was displayed as separate 3D coloured surface plots of the positive and negative lateral envelopes, using the 'surf' command. Each of the plots were displayed as distance travelled by the beam as it rotates around the transducer (mm) against the distance step as the hydrophone was moved further away from the transducer.

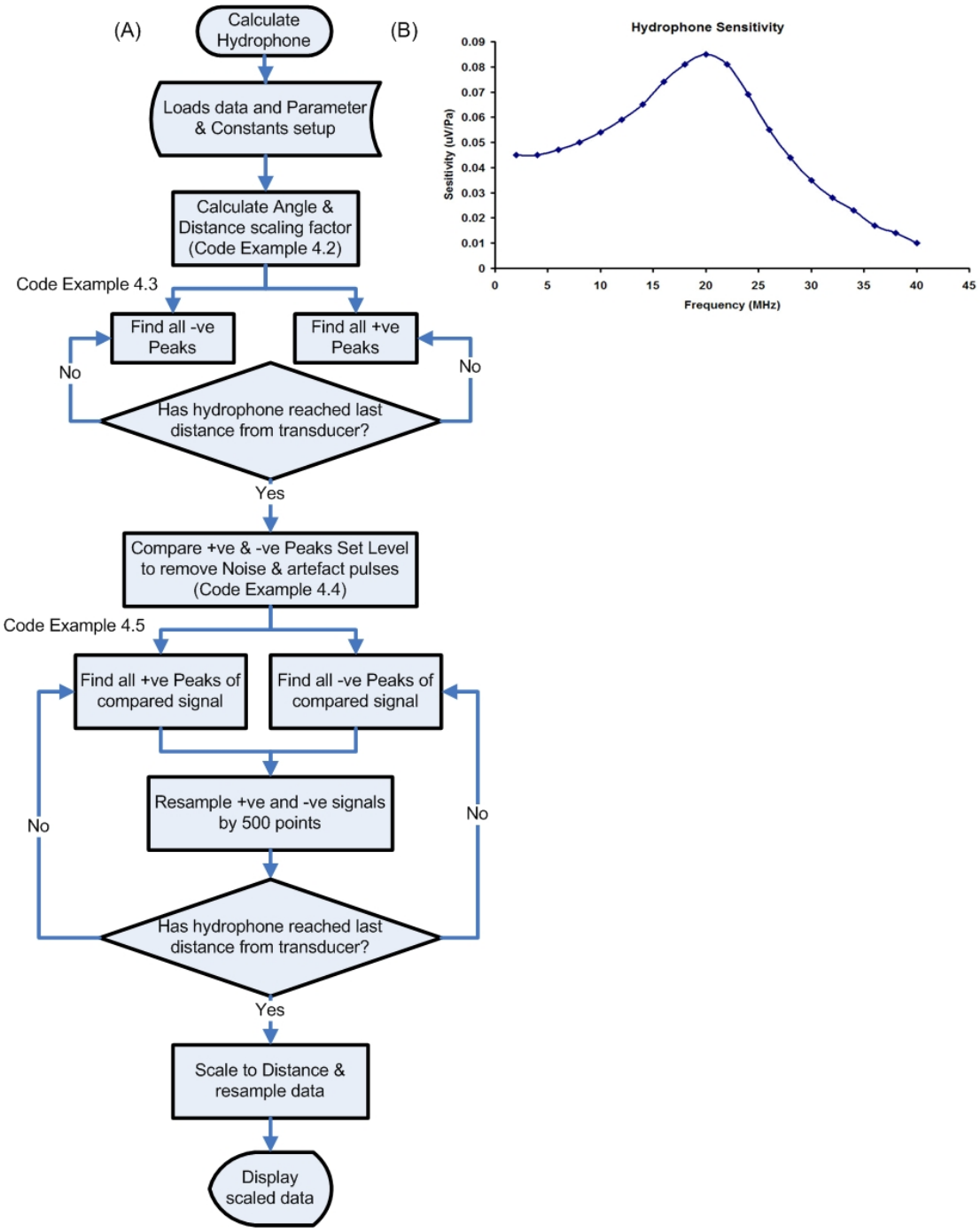

Figure 3.12 – (A) Basic structure and flow of the hydrophone lateral analysis program. (B) The graph of the hydrophone sensitivity was the x-axis is the Frequency (MHz) and the y-axis is the sensitivity in μV/Pa.

3.2.2. Results

The following results were derived from the waveforms obtained from the hydrophone measurements of the echoendoscopes (GF-UM20 and GF-UE260). The raw data was acquired from the digital storage oscilloscope using the HP BenchLink interface software via a RS-232 cable connected to the host laptop PC.

Figure 3.13 a & b display the acoustic pressure pulses, acquired at different distances from the transducer, obtained from the GF-UM20 echoendoscope at 7.5 and 12 MHz respectively. The signals were scaled from the voltage using equation 3.3. From these plots it was clear that the frequency had changed from the alteration of the duration and shape of the pulses. Figures 3.14 a & b show the calculated PSE of the acoustic pressure pulses at each of the corresponding distances, where the red was a chosen point close to the transducer, blue was at the focal point, and green was an arbitrary point after the maximum. Each of the PSE were normalised to the maximum power value at the corresponding frequency. The power spectral estimates were displayed over a frequency range of 0 to 40MHz.

Tables 3.5 and 3.6 summarise the results obtained from the measurements performed on the axial and lateral pulses acquired from the hydrophone measurements. Table 3.5 includes the locations of the frequency where the peak amplitude occurred and upper and lower -3dB points, the bandwidth at the -3dB points and the centre point of the bandwidth. At the 7.5MHz frequency setting of the GF-UM20 EUS system, the maximum power spectral peak was located at 6MHz, resulting in a 20% difference from the expected 7.5MHz centre frequency. The AWF was calculated at 7MHz, which was a lot closer to the expected central frequency, deviating only by 6.7%. At 12MHz, the maximum power spectral peak was located at 11MHz, resulting in an 8.3% difference from the expected 12MHz. However, the AWF was at 9.5MHz which had a greater error of 20.8% from the expected central frequency.

For the GF-UE260, at a frequency setting of 5MHz, the maximum power spectral peak was located at 5MHz, giving the expected 5MHz centre frequency. However, the AWF was calculated at 5.5MHz, deviating from the expected frequency by 10%. With a frequency setting of 7.5MHz, the maximum power spectral peak was located at 7.5MHz. In this case the AWF was 6.5MHz, resulting in a 13.3% error. As the frequency was increased to the 10MHz setting, the maximum power spectral peak was located at only 8MHz, giving a 20% difference from the desired 10MHz. The central point of the 10MHz, the AWF was only 7MHz, producing an error of 30%.

The voltage RF pulses were converted to acoustic pressure and plotted in figures. For the GF-UM20 echoendoscope, the peak to peak acoustic pressure was calculated as 1.907MPa at 7.5MHz and 1.278MPa at 12MHz. The pulse duration at 7.5MHz and 12MHz, derived from the PPI, were 0.1775μs and 0.0975μs respectively. When the GF-UE260 was analysed using figures 3.16 a to c, the peak to peak acoustic pressure were calculated as 2.370MPa at 5MHz, 2.789MPa at 7.5MHz and 2.629MPa at 10MHz. The pulse duration at 5, 7.5 and 10MHz, derived from the PPI, were 0.205, 0.16 and 0.1475μs respectively. When the frequency was set at 7.5MHz and the focal area was altered from 1 to 6 (1 being closest and 6 the furthest), the peak to peak acoustic pressure varied from 1.501MPa at F1 to the maximum of 3.35MPa at F4. After the 4^{th} focal region, the peak to peak pressure decreased to 2.811MPa by the 6^{th} focal region. The average pulse duration calculated over the focal regions was calculated as 0.158 ± 0.003 μs (mean ± standard deviation (std)).

Distance measurements were performed on the surface plots of the lateral waveforms obtained from the GF-UM20 echoendoscope (figures 3.15 a & b) at the frequencies of 7.5MHz and 12 MHz respectively. The measurements were performed at both the -6dB and -3dB points. The measured beam widths, at the -6dB point, of the positive and negative beams at 7.5 MHz were 1.65mm and 1.56mm at the focus of 18mm. The measured positive and negative beams widths at 12 MHz were 1.42mm and 1.29mm at the focus of 12mm.

Figures 3.16 a, b & c display the raw pressure pulses obtained from the GF-UE260 echoendoscope at 5, 7.5 and 10 MHz respectively. The change in colour indicates the pressure pulse acquired at different distances from the transducer. From these plots it was not clear that the frequency had changed with relation to the shape of the pulse. Only the difference in the duration of the pulse indicated that the frequency had altered. Figures 3.17 a, b & c detailed the calculated PSE of the acoustic pressure pulses obtained from the GF-UE260 echoendoscope at each of the corresponding distances, where the red was a chosen point close to the transducer, blue was at the focal point, and green was an arbitrary point after the maximum. Each of the PSE were normalised to the maximum power value at the corresponding frequency.

Table 3.5 – Results obtained from the analysis of the power spectral estimates of the calculated FFT's (figures 3.14 & 3.17), derived from the RF waveforms. (R = Red, G = Green, & B = Blue waveforms from each of the figures)

Frequency (MHz)	Plot	Location Of -3db Point		Acoustic Working Frequency (MHz)	Bandwidth (MHz)	Max. Peak Location (MHz)
		Upper (MHz)	Lower (MHz)			
(i) GF-UM20						
7.5	R	5	7	6	2	5.5
	G	5	9.5	7.25	4.5	6
	B	5	9	7	4	6
12	R	9	12.5	10.75	3.5	11
	G	7.5	12.5	10	5	11
	B	7	12	9.5	5	11
(ii) GF-UE260						
5	R	3.5	6.5	5	3	5
	G	4	7	5.5	3	5
	B	4	7	5.5	3	5
7.5	R	4	8.5	6.25	4.5	5.5
	G	4.5	9	6.75	4.5	7.5
	B	4.5	8.5	6.5	4	7.5
10	R	4	9.5	6.75	5.5	6
	G	5	9.5	7.25	4.5	8
	B	5	9	7	4	8

Table 3.6 – The tabulated results obtained from the hydrophone measurements performed on the GF-UE260 and GF-UM20 echoendoscopes. The measurements were performed at the point of maximum signal, which was assumed to be the focus point.

	Echoendoscope										
	UE260									UM20	
Setting	5	7.5	10	F1	F2	F3	F4	F5	F6	7.5	12
Positive Peak Pressure (MPa)	1.59	1.76	1.55	0.63	0.86	1.57	1.87	1.64	1.43	0.97	0.71
Negative Peak Pressure (MPa)	-0.77	-1.03	-1.08	-0.87	-1.17	-1.45	-1.48	-1.54	-1.38	-0.94	-0.57
Peak to Peak Pressure (MPa)	2.37	2.79	2.63	1.5	2.02	3.02	3.35	3.18	2.81	1.91	1.28
Peak Freq. (MHz)	5	7.5	8	7.5	7.5	6	7.5	6.5	6	6	11
Neg. Beam Focal Point (mm)	18	18	18	5	10	14	16	18	18	18	12
B.W. at -3dB (MHz)	3	4	4	4.5	4	4	4	4	4	4	5
Acoustic Working Frequency (MHz)	5.5	6.5	7	6.75	6.5	6.5	6.5	6.5	6.5	7	9.5
Beam width At -6dB Point (mm) +	2.49	2.55	2.62	6.91	3.95	2.12	2.66	2.62	2.54	1.65	1.42
Beam width At -6dB Point (mm) -	6.09	4.99	3.59	1.74	1.63	2.12	2.83	3.28	3.74	1.56	1.29
Beam width At -3dB Point (mm) +	1.65	1.77	1.79	5	2.91	1.58	1.88	1.92	1.7	0.97	0.89
Beam width At -3dB Point (mm) -	3.11	2.64	2.14	1.04	1.09	1.46	1.75	2.12	2.33	1.09	0.76
PPI max from raw (MPa)	52.1	63.7	52.78	24.4	53.1	86.4	102.5	104.5	70.4	39.6	11.5
Pulse Duration (μs)	0.21	0.16	0.15	0.16	0.16	0.16	0.16	0.16	0.16	0.16	0.10

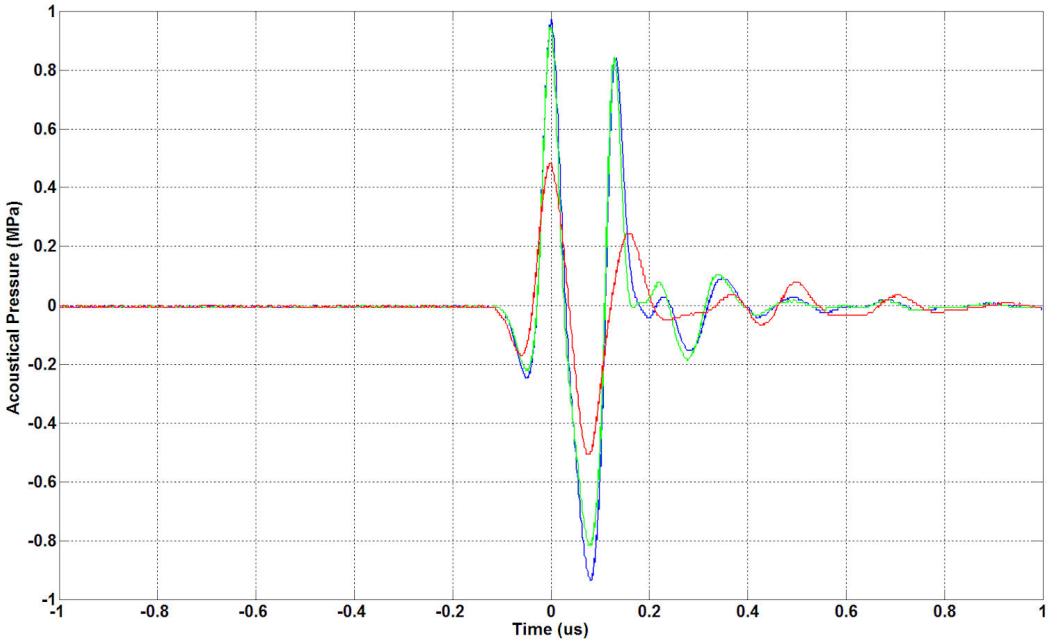

Figure 3.13a. – Examples of the single GF-UM20 7.5MHz transmit pulses acquired from the hydrophone (Acquired at 9mm (red), 22mm (green), & 18mm (blue)). The x-axis was Time (μs) and y-axis was Acoustic Pressure (MPa).

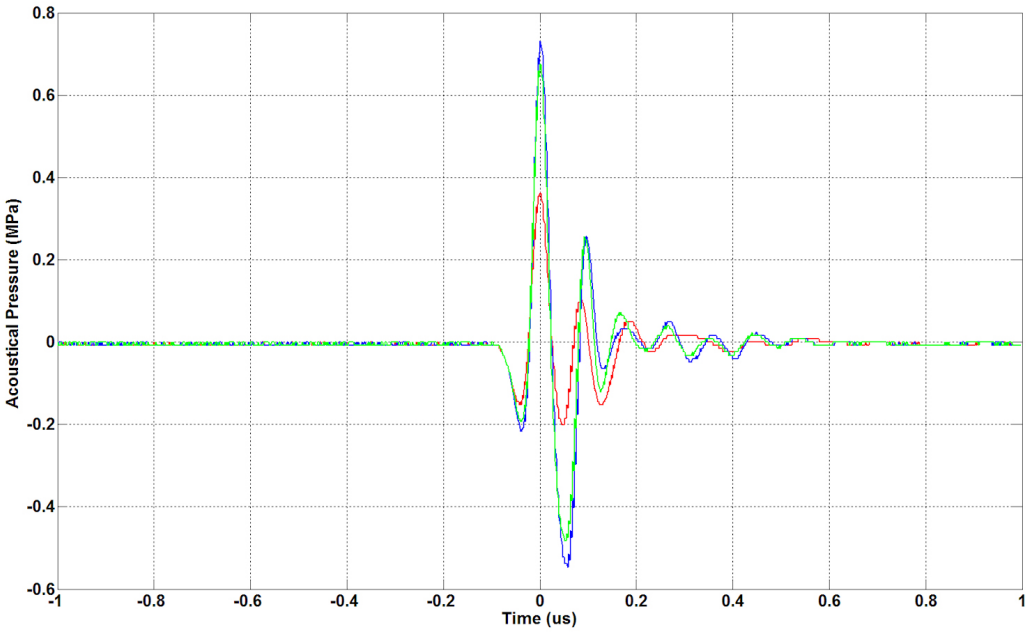

Figure 3.13b. – A single 12MHz transmit pulse from the GF-UM20 echoendoscope, acquired from the hydrophone (Acquired at 6mm (red), 16mm (green), & 12mm (blue)). The x-axis was Time (μs) and y-axis was Acoustic Pressure (MPa).

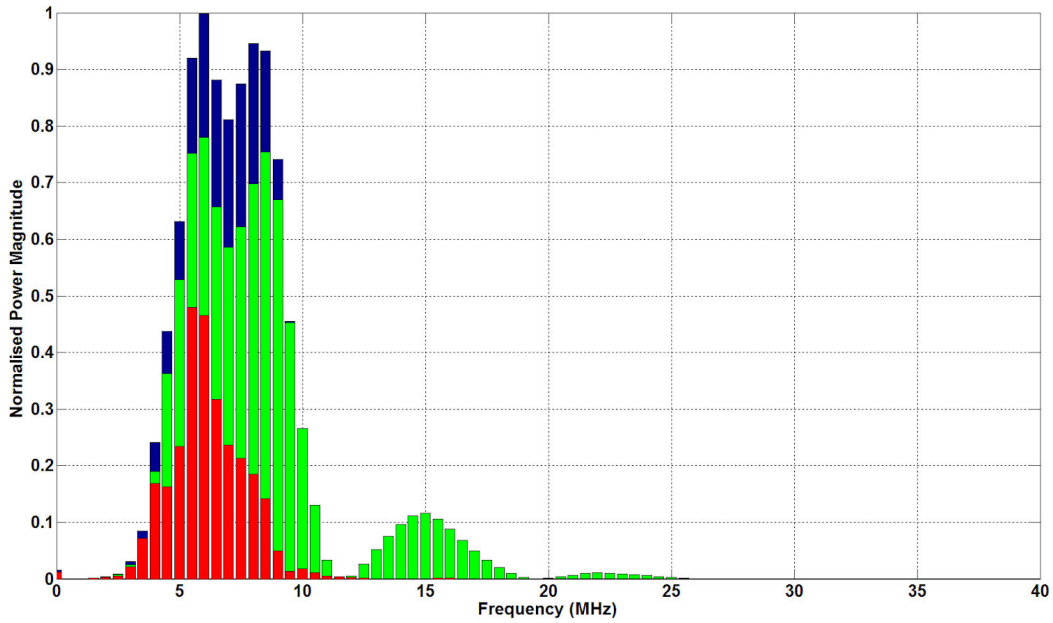

Figure 3.14a - FFT of the transmit pulse of the GF-UM20 7.5MHz pulses (Acquired at 9mm (red), 22mm (green), & 18mm (blue)). The x-axis was frequency (MHz) and y-axis was normalised power magnitude.

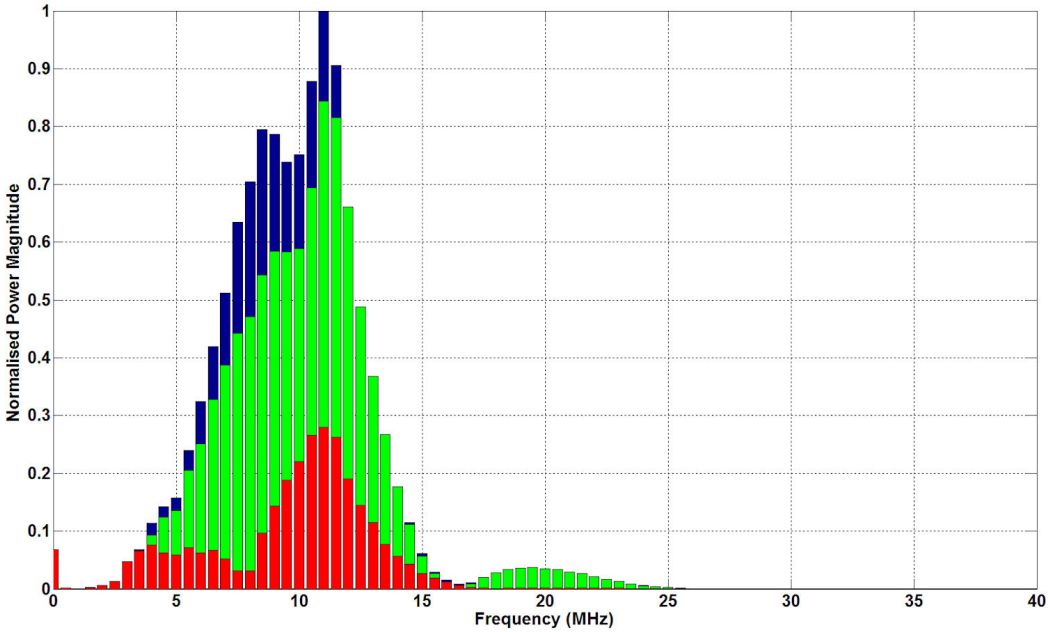

Figure 3.14b – FFT of the transmit pulses of the GF-UM20 echoendoscope at 12MHz (Acquired at 6mm (red), 16mm (green), & 12mm (blue)). The x-axis was frequency (MHz) and y-axis was normalised power magnitude.

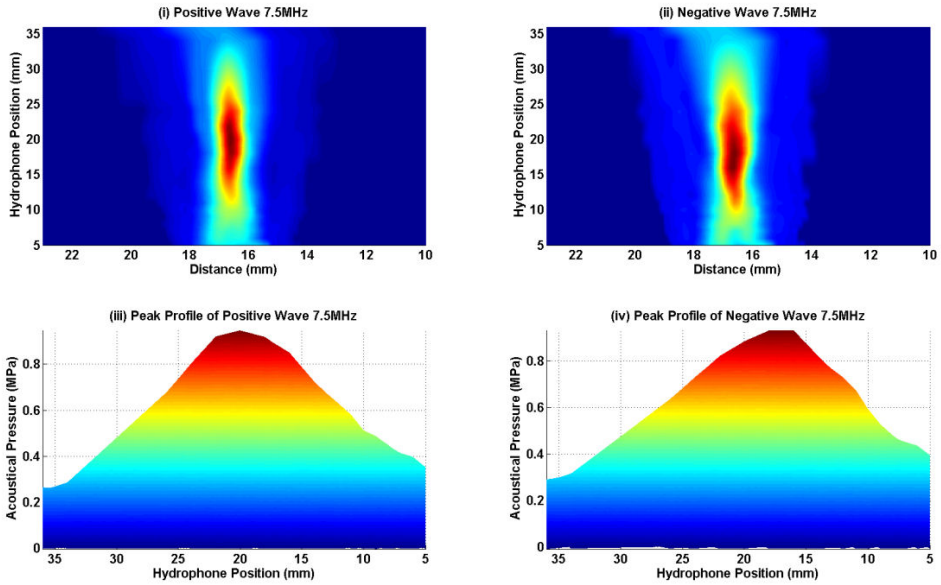

Figure 3.15a – Plots of the hydrophone lateral measurements from the GF-UM 20 echoendoscope at 7.5MHz. The positive (i) and negative (ii) lateral plots were displayed as distance against hydrophone position. The positive (iii) and negative (iv) profiles were displayed as hydrophone position (x) against signal amplitude (y).

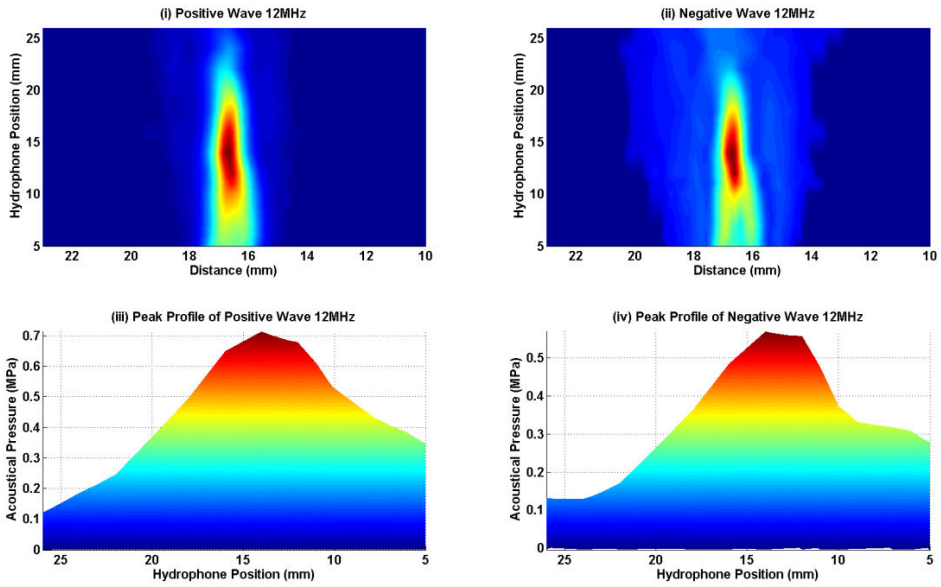

Figure 3.15b – Plots of the hydrophone lateral measurements from the GF-UM 20 echoendoscope at 12MHz. The positive (i) and negative (ii) lateral envelope plots were displayed as distance (mm) against hydrophone position in mm. The positive (iii) and negative (iv) profiles were displayed as hydrophone position against signal amplitude.

Distance measurements were performed on the surface plots of the lateral waveforms obtained from the GF-UE260 echoendoscope at the frequencies of 5, 7.5 and 10 MHz respectively. The beam widths at the focal points were measured on figures A.6.1 a to c and A.6.2 a to f within Appendix 6 using the callipers within the plot window toolset. The measurements were performed at both -6dB and -3dB points (25% and 50% of the intensity). Table 3.6 details the beam widths measurements at the -6dB and -3dB points. The average positive beam width between the 4th and 6th focal regions was 2.6 ± 0.06mm (mean ± std) at a focus of 22mm. The negative beam width increased between the 4th and 6th focal regions and were 2.83, 3.28 and 3.74mm at increasing focal lengths of 16, 17 and 18mm respectively.

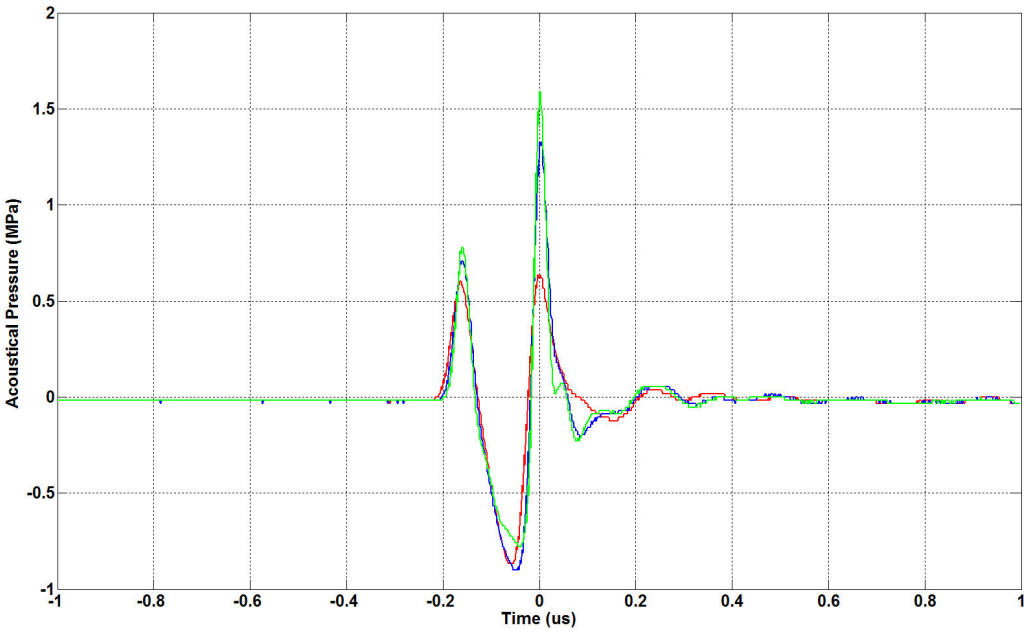

Figure 3.16a – Examples of the single 5MHz transmit pulses obtained from the GF-UE260 echoendoscope, acquired using the hydrophone (Acquired at 10mm (red), 26mm (green), & 18mm (blue)). The x-axis was Time (μs) and y-axis was Acoustic Pressure (MPa).

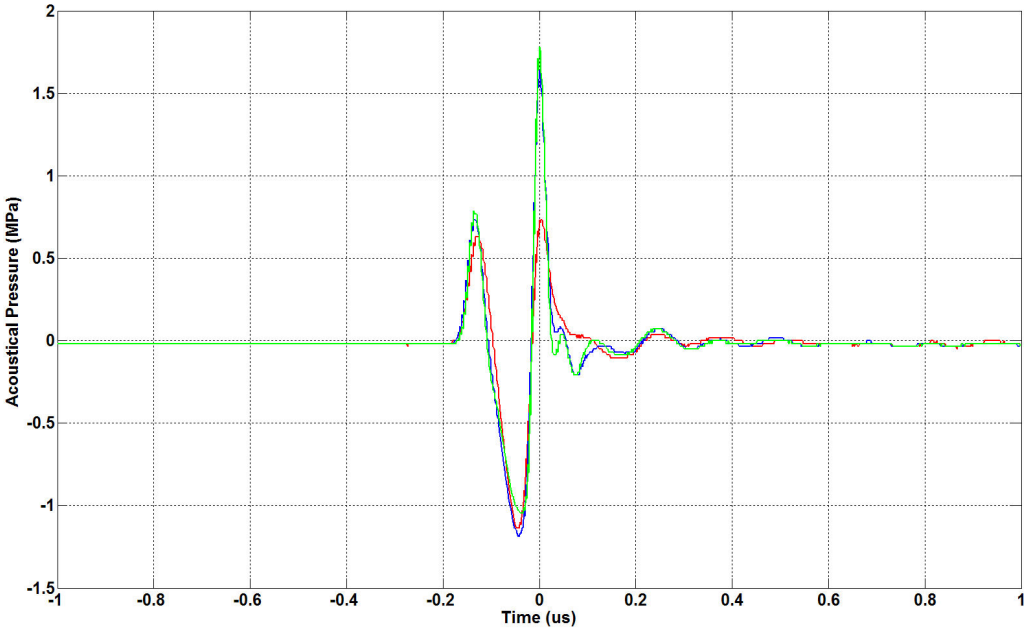

Figure 3.16b – Examples of the single 7.5MHz transmit pulses obtained from the GF-UE260 echoendoscope, acquired using the hydrophone (Acquired at 10mm (red), 26mm (green), & 20mm (blue)). The x-axis was Time (μs) and y-axis was Acoustic Pressure (MPa).

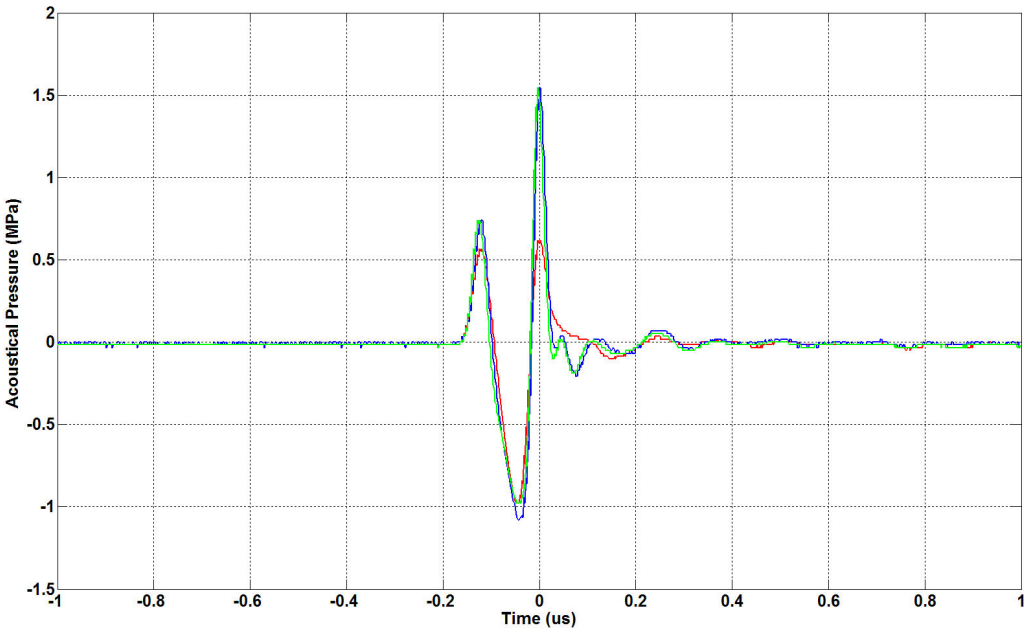

Figure 3.16c – Examples of the single 10MHz transmit pulses obtained from the GF-UE260 echoendoscope, acquired using the hydrophone (Acquired at 12mm (red), 26mm (green), & 22mm (blue)). The x-axis was Time (μs) and y-axis was Acoustic Pressure (MPa).

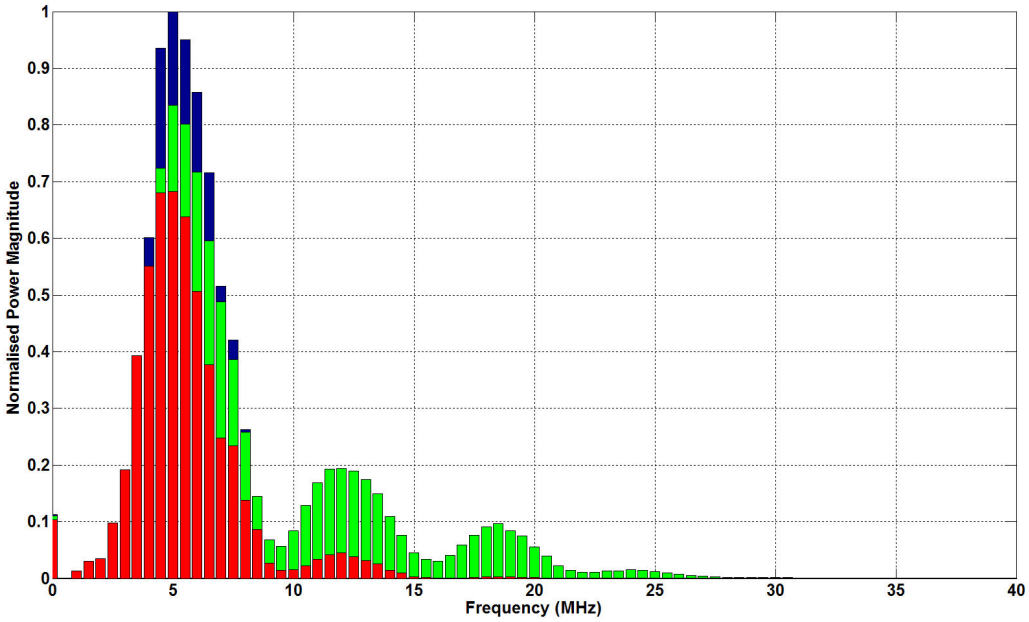

Figure 3.17a – FFT of the transmit pulses obtained from the GF-UE260 echoendoscope set at 5MHz (Acquired at 10mm (red), 26mm (green), & 18mm (blue)). The x-axis was frequency (MHz) and y-axis was normalised power magnitude.

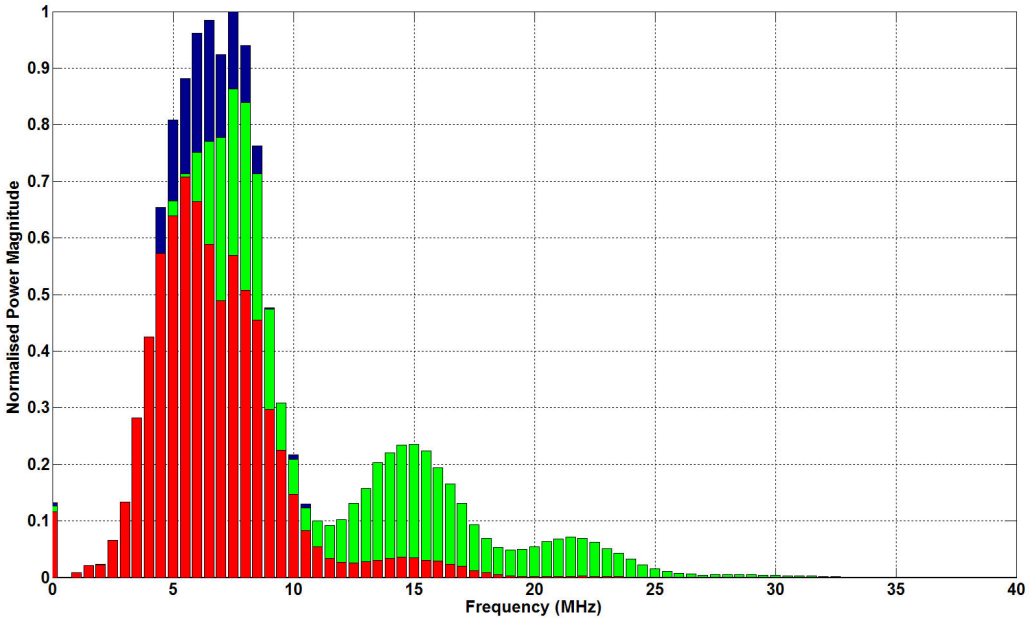

Figure 3.17b – FFT of the transmit pulses obtained from the GF-UE260 echoendoscope set at 7.5MHz (Acquired at 10mm (red), 26mm (green), & 20mm (blue)). The x-axis was frequency (MHz) and y-axis was normalised power magnitude.

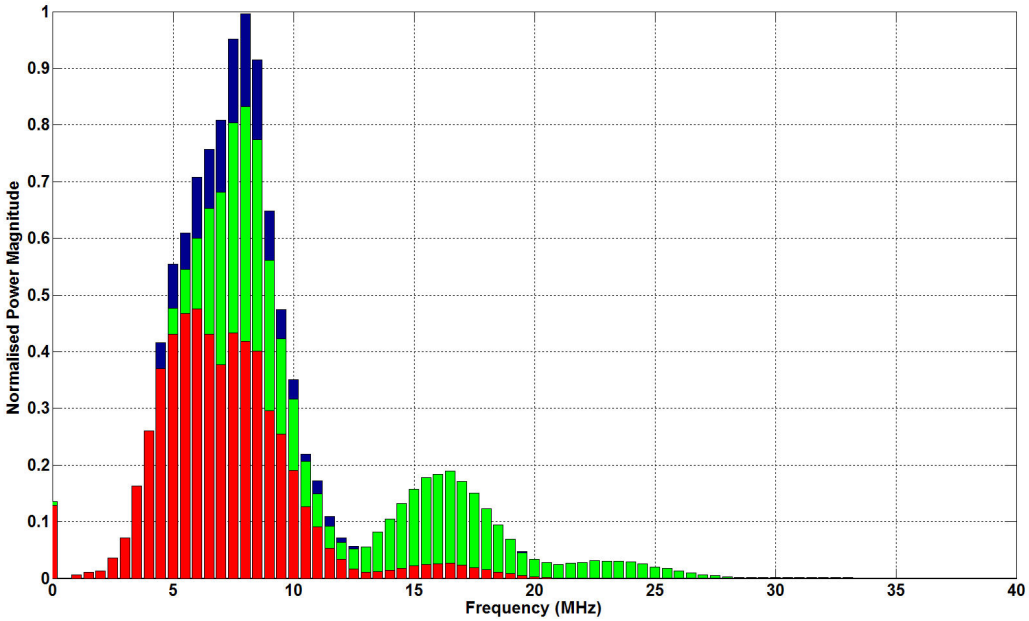

Figure 3.17c – FFT of the transmit pulses obtained from the GF-UE260 echoendoscope set at 10MHz (Acquired at 12mm (red), 26mm (green), & 22mm (blue)). The x-axis was frequency (MHz) and y-axis was normalised power magnitude.

3.2.3. Discussion

A hydrophone measurement technique was modified to allow for the measurement of the acoustic properties of the GF-UM20 and GF-UE260 radial echoendoscopes. This allowed for the visualisation and acquisition of both transmitted single pulse and pulse trains, or lateral measurements, as the rotating ultrasound beam swept over the hydrophone active element. As the hydrophone was moved away from the transducer, a series of measurements were acquired to locate the position of the focal point for the beam. Combining the pulse trains acquired at each position of the hydrophone allowed for the reconstruction of the ultrasound beam. This provided both the focal depth and beam width for each of the echoendoscopes. For the GF-UM 20, the ultrasound beam was reconstructed for each of the frequencies. As the GF-UE260 has greater flexibility, the beams were reconstructed with changes in frequency and focal depth.

A number of acoustic parameters were derived from the single pulses, including the acoustic working frequency, peak and peak to peak pressures. These measurements allowed for better insight into the operation of the echoendoscopes. The GF-UM20 echoendoscope had a stated operating frequency of 7.5 and 12 MHz and the GF-UE260 had a stated operating frequency of 5, 6, 7.5 and 10MHz. From the calculated pulse duration, the GF-UM20 had operating frequencies of 6.4 and 10.3MHz and the calculated AWF was 7 and 9.5 MHz. For the GF-UE260, the calculated pulse duration resulted in operating frequencies of 4.8, 6.3 and 6.8MHz and the calculated AWFs were 5.5, 6 and 7 MHz. The GF-UM20 varied by an average of 10.7 and 17.5% from the expected operating frequency of 7.5 and 12 MHz respectively. The GF-UE260 varied by an average of 6, 14.7 and 31% from the expected operating frequency of 5, 7.5 and 10 MHz respectively. The significant difference in the expected to measured frequency for the GF-UE260, operating at 10MHz, would mean that the endoscopist would have difficulty in visualising fine detail, such as small mucosal tumours or the mucosal thickening associated with Barrett's oesophagus.

The results obtained during the pipe phantom measurements indicated that the GF-UM20 echoendoscope might have a higher operating frequency, when compared to the GF-UE260, as it was able to visualise the 0.81mm pipe at both 7.5 and 12 MHz. The assumed main operating frequencies of the evaluated echoendoscopes were 5, 7.5, 10, and 12MHz, and the resultant expected RF pulse wavelengths would be 308, 205, 154, and 128 μm respectively. From the analysis of the RF pulses obtained from GF-UM20 echoendoscope, the calculated AWF were 7 and 9.5 MHz and the associated pulse wavelengths would be 220 and 162 μm. In comparison the calculated AWF for the GF-UE260, were 5.5, 6 and 7 MHz and the associated pulse wavelengths would be 280, 257 and 220 μm. The difference in the calculated AWF and stated operating frequency of the electronic radial echoendoscope could explain the reduced resolution experienced during the phantom study. Therefore, some layers of the upper GI tract may be difficult to resolve with the GF-UE260, especially

in the lower oesophagus where 7 layers could be visualised. However, the measurement of transmit beam does not take into consideration the filtering and processing performed by the ultrasound scanner and processing unit, on the received ultrasound signal.

The focal point for the GF-UM20 was fixed at 18 and 12mm for the 7.5MHz and 12MHz transducer respectively. Therefore the optimal and sharpest image will be obtained at this point. The GF-UE260 had a variable focal point with six different settings varying from 5 to 18mm. This allows the endoscopist greater flexibility in optimising the image for shallow or deep structures. This resulted in reduced image quality. This was especially noticeable when the focus was at the extreme focal setting (e.g. F1 or F6), where structures could become blurred and difficult to visualise at the opposite extreme.

The pressure peak to peak amplitude for the GF-UM20 was 1.91 and 1.28 MPa for frequencies of 7.5 and 12MHz respectively. The corresponding increase in the peak to peak amplitude for the GF-UE260 was 1.46 and 2.1 times greater, at frequencies 7.5MHz and 10MHz respectively, than the peak to peak amplitude obtained from the GF-UM20 at similar frequencies. This corresponded to the increased penetration of the ultrasound beam and the LCP. From the pipe phantom measurements, the GF-UM20 scope obtained an LCP of 55 and 36.5mm for frequencies of 7.5 and 12MHz. The corresponding LCP for the GF-UE260 was 74 and 70mm. The LCP for the GF-UE260 was 1.35 and 1.9 times greater, for the frequencies of 7.5 and 10MHz, to the LCP obtained from the GF-UM20 at similar frequencies. The increased pressure delivered by the electronic radial echoendoscope would allow the clinician to see deeper structures.

The results obtained from the hydrophone measurements, that had direct implications to the endoscopist were: (1) the 31% difference in the AWF from the expected 10MHz operating frequency of the electronic radial resulted in a lower resolution, reducing the ability to see small structures and fine detail, (2) the increased pressure delivered by the GF-UE260 was capable of resolving deeper structures than the GF-UM20. This was useful in staging of advanced, bulky tumours. And (3) the variable focal settings, available with the Aloka α5 scanner, allowed for the optimised visualisation of structures at different depths However, endoscopists who were familiar with the mechanical radial systems often did not vary the focus on the scanners.

Chapter 4 – Development of the 3D-Endoscopic Ultrasound System.

4.1. Design and Evaluation of the Prototype 3D-EUS System

Background

Endoscopic ultrasound is a well established technique for the study of a number of malignant and benign GI disorders. However, due to the complexity and difficulty of this procedure, it is possible to miss subtle changes within the ultrasound image. These omissions could alter the diagnosis and ultimately change the necessary planning to obtain a greater chance of a successful outcome, and is especially important in the staging and treatment planning of upper GI cancers. The application of 3D-EUS could increase the accuracy of the examination, provide accurate dimensional and volume measurements, and reduce the subjective nature of examination.

The only commercially available 3D-EUS system is a mechanical radial EUS catheter based system. The transducer is mounted on a rotating shaft that can be withdrawn over a set distance and by a set speed. However, this system has two main limitations, (1) The penetration is limited due to the size and frequency of the transducer, (2) the maximum travel distance of the transducer (Z) is 4cm with a maximum of 120 slices.

There have been a number of attempts by research groups, world wide, to produce a three dimensional EUS system using both radial and linear echoendoscopes and incorporated a wide variety of positional measurement and reconstruction methods. The published literature for radial 3D-EUS systems have either used no positional information (Kallimanis et al. 1995) or have used mini-probes and echoendoscopes with automated mechanical withdrawal systems (Gilja 2007, Molin et al. 1998, 1999, Andreassen et al. 2005). The remaining groups have used linear echoendoscopes, in conjunction with optical or magnetic position sensors. However, most of the published literature is preliminary and few details have been published regarding clinical and measurement accuracies.

This chapter details the development of a prototype three-dimensional endoscopic ultrasound technique using hardware and software components available within the Department. These components will be combined to assess the possible accuracies of a 3D-EUS system, using the custom designed EUS phantoms, and determine the requirements for a clinical system.

Aims

1. To develop a prototype 3D-EUS system.
2. To test the 3D-EUS system using the EUS phantoms.
3. To assess the intra and inter observer variation of dimensional and volume measurements performed using the 3Dscan application.

Materials

Table 4.1 – Table of the components of the prototype 3D-EUS system. There were 2 different packages used briefly for the 3D reconstruction and analysis.

Component	Name	Manufacturer	Version / Model No.
Hardware			
Tower Personal computer		Mesh	
Video Capture card	WinTV-PVR	Hauppauge	PCI (00880)
Software			
Capture software	WinTV Application	Hauppauge	3.5
Video editor	Media Studio Pro	Ulead	Ver. 6.5
Image Editor	Paint Shop Pro & Animation Shop	Jasc / Corel	Ver. 9.01 & Ver. 3.11
3D Reconstruction and Analysis (1.1)	3D Scan	In-House	2002

4.1.1. Design of the Prototype Three-Dimensional EUS System

Using the components detailed within table 4.1, the Prototype 3D-EUS system was produced. The Personal Computer (PC) used for the Prototype 3D-EUS system was a Mesh Tower PC (High-end machine: P4 3GHz, 2 Gb of memory, 256Mb NVidia FX5900 graphics card). Placed within the machine was a WinTV PVR video capture card (Hauppauge Computer Works UK Ltd. Borough High Street, London, UK.).

To determine a suitable card for the capture of the data, it was necessary to determine a suitable video format and the necessary compression. When the system was originally developed, there were few video capture cards that had built-in hardware codec encoding to minimise computer loading. With software encoding, there can be a number of cine capture issues, such as:

1. dropped frames and

2. the premature termination of the cine capture that could occur when the memory and hard drive loading becomes intensive during the operating system of the computer house keeping tasks the use of other programs during the capture.

The chosen video capture card (WinTV-PVR-PCI) was capable of acquiring both AVI (Audio Video Interleave) and MPEG (Moving Picture Experts Group) file formats. MPEG-1 format was a lossy compression format that was predominately used for the encoding of analogue composite VHS signals. However, this encodes the video to a maximum data rate of 1150 kbits/s, loosing picture detail and rendering a 'blocky' picture. MPEG-2 format is capable of higher quality capture data rates and more efficient compression algorithms, thereby reducing compression artefacts and loss of detail as well as reducing file size. The WinTV PVR card was capable of a number of different capture data rates from 2 to 12Mbits/s. The EUS processors (both EU-M30 and EU-M2000) and scanner (Aloka α5) were capable of exporting the live ultrasound image via both composite and S-Video video signal formats. The chosen video standard capture parameters for the 3D-EUS system were: MPEG-2 encoding, 704x576 video size, 25 frames per second (fps) and between 8 to 12MBits/s compression level (high-quality / low compression).

The WinTV application was activated to display the live video image to ensure that the video signal was being received. The WinTV application controlled the PVR card and the capture was activated just prior to the start of the pullback. This was to prevent loss of data that might otherwise occur during the initialisation of the card and the start of the streaming of the video to the disk. The time was monitored between the start of the video capturing and the initialisation of the echoendoscopes pullback, to minimise any positional error. When the echoendoscope reached the end of the pullback, the video capture was terminated and the video was appropriately named. A 3D measurement template file was completed with the following information and stored:

- Patient Identifier and file name (made from initials-date of procedure-start-end-time).
- Start point of the pullback determined from the scaling on the echoendoscope.
- End point of the pullback capture determined from the scaling on the echoendoscope.
- Total time of the video clip.
- Rate of capture (fps).
- The total distance of the capture.
- Delays from initialisation of the video capture to the start of the pullback and the stopping of the pullback to the termination of the video capture.
- Compression level used.

The following stages were followed to reconstruct a volume:

- The video file was converted to AVI format using the Ulead Media Studio Pro 6. The convert option within the file menu was used to re-encode the movie file.

- The AVI file was loaded into Jasc Animation Shop (ver.3.4). This program was capable of frame by frame viewing and editing of animation clip and certain video file formats. Each frame of the AVI file was simultaneously cropped to remove any irrelevant or patient sensitive information. The number of frames corresponding to the delays at the start and end of the video file were deleted from the strip. The frames of the processed strip were individually saved as bitmap images (.bmp).
- To reconstruct the volume, the in-house application 3DScan2002.exe was used. This program was written using the 3D reconstruction software libraries provided by Voxar (Voxar Ltd. Edinburgh, UK). The package allowed a user to reconstruct and scale the volume. It was possible to visualise the volume using three different techniques. In each technique it was possible to manipulate and analyse the resultant volume using a number of provided tools.
- The images were loaded into the program using the '3D scan' window. The selection 'volume – new – load from bitmap stack' enabled the bitmap stack of images to be load into the program. The 'root' text box allowed for custom directories and filenames to be entered into the load window. The number and file extension was removed. The first index number (e.g. 10001) was placed within the 1st index box and last image number was placed within the last index box. The step index box allowed for the skipping of frames to reduce the size of the volume in the Z direction. Appropriate scaling factors were calculated for x, y and z directions, and entered into the voxel dimensions boxes. The scaling factors dX, dY and dZ were calculated using the equations detailed within equation 4.1. It was possible to subsample the region of interest by changing the values of dW and dH (figure A.4.1). For large volumes changing the dW and dH values from 1 to 2 would effectively use only every second pixel for the reconstruction. Once the volume was reconstructed, it was displayed within the '3D Scan' window, where it was possible to perform a number of volume manipulations that included changing the brightness and opacity maps to visualise internal structures, inversion of the grey scale map (e.g. black to white) for enhanced visualisation of 'dark structures' (e.g. vessels), and the creation of surface renderings (figure A.4.2).

$$dX = \frac{Xd}{dW \times nPx}$$
$$dY = \frac{Yd}{dH \times nPy} \qquad \text{Eq. 4.1}$$
$$dZ = \frac{Zd}{si \times nF}$$

Where Xd is the dimension of ultrasound imaging window in the x direction, Yd is the dimension of ultrasound imaging window in the y direction, Zd is the pullback distance of the 3D acquisition, nPx is the number of pixels within the cropped image corresponding to the x dimension, nPy is the number of pixels within the cropped image corresponding to the y dimension, nF is the number of individual

images within the image stack, dW is the step factor for the x direction (normally 1), dH is the step factor for the y direction (normally 1), and si is the step index for the z direction (normally 1).

- The 3D Scan window allowed for a number of different rendering methods to display the volume. Normally the 'MPR' option was used to step through the reconstruction, frame by frame, and the volume (ramp) option to display the volume in three-dimensions.
- The 'S view' window, illustrated in figure A.4.3, allowed for the visualisation of the coronal, sagittal and transverse views of the reconstructed volume. By using the mouse it was possible to zoom in and out of the displayed planes (moving the mouse in either a north or south direction). To change the selected cut of the displayed planes, the mouse was placed over the window and moved in a left to right direction. Each window could be independently manipulated. Dimension, area and volume measurements could be performed using the tools available on this window. The 'S View' screen was the main window where all of the analysis was performed. Dimension measurements were performed by dragging a scaled line, via the mouse, over the area of interest.
- Figure A.4.4 illustrates the area or volume measurements window. Using the slider bar, the region of interest was located. The mouse was used to select the region using a rubber band box. The area was computed and stored in the list box next to the main window. The slider bar was used to select the next window and another region selected. This process was repeated until the entire region was selected and then the compute volume button was pressed to obtain the total volume.
- The final window available within the program was the 'Box view' window, shown in figure A.4.5. A wire frame was manipulated to allow the user to produce a selectable 3D cut out segment of the volume to better visualise the internal structure.
- The patient related demographics (e.g. Patient identifier [constructed from date of report and report id], date of procedure, procedure type, the 2D stage of the disease, length and location of pullback) were stored in a secure database.

4.1.2. Testing of the Prototype 3D-EUS system

To test the Prototype system, various phantoms were constructed with embedded objects of known dimensions and volumes. The feasibility and usefulness of the Prototype 3D-EUS system was evaluated and a number of clinical examinations were performed to see if more information could be obtained. Custom EUS phantoms were constructed as per the protocols designed within Chapter 2. With the Prototype phantoms, common object moulds (e.g. measuring spoons, ratchet sockets, ice cube containers) were cast and measured using a vernier calliper and the Microscribe positional digitising arm. The objects were then embedded within the phantom and allowed to set.

To perform phantom measurements, the echoendoscope was inserted into the central core of the EUS phantom. The EUS equipment parameters were recorded, including the gain, image display diameter,

measurement frequency and contrast. The start position, as defined by the measurement scale on the insertion tube of the echoendoscope, was recorded. The video capture was initiated and the time between the start of the pullback and the start of the video recording was noted. The echoendoscope was withdrawn from the central core of the phantom, at a constant speed. When the tip reached the surface of the phantom, the recording was terminated, and the end position was noted. The video was recorded at a resolution of 704x576 and at 25 fps. To simulate the meeting of resistance or stenotic areas, resistance was applied to the insertion tube of the echoendoscope at various points and at varying degrees of pressure during the pullback. This was accomplished by a second person enclosing and releasing their thumb and fore finger over the insertion tube. The Microscribe positional arm was used to monitor the speed and position of the echoendoscope during the pullback and recorded to the hard drive. The video and images were processed as per the Prototype 3D-EUS system protocol. The volumes were analysed to visualise the shapes and obtain dimensions of chosen objects.

The position of the digitising arm was used to monitor the position and speed of the endoscope during the Prototype 3D-EUS phantom studies but was not included within the reconstruction. Basic positional information was used in the majority of the studies clinical and phantom studies. This consisted of the start and stop point, and a constant speed withdrawal of known duration (Figure 4.1). To compare the accuracies of conventional EUS and the Prototype 3D-EUS system, a standard 2D EUS examination of the phantom was performed by entering the central core of the phantom and by manipulating the insertion tube of the echoendoscopes, embedded objects were located. When an object was found x, y and z dimensional measurements were performed using the tools provided within the Olympus EU-M2000 and EU-M30 processor units. Measurements were performed using the dimensional tools provided within the 3D Scan software package.

To assess inter and intra observer variation, repeated dimensional and volume measurements were performed on a reconstructed volume of the phantom and clinical reconstructions. The volume measurement error was analysed by comparing the actual and measured volumes obtained from the phantom. Measurements were performed by 3 observers with 3 repeats. Volume measurements were performed on three in-vivo reconstructions acquired by the Prototype 3D-EUS system, and analysed by 2 independent observers. Using the 3D scan program 3 repeated volume measurements were performed on chosen objects within the volume. Discrete objects, (e.g. nodes, GISTs) were chosen for volume measurements. The *in-vivo* volume measurements were compared to obtain inter and intra observer variability.

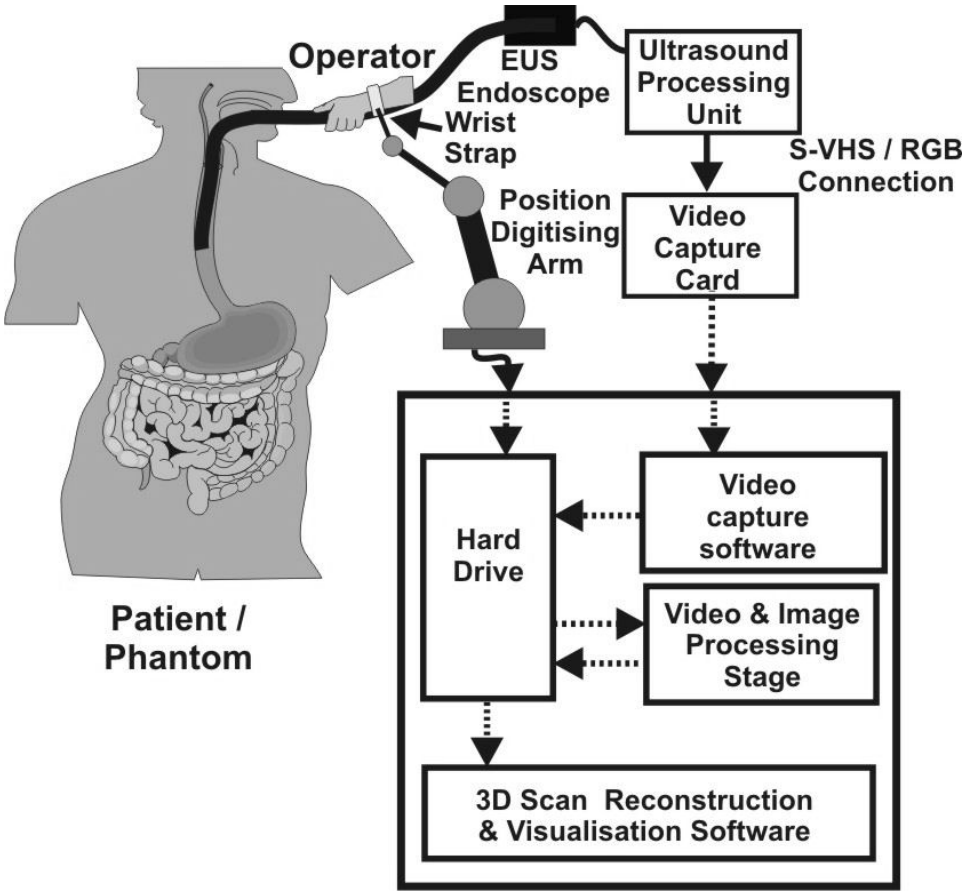

Figure 4.1 – The detailed schematic diagram of the Prototype 3D-EUS system. The position of the digitising arm was only included to monitor the position and speed of the endoscope during the later phantom studies. Basic positional information was used in the majority of the clinical and phantom studies. This consisted of the start and stop point, and a constant speed withdrawal of known duration.

4.1.3. Results

Repeated dimensional measurements were performed on the Mark 2 phantom by two experienced endoscopists. Three individual measurements were performed by the endoscopists and the values averaged. The measurements performed on the X-Y plane of the standard transverse view of the EUS processors resulted in a maximum error of 5% and an average of 3%. The standard Z measurements performed by the endoscopists produced an average error of 8% over all the measurements with a maximum error of 23%. Identical measurements were performed on the reconstructed volume by a single reviewer who obtained an average error of 2.2% and a maximum of 3.7%. Table 4.2 details the average and maximum percentage errors obtained from the endoscopist measurements and duplicate measurements on the volume reconstructed phantom.

Figures 4.2 a to e illustrate the differences in the shape of the bifurcation and associated objects with constant and interrupted pullbacks. Measurements performed to obtain the maximum dimensions of the bifurcation and associated object (node), shown in figure 4.2, are shown in table 4.3. The actual dimensions of the objects are 125mm for the bifurcation and 45mm for the node. A graph of the pullback distance travelled plotted against the time of the pullback is illustrated in figure 4.3.

Table 4.2 - Summary of the Z dimension measurements obtained from the scanning of the EUS phantom. The average error was obtained from two independent examinations of the phantom or reconstructed volume. Max error is the maximum error obtained from a single measurement obtained from the individual objects.

Object	**Endoscopist 1**		**Endoscopist 2**		**3D EUS**	
	Average Error (%)	**Maximum Error (%)**	**Average Error (%)**	**Maximum Error (%)**	**Average Error (%)**	**Maximum Error (%)**
1	15	23	8	8	1.85	2.3
2	11	11	5	11	1.3	1.5
3	3	8	7	7	3.1	3.5
4	11	19	6	10	1.65	1.8
5	4	11	10	18	3.3	3.7

Table 4.3 – The measurements performed on the mark 2 phantom using the initial 3D EUS system (Prototype). The error was the calculated error of the measured length to the actual length of the bifurcation and the node embedded within the phantom.

Reconstruction	Maximum Dimensions (mm)		Error (%)	
	Bifurcation	Node	Bifurcation	Node
CPB1	128	44	2.5	2.5
CPB2	120	40	4	11
IPB1	116	44	7	2.2
IPB2	133	22	6.4	51
IPB3	137	47	10	4.5

A number of volume measurements were performed on a reconstruction obtained from the Prototype 3D-EUS system, of the Mark 1 phantom. Two objects were chosen to be analysed, and three repeated measurement were performed on them by three independent observers. The accuracy between the 3D volume measurements and the measured volume of the two objects are shown in table 4.4. The measured volumes of Vol1 and Vol2 were 13055mm^3 and 12495mm^3 respectively. Measurements were performed on 2 chosen objects every 1 and 3mms. All observers underestimated the volume and the maximum error was 11.9% (range 5.03 to 11.90%).

Table 4.4 – Volume measurements using the Prototype 3D –EUS system on the Prototype Phantom.

Observer	Slice thickness	Vol1		Vol2		Error (%)	
		Mean Volume (mm^3)	Std	Mean Volume (mm^3)	Std	Vol1	Vol2
1	1mm	11778.73	305.23	11614.90	19.80	-9.78	-7.05
	3mm	12171.43	46.54	11808.80	41.40	-6.77	-5.49
2	1mm	11932.01	67.66	11867.18	51.04	-8.60	-5.03
	3mm	11981.62	61.11	11936.51	208.04	-8.22	-4.47
3	1mm	11500.83	333.67	11638.37	86.58	-11.90	-6.86
	3mm	12170.23	169.28	11786.83	52.86	-6.78	-5.67

A study was performed to determine the variation within each observers (intra-observer) measurement and between all observers (inter-observer). Three volume calculations were performed to obtain a single average result, within table 4.4. The volume calculations were performed using the volume tool

within the 3Dscan application. Table 4.5 shows the intra-observer variation obtained per observer during the three volume measurements. The maximum % intra-observer variation was calculated as 5.26% and ranged between 0.34% and 5.26%. The average intra-observer % variation from the mean was 1.9%.

Table 4.5 – % intra-observer variation from observers 1 to 3 between volume measurements.

Anatomical scenario	**Slice thickness**	**% Intra-Observer Variation**		
		Observer 1	**Observer 2**	**Observer 3**
Vol 1	1mm	4.89	1.05	5.26
	3mm	0.75	0.99	2.48
Vol 2	1mm	0.34	0.77	1.39
	3mm	0.70	3.39	0.85

For each group of measurements (e.g. all observers at 1mm slice thickness on Vol1), the maximum % volume deviation from the mean was calculated (Table 4.6). Over all anatomical scenarios and observers the maximum % variation was 10.47%.

Table 4.6 – Maximum % variation from the mean value, measured between observers 1 to 3 in different anatomical scenarios.

Anatomical scenario	**Slice thickness**	**% Deviation From Mean**	**Mean (mm^3)**
Vol 1	1mm	7.59	11737.19
	3mm	3.73	12107.76
Vol 2	1mm	3.00	11706.82
	3mm	3.41	11844.05

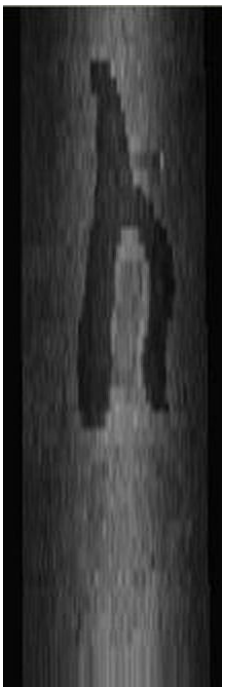

(a) Constant pullback of Mrk.2 phantom (CPB1)

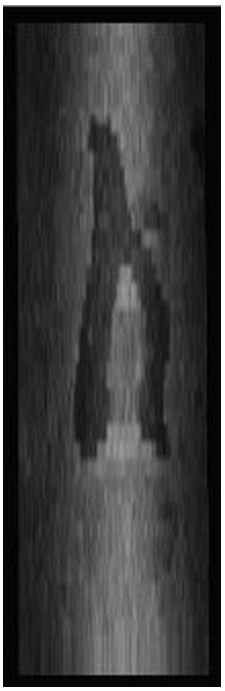

(b) Constant pullback of Mrk.2 phantom (CPB2)

(c) Irregular pullback of Mrk.2 phantom (IPB1)

(d) Irregular pullback of Mrk.2 phantom (IPB2)

(e) Irregular pullback of Mrk.2 phantom (IPB3)

Figure 4.2 – Examples of the 3 dimensional reconstruction of the mark 2 phantom using different pullback profiles.

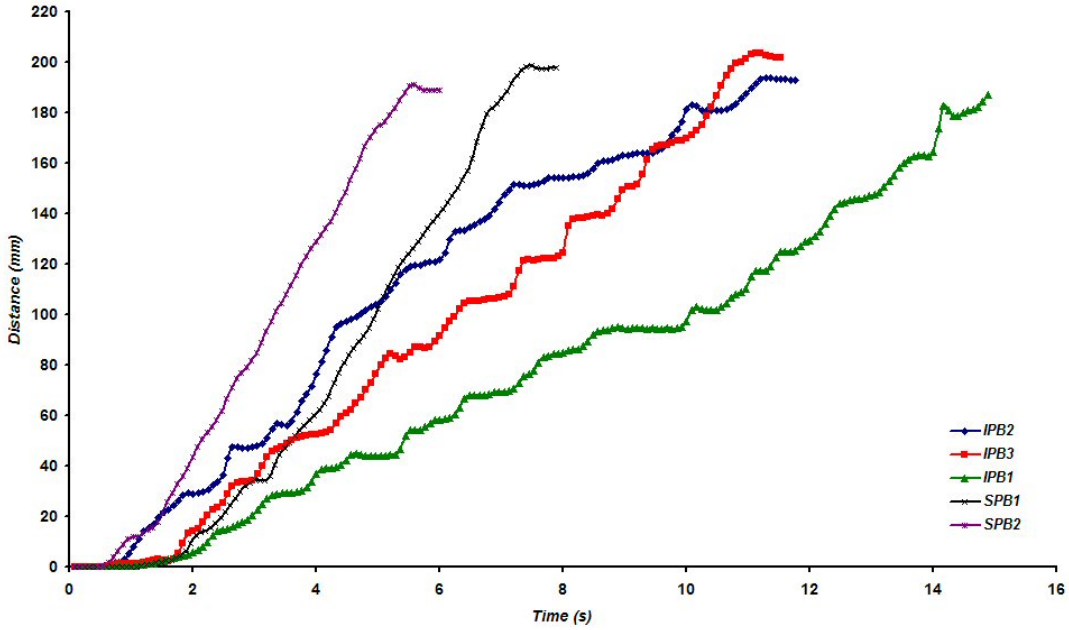

Figure 4.3 - Graph of the distance the scope has travelled plotted against time of pullback. The x-axis was the duration of the pullback in seconds and the y-axis was the distance travelled by the tip of the echoendoscope during the constant and irregular pullbacks on the phantom.

4.1.4. Discussion

The prototype 3D-EUS system was used to investigate the application of three-dimensional techniques in the field of gastro-intestinal EUS. It was also used to define the requirements for the second version of the 3D-EUS. Initial results indicated that it could be extremely useful in providing clinically relevant information. It was clear from the results that if a constant speed was maintained during the pullback, accurate dimensional measurements could be achieved. However, when pullbacks were interrupted, dimensional and volume measurement could have significant errors. The average error obtained from all volume measurements was 7.22 ± 2.1%.

The average intra and inter-observer % variation from the mean was 1.9% and 4.43% respectively. From the tests on the phantom to simulate irregular pullbacks, accuracy of the dimensional measurements varied significantly from 2.2 to 51 % for the small object and from 2.5 to 10% for the large object. The only way to rectify this would be to correct the reconstruction with positional information. This would also increase the accuracy of the volume measurements.

The 3DScan program had a number of limitations that made it impractical to continue to use for any clinical examinations. These included:

- Variable positional information could not be included into the 3DScan program.
- The S View window could not be zoomed into the extreme edges of the reconstruction, only into its centre.
- Long volumes could not be fully viewed without reducing the size significantly. Making any analysis difficult.

Precise localisation of coronal, sagittal and transverse could not be obtained therefore it was difficult to guarantee the same slice was visualised.

4.2. Design and Evaluation of the 3D-EUS V2 System

Background

The clinical comparative study by Kim et al. (2002) showed that is was possible to improve the staging of early and advanced cancers in the rectum. Using a rigid radial US probe, they showed that the accuracy increased from 84.8% to 90.9% by using 3D for staging of early tumours and from 75.8% to 84.8% for advanced tumours. It was hoped that similar accuracies could be obtained for upper GI cancer staging using flexible echoendoscopes, if a custom designed system could be designed and developed.

During the evaluation of the prototype 3D-EUS system, a number of advantages were identified over conventional EUS. These included:

1. The high frame rate of the video capture device allowed for a detailed three-dimensional reconstruction anatomy.
2. The use of the flexible echoendoscopes improved penetration and image quality, while eliminating the limited travel distance (Z) encountered by the 3D mini-probe system.
3. The duration of the capture phase of the 3D-EUS examination was short, only lasting for approximately one minute, therefore reducing the clinical examination time.
4. The offline reconstruction and analysis of the volume made it possible to detect features that were not observed during a conventional, or 2D, EUS examination.

However, the prototype 3D-EUS suffered from a number of deficiencies. The main problem with the prototype system was that there was no tracking of the position of the echoendoscope during the pullback. Therefore, accurate location, and dimensional and volume measurements could not be guaranteed. This would depend on the endoscopist maintaining a constant speed during the pullback. This was especially prevalent during clinical examinations, where stenotic regions could cause distinct changes in the speed.

A proposed second version of the 3D-EUS system was designed to rectify these problems and provide accurate and reliable dimensional and volume measurements to be made. Various positional monitoring systems were investigated during the project and the positional digitising arm was chosen as the preferred system due to its accuracy.

This chapter details the design and development of the second version of the 3D-EUS system. The design and development of the hardware, the reconstruction and analysis software and the overall system is included within the chapter. A schematic diagram illustrating the proposed 3D-EUS V2 system is illustrated in figure 4.4. The 3D-EUS V2 system will be evaluated using the custom developed EUS phantoms described in chapter 2. Comparisons of dimension and volume measurement accuracies were performed with the inclusion and exclusion of positional information during the reconstruction phase. A single clinical 3D-EUS examination is included within this chapter to highlight the effects of including positional information.

Aims

1. To design and develop an improved 3D-EUS system that will incorporate positional information and accurate measurements
2. To evaluate the reconstruction algorithms and measurement tools of the 3D-EUS system using the mark 3 EUS phantom.
3. To test the reconstruction algorithms, positional information and measurement tools of the 3D-EUS system on a clinical case.

Materials

The 3D-EUS V2 system was designed and developed using the components detailed in table 4.7.

Table 4.7 – Table of the components of the 3D-EUS V2 system.

Component	**Name**	**Manufacturer**	**Version / Model No. + Requirements**
Hardware			
Customised Tower Personal computer	Dimension	Dell	9100
Image Capture card	Morphis	Matrox	PCI
Positional Arm	Microscribe	Immersion	G2X
Software			
Image and position capture system	IC3D	In-House	Ver. 1.1 Requires: VB6, Mil-lite & Microscribe SDK
Programming development environment	Matlab	Mathworks	Versions 6 to 2008
3D EUS Reconstruction & Analysis Toolbox	3D EUS R&A	In-House	2007 Requires: Matlab

4.2.1. Design of the Three-Dimensional EUS Version 2 System

Using the components listed in Table 4.7, the 3D-EUS V2 system shown in Figure 4.4 was produced. The core of the 3D-EUS V2 system was a customised Tower PC (Dell Corporation, Dell House, Bracknell, Berkshire, UK) [High-end Dell Dimension 9100 Tower Unit: Core-2-Duo 2.6GHz, 4 Gb of memory, 512Mb NVidia 8800 graphics card, Dual boot MS Windows XP Pro 32bit & MS Windows XP Pro x64 operating system (OS)]. Placed within a PCI slot of the machine was a Matrox Morphis image capture card (Matrox Electronic Systems Ltd, Dorval, Quebec, Canada). The image capture card was equipped with four BNC composite capture channels. To acquire from an S-Video source, two channels were connected together via a special S-Video to BNC convertor cable. The two independent operating systems were required for different phases of the 3D reconstruction process. To acquire the images and positional data, the program was run on the windows XP Pro 32bit OS. This was necessary, as the companies did not provide 64bit compatible drivers. The difficulty arose with some of the large reconstructed data files. The 32bit version of Matlab (Mathworks Inc.

Massachusetts, USA) would not be able to reconstruct and display these files due to the memory requirements and inherent 2Gbyte system memory limitation within the 32bit XP OS. To overcome this problem, Windows XP x64 version was installed on the computer as a dual boot system. For large image stacks (e.g. > 300 images), the computer was rebooted from the 32bit to 64bit OS and reconstructed within the 64bit version of Matlab.

A stand alone program (IC3D) was written to simultaneously capture a series of images from the endoscopy system and positional information from a digitising arm. The program was written using the programming language Visual Basic 6 (VB6) (Microsoft Corporation, Berkshire, UK), the Matrox Mil-Lite image capture programming libraries (Matrox Electronic Systems Ltd, Dorval, Quebec, Canada) and the Microscribe software development kit (SDK) provided by Immersion (Immersion Corporation San Jose, California, USA). The main components and windows of the IC3D system are detailed in A.4.2 of Appendix 4. The S-Video output of the endoscopy stack was connected to the image capture card of the 3D-EUS capture system via a connector cable that consisted of an S-video plug to twin BNC sockets and two 3m 75Ω video BNC cables. One cable carried the luminance signal and the second cable carried the chrominance signal. These were connected to two corresponding BNC sockets of the 4 channel image capture card to be recombined to a higher quality S-video image. The Microscribe G2X positional arm was a USB bus powered device. It was connected to the USB 2 port of the computer and, once installed, the positional arm was activated. The tip of the arm was attached to a custom made wrist strap and securely placed around the wrist of the endoscopist. The endoscopist securely held the insertion tube of the endoscope and controlled the pullback during the 3D acquisition phase. As the insertion tube has a fixed length, the differential movements of the tip of the echoendoscope will relate to the movement of the wrist and positional arm.

The IC3D program included the necessary software libraries and control tools to operate, communicate with and continuously monitor the location of the tip of the positional digitising arm. Within the IC3D program it was possible to select the units of measurement (e.g. centimetres or inches and radians or degrees). As the arm could operate either via the USB2 or serial ports, the software would automatically switch between communication protocols. The Matrox Mil-Lite software libraries, contained within the IC3D program, were used to initialise, control and setup the image capture parameters of the Matrox Morphis Capture card. Two configurations of the program were compiled; one was configured to capture the entire video picture (720x576 pixels). This program was used to acquire images from the Aloka α5 ultrasound scanner. The second configuration was designed to capture a square image. This area could be sized to create a custom square region of interest that was user definable and could be positioned anywhere within the 720x576 image. The default window was set at 570x570 pixels, and positioned to acquire the ultrasound image from the EU-M30 and EU-M2000 EUS processors and important ultrasound information (e.g. ultrasound frequency, gain, image scale & dimension).

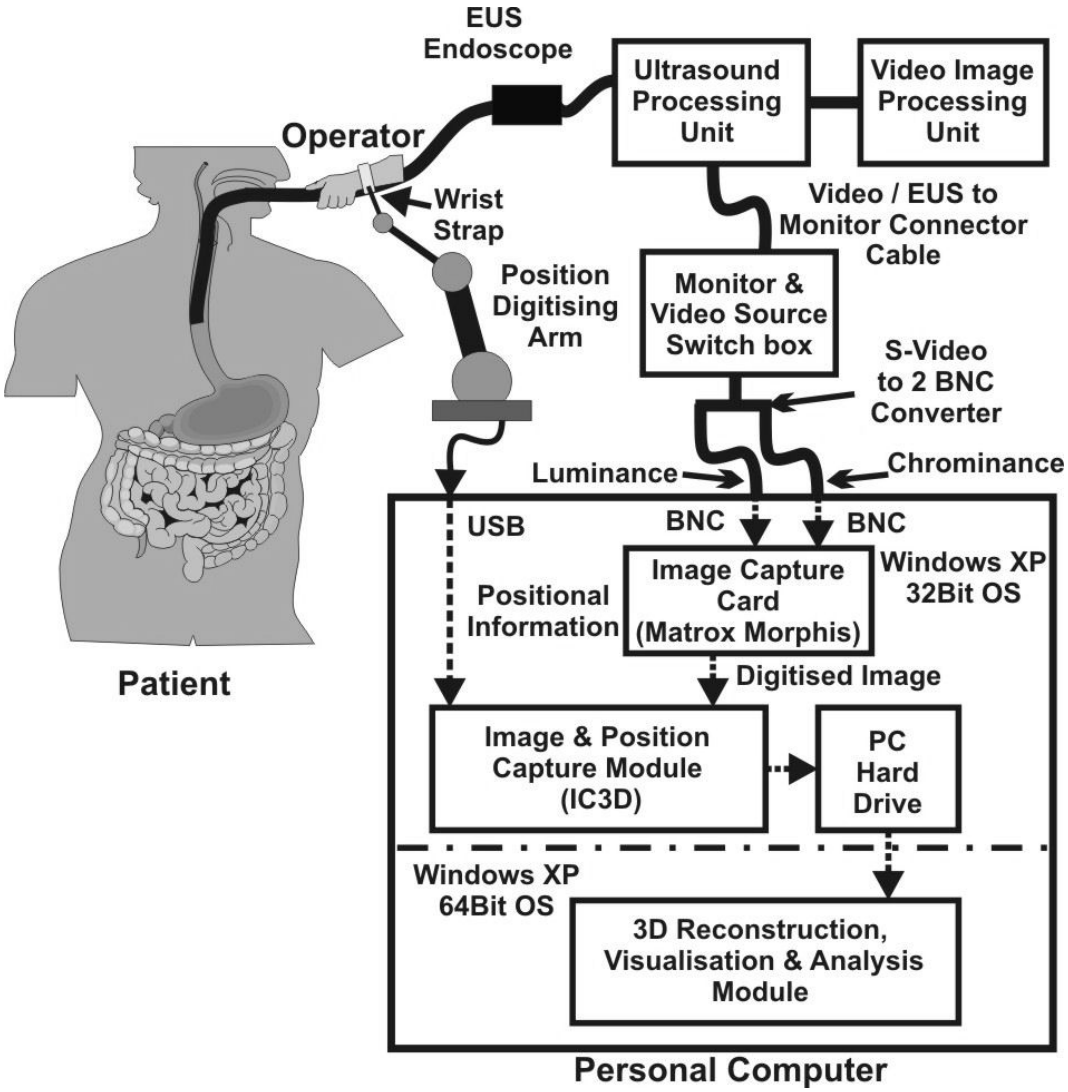

Figure 4.4 – Detailed block diagram of the 3D-EUS V2 system. Depending on the information required from the patient and the expected complexity of the anatomy, the position digitising arm may be substituted with basic positional information.

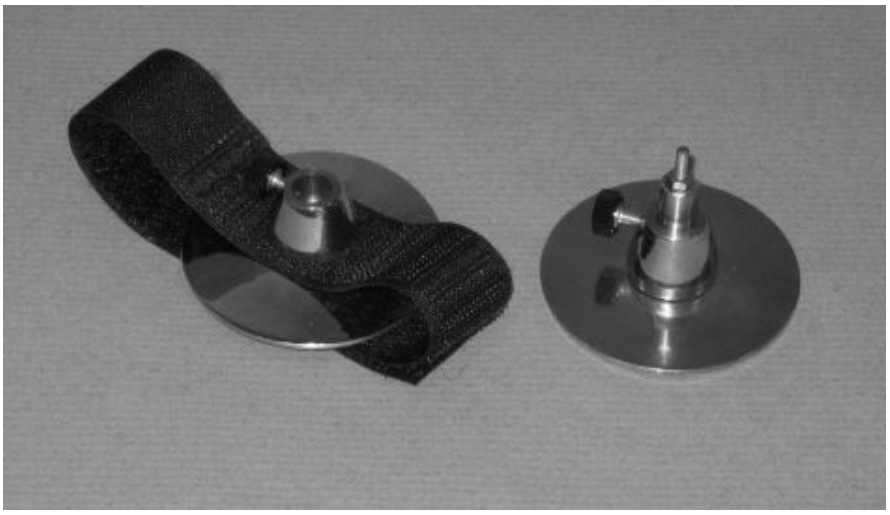

Figure 4.5 – Custom made positional strap and quick release cup to attach and secure the tip of the Microscribe positional arm to the hand or wrist that controls the depth and movement of the insertion tube of the endoscope.

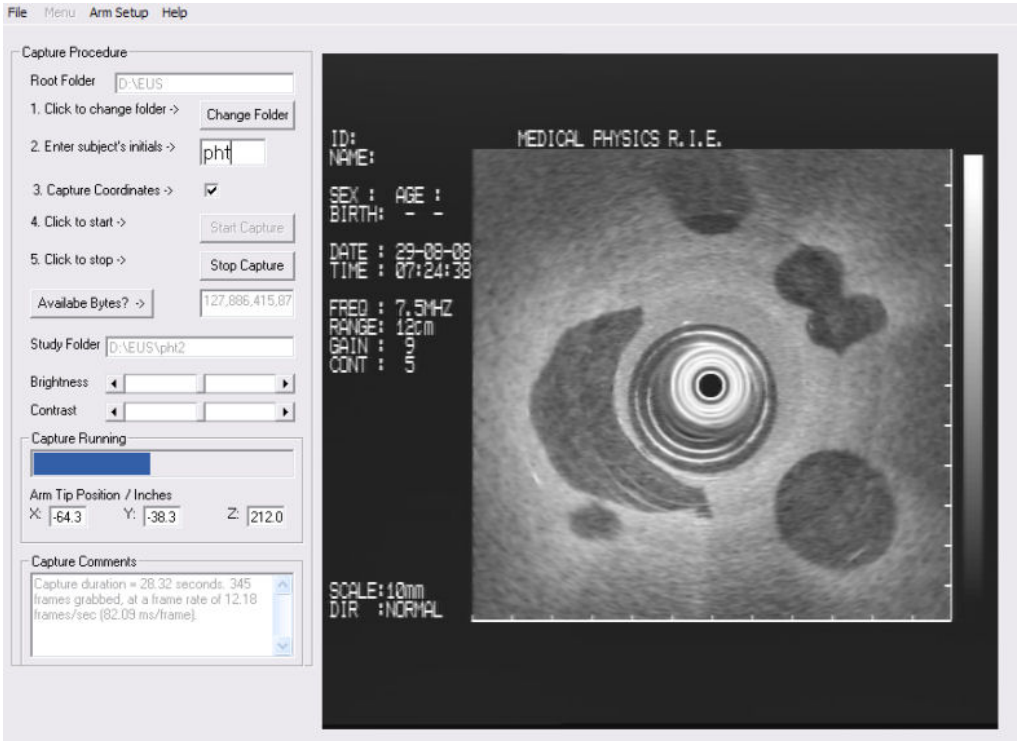

Figure 4.6 – The image and positional capture window was used to capture a series of images and XYZ positional information simultaneously. An alternate full screen capture version was produced to operate with the Aloka system. The ultrasound image was of the Mark 3 EUS phantom.

The IC3D program was used to capture the images from the EUS processor or ultrasound scanner and positional information obtained from the Microscribe positional arm. The IC3D program performed the following tasks:

- The main control of each component of the program.
- Capture of images with and without positional information.
- Control the image capture card and setup of the image parameters.
- Control, testing and setup of the communication protocols and capture units of the Microscribe positional arm.
- Defining of the image capture region of interest.

The primary window used to capture the data for the 3D-EUS system is illustrated in figure 4.6. The subject's initials were entered into the relevant text box and the acquisition initiated. A series of images were captured and, if the positional arm was connected, x, y, and z tip position data was stored within a text file. An example of the data stored within the text file is shown in table 4.8. Typically the images and positional data were captured simultaneously, every 80ms or at 12.5 frames per second (fps). An example of the image acquisition phase of the 3D-EUS study: a pullback lasting 40 seconds, captured an average of 500 images over a pullback distance of 20cm, resulted in an image captured every 0.4mm.

Table 4.8 – Example of the positional data obtained from the IC3D program

Image Name, X, Y, Z, Acquisition Time
GB10001,249.5174,-334.5247,214.837,.069
GB10002,249.5181,-334.526,214.6895,.137
GB10003,249.5843,-334.6688,214.8649,.217
GB10004,249.5174,-334.5247,214.837,.297

The following information, regarding the 3D-EUS acquisition was recorded:

- Patient / subject details and procedure information.
- Start point of the pullback determined from the scaling on the echoendoscope.
- End point of the pullback capture.
- Total number of images acquired.
- Rate of capture (fps).
- Ultrasound information – scope name, gain, frequency, image diameter, processor.

The 3D reconstruction, visualisation and analysis toolbox was designed and written in Matlab, a high level programming language and development environment. Using the GUI builder and the programming capabilities of Matlab a graphical toolbox was created to do the following:

- Enter the 3D study's demographics.
- Pre-process the images before reconstruction.
- Prepare the positional data depending on the source of the information.
- Reconstruct and save the volume data.
- 2D and 3D visualisation of the volume.
- Image processing of the displays and alteration of colour map.
- To perform distance, area and volume measurements on the volume.

Within Matlab, functions were a way of performing specific tasks and complex routines while minimising the total memory usage. The specified input and output variables of the function were the only information passed to and from the main program. All other variables within the function are destroyed when the function is terminated. Figure 4.7 shows the main routines of the 3D-EUS reconstruction and analysis program and the basic flow of the data. There were 4 primary programs and graphical user interfaces (GUI) written to allow for the entry, reconstruction and analysis of the data, marked 1 to 4 on figure 4.7.

1. Names: EUS.m, EUS_StartUp.m and EUS_StartUp.fig. The EUS.m function shown in figure A.4.7.a was the main menu for the toolbox where a number of different functions could be initialised. This included the entry of the data, the reconstruction of the volume, different visualisation methods and analysis tools. The selection of the 'Enter EUS data' button activated the 'EUS_Startup' function and initiates the GUI shown in figure A.4.7.b. The 3D EUS study demographics were entered into the text boxes and via the drop down menus and were saved. This initiated a separate window that displayed the first image of the captured series of EUS images. A user defined selection box ('rubber band box') was initiated and dragged over the region of interest, on the image, to remove any sensitive information and provide coordinates to the program. After selecting the area, a 3D-EUS parameter file was automatically saved with all the demographics and coordinates for use by the next stage of the process.

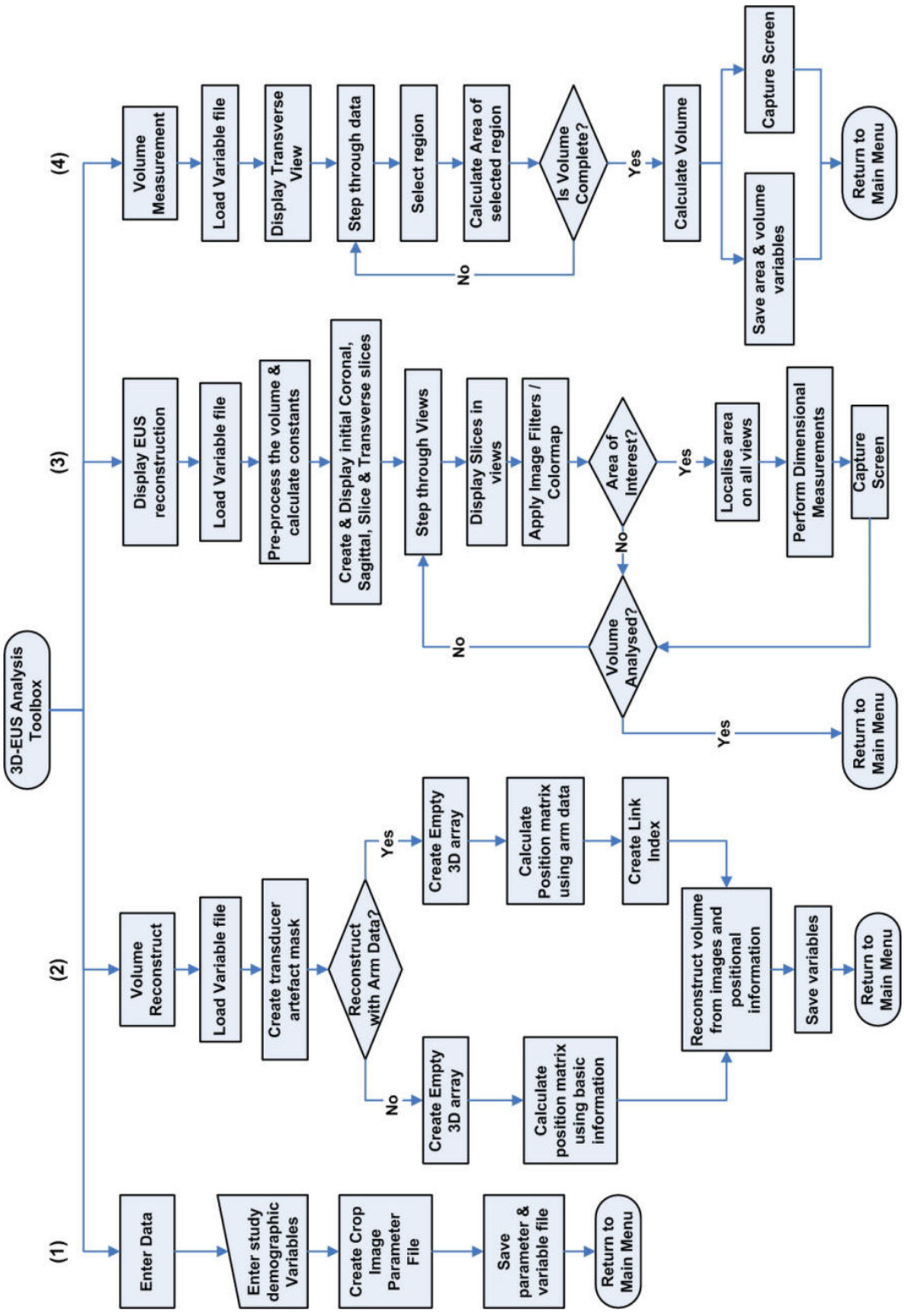

Figure 4.7 – Block diagram of the major components and data flow of the Matlab 3D-EUS Reconstruction and Analysis toolbox.

2. Name: EUS_reconstruct.m. The 'EUS_reconstruct' function performs a number of routines to process the images and reconstruct them into the volume. The first part of the function was to have the option to mask the transducer artefact. A series of images were acquired from each echoendoscope / processor combination at different frequencies, image diameter, quadrants, all placed within a water bath. Using the information obtained from the EUS parameter file, a specific transducer image was selected and cropped to create a 'mask' image. If the transducer removal was not selected, a blank 'mask' was generated. These would be used later in the function. The next step was to process the positional data. A choice was given to either use the basic positional data (e.g. the start & stop point and time of the capture, assuming that the pull back was constant), or the X, Y and Z information obtained from the positional digitising arm. For each image acquisition the X, Y & Z distances moved between each image acquisition were calculated and stored. For the basic positional data the distance between each image was calculated using equation 4.1. When positional information was acquired from the arm, equation 4.2 was used to calculate the distance travelled, from an arbitrary start point, by the tip of the arm for each image acquisition. It was assumed that the 3D analogue of a right-angled triangle was an irregular tetrahedron with cubic vertex. Where '*cubic vertex*' meant that the three faces adjacent to the vertex were right-angled triangles and that all three right angles touch the vertex and were derived from Pythagoras' Theorem in Three Dimensions.

$$dist_{basic} = \frac{pbd}{nF} \qquad \text{Eq. 4.1}$$

Where $dist_{basic}$ = Distance between each image.

pbd = Pull back distance.

nF = Total number of frames captured during the pullback.

$$dist_{arm} = \sqrt{\left(x\_tot^2 + y\_tot^2 + z\_tot^2\right)} \qquad \text{Eq. 4.2}$$

Where

$dist_{arm}$ = Distance between each image calculated from the arm.

x_tot= Distance moved at each image acquisition in x direction from the origin.

y_tot= Distance moved at each image acquisition in y direction from the origin.

z_tot= Distance moved at each image acquisition in z direction from the origin.

The first part of the positional and reconstruction function was to load in the raw positional data and refer the array to the start point of the pullback (origin). This was done by extracting from the text file the positional data. Each position axial data was loaded into separate arrays. The first data point of each array was designated as the origin and this point was subtracted from each of the points of the three arrays. A 'for' loop was created to calculate the distance of the hypotenuse for each tetrahedron, defined from the origin to the position of the tip of the Microscribe arm where the image was captured, using equation 4.2. This was repeated until the last point of the array was reached. This calculated the path of the tip in 3 dimensions. Figure 4.8 details the Function 2 part 1 as a block diagram depicting the calculation of the tip movement during the pullback. The routines main components are shown in code example A.3.6 of appendix 3.

Figure 4.8 - Function 2 part 1

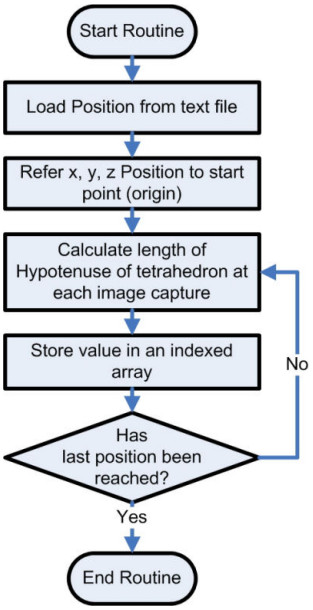

The next part of the positional and reconstruction function was to create an empty three-dimensional array that would house the final reconstruction and contain an arbitrary 500 slices. To obtain the dimensions of the 3D array, a single image was loaded and cropped to the previously defined size. The 3D array would have the dimensions defined by the x – y coordinates of the crop function and the 500 slices in the z direction. The actual pullback distance was determined from the subtraction of the maximum and minimum points on the tip path. A new sampling rate was calculated that would be the distance travelled at each slice of the volume. Within a loop, the difference between each acquisition and the preceding point was calculated for the entire array. From this variable, the data was divided by the sampling rate to obtain the actual number of slices that each image would populate within the volume. Figure 4.9 details the Function 2 part 2 as a block diagram depicting the creation of the volume array and calculates the distance changes per acquisition. The routines main components are shown in code example A.3.7 of appendix 3.

Figure 4.9 - Function 2 part 2

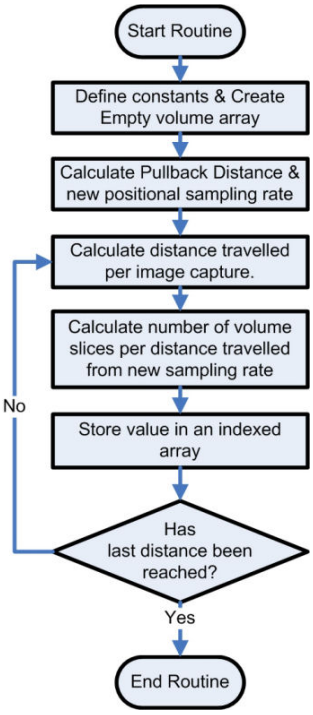

The third part of the positional and reconstruction function was to create an index file that would populate the voxels of the 3D volume array with specific pixel values. A nested series of loops and if statements were used to generate an index array that would selectively choose specific images, only when the tip was moved by a sufficient distance. A logical table was created that corresponded to all values obtained from the calculated number of volume slices per image.

An arbitrary sampling rate was calculated from the length of the entire pullback and the number of images (typically 500). At each sampling interval, the distance moved by the tip of the position sensor was calculated. If this distance was greater than or equal to the sample rate, it was assigned a logic value of 1 and if less than the sampling rate it was given a logic value of 0. Using this logical table, a conditional statement was created that would check to see if the volume slice would correspond to an acquired image. If it did not, the next entry in the logical table would be interrogated until it returned a true value. Each iteration of the main loop corresponded to an acquired image.

Figure 4.10 - Function 2 part 3.

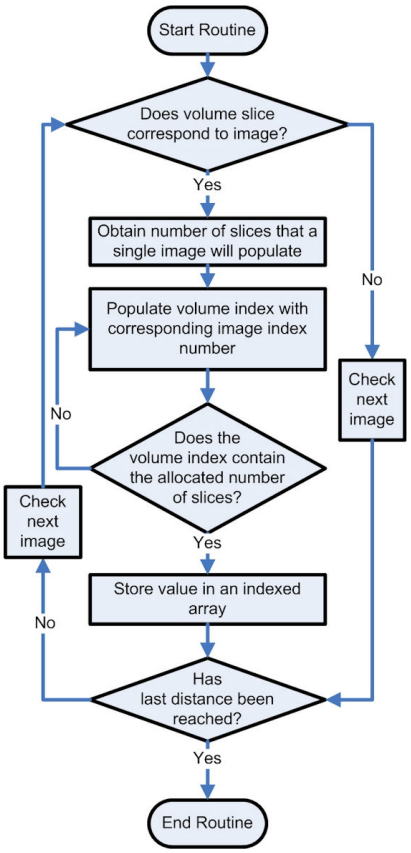

When a true value was obtained, the corresponding image ID was determined and stored within the volume index file at the first point of the volume index array. If the tip had moved a greater distance than one sample, then a second loop would be initiated to populate the volume index file with the same image ID until an appropriate number of slices had been allocated. The next value in the logical table was analysed and the volume index file populated until all images ID's, that corresponded to a true logical value, had been included within volume index array. When this was complete, the main loop was terminated and the next part of the volume index array was used within part 4 of the function. Figure 4.10 details the Function 2 part 3 as a block diagram depicting the creation of a volume index array. The routines main components are shown in code example A.3.8 of appendix 3.

The final part of the positional and reconstruction function was to reconstruct the voxels of the volume with appropriate pixel values selected by the volume index array. Prior to the population of the 3d volume array, two image processing steps were performed. The first step was to sequentially load each image file that corresponded to the values within the volume index array. Then each image was cropped using the coordinate data obtained during the creation of the 3D-EUS parameter file. Next, either the blank mask or transducer artefact mask, created to minimise the transducer artefact, was applied to each cropped image by image subtraction routines. All three above steps were placed within a loop and the empty array was populated to create the reconstructed volume. As each specified image was loaded, it was converted to a series of Cartesian coordinates with a set amplitude value. From the index file, the pixel values were assigned to corresponding voxel values within the volume and the slice was populated. The loop was repeated until all of the empty slices of the volume had been substituted with image data. The volume and a number of constants were saved in a Matlab variable file (.mat). Figure 4.11 details the Function 2 part 4 as a block diagram depicting the creation of 3D scaled volume. The routines main components are shown in code example A.3.9 of appendix 3.

Figure 4.11 - Function 2 part 4

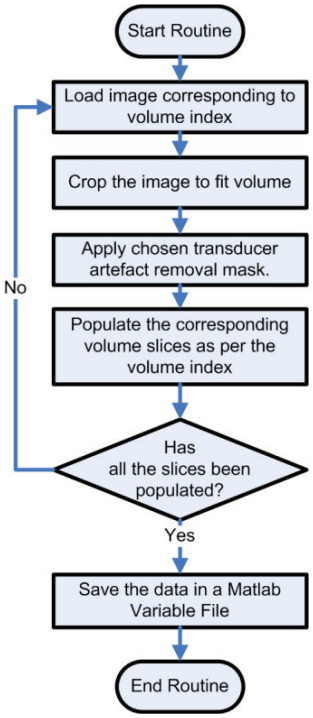

3. Name: EUS_Display.m and EUS_Display.fig. The Matlab GUI builder was used to construct the EUS_Display.fig GUI and the basic control functions within the EUS_Display.m program. An example of the EUS_Display GUI is illustrated in figure A.4.7.c. This interactive GUI contained four different views: the angle, coronal, sagittal and transverse planes of the volume. This program was the primary visualisation and analysis tool of the 3D-EUS toolbox. To perform the analysis, the transverse view was used to scan through the volume. If a structure of interest was observed within this transverse plane, the slider bars were altered to locate the structure within all other views. Dimensional measurements were performed on all relevant plots and a snap shot of the window was captured to record the sizes. This process was repeated for all other structures of interest until the entire volume was analysed. A more detailed description of this function is available in Appendix 4 section A.4.3.

4. Name: EUS_Display_Volume.fig EUS_Display_Volume.m. Volume and area measurements were performed using the EUS_Display_Volume window shown in figure A.4.7.d. This interactive GUI

contained a single plot window that displayed the transverse planes of the volume. A control slider bar was used to step through the volume. When a region of interest was located, the select area button was pressed and the 'getline.m' function was activated. This allowed a closed polyline to be drawn, using the mouse, around the region of interest. When the polyline was complete, an array containing the x and y vertices of the polygon were generated. Using the 'polyarea.m' function, the area defined by the polygon and the corresponding segment volume were calculated and stored within a separate array. This process was repeated though the entire volume of interest. A summation of all the volume segments was performed to obtain the total volume. The calculated area displayed was scaled to mm^2 and the volume in mm^3. At the end of the analysis, the calculated parameters were stored within a Matlab variable file (e.g. total area and volume, individual areas and segment volumes, the vertices of the selected polygon).

4.2.2. Testing of the 3D-EUS V2 system

To test the 3D-EUS V2 system, various phantoms were constructed with embedded objects of known dimensions and volumes. The 3D-EUS V2 system was also evaluated in a number of clinical examinations and in one case where the positional arm was used to acquire positional data to see the effects on the dimensions and position of the pathology including and excluding the positional information. Custom EUS phantoms were constructed as per the protocols designed within Chapter 2. The dimensions of the objects embedded within the mark 2 and 3 phantoms were measured, prior to the phantom casting, using a calibrated vernier calliper and the Microscribe positional digitising arm. The objects were then embedded within the phantom and allowed to set.

To perform phantom measurements, the echoendoscope was inserted into the central core of the EUS phantom. The EUS equipment parameters were recorded, including the gain, image display diameter, measurement frequency and contrast. The start position, as defined by the measurement scale on the insertion tube of the echoendoscope, was recorder. The wrist strap was attached by a Velcro strap to either the wrist or the back of the hand of the operator, used to control the movement of the echoendoscope's insertion tube (figure 4.6). A custom tip was manufactured to securely fit within the attached socket on the strap. The needle tip of the Microscribe was removed and replaced with the custom tip, and fitted within the socket. The tip of the echoendoscope was positioned to the bottom of the phantom, and a firm grip was applied to the insertion tube. The IC3D capture program was initiated and communication with the Microscribe positional arm was tested. The system was connected as per figure 4.4 and the measurement parameters were entered into the capture window. Once the echoendoscope was in position the start capture button was pressed to initiate capture of both images and position.

A number of captures were performed that would simulate both constant and irregular pullbacks. To simulate the meeting of resistance or stenotic areas, resistance was applied to the insertion tube of the echoendoscope at various points and at varying degrees of pressure during the pullback. This was accomplished by a second person enclosing and releasing their thumb and fore finger over the insertion tube.

To determine the accuracy of the reconstruction and Z measurements with changing pullback speed, the use of basic, one axial direction, and 3-dimensional positional information was investigated by performing a number of pullbacks on the Mark 3 phantom at different pullback speeds. Care was taken to try and pullback the insertion tube of the echoendoscope in one axial direction (Z). Positional information was captured using the Microscribe positional arm. Each pullback was reconstructed three times, and dimensional measurements were performed on 2 chosen objects (one in the middle and one at the top of the phantom).

The volumes were reconstructed and analysed to test the efficiency and accuracy of the position and reconstruction algorithms by performing dimensional and volume measurements, and then comparing them with the actual sizes.

To test the accuracy of the volume measurements a number of comparative volume measurements were performed on objects within the phantom with known volumes. The effects of speed of pullback and the chosen incremental step thickness of the volume analysis were investigated. The volume of the chosen object was measured by filling each mould half by a 2.5ml syringe until each was completely filled. To obtain an accurate reading each mould half was placed on the Sartorius 1202 MP 300g weighing balance (Sartorius AG Goettingen, Germany) and filled with water and measured to 2 decimal places.

To assess the effects of positional data acquisition on clinical data, an acquisition was performed as part of a clinical staging of oesophageal cancer. After a conventional EUS examination, the echoendoscope was positioned below any abnormal pathology. At the start of the controlled withdrawal of the echoendoscope, the capture program was initiated and images & positional data were captured at 12.5 frames per second (fps). The endoscopist signalled for the start of the capture and pullback and provided the length of the inserted tube of the echoendoscope, from the incisor teeth. At the end of the pullback, the endoscopist signalled for the termination of the acquisition and provided both the start and end point for the 3D scan records.

The three-dimensional volume of the anatomy and pathology of the oesophagus and disease was reconstructed and analysed using the 3D-EUS reconstruction and analysis toolbox. The volume was reconstructed twice:

1. With positional data acquired by the Microscribe arm.
2. With basic positional data. The start and stop positions and assumption of a constant speed pullback.

Scaled dimensional measurements were performed on areas of interest, utilising all three planes (coronal, sagittal and transverse views) to determine the differences between the volumes.

To test the 3D-EUS V2 system, a number of comparative dimensional measurements were performed on the phantom using the 2D EUS and 3D EUS methods. The 2D dimensional measurements were obtained by using the scaling on the endoscope to determine the Z dimension and the measurement tools of the EU-M30 processor to determine the X & Y measurements. Two independent observers performed three repeated measurements of the Z dimensions of five chosen objects. The 3D EUS measurements were performed using the visualisation and measurement tools of the 3D EUS package written in MATLAB.

4.2.3. Results

4.2.3.1. Phantom results

Table 4.9 shows the results of the dimensional measurement tests of the conventional EUS Z dimensional measurements and the 3D-EUS system Z dimensional measurements. Analysis of the measurements made by observer 1 resulted in an average error of 4.21%, over all of the measurements, using conventional EUS of 4.21%. A maximum error of 7.41% was obtained with conventional EUS when observer 1 measured the Z dimension on object 5.

The analysis of the measurements made by observer 2 resulted in an average error of 5.99%, over all conventional EUS measurements. The maximum error of 9.82% was obtained during the Z dimensional measurement of object 4 by conventional EUS. Identical, repeated, measurements were performed on the 3D reconstruction of the phantom to determine the Z dimension of each of the objects. The phantom was reconstructed using arm position information. The average error obtained with the 3D-EUS V2 system was 1.5% with a maximum error of 3.1%.

Tables 4.10 and 4.11 were obtained during the testing of the effects of pullback speed, the various methods used to correct the position during the reconstruction process. The two objects chosen for the test were the ‘tumour’, as it was located in the middle of the phantom, and the diameter of the aortic arch, as it was at the top of the phantom. The actual diameter of the tube used to simulate the aorta was 31mm and the length of the tumour was 56.3 mm. As can be seen from the tables, using basic positional information, the maximum errors obtained were 25.13% and 28.68% when measuring the aorta and tumour respectively, and was obtained on the ‘fph3’ pullback. The reconstruction of the basic position is shown in figure 4.12a.

Table 4.9 – Comparative Z dimensional measurements performed on the Mark 3 using conventional EUS and the 3D-EUS V2 system. The image included within the table shows the location of the chosen objects.

Object	Actual Length (mm)	2D EUS (observer 1) (mm) [mean ± std]	2D EUS (observer 2) (mm) [mean ± std]	3D EUS (mm) [mean ± std]
1	240	245 ± 5.0	253.33 ± 2.89	242 ± 0.58
2	92.6	88.33 ± 7.64	86.67 ± 2.89	90.6 ± 0.36
3	56.3	58.33 ± 2.89	53.33 ± 2.89	56.33 ± 0.76
4	25.8	26.67 ± 7.64	28.33 ± 2.89	25.0 ± 1
5	73.8	68.33 ± 2.89	71.67 ± 2.89	72.8 ± 1.25

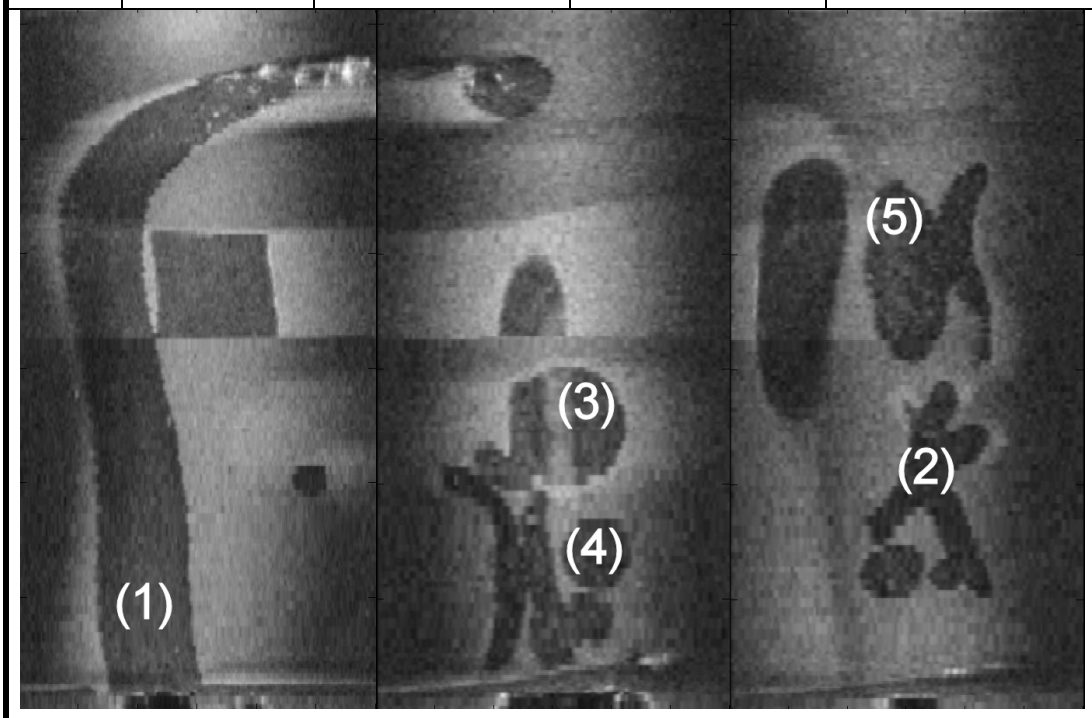

Location of the chosen objects for dimensional measurements. (With all objects all dimensions were measured, however only Z measurements were reported).

Table 4.10 - Measurements of diameter of the aorta simulation at the arch obtained on the sagittal slice at 60mm. NR – no reconstruction could be obtained. The diameter of the 'aorta' was 31mm.

File name	No. of images	Speed (cms^{-1})	Basic Position (mm)	Error (%)	Position Z only (mm)	Error (%)	Position X-Y-Z (mm)	Error (%)
fph2	238	1.54	26.3	15.16	29.39	5.19	30.38	2.00
fph3	386	0.96	24.02	25.13	27.45	11.45	30.27	2.35
fph4	424	0.85	30.16	2.71	30.15	2.74	30.79	0.68
fph5	174	2.08	27.84	10.19	28.42	8.32	30.76	0.77
fph6	121	2.68	NR	NR	24.16	22.06	26.49	14.55

Reconstructing the fph3 data set into a volume using only z positional information, improved the errors obtained for the z dimensional measurements of the aorta and tumour, to 11.45% and 5.27% respectively. The reconstruction of this single axis position corrected volume is shown in figure 4.12b. When the volume was reconstructed by using the 3-dimensional positional data (X, Y and Z) obtained from the positional arm and equation 4.3, the maximum errors reduced to 2.35% and 0.53% for the aorta and tumour respectively. The reconstruction of this three axis position corrected volume is shown in figure 4.12c. Each reconstruction was focused on the aorta.

The results of the tumour shown in the figures differ from those of table 4.11, as they were acquired on a different slice. Figure 4.13a plots the path of the tip of the positional arm as it was withdrawn from the phantom.

The average error obtained using basic positional information was 13.3% for the aorta and 15.86% for the tumour. Applying single axis positional information (Z), the average measurement error of the aorta decreased to 9.95%. This error would be reduced further to 6.93%, if it was not due to the large errors obtained during the fastest pullback ('fph6'). Between 0.85cm/s to 2.08cm/s, the maximum error obtained was 11.45%. The average error obtained during the measurement of the tumour object was 3.15% and ranged between 1.08 and 5.28%. The maximum error for the tumour was obtained at a speed of 0.96cm/s ('fph3') and resulted in a value of 5.28%.

When 3-dimensional positional information, was used within the reconstruction of the volume, the average measurement error of the aorta decreased to 4.07%. This error would reduce further to 1.45%, if it was not due to the large errors obtained during the fastest pullback ('fph6'). The average error obtained during the measurement of the tumour object was 1.21% and ranged between 0.11% and

4.05%. The maximum error was obtained at a speed of 2.68cm/s ('fph6') and resulted in a value of 4.05%.

Table 4.11 - Measurement of length of the tumour simulation on the sagittal slice was altered to obtain the maximum Z dimension. NR – no reconstruction could be obtained. The maximum dimensions of the tumour in the Z direction was 56.3mm.

File name	No. of images	Speed (cms^{-1})	Basic Position (mm)	Error (%)	Position Z only (mm)	Error (%)	Position X-Y-Z (mm)	Error (%)
fph2	238	1.54	65.39	-16.15	55.69	1.08	56.24	0.11
fph3	386	0.96	72.45	-28.69	53.33	5.28	56	0.53
fph4	424	0.85	47.22	16.13	54.68	2.88	56.47	-0.30
fph5	174	2.08	54.91	2.47	54.53	3.14	55.71	1.05
fph6	121	2.68	NR	NR	54.4	3.37	54.02	4.05

The measured volume of the tumour object was 48.93ml or 48930mm^3. Table 4.12 show the results of the calculated volumes obtained from the 3D-EUS V2 volume analysis tool. When the basic positional information was used for the reconstruction of the volume, significant errors were obtained in the resultant volume.

Table 4.12 – Volume measurements of the phantom tumour at different speeds and volume step sizes.

File name	Speed	Basic Position at different step size (mm^3)			Full 3D Position at different step size (mm^3)		
	(cm/s)	2	5	10	2	5	10
fph2	1.542	60837	62128	60646	48811	48557	48011
Error (%)		24.33	26.97	23.94	-0.24	-0.76	-1.88
fph4	0.853	40119	39590	39669	48242.9	49687.6	50019.2
Error (%)		-18.01	-19.09	-18.93	-1.40	1.55	2.23
fph5	2.083	51941	48885	50184	48792.1	49958.1	49234.9
Error (%)		6.15	-0.09	2.56	-0.28	2.10	0.62

The maximum overestimate and underestimate errors were 26.97% and 19.09%, and were obtained when sampling at every 5 slices. The average volume error obtained with a pullback speed of 1.542cm/s was 25.08%. The volume was overestimated due to the uneven movement of the positional arm during the withdrawal. When the speed was decreased to 0.853cm/s, the volume was

underestimated, with an average error 18.67%. At the fastest pullback speed, the average error was 2.94%. The maximum % variation of the volume at 0.853cm/s was 1.32%. When the speed was increased to 1.542cm/s, the maximum % variation increased to 2.42%. As the pullback speed was again increased to 2.08cm/s, the maximum % variation increased to 6.07%.

When the positional information was applied to the reconstruction, the average volume error obtained with a pullback speed of 0.853cm/s was 1.73% and the maximum % variation was 3.6%. When the speed was increased to 1.542cm/s, the volume was underestimated, with an average error 0.96% and the maximum % variation was 1.65%. At the fastest pullback speed, the average error was 1% and obtained a maximum % variation was 2.36%. The separated x, y and z coordinates of the tip of the positional arm against the duration of the pullback for the different speeds are shown in figure 4.13b.

The measured volume of the node object was 5.1ml or 5100mm^3. Table 4.13 shows the comparative results obtained with basic positional information and full positional information. With the smaller object and basic positional information, the errors varied from -38.16% to 23.3% and the maximum average error of 29.48%, was obtained with the fastest pullback speed.

Table 4.13 – Volume measurements of the phantom node at different speeds and volume step sizes.

File name	Speed	Basic Position at different step size (mm^3)			Full 3D Position at different step size (mm^3)		
	(cm/s)	2	5	10	2	5	10
fph2	1.542	5034.8	4743.96	5655.56	4891.96	4841.18	4839.70
Error (%)		-1.28	-6.98	10.89	-4.08	-5.07	-5.10
fph4	0.853	6250.89	6288.15	5727.77	4794.00	4968.30	4902.62
Error (%)		22.57	23.30	12.31	-6.00	-2.58	-3.87
fph5	2.083	3153.65	4181	3455.15	5011.51	4910.94	5308.81
Error (%)		-38.16	-18.02	-32.25	-1.74	-3.71	4.09

Applying full positional data increased the accuracy and reproducibility of the volume measurements, where the maximum error was 6% (underestimate). The average error values for a speed of 0.853cm/s was 4.15%, and the deviation from the maximum and minimum errors was 3.42%. Increasing the pullback speed to 1.542cm/s, the average error was 4.75% and the deviation from the maximum and minimum errors was 1.02%. As the pullback speed was increased to 2.083cm/s, the absolute average error was 3.18%, however the deviation from the maximum to minimum errors was 7.8%.

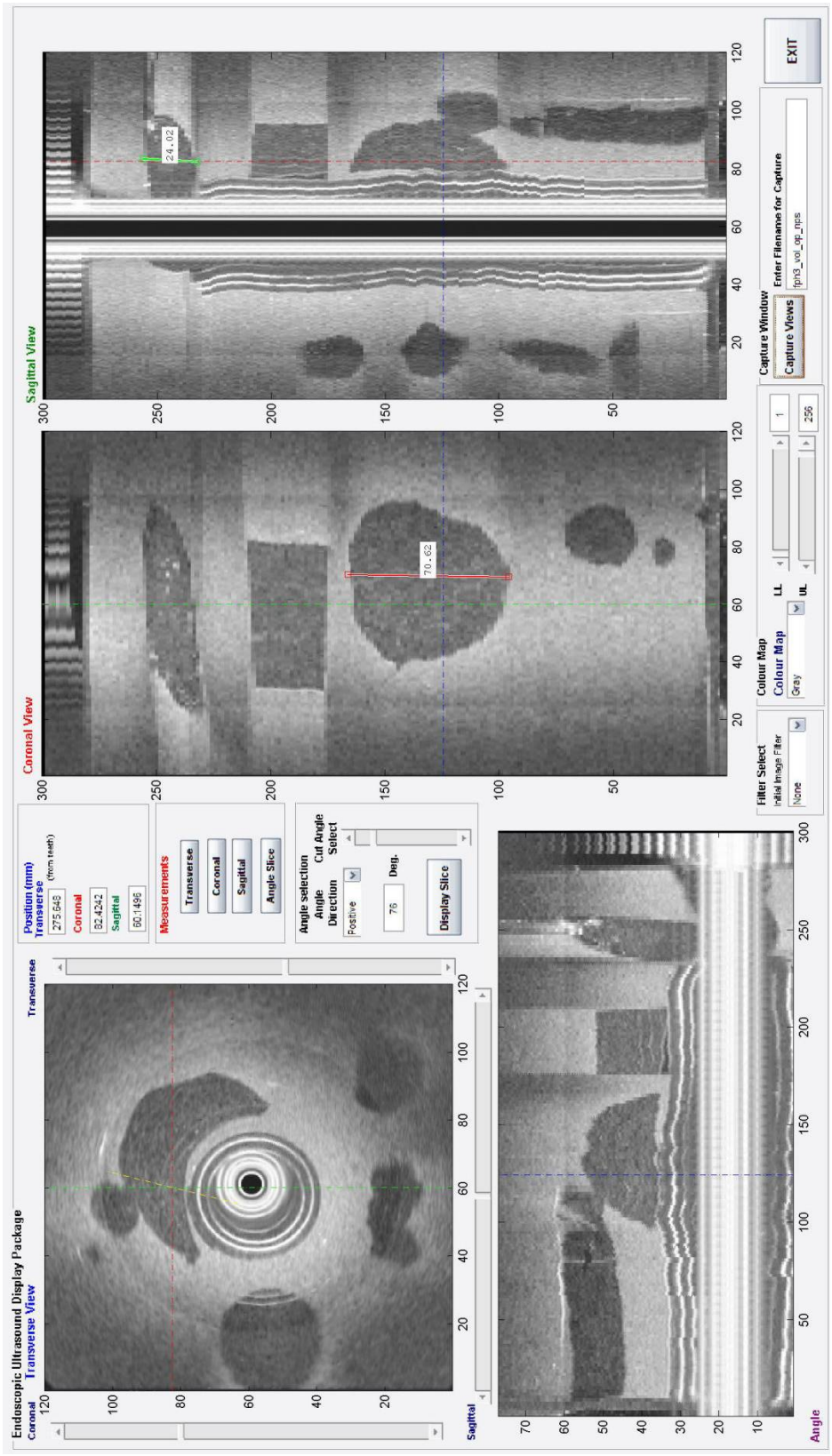

Figure 4.12a – Basic positional information included within the reconstruction of the pullback of the fph3 phantom examination.

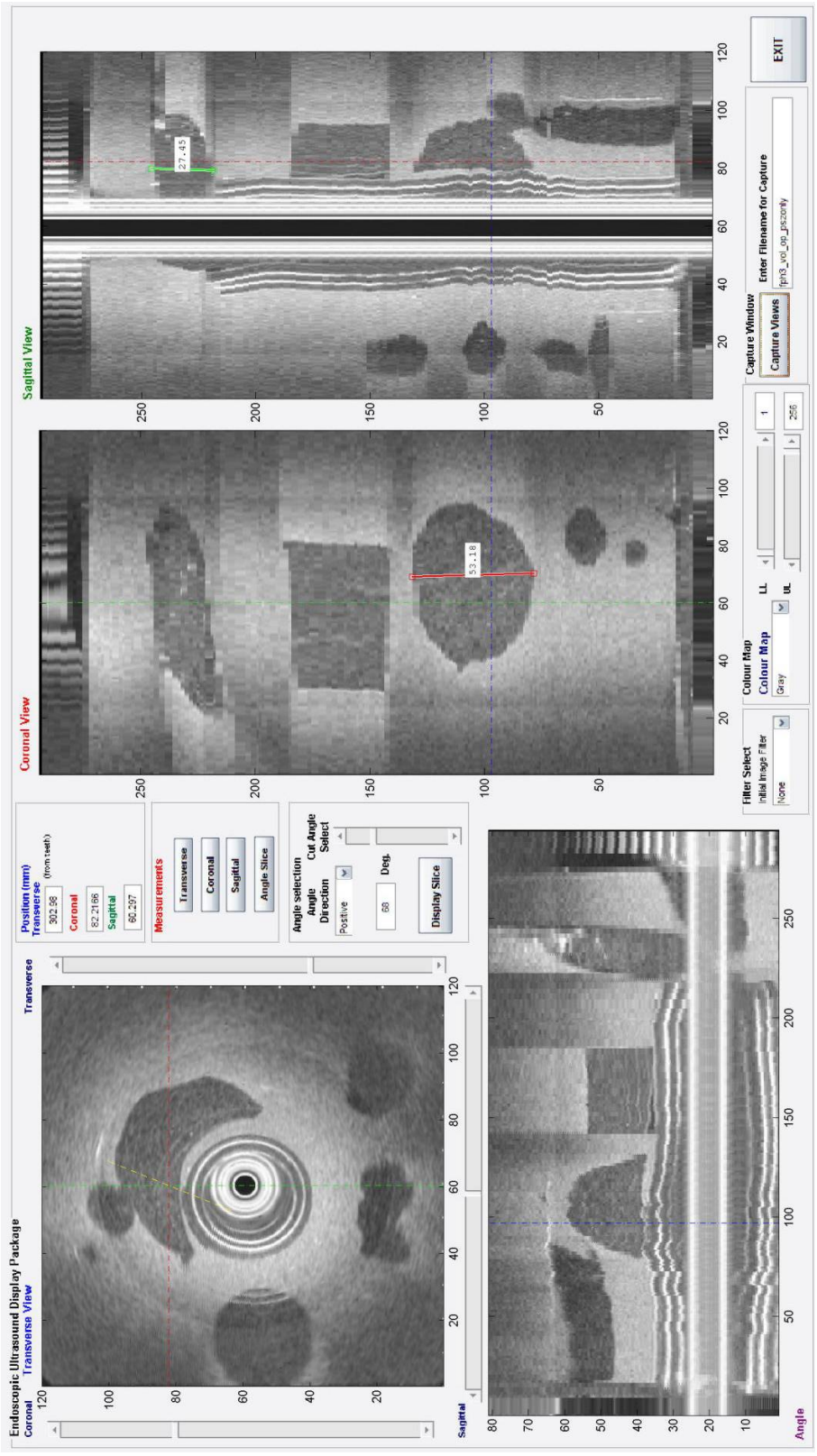

Figure 4.12b – Z positional information used to correct the reconstruction of the pullback of the fph3 phantom examination.

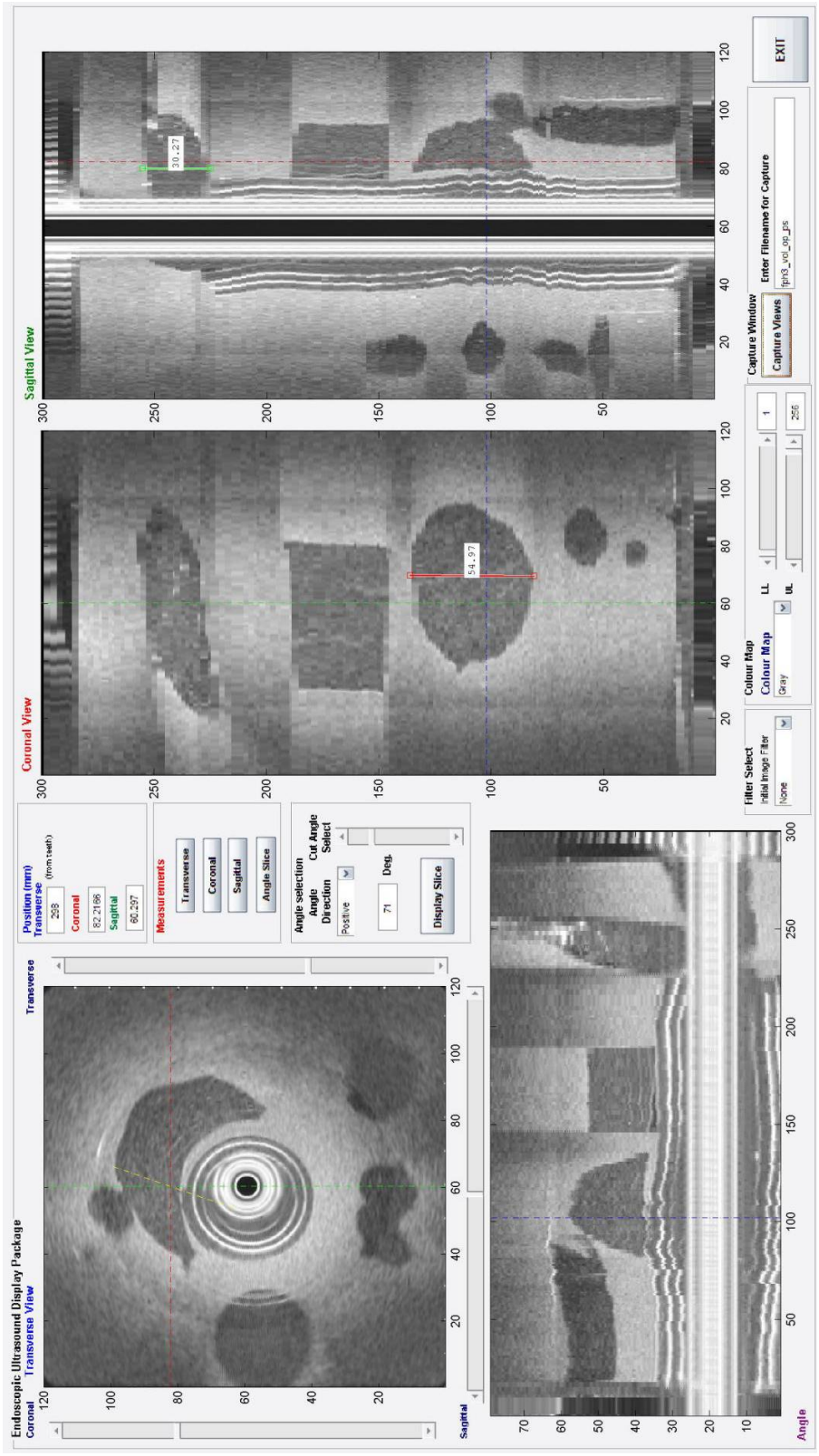

Figure 4.12c – X, Y, & Z positional information used to correct the reconstruction of the pullback of the fph3 phantom examination.

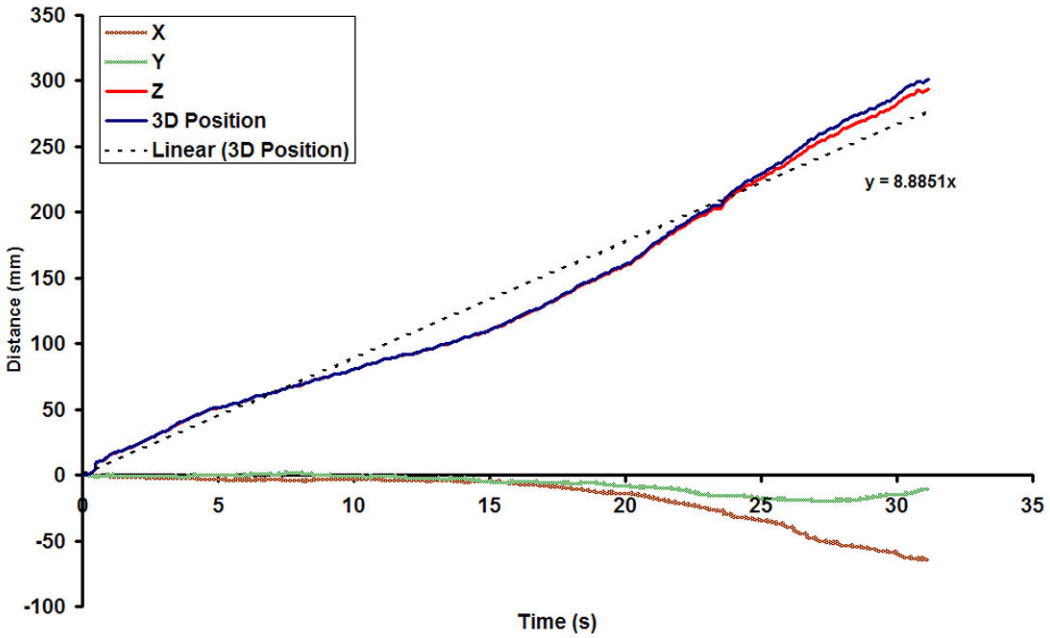

Figure 4.13a – The X, Y and Z position obtained from the Microscribe digitising arm during the pullback on the mark 3 phantom from file 'fph3' and the calculated path of the tip in 3 Dimensions ($\sqrt{(X^2+Y^2+Z^2)}$). Actual pullback distance was 30.1cm.

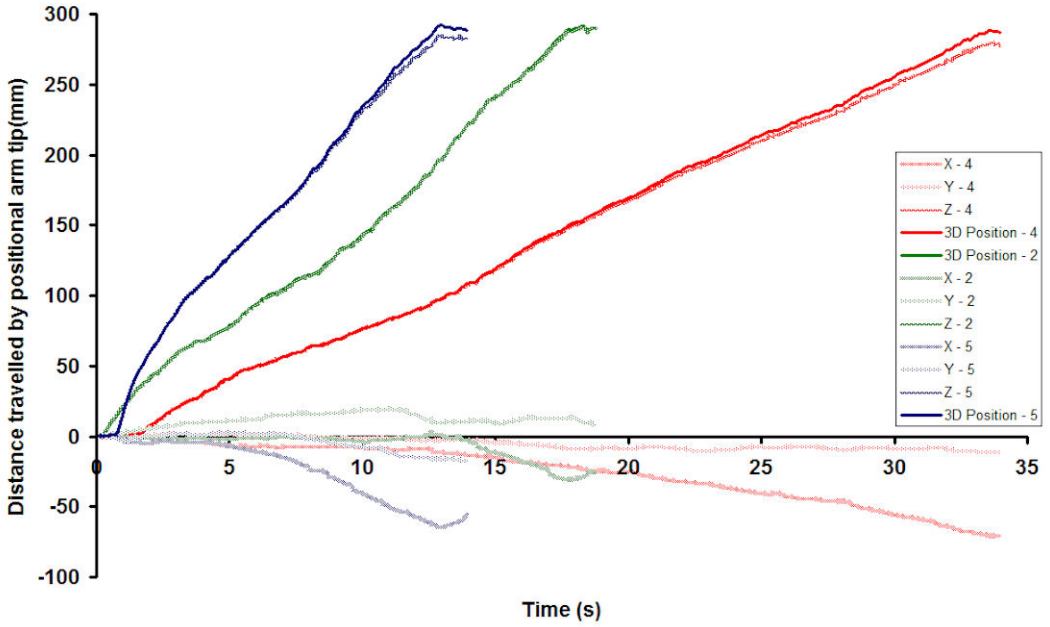

Figure 4.13b – The X, Y and Z position obtained from the Microscribe digitising arm during the pullbacks on the phantom obtained from 'fph2, fph4 and fph5' and the calculated path of the tip in 3 Dimensions ($\sqrt{(X^2+Y^2+Z^2)}$). Where x- axis is the time (s) and y-axis is distance travelled (mm).

4.2.3.2. Clinical 3D positional reconstruction example

During the conventional EUS, the tumour was located between 34 to 38cm with a maximum thickness of 2cm and length of 4cm. The oesophago-gastric junction was at 38cm. The report detailed that there were nodes present. The final diagnosis was T3 N1. Other pathology noted was a calcified aorta.

The 3D reconstruction of the clinical examination was reconstructed with the positional arm (GB1_vol_ps.mat) and with basic positional information (GB1_vol_nps.mat). The pull back was started at 49cm and lasted for 20cm, as determined by the endoscopist. The results obtained from the 3D volume reconstructed with basic position were:

- The tumour was located from 36 to 39.73cm.
- The tumour length was 37.26mm.
- Junction was located at 40cm.
- Maximum thickness was 20mm.

The volume reconstruction is shown in Figure 4.14. The figure shows the transverse, coronal, sagittal and angle planes. The volume reconstruction started at 49cm from the incisor teeth. Dimensional measurements were performed on each of the planes.

The results obtained from the 3D volume reconstructed with full positional data were:

- The tumour was located from 34.5 to 38.55cm.
- The tumour length was 40.45mm.
- Junction was located at 38.55cm.
- Maximum thickness was 21mm.

The volume reconstruction with X, Y & Z positional information is shown in figure 4.15. Again the figure shows the transverse, coronal, sagittal and angle planes. The same data was used to construct the volume and started at 49cm from the incisor teeth. Similar dimensional measurements were performed on each of the planes.

The most significant difference between the scans was the relative location of the tumour from the incisor teeth. The error in the location, between conventional EUS and basic position was 5.88%, compared with 1.47% when the full positional information was applied to the reconstruction. The error in the measurement of the length of the tumour when measured with conventional EUS and 3D EUS tumour lengths using basic and full position information were 6.85% and 1.125% respectively.

Figure 4.16a illustrates the path of the tip during the pullback of the echoendoscope. A linear line that intersected with the origin superimposed on the 3D position plot showed that the endoscopist was able

to perform a relatively constant pullback rate. The single maximum deviation from the linear path was close to the end of the pullback and was 14.89mm, with a maximum variation of 25.5mm over the entire pullback of 200mm. From 5s to 30s of the pullback, the path of the tip had a maximum deviation of 10.6mm and a maximum variation of 19.16mm. The consultant had a maximum variation of 12.5% over the entire pullback of 200mm. The error reduced to 9.58% during the central segment of the pullback. During this time, the maximum deviations occurred when the endoscopist encountered the OGJ and at the termination point of the tumour. The maximum deviation occurred at the end of the pullback, when the echoendoscope was paused during the withdrawal, so that the 3D acquisition could be terminated.

The discontinuities observed in the reconstruction was due to sudden anatomical changes that caused the tip of the echoendoscope to rapidly move forward until the endoscopist could regain control of the pullback. The stenotic area at 34cm, the upper discontinuity, was due to the echoendoscope passing quickly from the stenotic area of the tumour. However, the endoscopist controlled the 'pop out' from the tumour and the tip only moved by 1.8 mm. The second discontinuity at 38cm was due to the quick passage from the stomach to the junction via a hiatus hernia. The difference between the Microscribe positional tip movements between each image capture is shown in figure 4.16b.

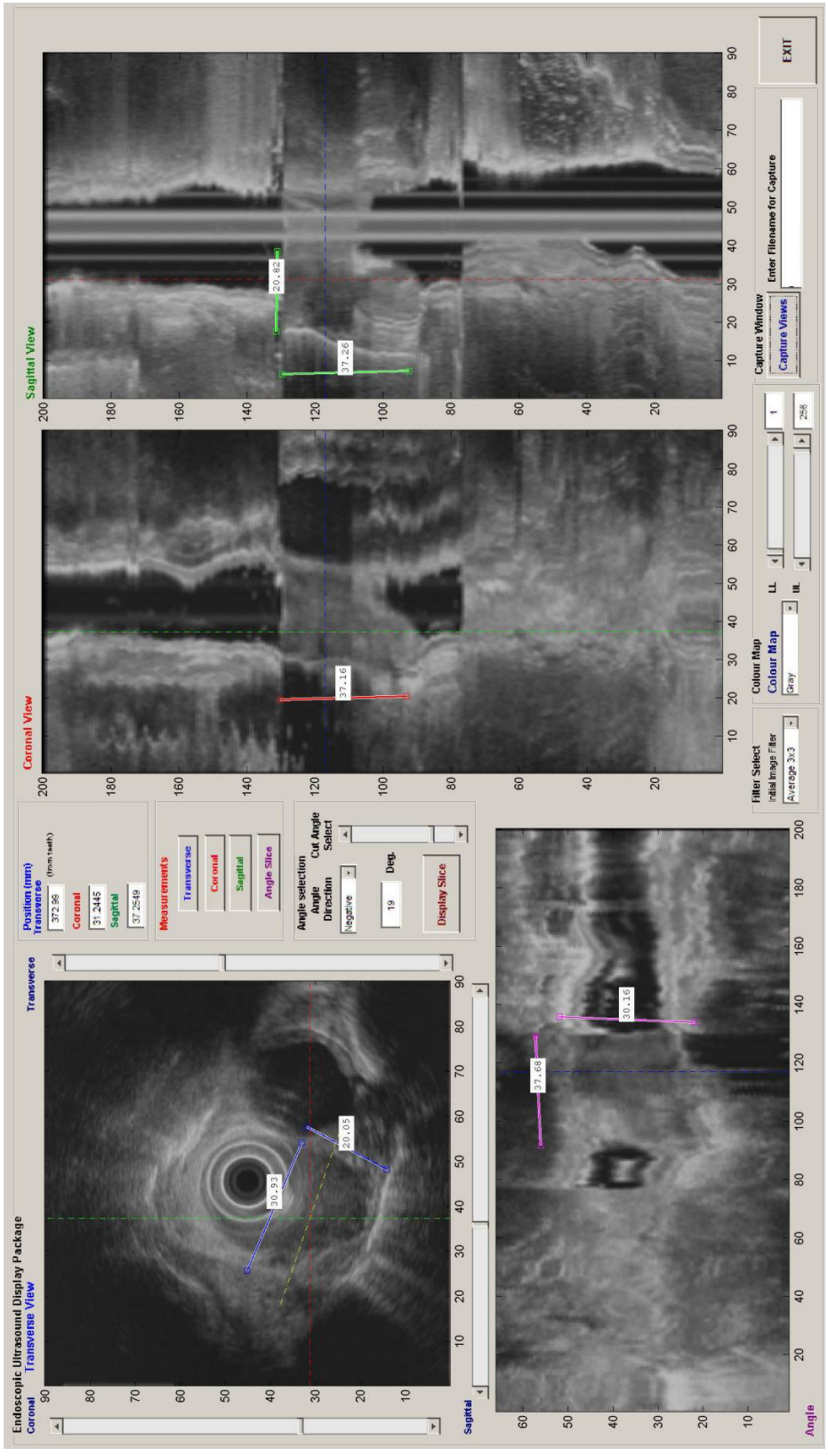

Figure 4.14– Basic positional information included within the reconstruction of the pullback of a clinical examination.

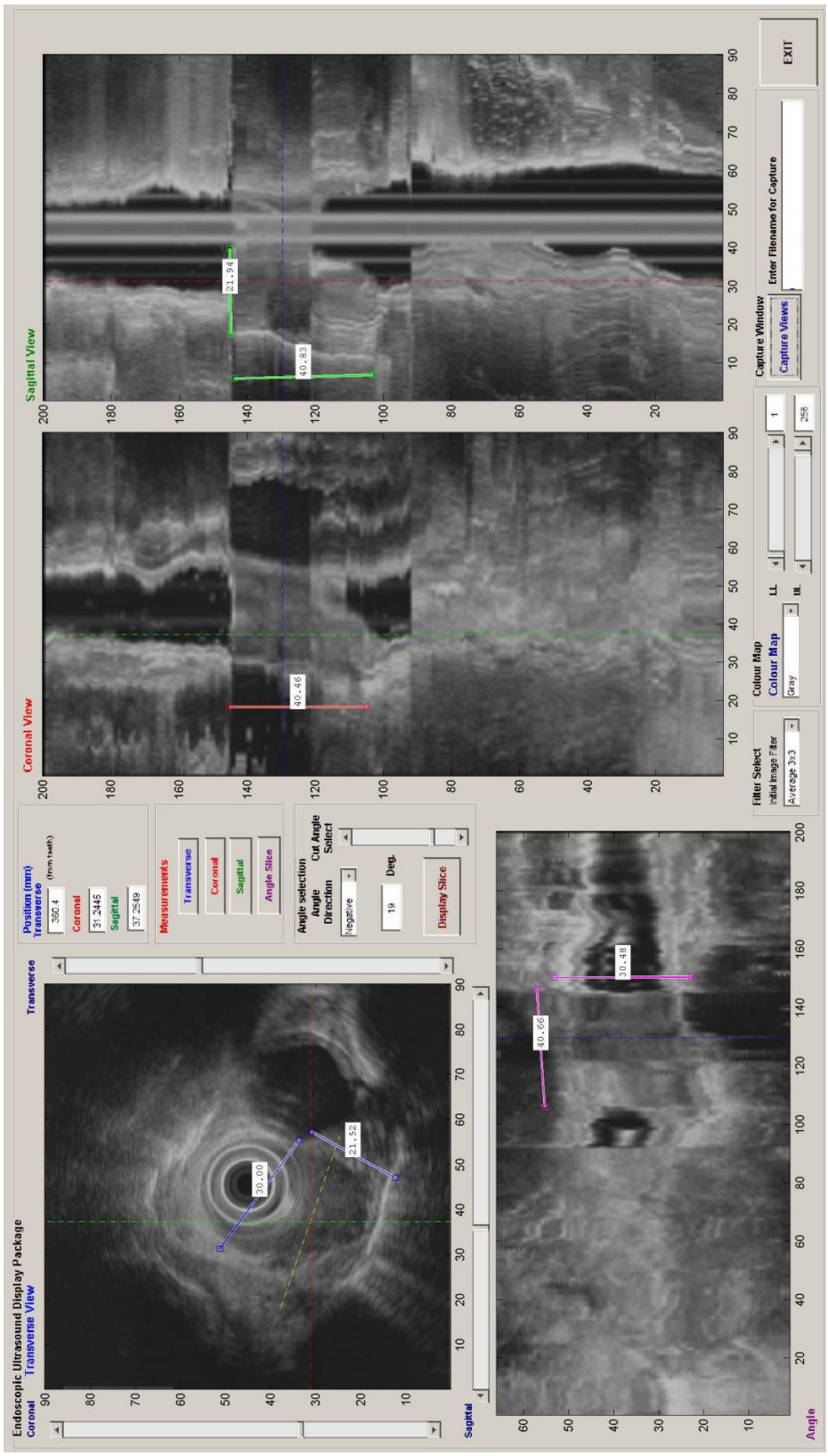

Figure 4.15 – X-Y-Z positional information included within the reconstruction of the pullback of the same clinical examination

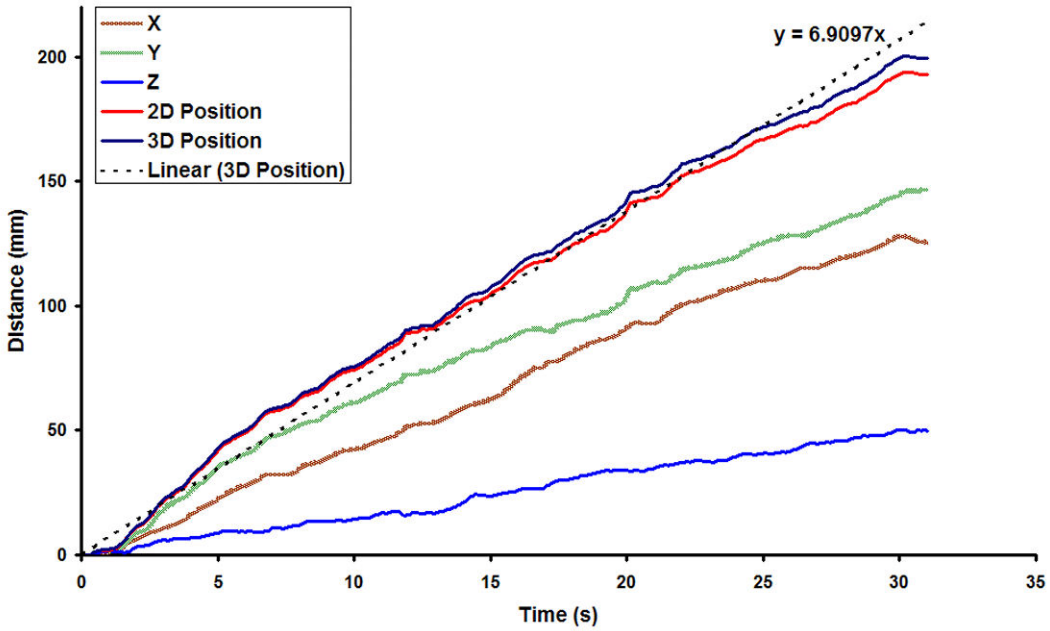

Figure 4.16a – Position obtained from the Microscribe digitising arm during the pullback of the clinical examination and the calculated path of the tip in 2 Dimensions ($\sqrt{(X^2+Y^2)}$) and in 3 Dimensions ($\sqrt{(X^2+Y^2+Z^2)}$). Actual pullback distance was 20cm. X-axis was the acquisition time in seconds and the Y-axis was the total distance travelled by the tip of the arm between each image acquisition in millimetres.

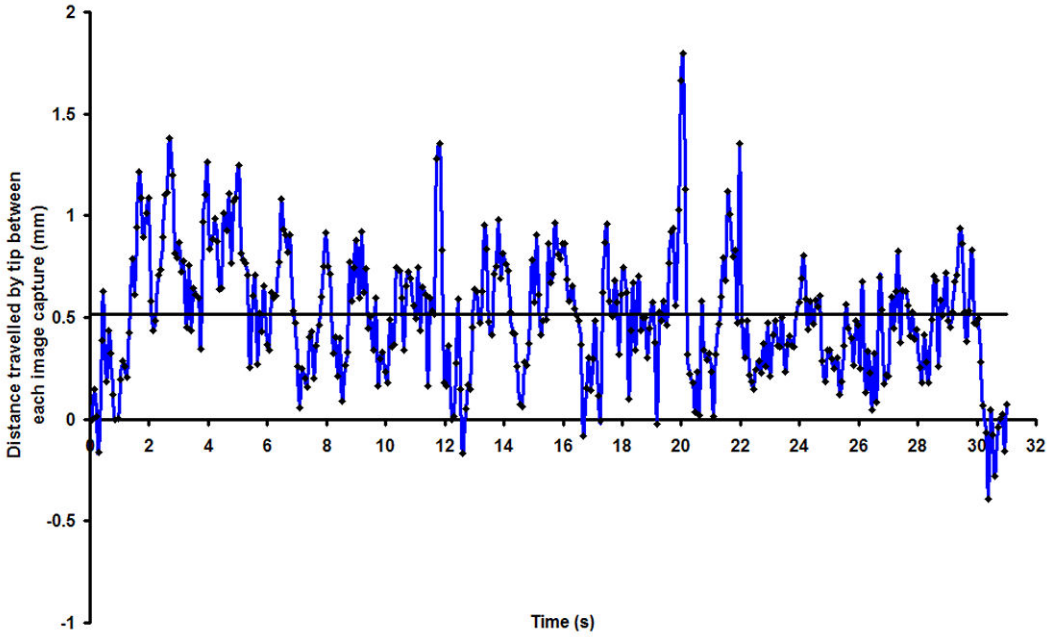

Figure 4.16b – The calculated difference in the distance between each image acquisition during the capture of the clinical data set. X-axis was the acquisition time in seconds and the Y-axis was the incremental distance travelled by the tip of the arm between each image acquisition in millimetres.

4.2.4. Discussion

The development of a practical freehand 3D-EUS system could be extremely useful in providing accurate information to the clinical staff for the evaluation of abnormal pathology and the planning of treatment. The application of 3D-EUS to the investigation of upper GI diseases, especially cancer staging, can allow for the complete examination of the pathology, minimise the possibility of missing any abnormal structures, and perform accurate dimensional and volume measurement to assess the effectiveness of treatment.

The 3D-EUS V2 system was designed to reduce the number of steps that were involved in the Prototype system, as well as resolve a number of limitations within the 3DScan program. The version 2 system could use both basic positional information and X, Y and Z position obtained from the Microscribe positional digitising arm. The inclusion of the tip positional data significantly increased the accuracy of dimensional and volume measurements. The application of this 3D-EUS V2 technique, with arm positional information would increase the accuracy of any dimensional and volume measurements performed on patients and would be useful in the following:

- The accurate localisation of the tumour with regards to anatomical structures.
- Accurate dimensional measurements of length in pathology of the oesophagus.
- Accurate assessment of the effectiveness of radiotherapy treatment by measurement of volumes pre and post treatment.

The 3D-EUS V2 phantom studies highlighted that applying full positional information provided the greatest accuracy and compensated for different pullback speeds. An anomaly occurred during the volume measurements tabulated in table 4.12, where the results for the basic positional information, at a fast pullback speed, were very small. This can be attributed to two possibilities:

1. During each phantom pullback study at different withdrawal speeds, a random restraining force was applied to the insertion tube of the echoendoscope. As such the amplitude of the error and the over or under estimation of size or volume obtained during the dimension and volume measurements would be random.
2. The measurements of the object volumes were performed by segmenting the object with a set number of slices of different thicknesses (either every 2, 5 or 10 slices). The accuracy of the volume measurement will depend upon the segmenting start point, the accuracy of the area selection and the reconstruction frame rate.

At fast pullback speeds, the reconstruction detail will be low and the accuracy of the volume measurement will be dependant upon where the frames were captured and if the restraining force was applied during the passage through the volume of interest.

The 3D reconstructions of the phantom (figure 4.12) highlighted a drawback with the application of an external position-monitoring device. The layers were not straight in the coronal and sagittal planes and the diameter of the layers appears to vary in the angle plane. This was due to small movements of the transducer within the central core of the phantom, during the pullback. It was not possible to compensate for this movement with an external positional arm. However, if transducer balloons were used during the phantom studies, the small movements would be minimised, as it would hold the transducer securely within the core of the phantom. Theoretically, this movement could also be minimised by software detection of the layers and then subsequent aligning of each image or by having a positional sensor at the tip of the echoendoscope. The software technique would not compensate for the physiological artefacts, as they would have different affects around the circumference of the oesophagus.

The average absolute error obtained for the dimension measurements on the phantom with the application of Z positional information was 3.2%. Applying the formula $\sqrt{(X^2+Y^2+Z^2)}$ reduced the error to 1.1%. The difference between the dimension measurements, using both techniques, was only 2.1% in the phantom as the scope was withdrawn in the Z direction with only minimal movements in the X and Y planes. Where the use of the formula $\sqrt{(X^2+Y^2+Z^2)}$ became apparent was in clinical studies as it was not possible just to withdraw the scope in one plane or direction. It compensated for the scope movement in x. y and z directions and increased the accuracy of the reconstruction.

In the clinical studies, no processing was performed to smooth, or average out, the discontinuities within the reconstruction, as it may introduce artefacts or remove structures that contain clinically relevant details. However, the acquisition technique may be modified to minimise the discontinuities. Before the scope is removed from the patient, the endoscopist may perform a pullback and then slowly re-introduce the transducer back down the oesophagus and passed the discontinuities, while simultaneously acquiring images and positional information. The images acquired during the scope re-introduction may be substituted with frames affected by the discontinuities. However, this would be best applied with tip positional information to reduce the differences in the transducer alignment from withdrawal to re-introduction.

Chapter 5 – The clinical application of 3D EUS in the upper GI tract.

5.1. Clinical Upper GI Examination

5.1.1. Computed Tomography Examination

Computed Tomographic scanning of the abdomen and thorax was performed within the Radiology department of the Royal Infirmary of Edinburgh and analysed by an experienced consultant radiologist, as part of the staging protocol implemented for upper GI cancer treatment within the RIE.

Prior to April 2003 the CT used to scan the patients was a single slice helical scanner; the Hi speed ADVANTAGE GE SCANNER (General Electric Medical systems, Milwaukee, USA). The standard imaging protocol used with the GE CT scanner was that images were acquired with a 10mm slice thickness and were reconstructed at 10mm intervals. After April 2003, a 16 slice scanner, multi-detector Toshiba Aquilion 16 (Toshiba Medical, Japan) CT scanner was used to perform the examination of the abdomen and thorax of upper GI cancer patients within the RIE. The Toshiba CT Scanner acquired images with a 1mm slice thickness which were reconstructed at 5mm intervals. Contrast agent was intravenously given to the patient to enhance the scans and was 100 ml of Niopam 300.

5.1.2. Conventional EUS Examination

Conventional EUS was performed using a variety of radial Olympus (Olympus Medical systems corp. Tokyo, Japan.) echoendoscopes GF-UM 20, GF-UM 200, GF-UM2000 and more recently GF-UE260. An appropriate echoendoscope was chosen to suit each case. For early tumours any of the available GF-U series echoendoscopes were normally used for the examination. The patient was placed in the left lateral position and given conscious sedation (i.v. Midazolam and opiates). After the patient was sedated the endoscopist inserted the echoendoscope orally into the GI tract.

A standard EUS examination was performed for establishing the TN staging. Using the optics of the echoendoscope, a cursory visual inspection was performed to localise the area of the cancer and negotiate the tip of the echoendoscope past the area of interest and deep into the stomach. The second part of the examination was to position the tip of the echoendoscope below the tumour, inflate the ultrasound balloon to obtain good contact with the wall, and look for distal metastatic disease (e.g.

nodes within the region of the diaphragm, celiac axis and areas below the oesophago-gastric junction). The third stage of the examination was to localise, measure and determine the stage of the disease, where the endoscopist will optimise the views to obtain the oesophageal wall structure and look for abnormal thickening and fusion of the layers. The fourth stage was to assess any further nodes within the region of the tumour and higher (e.g. bronchial area). The final stage was to look for any other abnormal structures that may complicate treatment (e.g. varicies).

5.1.3. Three-Dimensional EUS Examination

At the end of the standard EUS examination the tip of the echoendoscope was positioned at an appropriate location below the tumour or any corresponding nodes, and typically below an identifiable anatomical structure (e.g. Oesophago-gastric junction (OGJ)). At the start of the 3D examination the length of the inserted endoscope was recorded. The endoscope was withdrawn at a constant rate to a level above the lesion, typically to the level of an identifiable anatomical structure (e.g. Aortic Arch). The inflated balloon of the EUS scope was kept in contact with the wall of the oesophagus. Accurate positional information could be acquired using a positional digitising arm that was attached to the wrist of the endoscopist's hand guiding the endoscope using a custom harness.

The information obtained during this analysis, included number, shape and dimensions of any visible nodes, tumour dimensions (depth, width, & length), number of layers of the oesophagus involved by tumour, and location in relation to anatomical landmarks such as aortic arch, and OGJ and any additional abnormal pathology observed.

5.2. Early Oesophageal Cancer Staging

Background

Oesophageal cancer is an aggressive malignancy with an overall five-year survival of 5-10%; two-thirds of patients have irresectable disease at diagnosis. Accurate staging of oesophageal cancer is important because survival is closely correlated with tumour, nodal involvement and presence of metastases (TNM stage). When oesophageal cancer is detected early, there are a number of treatment options available to the patient for a curative outcome. However, some of these options require information from other imaging modalities (e.g. CT). The difficulties arise when the tumour cannot be resolved on the CT scan.

The application of 3D-EUS to these cases could provide the necessary anatomical information to the oncologists for successful treatment planning. In addition to the localisation of the tumour and nodes, clinically significant information could be obtained that would aid in the selection and planning of treatment options.

This chapter details the clinical evaluation of the developed 3D-EUS systems on patients diagnosed with early oesophageal cancer. The application of 3D-EUS to a sub set of oesophageal cancer staging is investigated. Most cancers at the presenting of symptoms are relatively advanced (e.g. T3 N0 or N1). The sub set studied within this chapter is the early cancer patients (e.g. T1 N0). Conventional EUS, 3D-EUS and, if available, MDCT will be compared to assess the ease of visualisation and localisation of the T1 tumour.

Aims

To investigate the role of 3D-EUS, to provide information regarding staging and localisation of early cancers of the oesophagus that were not detectable by CT scanning, for the facilitation of treatment planning and execution.

Subjects

Between 2002 and 2008, 16 patients (5 females and 11 males with mean ages of 72 ± 9.55 and 68 ± 9.75 years respectively) were diagnosed with early oesophageal cancer in the Royal Infirmary of Edinburgh (RIE).

5.2.1. Methods

During the standard investigative protocol for upper GI cancer at the RIE, the initial endoscopy with biopsies, confirmed the presence of cancer via histological examination. As part of the investigative protocol for the patient, a CT examination of thorax and abdomen was performed, as per section 5.1.1 by the Radiology Department at the RIE and examined by an experienced consultant radiologist. If there was no evidence of metastatic disease, the patient was referred to the Endoscopy Unit for a conventional EUS examination, as per section 5.1.2. At the end of the EUS examination the echoendoscope was situated below the tumour and a 3D EUS acquisition was performed, as per section 5.1.3. Within the endoscopy suite, a cursory examination of the 3D volume was performed to determine the staging. Subsequently a detailed examination of the reconstruction was performed 2 to 3 months post procedure and was anonymised and blinded from the previous 2D and 3D staging, to minimise any bias from the initial examination. The clinical details of these patients were retrospectively studied. The endoscopist provided the conventional EUS staging, at the time of the procedure and the author of this thesis interpreted the 3D-EUS volumes and provided the 3D staging.

5.2.2. Results

EUS visualised, in detail, the tumours in all 16 patients. Table A.7.1 details the demographics of the 16 cases of the early cancer staging and the chosen treatment options. CT could not image the tumour in any of the 16 cases. Staging by conventional EUS and 3D-EUS agreed in 15 out of 16 cases. The case that did not agree, conventional EUS staged as a possible T2 tumour. Nine patients had upper/mid oesophageal carcinoma and 7 patients had cancer located at the lower third of the oesophagus and oesophago-gastric junction. In addition to standard EUS, the 3D-EUS provided an accurate determination of tumour dimensions and layer involvement.

Figures 5.1a to c illustrate the comparison between 3DCT, acquired from a 16 slice MDCT and 3D-EUS, the transverse, coronal and sagittal cuts of both CT and EUS are show as 3.7cm below the bottom of the aortic arch. The EUS clearly showed the biopsy proven cancer with an increased thickening of 6mm associated with tumour infiltration. The CT did not show any evidence of wall thickening. The 3D CT scan was analysed by an experienced consultant radiologist who is part of the multi-disciplinary upper GI cancer team. Two additional cases were selected to illustrate the information that could be obtained from the 3D EUS.

Figure 5.2 - Patient 3: As this patient had chosen to receive radiotherapy treatment and the tumour could not be visualised by the CT, it was necessary to localise the tumour to anatomical structures. The lower border of Aortic Arch (AA) was measured on the 3D-EUS at 26.3cm from the incisor teeth. The upper tumour border was 1.63cm below that point. The tumour dimensions (LxBxH) were determined as 33.1 x 4.5 x 13.8mm, with no local nodes observed. Up to 7 layers within the wall of the GI tract could be observed during the course of the pullback. The EUS scanning frequency was set at 12MHz with an image dimension of 9cm.

Figure 5.3 - Patient 13: The anatomical structures were localised in case the patient chose to have radiotherapy. The lower border of Aortic Arch (AA) was localised at 26.4cm from the incisor teeth and the upper tumour border began at 3.3cm below the AA. The dimensions (LxBxH) of the tumour were 5x4x15mm with one possible reactive node observed. The EUS scanning frequency was set at 12MHz with an image dimension of 9cm.

3D EUS provided important information in two respects (a) an accurate T staging of the tumour and (b) the relationship between the tumour and key anatomical structures, such as the aortic arch, subcarinal area and the oesophago-gastric junction which was clinically significant for subsequent treatment planning.

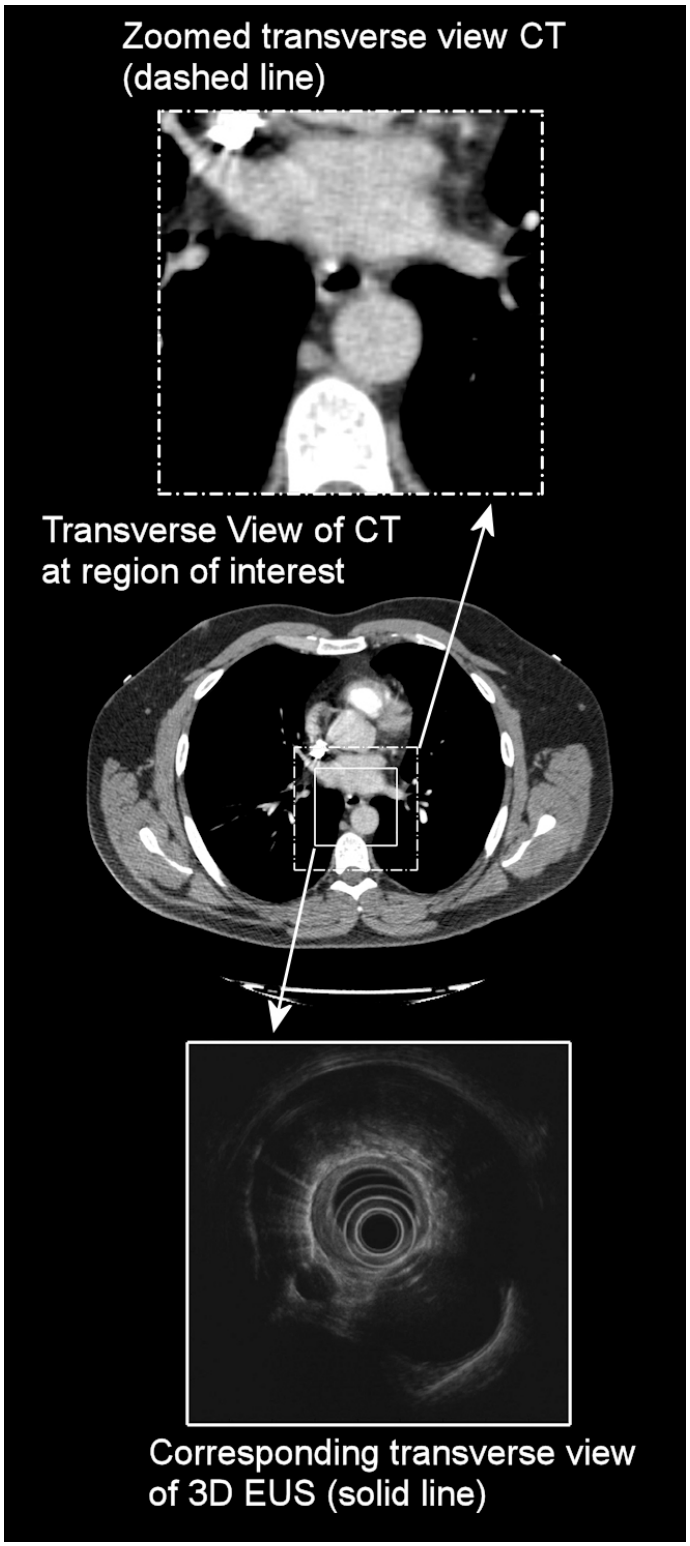

Figure 5.1a – Comparison of transverse views between CT and 3D EUS, the transverse cuts of both CT and EUS are show as 3.7cm below the bottom of the aortic arch. The EUS clearly showed an increase thickening of 6mm associated with tumour infiltration. The CT did not show any evidence of wall thickening.

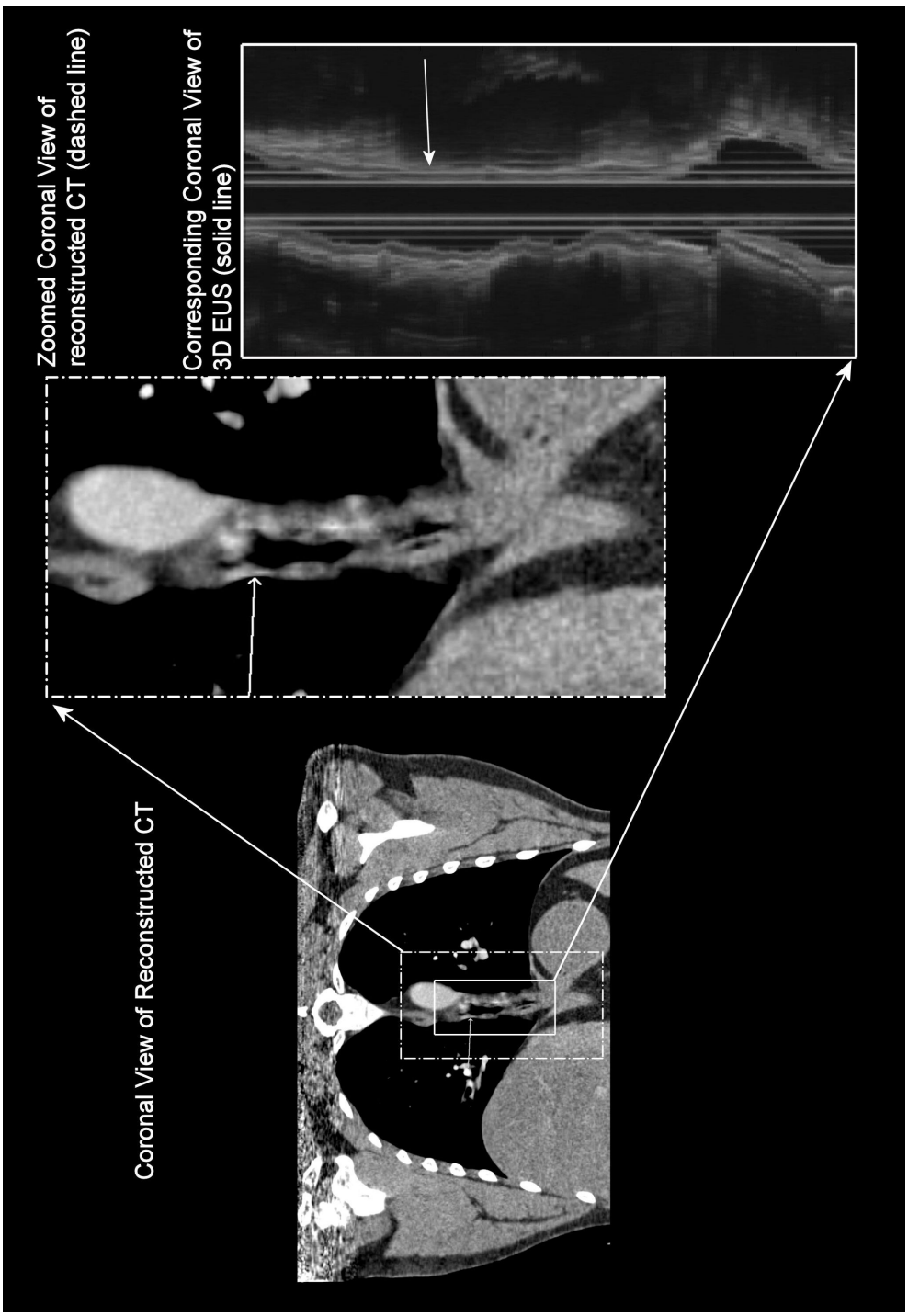

Figure 5.1b – Comparison of coronal views between CT and 3D EUS, the coronal cuts of both CT and EUS. Due to the plane of cut, neither CT nor EUS showed any evidence of wall thickening.

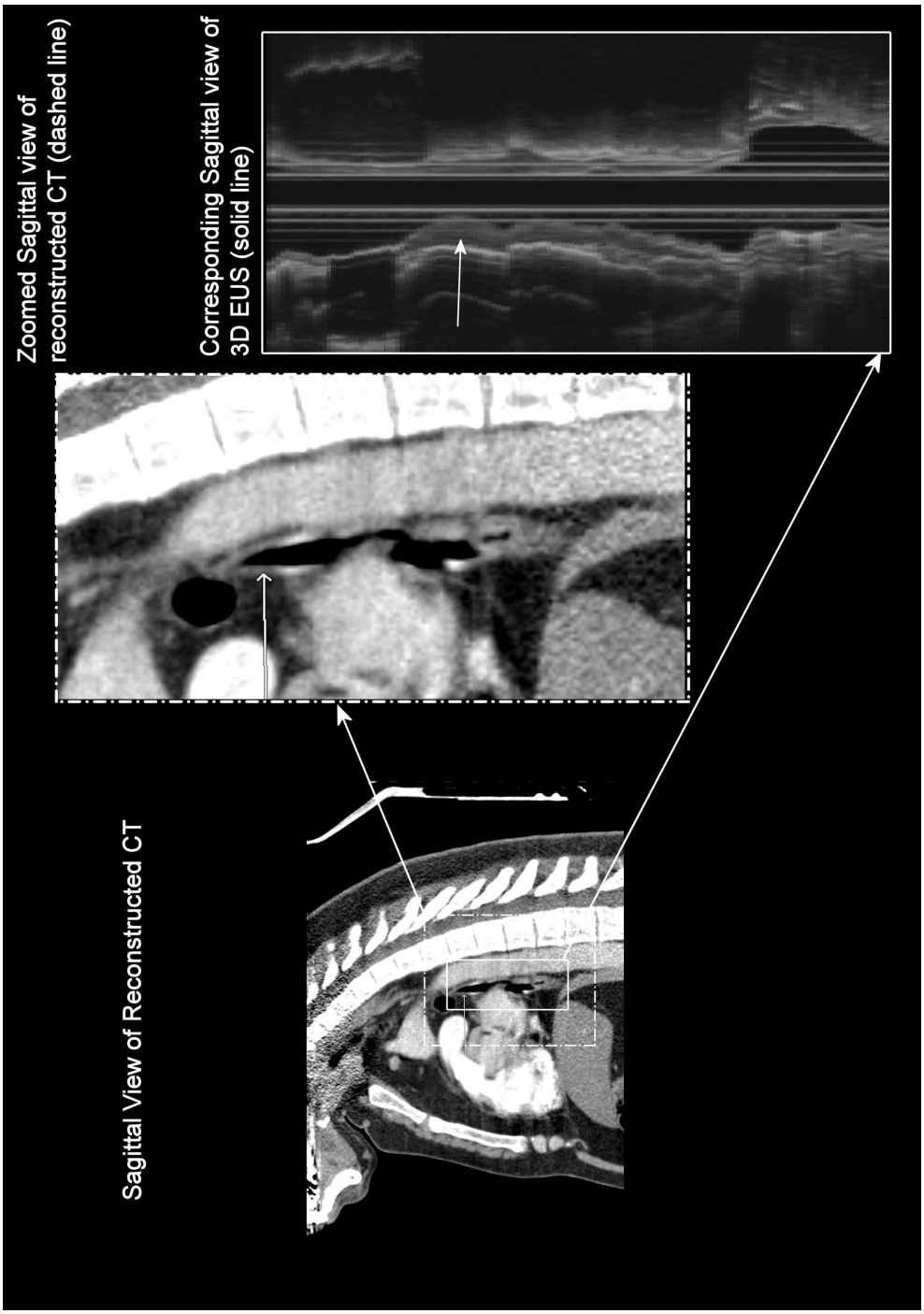

Figure 5.1c – Comparison of sagittal views between CT and 3D EUS, the sagittal cuts of both CT and EUS. The EUS clearly shows an increase thickening of 6 mm associated with tumour infiltration. The CT did not show any detectable evidence of wall thickening in the sagittal view.

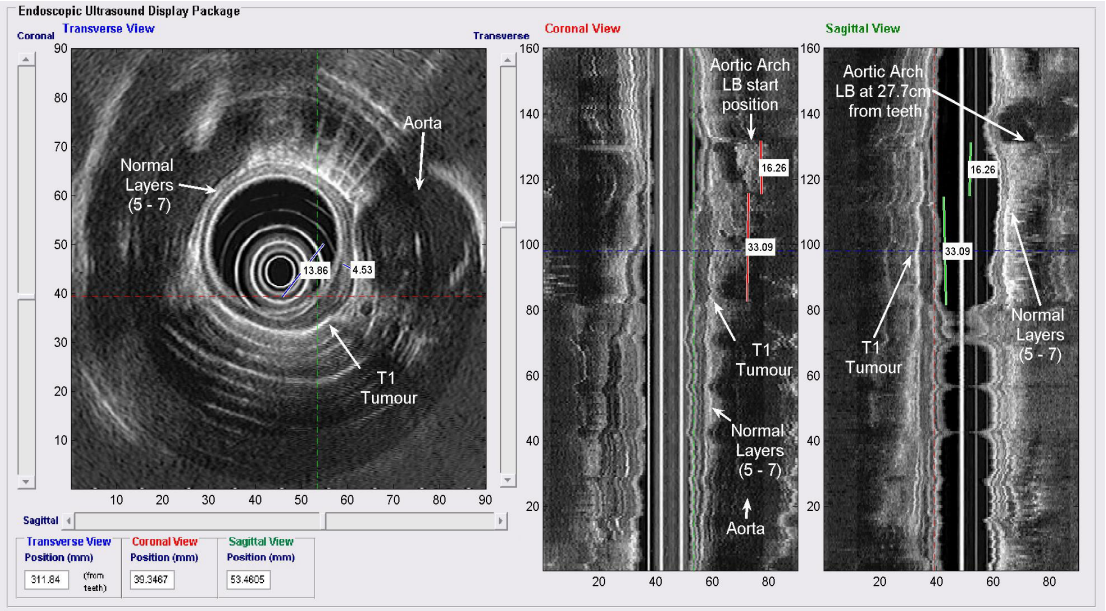

Figure 5.2 - Patient 3: Lower border of Aortic Arch (AA) 26.3cm from teeth. Upper Tumour border 1.63cm below AA Dimensions: (LxBxH) 33.1x4.5x13.8mm, no nodes. US frequency: 12MHz.

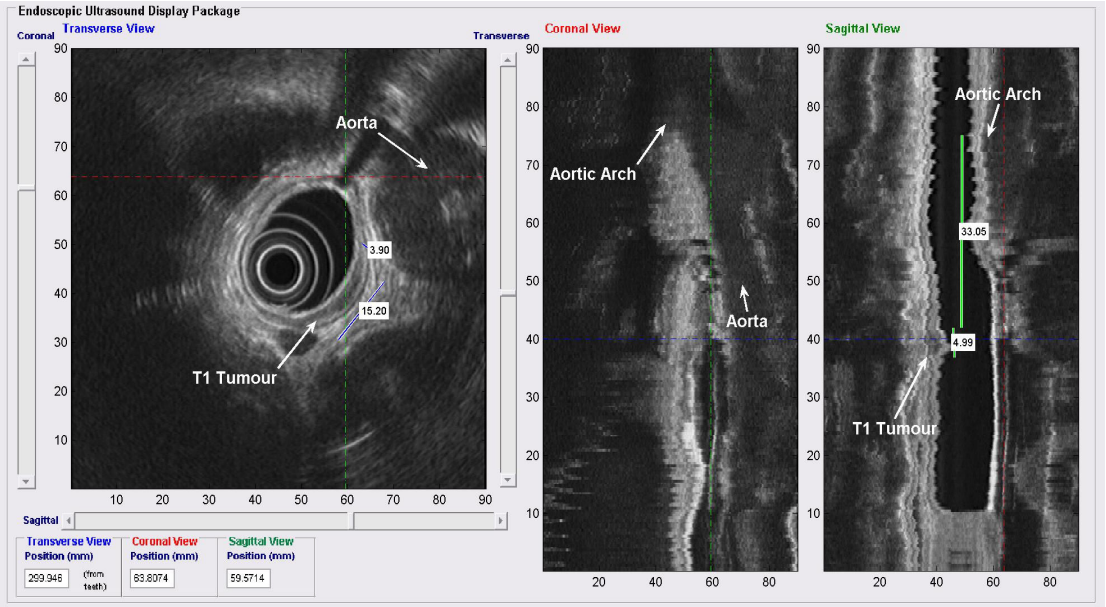

Figure 5.3 - Patient 13: Lower border of Aortic Arch (AA) 26.4cm from teeth. Upper tumour border: 3.3cm below AA. Dimensions (LxBxH): 5x4x15mm, one possible reactive node observed. US frequency: 12MHz.

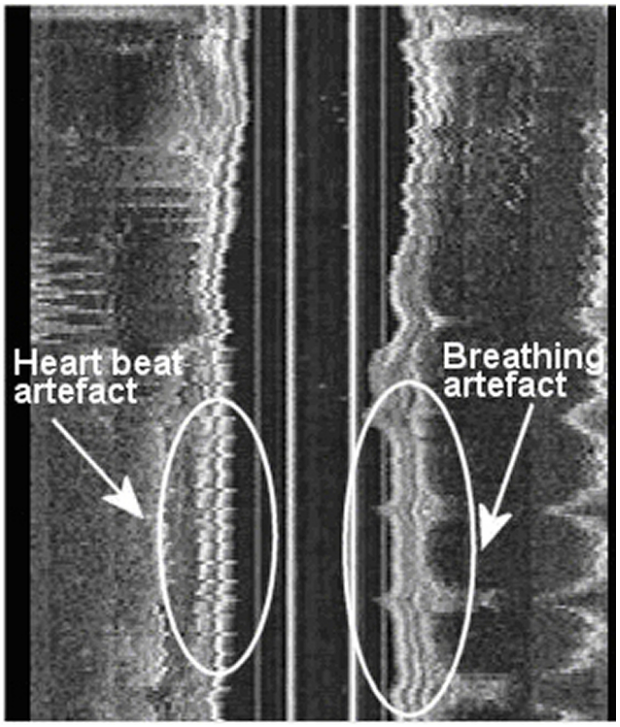

Figure 5.4 - Example of the cardiac and breathing physiological artefacts that can be observed during the 3D reconstruction.

5.2.3. Discussion

Early oesophageal cancer is particularly challenging for all imaging modalities to identify and diagnose. Currently EUS is the only imaging modality that can reliably detect T1 tumours. All of the cases detailed in table A.7.1 were confirmed as cancer from the tissue samples taken during the initial endoscopy. However, none of these tumours were located during CT (Figure 5.1).

Conventional EUS detected all tumours, apart from patient 13, where only glimpses of the tumour were obtained during the examination. For patient 13, 3D-EUS was used to locate, visualise and analyse the tumour. The acquisition of the 3D image data set was advantageous in a number of these early tumour cases. Patients with early tumours have a number of treatment options that include surgery and radiotherapy. However, to plan the treatment, it requires the tumour to be visible on the CT. As none of these cases were visible, it was necessary for the oncologists to request additional tumour location data from the endoscopist. As each patient had received both EUS and 3D-EUS examinations, it was possible to provide tumour location for treatment planning without repeating the EUS procedure.

Using 3D-EUS it was possible to determine the x, y and z dimensions of the tumour and the volume, to monitor the effectiveness of radiotherapy treatments. It was also capable of providing detailed reconstructions of the oesophagus and surrounding anatomy for analysis, minimising the possibility of missing clinically important information. The developed freehand 3D-EUS system allowed for the endoscopist to control the scope and maintain contact with the wall of the oesophagus during the pullback. However, using a freehand technique, it was difficult to remove the physiological artefacts (cardiac and respiration) experienced during clinical scanning (figure 5.4)

5.3. Advanced Oesophageal Cancer Staging

Background

The accurate staging of oesophageal cancer is important because survival is closely correlated with tumour and nodal classification and presence of metastases (TNM stage). The label, advanced oesophageal cancer (T3) is a generalised term that covers a wide range of tumours possibilities. An early T3 tumour may only have a small section of its length where it infiltrates the muscularis propria, which could be missed. In comparison, an advanced T3 tumour may infiltrate the entire length of the muscularis propria. As the stage of the disease increases, the available treatment options diminish. To successfully treat advanced cancers of the oesophagus, it is often necessary to apply additional treatment (e.g. radiotherapy / chemo-radiotherapy). However, it is necessary to clearly identify these cases to increase the possibility of a successful outcome.

This chapter details the comparison of the staging accuracies of conventional EUS and the developed 3D-EUS systems on patients with advanced cancer (T3N1). The EUS staging will be compared with the gold standard of histological staging, which was obtained after the patients progressed to surgical resection. The application of 3D-EUS may allow for the detailed study of the tumour and accurately determine the stage of the disease. It also may be able to provide additional information that can better classify the T3 tumour subgroup.

Aims

The aim of this study was to investigate the role of 3D-EUS in providing information regarding T and N classification of advanced cancers of the oesophagus and to compare the results with conventional EUS to see if the results would aid in the planning of treatment.

Subjects

Between 2002 and 2007, 98 patients were diagnosed with advanced oesophageal cancer (T3 N0 or 1) in the Royal Infirmary of Edinburgh (RIE), of those 24 patients progressed to possible curative surgery (7 females and 17 males with mean ages of 69.9 ± 8.2 and 60.8 ± 10.7 years respectively).

5.3.1. Methods

The standard investigative protocol for upper GI cancer at the RIE, called for an initial endoscopy with biopsies to confirm the presence of cancer via histological examination. As part of the upper GI investigative algorithm, the patient received a CT examination of thorax and abdomen, as per section 5.1.1. If there was no evidence of metastatic disease, the patient progressed to have a conventional EUS examination, as per section 5.1.2. At the end of the EUS examination the echoendoscope was situated below any abnormal pathology and carefully withdrawn. During this time a 3D EUS acquisition was performed, as per section 5.1.3. Within the endoscopy suite, a cursory examination of the 3D volume was performed to determine the staging. Subsequently, a detailed examination of the reconstruction was performed 2 to 3 months post procedure and was anonymised and blinded from the previous 2D and 3D staging, to minimise any bias from the initial examination. The clinical details of these patients were retrospectively studied. The endoscopist provided the conventional EUS staging, at the time of the procedure and the author of this thesis interpreted the 3D-EUS volumes and provided the 3D staging.

Pathology reports for all oesophageal cancers staged using EUS at the Royal Infirmary, Edinburgh from April 2002 to April 2007 were examined and those staged as T3N1M0/x were selected for analysis. Ambiguous reports were excluded. Information on nodal involvement and cancer type was also collated.

3D-EUS volumes were analysed and the data recorded within a spreadsheet and the conventional EUS reports were studied. During the 3D-EUS analysis, the tumours were analysed as segments of percentage staging lengths of tumour from T1 to T4 were calculated. Patient records were studied using various sources (Medtrack, RIE GI cancer database and paper records) to determine if the patients within the selected group were still alive, and if deceased what the cause of death was. Information was also collected to see if the patients had pre-surgical neo-adjuvant chemotherapy.

The data was retrospectively analysed to compare the collated results of 3D-EUS with conventional EUS and where available histological results.

5.3.2. Results

Between 2002 and 2007, 98 patients diagnosed with T3N1 oesophageal disease and had both conventional and 3D-EUS examinations. Of those 98 patients, only 24 progressed to possible curative surgery. In all cases the EUS visualised, in detail, the tumours in all 24 patients. Table 5.1 details the staging results obtained from conventional EUS and 3D-EUS, compared with the final histological staging from the surgical resection. Table A.7.2 details the date when the endoscopic ultrasound was performed and the length of the patient's survival. Table A.7.3 details the demographics of the 24 cases of the advanced cancer staging and each case progressed to surgical resection.

Table 5.1 – Comparative results obtained from conventional EUS and 3D-EUS compared with histological staging. All 24 cases had a histological staging of T3N1 from the surgical resection.

Staging	Conventional EUS		3D-EUS	
	No.	% Accuracy	No.	% Accuracy
T	18	75	22	91.2
N	19	79.2	21	87.5

Of the 24 patients, 10 patients were still alive at the time of the study end (14/09/2007). The average length of survival for the remaining 14 patients was 17.8 ± 15.5 months post EUS examination (max 52 and min 1.5 months). The pathology, on average, was analysed 1.67 ± 0.87 months after the EUS was performed. The surgery would have been performed just prior to the pathological examination of the surgically resected specimen. Six patients did not receive per surgical neo-adjuvant chemotherapy or radiotherapy to shrink the tumour and reduce the possibility of malignant nodes.

Table 5.2 – Breakdown of the incorrect staging obtained from conventional and 3D-EUS. The term 'Both' is when T and N were incorrect, T was when the tumour stage was wrong and N when the nodal staging was incorrect.

Method	Incorrect staging		
	Both	T	N
Conventional	3	3	2
3D-EUS	1	1	2

Table 5.2 detailed the break down of the cases where the staging differed from histological staging with both conventional and three dimensional EUS. Comparing the conventional EUS, there were 8 cases where the pathological staging of the surgically resected specimen differed from the EUS TN

staging. Conventional EUS under staged the tumour in 6 of the 8 cases, and did not detect malignant nodes in 5 of the 8 cases. Using 3D-EUS, the TN staging only differed in 4 cases. Of those 4 cases 3D-EUS under staged the tumour in 2 cases, and did not detect malignant nodes in 3 cases.

Of the 24 cases of T3 N1, only 9 conventional EUS staging reports stated a definitive number of nodes. The majority of reports used vague terms such as several to describe the number of nodes. Of those 9 cases, conventional EUS detected a total of 27 nodes. In comparison 3D-EUS detected a total of 77 nodes. Conventional EUS only detected 35% of the nodes, which were detected by 3D-EUS.

Figures 5.5 to 5.7 demonstrate some of the reconstructions obtained during the 3D-EUS examinations. Patients 9, 14, and 16 were chosen as examples. The following measurements were performed on the reconstructions to characterise the tumour and locate and measure the significant nodes. Other nodes were counted but not measured.

Patient 9 (figure 5.5a) had segments of T1 tumour at 326 - 340mm and 374 - 387mm, T2 at 340 - 344, and T3 at 344 - 374mm. There was significant node clusters of size 21x18x20 at 345mm and a second one of 20x19x20mm at 356mm, 8x4x5mm at 347mm, single nodes were seen at 368mm, 371mm and at 430mm from the incisor teeth with sizes of 4x3x15mm, 3x2x2mm and 22x16x35mm respectively. The length of the tumour was measured at 61mm. Figure 5.5b shows the 3D reconstruction when this patient was re-staged after the application of neo-adjuvant chemotherapy.

For patient 14 (figure 5.6), the tumour segments for T1 were at 302 - 310mm and 369 - 378mm. The T2 segments were at 310 - 317mm and 352 - 363mm. The advanced tumour segments (T3) were at 317 - 352mm and at 363 - 369mm. The significant nodes were located at 468mm, 442, 402, 400, 309, and 347mm from the incisor teeth and were 12mm, 4mm, 5mm, 7mm, 8mm, and 5mm in dimensions respectively. The length of the tumour was 76mm.

Patient 16 (figure 5.7) had tumour segments of T1 tumour at 295 - 301mm and 316 - 360mm. Segments of T2 tumour at 301 - 303mm and 308 - 316mm. The segment of advanced (T3) tumour was between 303 - 308mm. The maximum length of the tumour was 65mm. The nodes were located at 286mm, 348mm, and at 409mm and were measured at 6mm, 2mm, and 4mm respectively.

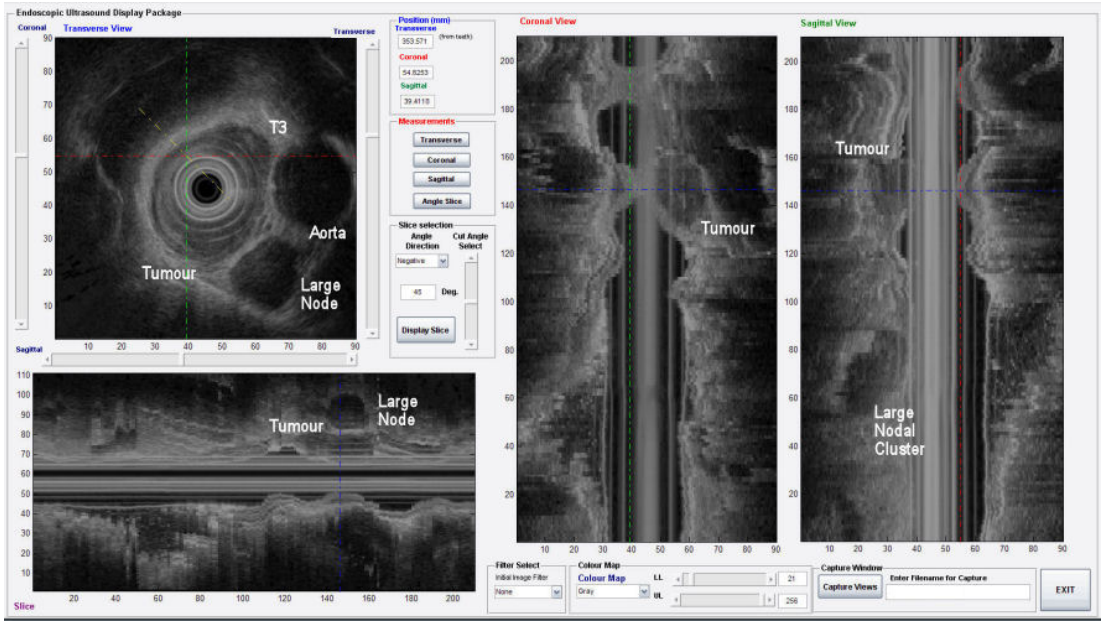

Figure 5.5a - Patient 9: T1 326 - 340mm, T2 340 - 344, T3 344 - 374mm, T1 374 - 387mm. Nodes: cluster 21x18x20 at 345mm, 8x4x5mm at 347mm, cluster 20x19x20mm at 356mm, 5x4x2mm at 358mm, 4x3x15mm at 368mm, 3x2x2mm at 371mm, 22x16x35mm at 430mm. Tumour length: 61mm.

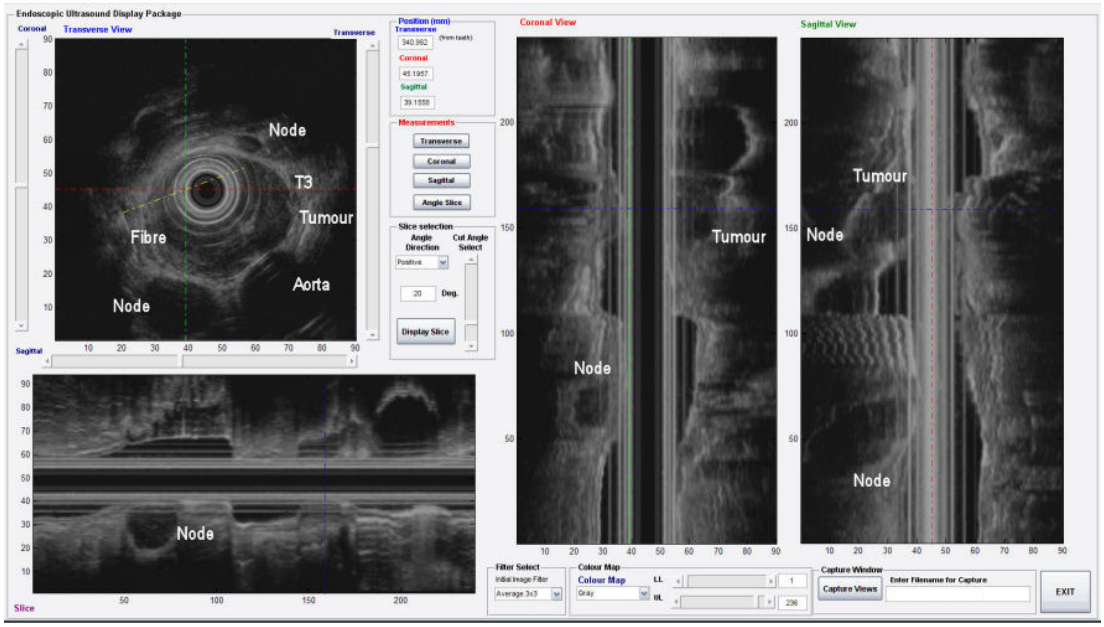

Figure 5.5b - Patient 9: Tumour and nodes after Neo-adjuvant chemotherapy. The tumour and nodes were unresponsive to the pre-surgery treatment. Figures 5.5a and b are shown at a similar level.

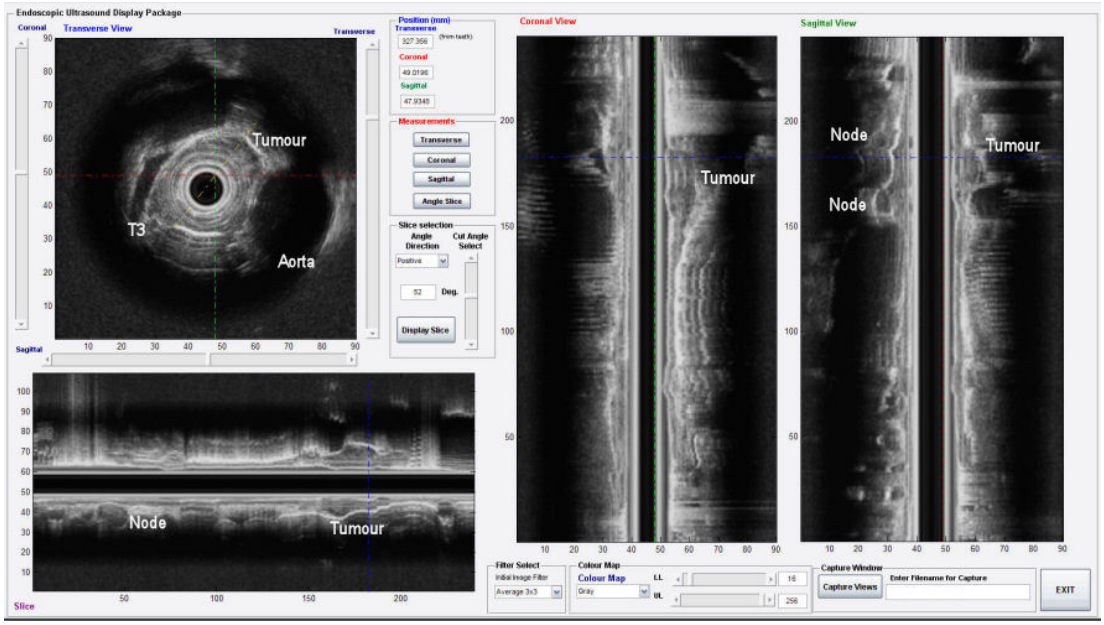

Figure 5.6 - Patient 14: T1 302 - 310mm, T2 310 - 317mm, T3 317 - 352mm, T2 352 - 363mm, T3 363 - 369mm, T1 369 - 378mm. Nodes: 12mm at 468mm, 5mm at 402mm, 7mm at 400, 8mm at 309mm, 5mm at 347mm, 4mm at 442mm.

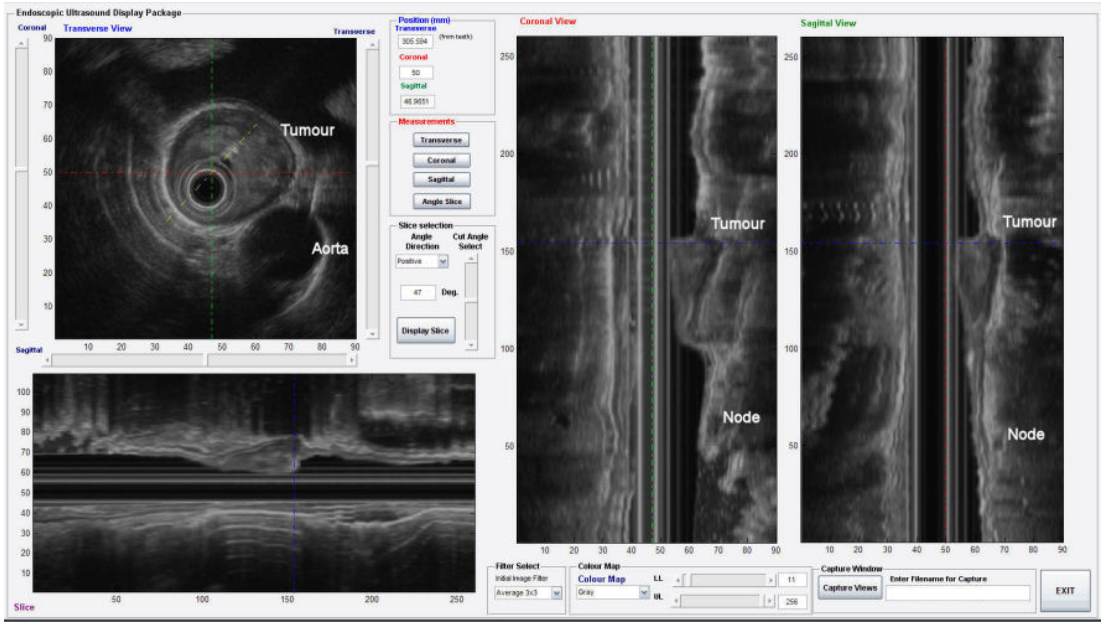

Figure 5.7 - Patient 16: T3 tumour with nodes: T1 295 - 301mm, T2 301 - 303mm, T3 303 - 308mm, T2 308 - 316mm, T1 316 - 360mm. Nodes; 6mm at 286mm, 2mm at 348mm, 4mm at 409mm. Tumour length: 65mm.

5.3.3. Discussion

In comparison with early tumours, advanced tumours can be easily visualised by both CT and EUS. Where CT provides accurate positional information of the main bulk of the tumour and any distal metastatic disease, it still does not give the definitive stage or truly define the borders of the disease. Small, early extended segments of the cancer could be missed.

Conventional EUS has been shown to be more accurate at providing the correct stage of the disease, compared with CT. From the retrospective analysis of the surgically resected histological, conventional EUS and 3D-EUS staging, it was shown that 3D-EUS increased the tumour staging accuracy from 75% to 91.2% and nodal staging from 79.2% to 87.5%, when compared with the gold standard of histological staging.

For patient 9, 3D-EUS was also found to be useful in the re-evaluation of cancer pre and post chemo-radiotherapy treatment (figure 5.5). Another advantage of 3D-EUS was found to have the ability to distinguish between segments of tumour (e.g. T1 x%, T2 y% and T3 z%). However, the % segmentation of the tumour staging is dependant upon accurate positional information. The 3D-EUS system may be able to provide an empirical method to distinguish between early and advanced T3 tumours and have implications in treatment planning. The main problem faced during the analysis of the volumes were (1) the tight strictures introducing artefacts due to the transducer and balloon entering (slowing) and exiting (accelerating) from stenotic region, and (2) with the mechanical radial echoendoscopes, the dead space and ring artefact can mask stenotic regions and introduce artificial rings that may be mistaken for layers.

5.4. 3D-EUS examination of other Upper GI conditions

Background

EUS is used in the diagnosis and monitoring of a number of benign and pre-malignant GI conditions (e.g. varicies, GIST, polyps) that are not accessible to standard endoscopic video examination and biopsies. These conditions often require monitoring over extended periods of time (months to years) to look for changes that would indicate malignant changes. Or in the cases where patients have multiple pathologies, it is often necessary to distinguish between these conditions to determine treatment options.

Applying 3D-EUS to the investigation of these conditions may provide additional information to enable accurate evaluation and monitoring of these conditions (e.g. accurate dimensional and volume measurements).

This chapter introduces the use of the developed 3D-EUS systems for the investigation of patients with benign conditions. Each benign condition will be investigated on an individual basis and will be performed to either exclude malignant disease, or monitor the conditions progression over time or investigate possible treatment options.

Aims

The aim of this part of the clinical evaluation of 3D-EUS was to investigate its usefulness in the study of a number of benign and pre-malignant upper GI disorders. Examples will be used to demonstrate its usefulness in various disorders between 2002 and 2008.

Subjects

Between 2002 and 2007, 68 patients were diagnosed with non-cancer related GI conditions within the Royal Infirmary of Edinburgh (RIE), of those 6 cases of non-cancer GI conditions were chosen to illustrate the application of 3D-EUS (1 female and 5 males with mean ages of 60 and 67.4 ± 18.9 years respectively).

5.4.1. Methods

To investigate a non-cancer GI condition, an initial endoscopy with biopsies, was performed to confirm the absence of cancer and identify the disorder via histological and visual examination. If there were no definitive results obtained from the endoscopy and histology, the patient was referred to the Endoscopy Unit for a conventional EUS examination, as per section 5.1.2. At the end of the EUS examination the echoendoscope was situated below the pathology and a 3D EUS acquisition was performed, as per section 5.1.3. Subsequently these patients were retrospectively studied. The endoscopist provided the conventional EUS diagnosis, at the time of the procedure and the principle investigator interpreted the 3D-EUS volumes and provided the 3D diagnosis.

The condition was studied as per the clinical need. For example, to confirm varicies, colour flow imaging of the GF-UE260 and Aloka α5 was used. For pathology situated within the wall of the GI tract (e.g. GIST, wall thickening), the echoendoscope was set at high frequencies (10 to 20MHz depending on the echoendoscope used).

5.4.2. Results

Table 5.3 is a break down of these non-cancerous upper GI cases by type and studied by 3D-EUS. Examples of these conditions are shown in figures 5.8 to 5.13. Of those, 1 x cyst, 1 x oesophageal varicies, 1 x multiple pathology (gastric varicies and polyps) and 3 x GISTs were chosen.

Table 5.3 – Break down of the non-cancer upper GI conditions studied via 3D-EUS

Conditions	**Count**
Other – (e.g. normal exams, liver, node, pancreatic & biliary studies)	8
Polypoid Lesions and polyps	3
Barrett's & High Grade Dysplasia (e.g. pre-cancerous wall thickening)	8
Gastro-intestinal stromal tumours (GIST) & sub-mucosal lesions (SML)	24
Lymphoma	2
Cyst (e.g. Cystic lesions, pseudo-cyst)	4
Varicies (e.g. oesophageal varicies and portal hypertension)	9
Non-Ca wall thickening (e.g. muscular wall thickening, inflammation)	8
Ulcer	2

Figure 5.8 details a large pancreatic pseudo-cyst of dimensions 70x66x40mm (LxBxH). The maximum wall thickness between the cavity of the GI tract and the cyst should be less than 5mm. However, after assessment by EUS and 3D-EUS, it was not possible to find a location that was free of vessels and less than 7mm.

A patient with a large lump in the stomach was referred to the endoscopy unit for an EUS investigation. Previous biopsies had only shown normal mucosa. After the EUS and subsequent 3D-EUS, the patient was diagnosed with a complex GIST (figure 5.9). A normal leiomyoma arises from the 4th layer, as this one did, however they are usually uniform echolucent structures (same echogenicity to the 4th layer). In this case the structure was multi-lobular with a number of darker structures within the tumour. This indicated that the leiomyoma had malignant characteristics and required to be investigated further. The size of the leiomyoma was 80x67x53mm (LxBxH) on the 3D reconstruction.

Figure 5.10 was of a 3D reconstruction of another GIST / leiomyoma in the fundus of the stomach. Once again a patient was referred to the endoscopy unit for an EUS examination as the initial endoscopy saw a large lump within the fundus and resultant biopsies were normal. The EUS and 3D-EUS examination observed a leiomyoma arising from the 4th layer of the stomach wall. The dimensions of the GIST were 47x24x20mm (LxBxH).

Figure 5.11 was of a 3D reconstruction of another GIST, this time a lipoma, within the oesophagus. The patient was referred to the endoscopy unit for an EUS examination as the initial endoscopy saw a lump within the oesophagus and resultant biopsies were normal. The EUS and 3D-EUS examination observed a lipoma arising from the 3rd layer of the oesophageal wall. The dimensions of the lipoma were 23x9x4.3mm on the 3D reconstruction (LxBxH).

Figure 5.12 was a 3D reconstruction of a vascular area within the oesophagus. The patient was referred for an EUS to assess a known area of varicies within the oesophagus. An area of varicies was visualised close to the oesophageal wall, on the 3D scan and was measured at 62x24x17mm (LxBxH).

A patient was referred for an EUS examination to assess a lumpy area within the stomach that had the appearance of either polyp or vascular structures. An EUS and subsequent 3D-EUS were performed to assess this lumpy area and were found that the patient had both polyps and portal hypertension (or varicies) within the stomach. From the measurements performed on the 3D scan displayed in figure 5.13, there was a large vascular area of 52x60mm (LxB) adjacent to a number of polyps, the largest of which were 21x15x15mm (LxBxH) and 14.6x15x14mm (LxBxH).

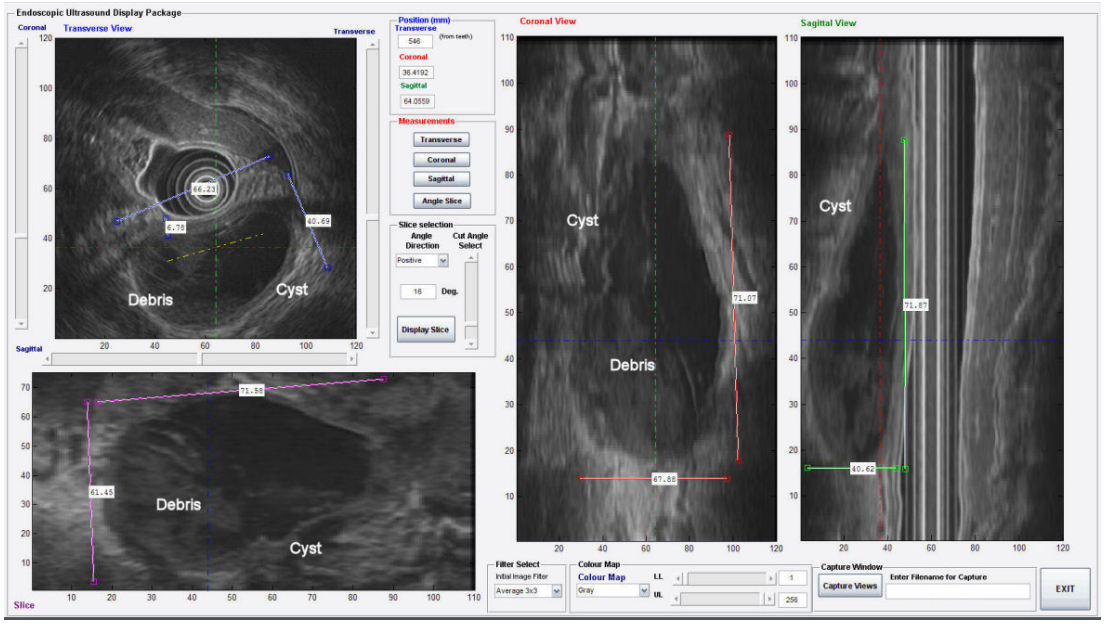

Figure 5.8 - Large pancreatic Pseudo-cyst assessed for endoscopic drainage. The pseudocyst had a large area of viscous debris within its walls that would be difficult to remove via this drainage technique. The dimensions of the pseudo-cyst were 70x66x40mm (LxBxH). The minimum distance between the GI cavity and the cyst was 7mm.

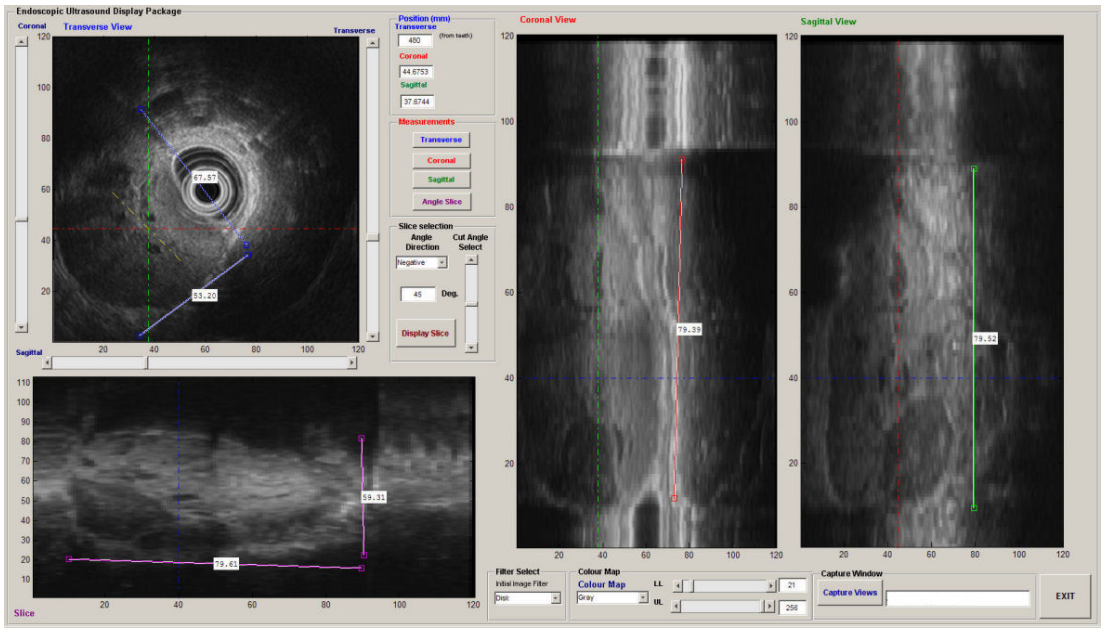

Figure 5.9 - Example of a Complex GIST or leiomyoma with possible malignant features. The size of the object was 80x67x53mm (LxBxH) by the 3D reconstruction.

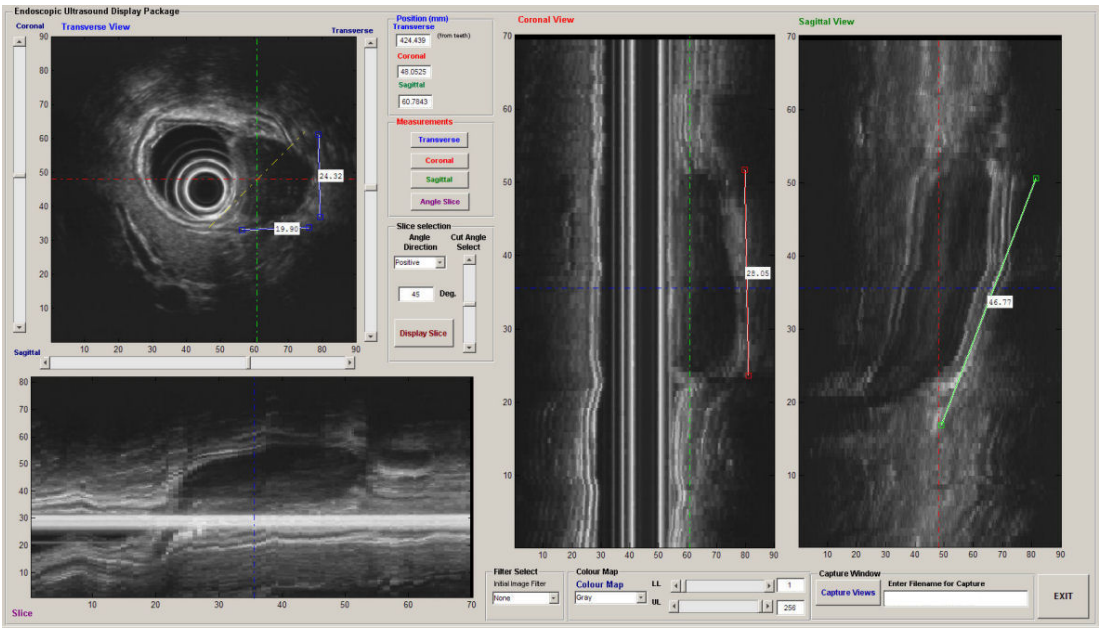

Figure 5.10 – A 3D reconstruction of a GIST / Leiomyoma in the fundus of the stomach. The dimensions of the GIST were 47x24x20mm (LxBxH) and arose from the 4th layer of the stomach wall.

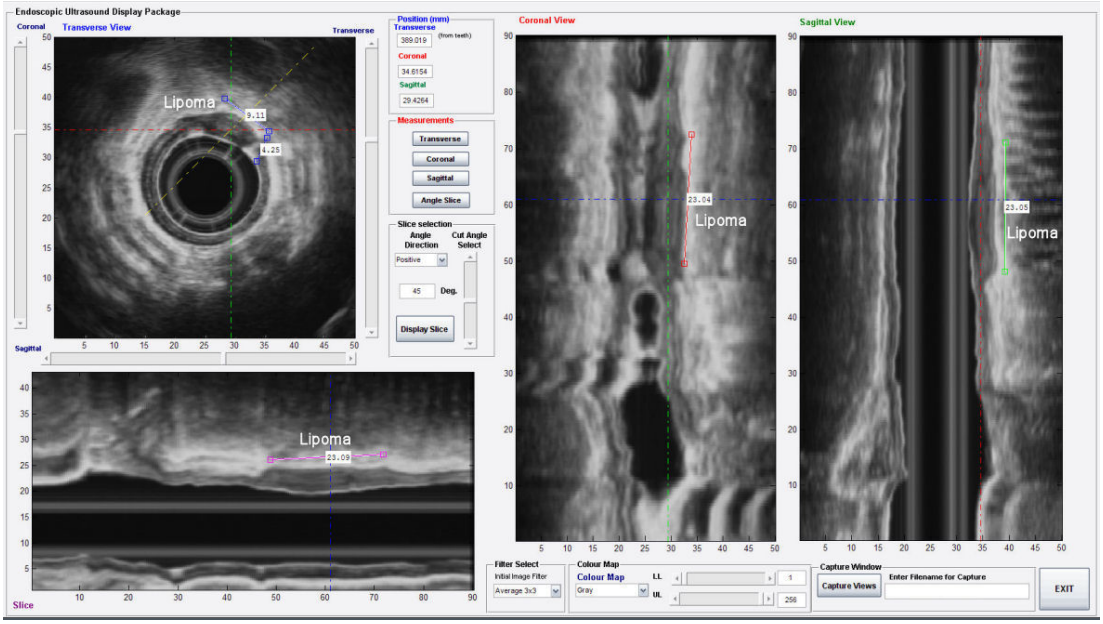

Figure 5.11 – A 3D reconstruction of a lipoma arising from the 3rd layer of the oesophageal wall. The dimensions of the lipoma were 23x9x4.3mm on the 3D reconstruction (LxBxH).

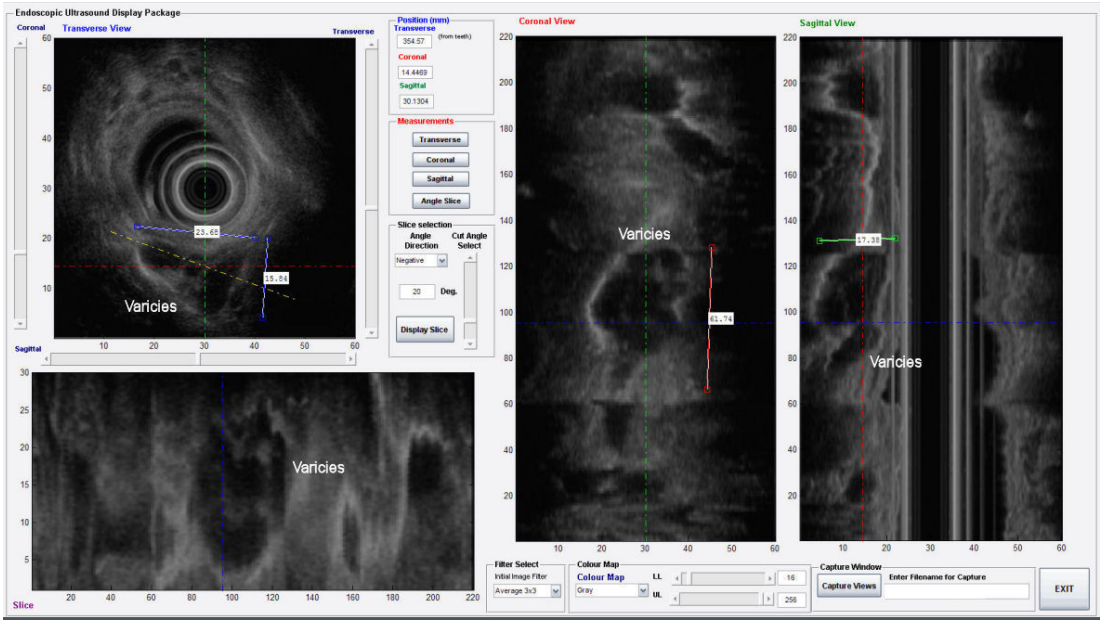

Figure 5.12 – A 3D reconstruction of varicies within the oesophagus. The vascular area measured 62x24x17mm (LxBxH).

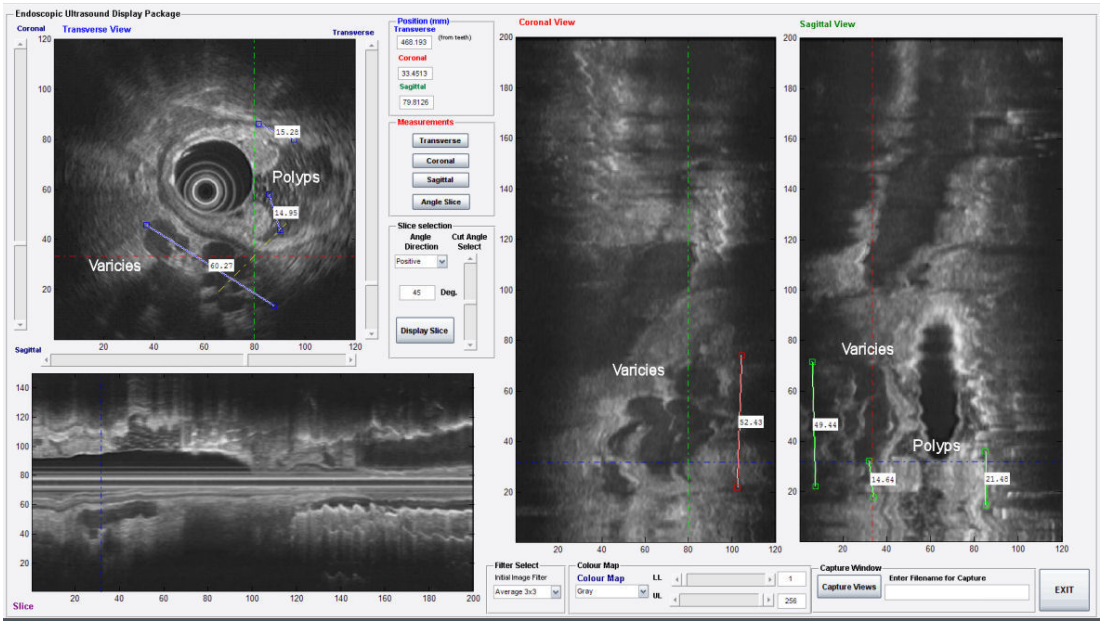

Figure 5.13 - Example of multiple pathology including Portal Hypertension and polyps within the stomach. There was a large vascular area of 52x60mm (LxB) adjacent to a number of polyps, the largest of which were 21x15x15mm (LxBxH) and 14.6x15x14mm (LxBxH).

5.4.3. Discussion

EUS is used extensively in the diagnosis of GI disorders that cannot be diagnosed via standard endoscopic examination and biopsies. Pathology that is below the mucosa cannot be sampled by biopsies. Often, all that is seen under direct vision is an unexplained bulge in the anatomy that cannot be explained. Therefore, the only way to ascertain the presence of the disorder is by imaging via endoscopic ultrasound. Often these cases are investigated to exclude the presence of cancer. Unlike cancer staging, these cases are often investigated on an individual basis and are dependent on the questions being asked by the referring physician. On occasion, it is necessary to re-examine the patient after a period of time to ensure that the abnormal pathology has not gained malignant characteristics.

Three-dimensional EUS was able to provide detailed examination of the pathology without prolonging the procedure time. The study of benign GISTs by 3D-EUS allowed the clinician to visualise the GIST and measure perform dimensions and volume measurements. Therefore, three-dimensional EUS provided an accurate method for monitoring the progression of the disease or any applied treatment. The 3D reconstruction of variceal networks (figures 5.12 and 13) can allow the clinician to target treatments, such as banding or thrombin injection, and allow for the monitoring of there effectiveness.

The occasion can arise when the endoscopist has been asked to provide colleagues with information that will affect the subsequent treatment of these cases (e.g. endoscopic drainage of a cyst (figure5.7)) where a detailed examination of the surrounding and underlying anatomy is imperative. Three-dimensional EUS allowed the endoscopist to perform this examination without causing the patient further discomfort and accurately measure the distance between the GI tract and the cyst to locate the optimal point.

Chapter 6 - Discussion & Conclusions

6.1. Discussion

Conventional EUS is a well established technique for the investigation of abnormal conditions within the upper GI tract (ASGE Standards of Practice Committee 2007). However, it is operator dependent (Bergele & Giovannini 2004, Lennon & Penman 2007) and is affected by artefacts (Hwang and Kimmey, 2006) and its primary use is the staging of GI malignancies. The acquisition of accurate TNM staging is clinically important as it influences the treatment decision and predicts outcome (Harewood & Kumar 2004). The endoscopist is often faced with additional challenges that can compromise the results. EUS has been shown to be superior to CT scanning in the pre-therapeutic loco regional staging of oesophageal cancer (Lowe et al. 2005, Sandhu & Bhuntani 2002), particularly in early (T1) oesophageal cancer and in cases where radiotherapy is used for treatment (Thomas et al. 2004, Yasuda et al. 2005). The examination can be lengthy, lasting between 20 to 60 minutes, and is one of the most difficult procedures performed by the endoscopist (ASGE Standards of Practice Committee 2007).

To reduce the possibilities of missing clinically relevant data and obtain accurate position, distance and volume measurements, three-dimensional EUS techniques were investigated. It was also hypothesised that three-dimensional EUS might be able to reduce operator dependency and increase diagnostic information; by allowing the user to observe objects in three dimensions, provide accurate volume estimation for planning and monitoring of chemo-radiotherapy, and accurate xyz measurements to facilitate tumour treatment.

To truly compare imaging modalities it would be necessary to compare the accuracies of tumour limits and the incidence of tumour re-occurrence. It has been observed that significant differences in the positioning and dimensions of the tumour can be reported with EUS and CT. Where CT defined a shorter segment of tumour compared with EUS (Thomas et al. 2004).

The commercial 3D-EUS system currently available included the Olympus dual planner EUS mini-probe catheter and 3D display package. However, mini-probes have limited penetration (2 - 4 cm, depending on frequency) (Liu et al. 2000, Stergiou et al. 2003, Wu et al. 2003, Okamura et al. 1999), a maximum travel distance of 4cm and reduced accuracy with increasing depth (Okamura et al. 1999). A 3D rendering package included in the Hitachi scanner and used in conjunction with echoendoscopes could be used to produce volumes. However, no positional information was reported to be used with this system (Giovannini 2008, Kawashima et al. 2006). A number of research groups

have been developing 3D-EUS using different EUS equipment and various techniques. Molin et al. (1998, 1998, and 1999) used a computer controlled mechanical pullback system with radial echoendoscopes and mini-probes. This device was capable of moving the echoendoscope / probe in 0.1 – 0.2mm steps (Gilja 2007) and can include ECG gating. However, problems using this system could be the control of the balloon which relies on tactile feel and small adjustments by the endoscopist for safe navigation through the tumour, and locational accuracy will decrease in spacious organs (e.g. stomach) where tip tracking would be required.

The preliminary study by Kallimanis et al. (1995) used a 'stabilised' withdrawal of the radial echoendoscope. They highlighted various artefacts that were also observed during this study, including the ring artefact, physiological artefacts (e.g. peristalsis, circulatory pulsation, and breathing), variation in the pullback speed and navigation through stenotic regions. The main advantage of the radial systems was that they, theoretically, had an unlimited field of view.

Three-dimensional EUS systems have been designed around the linear echoendoscope and electromagnetic position sensor attached to the handle of the scope (Sumiyama et al. 2002, 2003, and Fritscher-Ravens et al. 2005). Instead of withdrawal, the transducer is rotated. Very few studies have been published that document any accuracies of dimensional or volume measurements (Sumiyama et al. 2003) and clinical trials with the linear system (Sumiyama et al. 2002, 2003, and Fritscher-Ravens et al. 2005). The limitations stated by these systems include the lack of tip orientational data and limited field of view (Fritscher-Ravens et al. 2005).

The prototype system was used to identify key requirements to develop an accurate and practical 3D-EUS system. The core components of this system was a video capture card, video and image processing software, and the custom 3D reconstruction and analysis software (3DScan.exe). It was assumed that the echoendoscope would be withdrawn at a constant speed and the start and end points were known, but could not be guaranteed, especially in clinical cases of advanced tumours where stenotic regions would have to be navigated (Kallimanis et al. 1995). This was simulated in phantoms, generating dimensional errors from 2.2 to 51%, and was dependent on the size of the object. In the phantom studies used to investigate the endoscopists estimation of length and comparison with 3D-EUS, it was found that 3D-EUS reduced the average error by 3.6 times in the z dimension from 8% to 2.2%, and the maximum error of 23%, reduced to 3.7% using 3D-EUS. The volume measurement results were found to be dependent on the precision of definition of individual areas, the sampling of the volume and the accuracy of the positional information. However, if a relatively constant speed was maintained during the withdrawal, the accuracies were significantly improved over conventional EUS. Physiological artefacts were also observed and were predominately due to the circulatory system.

After the evaluation of the prototype 3D-EUS system, a number of deficiencies were identified and led to the development of the second version of the 3D-EUS system. These were:

- The inability to integrate accurate positional information into the volume reconstruction and no facility to include positional information within the 3DScan application;
- To visualise long volumes within the S-view application, it was necessary to zoom out, reducing the ability to identify structures. Also the zoom function focused into the centre of the volume making it impossible to study, the periphery of the volume;
- It was difficult to define the location of each visualised frame in the S-view application;
- A number of steps were required to generate the 3D dataset;
- It was not possible to synchronise the capture of the video clip and the simultaneous acquisition of positional information.

The second version of the 3D-EUS system was designed to try and rectify these deficiencies and provide the endoscopist with an accurate clinical system. Previously developed research on 3D-EUS systems, which were based on echoendoscopes, used a variety of techniques to monitor the position, and included mechanical automated pullback, optical tape and magnetic positional sensors (Molin et al. 1999, Koizumi et al. 2002, Sumiyama et al. 2003). Each positional monitoring technique had advantages and disadvantages, however to develop clinically useful and accurate 3D-EUS systems it was necessary to incorporate positional monitoring so the endoscopist would maintain control over the procedure ensuring patient safety and optimal views could be acquired. One of the constraints of the project was to develop a 3D-EUS technique that could be used clinically and as the equipment was all in clinical use; it was not possible to modify them in any way.

Positional measurement techniques were investigated; optical tracking was eliminated at the start of the project as it required a clear field of view to monitor the position. This could not be guaranteed during a clinical examination due to the manipulation required for the use of the echoendoscope and the number of staff that surround the patient. The flock of birds (Ascension) electromagnetic position sensors were capable of accuracies of 1.312mm (Rousseau & Barillot 2002). The transducers of newer electromagnetic positional systems (e.g. Ascension Micro-Bird) have decreased in size and could lead to the acquisition of tip positional data. The final positional system investigated was a positional digitising arm that provided accurate positional information (e.g. accuracy of 0.23mm RMS) that could be related to the location of the transducer by creating a fixed point on the insertion tube of the echoendoscope. These systems have a fixed measurement field and could hinder the scanning of structure due to arm orientation (Rousseau & Barillot 2002). Out of the four positional trackers investigated, the positional digitising arm was chosen as the most suitable positional monitoring system for the 3D-EUS V2 technique. However, the only way to provide true tip position and orientation data was the newest electromagnetic position sensor.

To assess accuracy of the positional arm a small calibration phantom was manufactured that consisted 3 prongs protruding from a central point, at 90º to each another (e.g. X, Y and Z axis). On the prongs, three holes were drilled at 1, 5 and 10cm. The arm could obtain accurate positional readings of each of these holes with a typical error of 0.3mm, and a maximum error in the location of 0.5mm.

The 3D-EUS V2 system consisted of an image capture card, the Microscribe G2X positional digitising arm, the IC3D control, image and positional capture software package, and the 3D EUS reconstruction and analysis toolbox for Matlab. The IC3D package was written specifically for this project, to control the system and simultaneously capture images and positional data. Matlab was chosen to develop the toolbox as it was a powerful development environment that had a significant number of mathematical, signal and image processing functions that could be used in the 3D-EUS toolbox design.

Reconstructions of the phantom were performed with basic position, 1-axial and 3-axial positional information (e.g. z direction only and x, y and z directions combined, respectively), and at different speeds of echoendoscope withdrawal. Two objects were chosen to monitor the accuracy and errors of the reconstruction. One object was the ‘tumour’, close to the centre of the phantom, and the ‘aorta’ that ran the length of the phantom. A pullback was performed to obtain the data necessary to reconstruct the volume. As was expected basic positional information gave the greatest differences in measured dimensions, with single axial positional information, the errors decreased in the ‘aorta’ and ‘tumour’ measurements. With the inclusion of three-axial positional information, the errors in the ‘aorta’ and ‘tumour’ measurements reduced further. The majority of the maximum errors were obtained at the fastest pullback speed (2.68cm/s) and hence the lowest resolution. If this pullback was omitted, the maximum errors for the ‘aorta’ and ‘tumour’ reduced to 11.45% and 5.28% respectively for single axial data and 2.35% and 1.05% respectively for three-axial data.

A number of dimensional and volume comparative tests were performed to determine the accuracy of conventional EUS and the 3D-EUS V2 system and the effects of the inclusion of positional information. Careful measurements on the EUS phantom, using conventional EUS methodology, on various structures within the mark 3 phantom resulted in an average error of 5.1% between the 2 observers. Identical measurements performed on a volume that had been corrected with positional information resulted in an average error of 1.5%. These errors were obtained from the phantom, where the embedded objects had well demarcated borders that could be clearly identified and measured. The measurement errors would be expected to increase on clinical data as the shapes could be far more complex and the borders less clearly defined. The only phantom study reported, used a 3D-EUS linear system for dimensional measurements had an average error of 2.71% (Sumiyama et al. 2003). Most other studies have been clinical or tissue model based studies.

To investigate the accuracy of the volume measurements, the speed of the pullback, position information and volume slice thickness were varied. The measurements were performed on two structures (e.g. pseudo tumour and node) of different volumes (48.93ml and 5.1ml). The average absolute errors, for all conditions, using basic positional information for the pseudo tumour and node was 15.56 ± 10.02 % and 18.42 ± 11.94% respectively (mean ± SD). The maximum overestimated and underestimated errors were 26.97 % and 19.09% respectively, for the tumour, and 23.3% and 38.16% respectively, for the node. Applying full positional information, the absolute errors reduced, for the pseudo tumour and node, to 1.23 ± 0.77 % and 4.03 ± 1.31% respectively (mean ± SD). The maximum overestimated and underestimated errors were 2.23 % and 1.88% respectively, for the tumour, and 4.09% and 6% respectively, for the node, illustrating that error increased with decreasing volume. At lower pullback speeds, the errors increased with increasing volume sample step size. The application of three-axial positional information and slow pullback speeds ensured that the dimensional measurement errors were below the accepted 5% error level. Similar three-dimensional EUS volume studies using the mini-probe technique, on pseudo tumours of known volumes (0.1ml to 1ml) in tissue models resulted in errors between 0.15 to 12.67% (Vegesna et al. 2006) and 3.8 to 26.6% (Liu et al. 2000). Each study agreed that the average error decreased with increasing volume size. The 3D-EUS system developed by Fried et al. (1997) obtained volume estimate errors between 5 to 10%.

The 3D-EUS volume measurements were based on the sum of all the errors that could occur during an examination. These errors included the calibration of the pullback and measurement systems, the quality of the acquired images, human error in the selection of the volume, the accuracy of the pullback system, the speed of the withdrawal, and the accuracy of the volume measurement of the embedded objects. The phantom was used to obtain the volumes and provided an anatomical scenario where the objects were of known volume and the physiological artefacts, such as respiration, and vascular motion, were excluded. During clinical examinations, the physiological factors and image quality will generate artefacts that will reduce the accuracy of the volume measurements.

The main assumption that allowed for the application of the 3D-EUS system to clinical examinations was that the oesophagus was a straight tube during the withdrawal of the echoendoscope. From CT examination of the upper GI tract, the oesophagus is not a straight tube when at rest (figure 1.3). However, when the echoendoscope is introduced into the oesophagus, inflated with air, and the balloon, situated over the transducer, is inflated to fit the lumen of the oesophagus, the anatomy will be distorted. Theoretically, the oesophagus can be modelled as a flexible tube attached between two fixed points (e.g. the OGJ and the diaphragm, and oral cavity). During the pullback a certain amount of pressure will be asserted on the oesophagus and will straighten at the point of the balloon, to conform to the insertion tube of the echoendoscope.

Three-dimensional EUS was applied to a number of clinical studies. These studies included 16 patients with early oesophageal cancer, 24 patients with advanced oesophageal cancer and 6 benign GI pathology cases. The early oesophageal carcinoma study demonstrated that in these cases 3D-EUS provided accurate and detailed information regarding the location and depth of tumour invasion, the upper and lower limit of the tumour estimating the exact length and the visualisation of the volume and progression of the disease. In all cases CT was unable to visualise the tumour, and in one case conventional EUS was unable to clearly locate the tumour and required the study of the volume data to confirm the location of the disease. The detailed information was valuable for defining target volumes as well as tumour margins in relation to reference anatomical structures such as the aortic arch, subcarinal area or the oesophago-gastric junction in particular for cases treated by radiotherapy.

Accurate staging of advanced cancers of the oesophagus (T3N0/1) is important for the planning of treatment. To accurately determine the stage of the disease and assess any loco regional nodes is necessary, as this will determine if the patient can progress to either surgery or require pre-surgical treatment with radiotherapy or neo-adjuvant chemotherapy. The conventional EUS had under staged the cancer in 8 cases. Six of the 8 cases had a different T staging and 5 of the 8 cases had a different N stage from the pathological staging. The 3D-EUS under staged the tumour stage in 3 cases, of which, 1 case out of the 3 had a lower T stage and 2 cases of the 3 had a lower N stage when compared with the pathological staging from the resected tumour. The application of 3D-EUS to advanced tumour staging may allow for these tumours to be characterised further by the application of percentage lengths of tumour stages. From the retrospective analysis of the histological, conventional EUS and 3D-EUS staging, it was shown that 3D-EUS increased the tumour staging accuracy from 75% to 91.2% and nodal staging from 79.2% to 87.5%, when compared with the gold standard of histological staging. For patient 9, 3D-EUS was also found to be useful in the re-evaluation of cancer pre and post chemo-radiotherapy treatment (figure 5.4). Having the 3D-EUS reconstructions in both cases it was possible to review the cases and assess the effectiveness of the treatment. In this case the tumour did not respond to the treatment and grew between the procedures. Another advantage of 3D-EUS found was the ability to distinguish between segments of tumour (e.g. T1 %, T2 % and T3 %), however, this was preliminary work and no correlation with survival was sought. A larger prospective trial would be required to obtain any correlation. The 3D-EUS system may be able to provide an empirical method to distinguish between early and advanced T3 tumours. Studies of 3D-EUS in rectal (Kim et al. 2002, 2006) and upper GI tumours (Hünerbein et al. 1997, Sabet et al. 2002) have shown similar increases in accuracy. Three-dimensional EUS offered additional information related to nodal involvement, as it was possible to detect a larger number of loco-regional small nodes compared with CT or conventional EUS. Such information can influence management decision, e.g. radiotherapy or surgery in favour of EMR. After the EUS examination has been completed, the endoscopist must answer the question: ‘Have I seen all clinically relevant information to make an informed clinical decision?’ For this study this question could be answered in the positive for 75% of cases, however, in 25% (or 6

patients) in the cohort of 24 patients of histologically proven advanced oesophageal cancer, that answer was incorrect and would have changed the treatment planning.

A number of benign conditions could benefit from the application of 3D-EUS. For example, a 3D reconstruction of the assessment and re-assessment of GISTs would allow for visual, dimensional and volume comparisons to ensure that it had not developed malignant characteristics. These conditions require to be re-assessed after an extended period of time. To have a visual record of these examinations can be of great advantage to the endoscopist, as it would allow them to accurately assess whether the condition had advanced. It can also provide them with empirical data that could be used as references during reassessment of conditions and the planning of treatment. Examples of these include varicies, pre-banding and post banding treatment to see if they had been eradicated, or to provide the volume of a cyst to the surgeons so they can estimate if they have fully drained a cyst.

From the clinical examination of the volumes, there were two levels of information obtained from the 3D-EUS scan; (1) the detailed study of the pathology and 2D measurements, effectively performing an offline conventional examination, which provides more information than a standard EUS and allowed for frame by frame study to confirm clinical diagnosis (e.g. staging); and (2) the quantifiable measurements of length, volume and position of pathological structures that can only be accurately obtained with the inclusion of positional information.

It was difficult to compare the clinical accuracies of conventional and 3D-EUS. There were a number of artefacts and errors observed during both EUS and 3D-EUS examinations. The physiological artefact that was prevalent on the 3D reconstruction was due to circulatory pulsation of the heart and aorta. ECG gating has been successfully applied to the mechanical pullback systems (Molin et al. 1998, Hünerbein et al. 1997) and was found to remove this artefact. However, the value of ECG gating in freehand pullback systems has not been proven. The main difficulty with freehand ECG gating would be that pausing the capture (i.e. as with mechanical pullback) would not pause the pullback and cause a number of frames to be omitted and reduce the accuracy of the reconstruction.

Clinical 3D-EUS and EUS examination artefacts and errors included, poor contact, rotation of the echoendoscope, oblique cutting due to the transducer positioning, scanning of anatomy where it is not straight, stenotic regions where the pullback speed is significantly altered and the variability in image quality. The inclusion of the positional monitoring device allowed for the endoscopist to minimise two of these artefacts. As the endoscopist could slow or stop the withdrawal during the 3D dataset acquisition, contact could be altered as required. This was similar to the navigation of stenotic regions, where the positional arm would be able to correct for the slowing down and ‘pop’ out of the transducer as it would enter and exit the stenosis.

The effects of echoendoscope rotation will cause dislocation within the structures of the volume and may introduce interpretation errors, and was minimised during the acquisition phase by the endoscopist. Oblique cutting of the wall (Hwang & Kimmey, 2006) was minimised by the endoscopist centralising the endoscope controls and allowing the balloon to be used to hold the transducer at right angles to the wall. When deviations in the anatomy caused the transducer to cut at an oblique angle, it was possible to detect these regions on the 3D reconstruction, and was indicated by all the layers becoming thicker. Non-straight anatomical paths (e.g. stomach, duodenum) and the oblique transducer tip could be taken into consideration by the inclusion of tip positional data via a catheter based electromagnetic positional sensor. The biggest uncertainty that is faced by the endoscopist performing the EUS examination was the variability in the ultrasound properties and image quality between patients. Various image filters (e.g. edge enhancements and averaging filters) and manipulation tools (e.g. brightness, contrast and colour map alteration tools) have been included to try and minimise the variability between patients.

The main advantages of the clinical 3D-EUS system include, accurate dimensional and volume measurements; it could be used with any radial echoendoscope; longitudinal tumour extension and invasion of the wall layers could be visualised; locoregional nodes could be accurately assessed and distinguishable between vessels; locoregional oesophageal tumours could be accurately classified; the examination time could be significantly reduced, especially in patients that do not tolerate the echoendoscope; it reduced the complexity of the procedure and operator dependency; increased the anatomical details under investigation and reliably detected smaller objects.

In the development of a EUS phantom, it was demonstrated that it was possible to design and construct a complex acoustic EUS phantom. In addition, by varying the scatterer particle concentration a wide range of materials with different attenuation and backscatter properties could be manufactured without compromising the speed of sound. The techniques developed to manufacture the phantom could be used to construct a wide number of anatomical and pathological anatomical scenarios and for different tasks (e.g. anthropomorphic phantom or simplified structures for QA purposes). The similar TMM comparative study by Browne et al. 2003, using the SAM system, highlighted the acoustic properties of a number of available TMM's. The results of the agar based TMM was in agreement with the results obtained during this study.

The first part of the study concentrated on the characterisation of the acoustic properties for TMM mixtures with decreasing concentrations of scattering and attenuating particles compared to the standard TMM (TCP100) formulation. Each of the ingredients was found to contribute to specific acoustic properties of the TMM (Table 1.2). The water, glycerol and agar produced the speed of sound of 1540m/s. The Al_2O_3 (0.3 and 3μm) contributed predominately to the value of the attenuation coefficient. The SiC particles predominately contributed to the backscatter. The SiC particles were

used to produce a similar ultrasound speckle to liver. The Al_2O_3 (0.3 and 3μm) and SiC particles were used to stabilise and normalise the attenuation coefficient over a wide range of frequencies with the TCP100 recipe.

Using the TMM manufacturing technique described it was possible to generate a tissue mimicking material with the desired properties, detailed in IEC 61685. Altering the particle concentration was found to alter the attenuation and backscatter. The attenuation coefficient detailed in figure 2.5 showed that decreasing the particle concentration from 100%, decreased the attenuation, but also increased the gradient of the plot over the range of frequency. This was attributed to the increasing influence of the frequency response of the agar (TCP0) as the particle concentration reduced. The average values of attenuation, at 7.5, 10 and 12MHz, were singled out to investigate the relationship with increasing particle concentration. The values were averaged, obtaining the mean and standard deviation over that frequency range. It can be seen from figure 2.6 that there is a linear relationship between the attenuation coefficient and particle concentration. The error bars indicate that at higher particle concentrations, the attenuation is consistent over the frequency range. However, as the particle attenuation reduced below TCP50 the effects of the agar on the gradient become noticeable.

With the chosen TMM mixture, it was found that there was a set maximum and minimum value for attenuation and backscatter that could not be exceeded. Reducing the concentration of agar could further reduce the attenuation coefficient and backscatter power. However, this compromised the material's speed of sound and mechanical strength. An alternative agar or gelatine could also be used to lower backscatter power, but this would also alter the acoustic and physical properties. This would be required if it was necessary to simulate fluid filled cysts and other similar pathology.

The ideal backscatter trend (figure 2.7) was plotted with the results obtained from the backscatter measurements. At particle concentrations lower than 10% the scatterer particle concentration (TCP10) effects of the agar contributed to the backscatter power and caused the results to deviate from the ideal trend. In practice, changing the scatterer recipe from TCP10 to TCP50 resulted in the greatest change in the B-mode images of object echolucency due to the log compression of the displayed grey scale image. The backscatter measurements required the averaging of the data from each point of the raster scan for both the reference (TCP100) and the data. The small reflection obtained from the surface of the material, and resultant spectrum of the signal through the material was very small. The signal to noise ratio of the RF data for the backscatter measurements was a maximum of 3:1 on single measurements for the high particle concentration materials. At the lower particle concentrations, the signal could be masked within the noise. The backscatter measurement technique used with the SAM system was not optimal. Using figures 2.6 and 2.7 it was possible to design and manufacture a number of different materials for the phantom with known acoustic properties and to determine the required particle concentration to obtain the desired attenuation or backscatter power. Testing of the

manufactured materials ensured that the mixture and manufacturing processes were consistent. The maximum deviation from the expected attenuation and backscatter values was less than 10% at the lower concentrations of scatterer particles (0% - 15%).

Hyperechoic tissue characteristics were predominately associated with benign lesions or tumours of the third layer, examples include calcified nodes, lipoma and carcinoid tumours. The majority of the pathological structures were found to be increasingly hypoechoic compared with normal tissue (e.g. GIST, varicies, malignant nodes, cancer, and vessels). The tumours were represented by dark, echolucent complex structures of various sizes and nodes by echolucent spheres of various sizes (malignant looking) (TCP0 - TCP20) or different shapes (benign nodes) of various concentrations of scatterer particles (TCP20 - TCP50). Vessels and the aorta were manufactured from TCP0 TMM. A major problem observed during the manufacture of the phantom was the visual variation in the backscatter and was attributed to the particle settling during manufacture. Mixing stirrers were modified and designed to improve stirring efficiency. The majority of the designs (figure A.8 a to c) suffered from particle settling (specifically SiC) below the stirrer shaft. The final paddle (figure A.8 d) was designed to eliminate any central particle settling due to the additional scooping effects at the top and the bottom, and the creation of a more turbulent flow for increased mixing capabilities.

The moulding techniques used in the manufacture of the mark 2 phantom objects was able to construct complex shapes; however, were limited to 3 sided structures with a flat plane and unreliable volume measurements. A new moulding technique was devised for the mark 3 EUS phantom to produce complex anatomical three-dimensional structures. Plasticine was used to create the object masters with similar shapes to anatomical structures. Plaster of Paris was used to create the moulds for the casting of the TMM shapes. The one problem with plaster of Paris was that it is a porous material and would draw out the fluids of the TMM, theoretically changing the acoustic properties. To combat this Marvin Medium (PVA glue) was applied to the surface of the plaster. An unexpected benefit of the use of Marvin Medium was that it became slippery when in contact with the TMM; the objects were easier to remove. Different layer materials were investigated (e.g. latex, polythene and tin foil) at various thicknesses. Polythene (25μm thickness) was chosen as the most desirable material for the layers as it produced a bright layer at all the measurement frequencies and minimal reflection artefact production.

The Mark 2 and 3 phantoms were designed to simulate a simplified anatomy of the oesophagus (wall layers of oesophagus, aorta and vessels) and pathological and diseased structures of the oesophagus (malignant and benign looking nodes, tumour, and thickening). The structures that were embedded into the mark 3 phantom were manufactured with known dimensions (X, Y & Z directions) and volumes. It was observed from the images of the phantom that there was minimal interface reflection due to either perpendicular wall layer reflections or trapped air bubbles. Figure 2.16 and 2.17 illustrate

the images received from the Mark 2 phantom and figure 2.23 and 2.24 shows the Mark 3 phantom. The simplicity or complexity of the contents was varied dependant on the application of the phantom (e.g. a QA phantom had less anatomy mimicking structures).

The examination of the oldest and newest echoendoscopes, using the pipe phantom, allowed for the measurement of various imaging properties, including LCP, dead space, near and far field. From the results it was clear that the GF-UE260 electronic radial echoendoscope was a significant improvement over the GF-UM20 mechanical radial echoendoscope, in dead space, LCP and near and far fields. The significant ring artefact that was visible on all mechanical radial echoendoscopes was minimised in its electronic counterparts. However, the GF-UM20 scope could reliably visualise smaller pipes with both 7.5 and 12 MHz. The reduction in the resolution of the GF-UE260 could be attributed to the manufacture of the wideband transducer. The pipe phantom measurements were based on the sum of all the errors that could occur during measurements. These errors included the setup of the ultrasound systems, the quality of the displayed image, the setup of a constant mid gray scale and speckle image, the variation in the acoustic properties of the TMM, human error in locating the pipes and measurement of the start and stop points of the pipe. Care was taken during the pipe measurements to try and minimise any human errors. A support was used to maintain the transducer position within the rough location of the pipe. The TMM material was manufactured using the protocol set out in section 2.1.1.

From the hydrophone measurements performed on the GF-UM20 and GF-UE260 echoendoscopes, a number of acoustic parameters were calculated. The most noticeable acoustic results were the difference in the expected and actual acoustic working frequency for the mechanical and electronic radial echoendoscopes. The differences for the GF-UM20 were reductions of 6.67% and 20.8% from the expected frequencies of 7.5MHz and 12MHz respectively. Similarly the GF-UE260 had deviations of +10%, -13.3% and -30% from the expected frequencies of 5, 7.5 and 10MHz. These differences could explain the reduced small pipe resolution observed during the comparative pipe phantom measurements, between the electronic and mechanical radial echoendoscopes. However, these were preliminary measurements and to confirm these differences it would be necessary to test all other available echoendoscopes and try to test other manufacturer's equipment. Technical information regarding these devices could not be obtained from the manufacturer to confirm these measurements, and it is unknown what processing will be done, by the scanner, on the received ultrasound pulses. To minimise errors due to the water, the tank and water were prepared 24 hours prior to the measurements, to minimise temperature changes, bubble formation and suitably degassed.

The beam plots were performed to visualise the focal points and the shape of the transmitted beams different frequencies and focal points. However, the sampling rate of the oscilloscope at the required time bases setting, so that the hydrophone pulse trail could be visualised, resulted in the acquisition of

only 2 points per pulse, and it could not be guaranteed that the point would occur at the peak of the pulse. Therefore the shape and duration of the pulse would be subject to under sampling. This would require a higher sampling rated device or capture card to be used to acquire the pulse train at frequencies higher than 50MHz and would allow for the acquisition of the entire waveform. Small deviations or angling in the beam plots were attributed to the program used to rectify any triggering errors that occurred during the acquisition.

The hydrophone measurements were an accumulation of all the errors that could occur during the measurements. These errors included conditions of the water (e.g. temperature changes, bubbles adherent on the surface of the hydrophone, source of the water), distortions due to high amplitude signals, and triggering and sampling rate of the oscilloscope and the setup of the ultrasound systems (Preston 1986, Harris 1988, Martin 1988, and Bacon 1991). This can result in deviations of the average pressures by a few percent. Other stated maximum systematic uncertainties include calibration (±10%), hydrophone electrical loading and hydrophone measurement of the signal (±4%), spatial averaging (±4%), and random uncertainties (±10%) (Preston 1986).

6.2. Conclusions

An accurate freehand three-dimensional endoscopic ultrasound system was developed to be used in conjunction with any radial echoendoscope, for use in the oesophagus. A freehand 3D-EUS system was developed that incorporated a positional arm to monitor the withdrawal of the echoendoscope and allow for the accurate reconstruction of the volume. The evaluation of the 3D-EUS technique on the phantom resulted in accurate dimensional and volume measurements with average dimensional errors of 1.5% and volume measurement errors for small and large objects 4.03% and 1.23% respectively (actual volumes 5.1ml and 48.93ml). The primary use of the developed 3D-EUS system was to aid in the staging of oesophageal cancer. Studies of early and advanced oesophageal tumours have shown that 3D-EUS provided additional and clinically useful information, such as location in relation to anatomical structures, accurate stage of the disease, detection of a greater number of nodes and detecting abnormalities missed during standard EUS. During the comparative study of advanced tumours in a small cohort of patients showed that the staging accuracy increased from 75% with conventional EUS, to 91.2% with 3D-EUS, indicating that 3D-EUS could prove to be an effective tool in staging oesophageal cancer. Three-dimensional endoscopic ultrasound also provided an effective method for recording and documenting the procedure for later review, the study of the progression of the disease with repeat patients, and the application of dimensional and volume measurements to provide an empirical method to assess the effectiveness of the treatment.

The design of the complex EUS phantom allowed for a controlled environment to aid in the development and evaluation of 3D-EUS techniques. Complex irregularly shaped objects were embedded within the phantom with known dimensions and volumes. The techniques developed for the manufacture of the complex objects allowed for a flexible technique that could be used to design a variety of anatomical scenarios.

The study of the imaging properties, via the phantom, including resolution, LCP, dead space, etc. highlighted the advantages and disadvantages of the electronic and mechanical echoendoscopes. The electronic radial had increased penetration and visual field, and reduced ring artefact and dead space. In comparison, the mechanical radial had increased resolution and was able to visualise smaller pipes.

The hydrophone measurements allowed for the characterisation of the transmitted pulse, the calculation of a number of acoustic parameters and the plotting of the beam shape. This was a preliminary study of the oldest and newest echoendoscopes available for this project. The calculated acoustic parameters included the acoustic working frequency, peak pressures, and pulse duration, and allowed for a better understanding of the technology.

6.3. Future Work

To further develop the freehand radial 3D-EUS technique it would be useful to study the effects of physiological signal gating (ECG & respiratory) on the accuracy of the freehand reconstruction and the smoothing of the small discontinuities observed in the coronal and sagittal planes. It would be necessary to study the effects of pausing the image and positional acquisition, during the ECG gating, to ensure that a minimal number of frames would be missed. Ethical approval would be required as it would result in a change to the protocol for standard clinical examination.

It may be possible to obtain tip positional data via the biopsy channel with the advancement of positional measurement technology and the development of catheter based electromagnetic endoscope positional tracking systems (e.g. the E3DI system from Endoscopy UK [1 Mead Lane, Lydney, GL15 5EU, Gloucestershire]). In collaboration with the company, it may be possible to modify the device to interface with the 3D-EUS system to obtain tip locational and orientational data. This will allow the 3D-EUS system to be used accurately within other organs of the GI tract (e.g. stomach, colon) and reduce the imaging errors that may occur due to the tangential scanning. The problem with this technology is that it has accuracy rating of 1 to 2mm RMS; therefore it will be necessary to combine the existing 3D-EUS positional tracking technique with the catheter based system to maintain the accuracy.

A prospective clinical trial that will study the application of 3D-EUS in the staging of oesophageal cancer is required. The trial would consist of a blinded study that would compare staging, location, dimensional and volume measurements of the disease using different imaging modalities (e.g. MDCT, or CT). The results will be compared to investigate the differences the results of the modalities. This would expand of the preliminary work performed by Thomas et al. (2004).

References

AIUM Standard. AIUM Technical Standards Committee 1990. American Institute of Ultrasound in Medicine. Standard methods for measuring performance of pulse-echo ultrasound imaging equipment. AIUM Standard (1990).

AIUM/ NEMA. Standard for Real Time Display of Thermal and Mechanical Indices of Diagnostic Ultrasound Equipment, Laurel, M D,. Amer. Inst. Ultrasound Med, 63 pp , 1992

Akhnak M, Martinez O, Ullate L G, Montero de Espinosa F; 64 Elements two-dimensional piezoelectric array for 3D imaging. Ultrasonics, Volume 40, Issues 1-8, May 2002, Pages 139-143

Andreassen A H, Ellingsen I, Nesje LB, Gravdal K, Ødegaard S; 3-D endobronchial ultrasonography—A post mortem study. Ultrasound in Medicine & Biology, Volume 31, Issue 4, Pages 473-476, April 2005

ASGE Standards of Practice Committee, Gan SI, Rajan E, Adler D G, Baron T H, Anderson M A, Cash B D, Davila R E, Dominitz J A, Harrison III M E, Ikenberry S O, Lichtenstein D, Qureshi W, Shen B, Zuckerman M, Fanelli R D, Lee K K, Van Guilder T; Role of EUS. Gastrointestinal Endoscopy, Volume 66, Issue 3, Pages 425-434, September 2007.

ASGE technology committee; Wong Kee Song L M, Adler D G, Conway J D, Diehl D L, Farraye F A, Kantsevoy S V, Kwon R, Mamula P, Rodriguez B, Shah R J, Tierney W M; Narrow band imaging and multiband imaging. Gastrointestinal Endoscopy, volume 67, issue 4, pages 581-589 , April 2008.

Bamber J C; Attenuation and Absorption; Hill C. R., Bamber J. C., Haar G. (Eds) Physical Principles of Medical Ultrasonics; John Wiley and Sons, p93-156, 2004

Barawi M, Gress F; EUS-guided fine-needle aspiration in the mediastinum. Gastrointestinal Endoscopy, Volume 52, Issue 6, Supplement 1, Pages S12-S17, December 2000,

Bell G D, Rowland R S, Rutter M, Abu-Sada M, Dogramadzi S and Allen C; Colonoscopy aided by magnetic 3D imaging: assessing the routine use of a stiffening sigmoid overtube to speed up the procedure Medical and Biological Engineering and Computing Volume 37, Number 1 / January, pp 605-611, 1999

Bergele C, Giovannini M; EUS and Common bile duct stones. Annals of Gastroenterology 17(3):246-252, 2004,

Berger A C, Walter J S; Non-invasive staging of esophageal carcinoma Journal of Surgical Research 2004;117:127-133

Blackshaw G, Lewis W G, Hopper A N, Morgan M A, Al-Khyatt W, Edwards P, Roberts S A; Prospective comparison of endosonography, computed tomography, and histopathological stage of junctional oesophagogastric cancer. Clinical Radiology, Volume 63, Issue 10, Pages 1092-1098, October 2008

Bladen J S, Anderson A P, Bell G D., Rameh B, Evans B, Heatley D J T; Non-radiological technique for three-dimensional imaging of endoscopes. Lancet. Volume 341, Issue 8847, Pages 719-722, 20 March 1993.

Blechinger J C, Madsen E L, Frank G R; Tissue mimicking gelatine-agar gels for use in magnetic resonance imaging phantoms. Med. Phys. 15: 629-636. 1988;

Browne J E, Ramnarine K V, Watson A J, Hoskins P R; Assessment of the acoustic properties of common tissue-mimicking test phantoms Ultrasound in Medicine & Biology Volume 29, Issue 7, Pages 1053-1060, July 2003.

Brugge W R, Lee M J, Carey R J, Mathisen D J; Endoscopic ultrasound staging criteria for esophageal cancer Gastrointest Endosc;45:147-52. 1997

Brunette J, Mongrain R, Cloutier G, Bertrand M, Bertrand O F, Tardif J-C; A novel realistic three-layer phantom for intravascular ultrasound imaging. International Journal of Cardiac Imaging; 17(5): 371-381., 2001

Buchner A M, Wallace M D; Future expectations in digestive endoscopy: Competition with other novel imaging techniques. Best Practice & Research Clinical Gastroenterology, Volume 22, Issue 5, Pages 971-987, October 2008

Burlew M M, Madsen E L, Zagzebski J A, Banjavic R A, Sum S W; A New Ultrasound Tissue Equivalent Material. Radiology; 134: 517-520, 1980.

Bush N L and Hill C R; Gelatine-alginate complex gel: a new acoustically tissue-equivalent material. Ultrasound Med. Biol.; 9: 479-484. 1983

Buscarini E, Buscarini L; The role of endosonography in the diagnosis of choledocholithiasis. European Journal of Ultrasound Volume 10, Issues 2-3, Pages 117-125, 1999

Cho E, Mochizuki N, Ashihara T, Yaduda K, Nakajima M; Three-dimensional endoscopic ultrasonography (3D-EUS) in the diagnosis of colorectal diseases. Gastrointestinal Endoscopy, Volume 45, Issue 4, Page AB27, April 1997

Chu K C and Rutt B K; Polyvinyl alcohol cryogel: An ideal phantom material for MR studies of arterial flow and elasticity. Magnetic Resonance Medicine.; 37: 314-319. 1997

Culliford A N, Lightdale C J, Stavropoulos S N, Stevens P D; A 360º Radial Electronic Echoendoscope: A New Technology in Endoscopic Ultrasound (EUS). Gastrointestinal Endoscopy Volume 59, No. 5, P220, 2004

Curvers W L, Kiesslich R, Bergman J J G H M; Novel imaging modalities in the detection of oesophageal neoplasia Best Practice & Research Clinical Gastroenterology, Volume 22, Issue 4Pages 687-720, August 2008

Cysewska-Sobusiak, A, Skrzywanek P, Sowier, A; Utilization of Miniprobes in Modern Endoscopic Ultrasonography. Sensors Journal, IEEE. Volume 6, Issue 5, Page(s):1323 - 1330 Oct. 2006

Darlas Y & Couard R; Physical Principles: Endosonograpic Appearance of the Normal Gastrointestinal Tract Wall; Dancygier H., Lightdale C. J., Brüggemann A., Endosonography in Gastroenterology: Principles, Techniques, Findings. Thieme, 1999

Delaney P, Thomas S, McLaren W; Development and Current Technological Status of Confocal Laser Endomicroscopy Kiesslich, R; Galle, P R; Neurath, M F (Eds.); Atlas of Endomicroscopy Springer pages 17-23, 2008

Dineley J, Meagher S, Poepping T L, McDicken W N, Hoskins PR; Design and characterisation of a wall motion phantom. Ultrasound in Medicine & Biology, Volume 32, Issue 9, Pages 1349-1357, September 2006,

Duck F A; Physical Properties of Tissue 1990

Erickson R A; Linear Array Endosonography: Normal EUS Anatomy. Frank Gress, Ishan Bhattacharya Endoscopic Ultrasonography. Blackwell Publishing, 58 – 69, 2000.

ESGE - European Society of Gastrointestinal Endoscopy Guidelines. Working party: Caletti G, Deviere J, Fockens P, Lees W R, Mortensen B, Odegaard S, Rösch T, Souquet J C, Vilmann P; Endoscopic Ultrasonography Part I Technique and Upper Gastrointestinal Tract. 1996.

Fried R, Beglinger C, Fischer H, Stalder G; Three-dimensional endoscopic ultrasonography: Evaluation of a desktop-based system. Gastrointestinal Endoscopy, Volume 45, Issue 4, Page AB172, April 1997

Fusaroli P, Caletti G; Endoscopic ultrasonography. Endoscopy.; 35(2): 127-135. 2003

Fujinon Corporation, F.I.C.E. Fujinon Intelligent Colour Enhancement – catalogue / brochure. 2007

Fukuda M; Endoluminal gastroenterology. Ultrasound in Medicine & Biology, Volume 26, Supplement 1, Pages S79-S81, May 2000

Fritscher-Ravens A; Endoscopic ultrasound evaluation in the diagnosis and staging of lung cancer. Lung Cancer, Volume 41, Issue 3, Pages 259-267, September 2003

Gatzoulis L, Ramnarine K V, Pye S D, Anderson T, Newby D E and McDicken W N; Doppler colour flow imaging and flow quantification with a novel forward-viewing intravascular ultrasound system. Ultrasound in Medicine & Biology.; 29, 1: 53-64. 2003

Gee A, Prager R, Treece G, Berman L; Engineering a freehand 3D ultrasound system; Pattern Recognition Letters, Volume 24, Issues 4-5, Pages 757-777, February 2003

Gilja O H, Detmer P R, Jong J M, Leotta D F, Li X–N, Beach K W, Martin R, And Strandness Jr D E; Intragastric Distribution and Gastric Emptying Assessed by Three-Dimensional Ultrasonography, Gastroenterology;113:38–49, 1997

Gilja O H; Three-dimensional ultrasound of the gastrointestinal tract Maconi, G.;. Bianchi Porro, G. (Eds.) Ultrasound of the Gastrointestinal Tract. Springer, pp 199-211, 2007.

Giovannini M; Endosonography: New Developments in 2008. DDW session handout SP267, June 2008.

Giovannini M; Ultrasound-guided endoscopic surgery. Best Practice & Research Clinical Gastroenterology, Volume 18, Issue 1, Pages 183-200, February 2004

Gossner L; Potential contribution of novel imaging modalities in non-erosive reflux disease. Best Practice & Research Clinical Gastroenterology, Volume 22, Issue 4, Pages 617-624, August 2008

Greene F L, Compton C C, Fritz A G, Shah J, Winchester D P (Eds.); Chapter 9. Esophagus. AJCC Cancer Staging Atlas, Springer, p 77- 88, 2006.

Harewood G C, Kumar K S; Assessment of clinical impact of endoscopic ultrasound on oesophageal cancer. Journal of Gastroenterology and hepatology;19:433-439, 2004

Harris G R; Hydrophone measurements in diagnostic ultrasound fields; Ultrasonics, Ferroelectrics and Frequency Control, IEEE Transactions on; Volume 35, Issue 2Page(s):87 - 101, March 1988

Hashimoto S, Hirooka Y, Itoh A, Itoh T, Kawashima H, Hara K, Kanamori A, Ohmiya N, Niwa Y, Goto H; Virtual Pancreatoscopy Using Three-dimensional Endoscopic Ultrasonography. Gastrointestinal Endoscopy Volume 59, No. 5, P220, 2004

Hawes R H; New Devices for EUS Study. Digestive Endoscopy. Volume 16, Issue s2, Pages: S249-S250, Date: November 2004

Hawes R H; Electronic Radial Ultrasound Endoscope. Digestive Endoscopy. Volume 16, Issue s2, Pages: S223-S224, Date: November 2004

Hawes R H; New approaches in interventional EUS. Gastrointestinal Endoscopy, Volume 56, Issue 4, Supplement 1, Pages S62-S65, October 2002

Hill C R; Detection and Measurements of Acoustic Fields; Hill C. R., Bamber J. C., Haar G. (Eds) Physical Principles of Medical Ultrasonics; John Wiley and Sons, p70-91, 2004

Hoskins P R and Ramnarine K V; Doppler Test Devices. In: Doppler Ultrasound: Principles, Instrumentation and signal processing. Pp 382-404. 2nd Edition. Evans D H and McDicken W N. Wiley, Chichester, UK, 1999.

Hünerbein M, Ghadimi B M, Gretschel S and Schlag P M; Three-dimensional endoluminal ultrasound: a new method for the evaluation of gastrointestinal tumors. Abdominal Imaging, Volume 24, Number 5 / September, 1999

Hünerbein M, Gretschel S, Ghadimi B M and Schlag P M; Three-dimensional endoscopic ultrasound of the esophagus Preliminary experience Surgical Endoscopy, Volume 11, Number 10 / October, 1997

Hurrell A; Voltage to pressure conversion: are you getting `phased' by the problem?, J. Phys.: Conf. Ser. Vol. 1, p57-62, 2004.

Hwang J H and Kimmey M B; Principles of Ultrasound. Robert H. Hawes Paul Fockens (Ed.) Endosonography, Saunders pp 3 – 15, 2006.

Inglis S, Ramnarine K V, Plevris J N, and McDicken W N; An Anthropomorphic Tissue-Mimicking Phantom of the Oesophagus for Endoscopic Ultrasound. Ultrasound in Med. & Biol., Vol. 32, No. 2, pp. 249–259, 2006

International Electrotechnical Commission; Ultrasonics Flow measurement systems- flow test object. IEC 61685 standard, 2001.

International Electrotechnical Commission; Ultrasonics – Real-time pulse-echo systems – Guide for test procedures to determine performance specifications. IEC 61390 standard, 1997.

Irisawa A, Shibukawa G, Obara K, Saito A, Takagi T, Shishido H, Odajima H, Abe M, Sugino T, Suzuki T, Kasukawa R, Sato Y; Collateral vessels around the oesophageal wall in patients with portal hypertension: comparison of EUS imaging and microscopic findings at autopsy.: Gastrointest. Endosc.; 56(2): 249-253. 2002

Irisawa A, Obara K, Sato Y, Saito A, Takiguchi F, Shishido H, Sakamoto H, Kasukawa R; EUS analysis of collateral veins inside and outside the oesophageal wall in portal hypertension. Gastrointestinal Endoscopy.; 50(3): 374-380. 1999

Kallimanis G, Garra B S, Tio T L, Krasner B, Al-Kawas F H, Fleischer D E, Zeman R K, Nguyen C C, Benjamin S B; The feasibility of three-dimensional endoscopic ultrasonography: A preliminary report, Gastrointestinal Endoscopy, Volume 41, Issue 3, Pages 235-239, March 1995

Kameyama H, Niwa Y, Arisawa T, Goto H, Hayakawa T; Endoscopic ultrasonography in the diagnosis of submucosal lesions of the large intestine, Gastrointestinal Endoscopy, Volume 46, Issue 5, Pages 406-411, November 1997

Kawashima H, Hirooka Y, Itoh A, Hara K, Kanamori A, Uchida H, Goto J, Nonogaki K, Matsumoto Y, Ohmiya N, Niwa Y, and Goto H; Progress of endoscopic ultrasonography and intraductal ultrasonography in the diagnosis of malignant biliary diseases. J Hepatobiliary Pancreat Surg 13: 69–74. 2006

Kelly S, Harris K M, Berry E, Hutton J, Roderick P, Cullingworth J, Gathercole L, Smith M A; A systematic review of the staging performance of endoscopic ultrasound in gastro-oesophageal carcinoma Gut;49:534–539, 2001

Kienle P, Buhl K, Kuntz C, Düx M, Hartmann C, Axel B, Herfarth C, Lehnert T; Prospective Comparison of Endoscopy, Endsosonography and Computed Tomography for Staging of Tumours of the Oesophagus and Gastric Cardia. Digestion; 66:230-236, 2002

Kiesslich R, Neurath M F; Endoscopic detection of early lower gastrointestinal cancer. Best Practice & Research Clinical Gastroenterology, Volume 19, Issue 6, Pages 941-961, December 2005

Kim J C, Kim H C, Yu C S, Han K R, Kim J R, Lee K H, Jang S J, Lee S S, Ha H K; Efficacy of 3-dimensional endorectal ultrasonography compared with conventional ultrasonography and computed tomography in preoperative rectal cancer staging. The American Journal of Surgery, Volume 192, Issue 1, Pages 89-97, July 2006

Kim J C, Cho Y K, Kim S Y, Park S K, and Lee M G; Comparative study of three-dimensional and conventional endorectal ultrasonography used in rectal cancer staging. Surgical Endoscopy, Volume 16, Number 9 / September, 2002

Koizumi N, Sumiyama K, Suzuki N, Hattori A, Tajiri H and Uchiyama A; Development of Three-Dimensional Endoscopic Ultrasound System with Optical Tracking. Dohi T. Kikinis R. (Eds) Medical Image Computing and Computer-Assisted Intervention pp60-65 2002.

Kwee RM & Kwee TC; Imaging in local staging of gastric cancer: a systematic review. J. Clinical Oncology 25; 15 2107-2116. 2007.

Lennon A M and Penman I D; Endoscopic ultrasound in cancer staging. British Medical Bulletin; 84: 81–98, 2007

Liechty B C, Webb B W; The use of plasticine as an analog to explore material flow in friction stir welding. Journal of Materials Processing Technology. Vol. 184, Issues 1-3, Pages 240-250, 12 April 2007

Lightdale C J, Kulkarni K G; Role of endoscopic ultrasonography in the staging and follow-up of oesophageal cancer. J Clin Oncol; 23: 4483-4489, 2005

Lowe V J, Booya F, Fletcher J G, Hathan M et. al.; Comparison of Positron Emmision Tomography, Computed Tomography, and Endoscopic Ultrasound in the initial staging of patients with esophageal cancer. Mol. Imaging Biol. 7; 422-435. 2005

Liu J-B, Miller L S, Chung C Y, Overton D A, Sheera M, Forsberg F, Goldberg B B; Validation of volume measurements in esophageal pseudotumors using 3D endoluminal ultrasound. Ultrasound in Medicine & Biology, Volume 26, Issue 5, Pages 735-741, June 2000

Madsen E L, Zagzebski J A, Banjavie R A, Jutila R E; Tissue mimicking materials for ultrasound phantoms. Med. Phys.; 5: 391-394. 1978

Madsen E L, Zagzebski J A, Frank G R; Oil-in-gelatine dispersions for use as ultrasonically tissue mimicking materials. Ultrasound Med. Biol.; 8: 277-287. 1982

Madsen E L; Ultrasonically soft tissue mimicking materials and phantoms. In Greenleaf JF (ed): Tissue Characterisation with Ultrasound. Volume 1, Methods. Boca Raton, Florida, CRC Press, 165-181 , 1986

Martin, K; Measurement of acoustic output parameters from medical ultrasound devices with an RF power meter system; Ultrasonics, Ferroelectrics and Frequency Control, IEEE Transactions on; Volume 35, Issue 2Page(s):140 - 145, March 1988

Martin K, Fernandez R; A thermal beam-shape phantom for ultrasound physiotherapy transducers; Ultrasound in Medicine & Biology, Volume 23, Issue 8, Pages 1267-1274, 1997

Martin K and Ramnarine K V; Physics; Hoskins PR, Thrush A, Martin K, and Whittingam TA (Eds); Diagnostic Ultrasound: Physics and Equipment p 9 – 22; 2003

Martin K; Properties, Limitations and artefacts of B-mode imaging; Hoskins PR, Thrush A, Martin K, and Whittingam TA (Eds); Diagnostic Ultrasound: Physics and Equipment p 63 – 74; 2003

Martin K and Spinks D; Measurements of the Speed of Sound in Ethanol/Water Mixtures. Ultrasound Med. Biol; 2: 289-291. 2001

May A, Gunter E, Roth F, Gossner L, Stolte M, Vieth M, Ell C; Accuracy of staging in early oesophageal cancer using high resolution endoscopy and high resolution endosonography: a comparative, prospective and blinded trial. Gut;53:634-640, 2004

McDicken W N; Diagnostic Ultrasonics: Principles and Use of Instruments 1st Edition, Crosby Lockwood, 1976.

McLean A & Fairclough P; Endoscopic Ultrasound – Current Applications. Clinical Radiology 51, 83-98, 1996.

McGlave S A, Jones W F, Evans W B; Do physician attitudes and practices limit use of EUS in the staging and the treatment of esophageal carcinoma? Gastointestinal Endoscopy;61(7) 840-848, 2005

Meagher S, Poepping T L, Ramnarine K V, Black R A, Hoskins P R; Anatomical flow phantoms of the nonplanar carotid bifurcation, Part II: Experimental validation with Doppler ultrasound. Ultrasound in Medicine & Biology Volume 33, Issue 2, Pages 303-310, February 2007

Mercier L, Langø T, Lindseth F, Collins D L; A review of calibration techniques for freehand 3-D ultrasound system.. Ultrasound in Medicine & Biology, Volume 31, Issue 4, Pages 449-471, April 2005

Miller Y S. Endoscopic ultrasound in the evaluation of portal hypertension. Techniques in Gastrointestinal Endoscopy, Volume 7, Issue 1, Pages 41-48 , January 2005

Molin S -O, Nesje L B, Ødegaard S; Critical acquisition of ultrasound data in 3d-eus. European Journal of Ultrasound, Volume 7, Supplement 1, Page S43, February 1998

Molin S -O, Engström A, Nesje L B, Gilja O H, Ødegaard S; Improvement of 3D EUS using ECG- and respiratory-triggered acquisition. European Journal of Ultrasound, Volume 7, Supplement 1, Page S54, February 1998

Molin S -O, Nesje L B, Gilja O H, Hausken T, Martens D, Ødegaard S; Preliminary experience of 3D-EUS in tumor staging. European Journal of Ultrasound, Volume 7, Supplement 1, Page S39, February 1998

Molin S -O, Nesje L B, Gilja O H, Hausken T, Martens D, Ødegaard S; 3D-endosonography in gastroenterology: methodology and clinical applications European Journal of Ultrasound Volume 10, Issues 2-3, Pages 171-177, November 1999

Nelson T R, Pretorius D H; Three-dimensional ultrasound imaging. Ultrasound in Medicine & Biology, Volume 24, Issue 9, Pages 1243-1270, December 1998

Niwa K, Hirooka Y, Niwa Y, Itoh A, Ohmiya N, Hashimoto S, Ishikawa H, Okada N, Itoh T, Goto H; Comparison of image quality between electronic and mechanical radial scanning echoendoscopes in pancreatic diseases. Journal of Gastroenterology and Hepatology. Volume 19, Issue 4, Pages: 454-459, Date: April 2004

Ødegaard S; High-resolution endoluminal sonography in gastroenterology. European Journal of Ultrasound Volume 10, Issues 2-3, Pages 85-91, November 1999

Ogawa M, Yasuda K, Cho E, Tanaka K, Uno K, Nakajima M; Clinical Use Of The Newly Developed Electronic Radial Ultrasound Endoscope. Digestive Endoscopy. Volume 18, Issue 1, Pages: 49-54, Date: January 2006

Okamura S, Tsutsui A, Muguruma N, Ichikawa S, Sogabe M, Okita Y, Fukuda T, Hayashi S, Okahisa T, Shibata H, Ito S, and Sano T; The utility and limitations of an ultrasonic miniprobe in the staging of gastric cancer. J. Med. Invest. 46 : 49-53, 1999.

Osawa H, Yoshizawa M, Yamamoto H, Kita H, Satoh K, Ohnishi H, Nakano H, Wada M, Arashiro M, Tsukui M, Ido K, Sugano K; Optimal band imaging system can facilitate detection of changes in depressed-type early gastric cancer. Gastrointestinal endoscopy, volume 67, issue 2, pages 226-234, February 2008

Pfau P R, Perlman S B, Stanko P, Frick T J, Gopal D V, Said A, Zhang Z, Weigel T; The role and clinical value of EUS in a multimodality esophageal carcinoma staging program with CT and positron emission tomography. Gastrointestinal Endoscopy, Volume 65, Issue 3, Pages 377-384 , March 2007

Plukker J Th M, van Westreenen H L; Staging in oesophageal cancer. Best Practice & Research Clinical Gastroenterology, Volume 20, Issue 5, Pages 877-891, 2006

Poepping T L, Nikolov H N, Rankin R N, Lee M, Holdsworth D W; An in vitro system for Doppler ultrasound flow studies in the stenosed carotid artery bifurcation. Ultrasound in Medicine & Biology.; 28(4): 495-506. 2002

Polglase A L, McLaren W J, Skinner S A, Kiesslich R, Neurath M F, Delaney P W; A fluorescence confocal endomicroscope for in vivo microscopy of the upper- and the lower-GI tract. Gastrointestinal Endoscopy, Volume 62, Issue 5, Pages 686-695, November 2005

Preston, R C; Measurement and characterisation of the acoustic output of medical ultrasonic equipment Part 1.Med. & Biol. Eng. & Comput., 24, 113 – 120, 1986

Preston, R C; Measurement and characterisation of the acoustic output of medical ultrasonic equipment Part 2.Med. & Biol. Eng. & Comput., 24, 225 – 233, 1986

Preston, R C; Hydrophone-Based Measurements on a specific acoustic pulse, Part 1 Field Characteristics; Preston RC (Editor) Output Measurements for Medical Ultrasound, Springer, p91 – 105, 1991

Preston R C, Bacon D R, Livett A J, and Rajendran K; PVDF membrane hydrophone performance properties and their relevance to the measurement of the acoustic output of medical ultrasonic equipment; J. Phys. E: Sci. Instrum. 16 786-796 1983

Pye S D, Ellis W and MacGillivray T; Medical ultrasound: a new metric of performance for greyscale imaging. Journal of Physics: Conference Series 1 187–192. 2004

Ramnarine K V, Anderson T, Hoskins PR; Construction and geometric stability of physiological flow rate wall-less stenosis phantoms. Ultrasound in Medicine & Biology.; 27(2): 245-250. 2001

Raj M, Chen R Y; Interventional applications of endoscopic ultrasound Journal of Gastroenterology and Hepatology. Volume 21, Issue 2, Pages: 348-357, Date: February 2006

Rickey D W, Picot P A, Christopher D A, Fenster A; A wall-less phantom for Doppler ultrasound studies. Ultrasound Med. Biol; 21: 1163-1176. 1995

Robinson S P; Hydropones; Preston RC (Editor) Output Measurements for Medical Ultrasound, Springer, p 57-73; 1991

Rousseau F, Barillot C; Quality Assessment of Electromagnetic Localizers in the Context of 3D Ultrasound Research Report, RR-4408 [inria-00072180 − version 1] 2002

Ryan L K, & Foster F S; Tissue equivalent vessel phantoms for intravascular ultrasound. Ultrasound in Medicine & Biology.; 23(2): 261-273. 1997

Sandhu I S, Bhutani M S; Gastrointestinal endoscopic ultrasonography. Med Clin N Am; 86:1289-1317, 2002

Sandha G S, Severin D, Postema E, McEwan A, and Stewart K; Is positron emission tomography useful in locoregional staging of esophageal cancer? Results of a multidisciplinary initiative comparing CT, positron emission tomography, and EUS. Gastrointestinal Endoscopy 67: 3 402-409. 2008

Saunders B P, Bell G D, Williams C B, Bladen J S, and Anderson A P; First clinical results with a real time, electronic imager as an aid to colonoscopy. Gut; 36: 913 - 917, Jun 1995

Saunders B P, Shah S G; Magnetic Imaging of Colonoscopy; Waye J D., Rex D K., Williams C B Colonoscopy: Principles and Practice Blackwell Publishing, pages 265 - 276; 2003

Schrager J J, Tarpley J L, Smalley W E, Austin M T, Pearson A S; Endoscopic Ultrasound: impact on survival in patients with oesophageal cancer Am Jour Surg;190:682-686 2005

Schwartz D A, Wiersema M J, Dudiak K M, Fletcher J G, Clain J E, Tremaine W J, Zinsmeister A R, Norton I D, Boardman L A, Devine R M, Wolff B G, Young-Fadok T M, Diehl N N, Pemberton J H, Sandborn W J; A Comparison of Endoscopic Ultrasound, Magnetic Resonance Imaging, and Exam Under Anesthesia for Evaluation of Crohn's Perianal Fistulas. Gastroenterology, Volume 121, Issue 5, Pages 1064-1072, November 2001

Sheski F D and Mathur P N; Endobronchial Ultrasound. Chest; 133: 264 - 270 , Jan 2008

Smith S W, Chu K, Idriss S F, Ivancevich N M, Light E D, Wolf P D; Feasibility study: Real-time 3-D ultrasound imaging of the brain. Ultrasound in Medicine & Biology, Volume 30, Issue 10, Pages 1365-1371, October 2004

Solberg O V, Lindseth F, Torp H, Blake R E, Hernes T A N; Freehand 3d Ultrasound Reconstruction Algorithms— A Review. Ultrasound in Med. & Biol., Vol. 33, No. 7, pp. 991–1009, 2007.

Stergiou N, Haji-Kermani N, Schneider C, Menke D, Köckerling F, Wehrmann T; Staging of colonic neoplasms by colonoscopic miniprobe ultrasonography. Int J Colorectal Dis., 18:445–449. 2003

Sumiyama K, Suzuki N, Kakutani H, Hino S, Tajiri H, Suzuki H, Aoki T; A novel 3-dimensional EUS technique for real-time visualization of the volume data reconstruction process. Gastrointestinal Endoscopy, Volume 55, Issue 6, Pages 723-728, May 2002

Sumiyama K, Suzuki N, Suzuki S, Hattori A, Hayashibe M, Otake Y, Odagi I, Kakatuna H, Tajiri H; Gastrointestinal: Fine-needle aspiration biopsy using three-dimensional endoscopic ultrasound. Journal of Gastroenterology and Hepatology. Volume 20, Issue 12, Pages: 1941-1941, Date: December 2005

Teirlinck C J P, Bezemer R A, Kollmann C, Lubbers J, Hoskins P R, Ramnarine K V, Fish P, Fredfelt K E and Schaarschmidt U G; Development of an example flow test object and comparison of five of these test objects, constructed in various laboratories. Ultrasonics.; 36: 653-660. 1998

Thomas E, Crellin A, Harris K, Swift S, Montefiore D S; The role of Endoscopic Ultrasound (EUS) in planning radiotherapy target volumes for oesophageal cancer. Radiotherapy and Oncology;73:149-151, 2004

Tio T L, Coene P P, Schouwink M H, and Tytgat G N; Esophagogastric carcinoma: preoperative TNM classification with endosonography. Radiology; 173: 411. 1989

Tio T L. Endosonography in Gastroenterology Springer-Verlag 1988.

Tio T L, Kimmings N, Rauws E, Jansen P, Tytgat G; Endosonography of gastroesophageal varices: Evaluation and follow-up of 76 cases, Gastrointestinal Endoscopy, Volume 42, Issue 2, Pages 145-150, August 1995

Tsutsui A, Okamura S, Muguruma N, Tsujigami K, Ichikawa S, Ito S, Umino K; Three-dimensional reconstruction of endosonographic images of gastric lesions: Preliminary experience. Journal of Clinical Ultrasound. Volume 33, Issue 3, Pages: 112-118, Date: March/April 2005

Vegesna A, Raju R, Asfari W, Korimilli A, Varia A, Orfanidis N, Gaughan J, Ramzan Z, Miller L S; Three-dimensional US volume analysis of gastric pseudotumors in a porcine model. Gastrointestinal Endoscopy, Volume 64, Issue 4, Pages 635-640, October 2006

Veuillez V, Rougier P, Seitz J-F; Multimodal treatment of oesophageal cancer. Best Practice & Research Clinical Gastroenterology, Volume 21, Issue 6, Pages 947-963, December 2007

Wakelin S J, Deans C, Crofts T J, Allan P L, Plevris J N, Paterson-Brown S; A comparison of computerised tomography, laparoscopic ultrasound and endoscopic ultrasound in the preoperative staging of oesophago-gastric carcinoma. Eur J Radiol.; 41(2):161-167. 2002

Wallace M B, Ravenel J, Block M I, Fraig M, Silvestri G, Wildi S, Schmulewitz N, Varadarajulu S, Roberts S, Hoffman B J, Hawes R H, Reed C E; Endoscopic ultrasound in lung cancer patients with a normal mediastinum on computed tomography. The Annals of Thoracic Surgery, Volume 77, Issue 5, Pages 1763-1768, May 2004

Wallace M B, Sullivan D, Rustgi A K and AITGN Symposium Faculty; Advanced Imaging and Technology in Gastrointestinal Neoplasia: Summary of the AGA-NCI Symposium October 4–5, 2004. Gastroenterology, Volume 130, Issue 4, Pages 1333-1342, April 2006

Wallace M B, Hawes R H; Emerging indications for EUS; Gastrointestinal Endoscopy, Volume 52, Issue 6, Supplement 1, Pages S55-S60, December 2000

Williams C, Saunders B, Guy C N, Gillies D F; Electronic three-dimensional imaging of intestinal endoscopy. Lancet. Volume 341, Issue 8847, Pages 724-725, 1993.

Wong Kee Song L M, Wilson B C; Endoscopic detection of early upper GI cancers. Best Practice & Research Clinical Gastroenterology, Volume 19, Issue 6, Pages 833-856, December 2005

Wu L F, Wang B Z, Feng J L, Cheng W R, Liu G R, Xu X H, Zheng Z C; Preoperative TN staging of esophageal cancer: Comparison of miniprobe ultrasonography, spiral CT and MRI. World J Gastroenterol; 9(2): 219-224, 2003

Yamao K, Irisawa A, Inoue H, Matsuda K, Kida M, Ryozawa S, Hirooka Y, Kozu T; Standard Imaging Techniques Of Endoscopic Ultrasound-Guided Fine-Needle Aspiration Using A Curved Linear Array Echoendoscope. Digestive Endoscopy. Volume 19, Issue s1, Pages: S180-S205, Date: July 2007

Yasuda K, Ogawa M, Nakajima M; Newly developed ultrasound endoscope with an electronic radial array transducer. Digestive Endoscopy. Volume 16, Issue s2, Pages: S219-S222, Date: November 2004

Yasuda K, Kamagushi M, Morikawa J, Honda M, Nakajima M; Role of Endoscopic ultasonography in the diagnosis of early esophageal carcinoma. Gastrointest Endosc Clin N Am;15(1):93-99, 2005

Yong A A, Roberts S A; Interventional Endoscopic Ultrasound. Clinical Radiology, Volume 58, Issue 1, Pages 32-43, January 2003

Yusuf T E, Tsutaki S, Wagh M S, Waxman I, Brugge W R; The EUS hardware store: state of the art technical review of instruments and equipment. Gastrointestinal Endoscopy, Volume 66, Issue 1, Pages 131-143, July 2007

Zagzebski J A, Madsen E L, Frank G R; A teaching phantom for sonographers. Journal of Clinical Ultrasound.; 19(1): 27-38. 1991

Zeqiri, B; UK inter-laboratory comparison of ultrasonic attenuation and velocity measurements - a preliminary report. Proceedings of the Institute of Acoustics, Vol. 13, Part 2, 137-142, 1991

Zeqiri, B; Reference liquid for ultrasonic attenuation, Ultrasonics, Vol. 27, 314-315, 1989.

Zhang X, Watson DI, Lally C, Bessell J; Endoscopic ultrasound for preoperative staging of esophageal carcinoma. Surg. Endoscopy; 19:1618-1621, 2005

Appendices

Appendix 1. – EUS equipment within the RIE.

The endoscopy unit had a number of echoendoscopes available for clinical examinations and are detailed within table A.1.1. The processors used to drive these echoendoscopes are detailed in table A.1.2. As the only echoendoscopes available for testing the 3D-EUS were in clinical use, it would not be possible to perform modifications, (e.g. the integration or attachment to the insertion tube of positional sensors) to any of the endoscopes that would compromise its integrity, the ability to be sterilised and its use on patients.

Table A.1.1. - Breakdown of Olympus echoendoscopes available within the Endoscopy Unit of the Royal Infirmary of Edinburgh as of 2007.

Scope Model (Olympus)	**Orientation**	**Operating Freq. (MHz)**	**Viewing Angle**	**Depth Of Field, (mm)**	**Ultrasound Transducer Configuration**	**Required Processor**
GF-UM20	Mechanical Radial	7.5, 12	45° Forward oblique	3-100	Dual single crystal transducers	EU-M30, EU-M2000
MH-908	Mechanical Radial	7.5	None		Single crystal transducer	EU-M30, EU-M2000
GF-UM200	Mechanical Radial	7.5, 12	50° Forward oblique	3-100	Dual Single crystal transducer	EU-M30, EU-M2000
GF-UM2000	Mechanical Radial	5, 7.5, 12, 20	50° Forward oblique	3-100	Dual crystal transducers	EU-M2000
GF-UE 260	Electronic Radial	5, 6, 7.5, 10	55° Forward oblique	3-100	Multi-element transducer	Aloka SSD-α5
GF-UC240P	Electronic Linear	5, 6, 7.5, 10	55° Forward oblique	3-100	Multi-element transducer	Aloka SSD-α5
GF-UCT240	Electronic Linear	5, 6, 7.5, 10	55° Forward oblique	3-100	Multi-element transducer	Aloka SSD-α5

Table A.1.2. - The EUS processors used to drive the echoendoscopes based at the RIE.

Manufacturer	Model	Ultrasound Drive Unit	Package Format	Comments
Olympus	EU-M30	Mechanical	Video Stack module	Olympus stack required for video. Analogue electronic system can only be used with old EUS scopes. Drives the GF-UM20, GF-UM200, MH908 scopes
Olympus	EU-M2000	Mechanical	Video Stack module	Olympus stack required for video. PC based system but has lower frame rate. Drives the GF-UM2000, GF-UM20, GF-UM200, MH908 scopes
Aloka	SSD-α5	Electronic	Ultrasound Scanner	Olympus stack required for video. Digital system can only use the electronic EUS scopes. Drives the GF-UE260, GF-UC240P & GF-UCT240 scopes

Appendix 2. – Results obtained from Mark 3 Materials testing

	EUS : 7.5mhz & Scale Depth : 12cm	EUS : 12mhz & Scale Depth : 12cm
(a) Normal Image without layer material	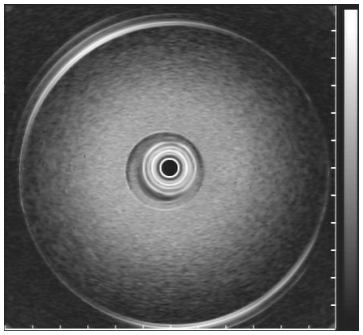	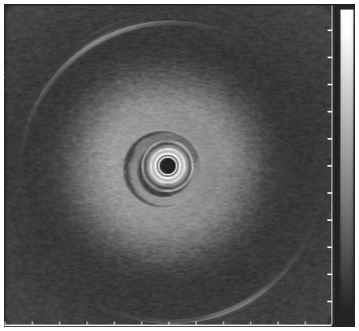
(b) Cling Film (Polythene) with a thickness of 11 µm	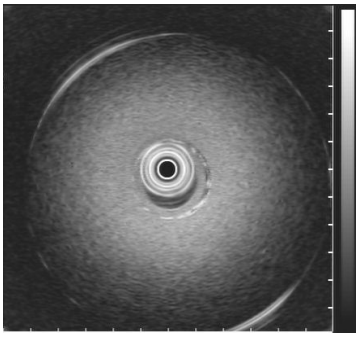	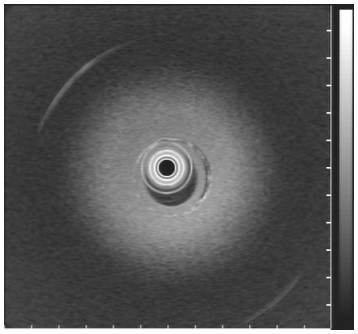
(c) Stretch Film (Polythene with a thickness of 25 µm	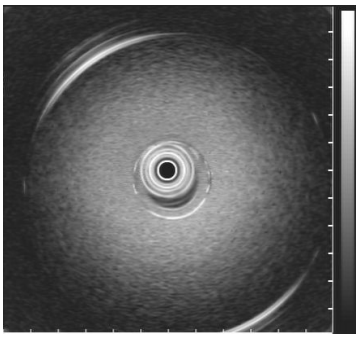	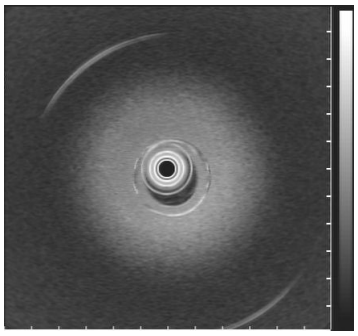
(d) Polythene with a thickness of 130 µm	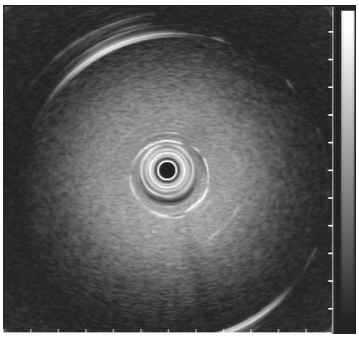	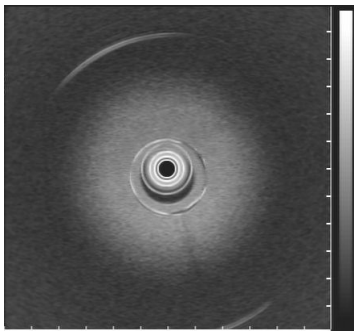

Figure A.2 - Images obtained from the GF-UM20 echoendoscope when placed into the test phantom and manipulated to the side.

(e) Latex Condom with a thickness of 80 μm

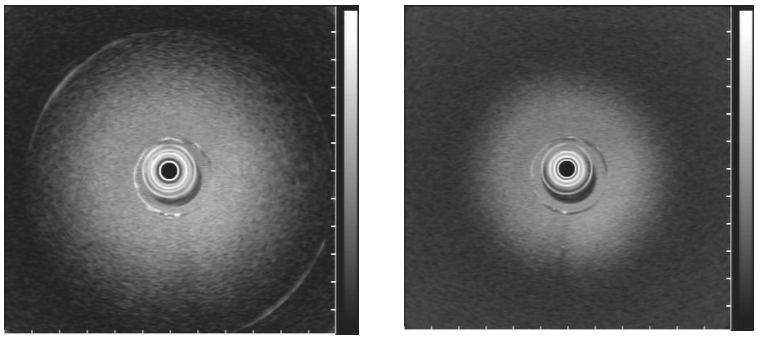

(f) Latex TOE Probe sheath with a thickness of 300 μm

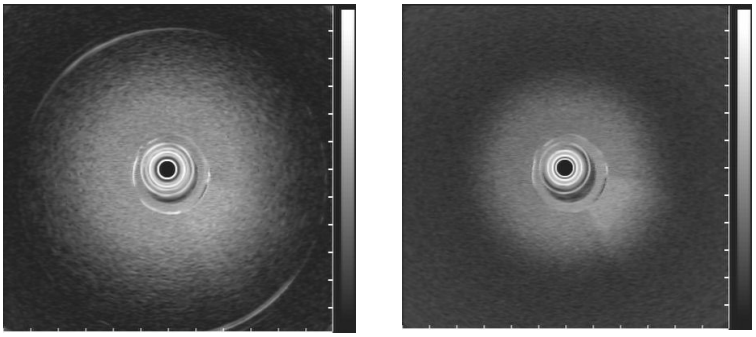

(g) Latex Tyre Inner with a thickness of 700 μm

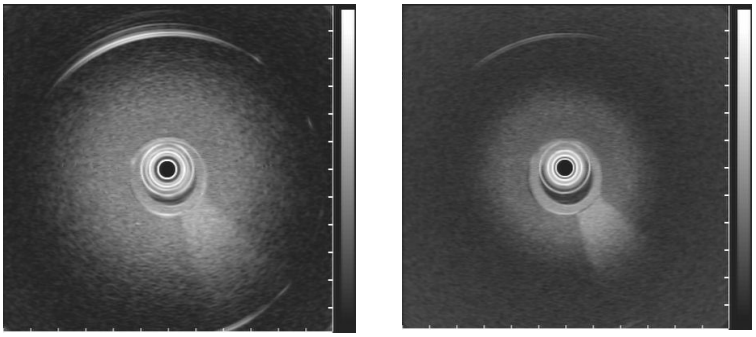

(h) Tin Foil with a thickness of 25 μm

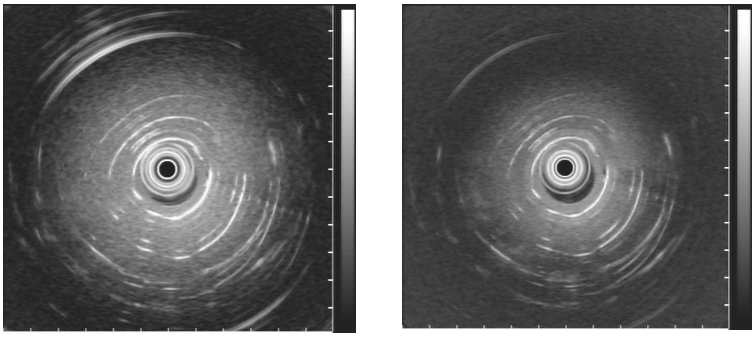

Figure A.2 - Images obtained from the GF-UM20 echoendoscope when placed into the test phantom and manipulated to the side.

Appendix 3. – Code examples of analysis and reconstruction programs

Examples of the Matlab code written and implemented during the project have been included within this appendix. The code used within chapter 3 for the analysis of the hydrophone data. The program can be seen in Appendix 4.

Code example A.3.1

```
Range = 1:N;
Frequency range = (Range-1)/N*Fs;        % Calculates the Frequency range for plotting.
PSE = X * conj(X)/N;                     % calculates Power Spectral Estimate of FFT
Bar (Frequency range, PSE).              % to display PSE as Bar graph (see figure 4.11)
Where        X = FFT of the RF pulses
             N = Number of points of data (e.g. 1000).
             Fs = Sampling frequency of Oscilloscope (e.g. 500MHz).
             PSE = Resultant Power Spectral Estimate of the data.
```

Code Example A.3.2 - of the analysis for the GF-UM20 echoendoscope.

```
% scaling to convert from Time to distance data.
Rotation = 6.25;      %  Hz
time_rotation = 1/rotation;
time_per_deg = time_rot/360;
transducer_diameter = 11; % mm
radius = trans_diameter/2; % Radius calculated from transducer_diameter
Circumference = 2*pi*radius; % Circumference of the transducer
Distance_per_degree = Circumference /360;
Speed = Circumference / time_rotation; % Speed of the  rotation
time_per_pnt = 20e-6;
dist_per_pnt = speed * time_per_pnt;
ang_per_pnt  =  atand(dist_per_pnt / radius); % Eq.4.1
ang_per_pnt_half  =  atand(2*(dist_per_pnt) / radius);
plot_x_dist  =  tand(ang_per_pnt_half)*(Hydrophone_step + radius); % Eq 4.4
tot_plot_dist =plot_x_dist*499;
```

Code Example A.3.3

```
count = 0;
for index = 1: length(Hydrophone_steps)
   count = count+1;
   temp  = data_array_latitude(:,count);
   [pos_latit1, pos_location1] = findpeaks((temp*1),'threshold', 0);
   pos_lat_peaks(:,count) = pos_latit1;
   pos_location(:,count) = pos_loction1;
   [neg_latit1, neg_location1] = findpeaks((temp*-1),'threshold', 0);
   neg_lat_peaks(:,count) = neg_lat1;
   neg_location(:,count) = neg_location1;
end
```

Code Example A.3.4

```
Mask_pos = pos_lat_peaks > 0.03;
pos_lat_tmp = pos_lat_peaks .*Mask_pos;
Mask_neg = neg_lat_peaks >0.032;
neg_lat_peaks = neg_lat_peaks* -1;
neg_lat_tmp = neg_lat_peaks .* Mask_neg;
```

Code Example A.3.5

```
x = 1:499;
count = 0;
for i = 1: length(Hydrophone_steps)
   count = count+1;
   [pos_lata, pos_loca] = findpeaks(pos_lat_tmp(:,count));
   pos_y = interp1(pos_loca, pos_lata, x);
   pos_max = max(pos_loca);
   pos_min = min(pos_loca);
   [neg_lata, neg_loca] = findpeaks((neg_lat_tmp(:,count)*-1));
   neg_y = interp1(neg_loca, neg_lata,x);
   neg_max = max(neg_loca);
   neg_min = min(neg_loca);
   pos_lat_tmp1 = pos_lat_tmp(:,count);
   pos_lat_tmp1(pos_min:pos_max) = pos_y(pos_min:pos_max)';
   pos_lat_smth(:,count) = pos_lat_tmp1;
   neg_lat_tmp1 = neg_lat_tmp(:,count);
   neg_lat_tmp1(neg_min:neg_max) = neg_y(neg_min:neg_max);
   neg_lat_smth(:,count) = neg_lat_tmp1;
end
```

Chapter 5 - The Mark 2 3D-EUS system code examples, implemented within the reconstruction and positional scaling of the volume. The program can be seen in Appendix 5.

Code Example A.3.6

```
x = x1 - x1(1);
y = y1 - y1(1);
z = z1 - z1(1);
count = 0;
for i = 1:length(x1) -1
        count  = count +1;
        dist(count) = sqrt((power(x(count),2)+ power(y(count),2)+ power(z(count),2)));
end;
```

Code Example A.3.7

```
noframes = 500;
image = imread(filename);
image = flipud(image);
image = imcrop(image,finalRect);
x_im = size(image,1);
y_im = size(image,2);
volume = zeros(x_im, y_im, noframes);
actual_pullback_distance = max(dist) - min(dist);
sample_rate = act_pull_dist / noframes;
count = 0;
      for i = 1:length(dist) -1
         count  = count +1;
           Dif = dist(count+1)-dist(count);
         image_ID(count) = Dif / sample_rate;
      end;
image_ID2 = round(image_ID);
```

Code Example A.3.8

```
imag = image_ID2 > 0;
ID = 1:length(image_ID2);
Im_ID = imag.*ID;
volume_index =zeros(1,noframes);
count = 0;
count2 = 0;
for i = 1:length(x) -2;
    count = count + 1;
       if imag(count) == 1
             samp_im = image_ID2(count);
           for i = 1 : samp_im
              count2 = count2 + 1;
              volume_index(count2) = Im_ID(count);
           end;
       end;
end;
```

Code Example A.3.9

```
count = 0;
for i = 1: noframes - 2
           count = count + 1;
           file = 10000 + volume_index(count);
           fileno = num2str(file);
           filename = strcat(path,studyinit,studynum,div,studyinit,fileno,ext);
           image = imread(filename);
           image = flipud(image);
           image = imcrop(image,finalRect);
           image_a = imsubtract(image,mask);
           volume(:,:,count) = image_a;
end;
```

Appendix 4. - IC3D Program & GUI's of the 3D-EUS V2 system.

A.4.1. – Windows of the Prototype Three-Dimensional EUS System

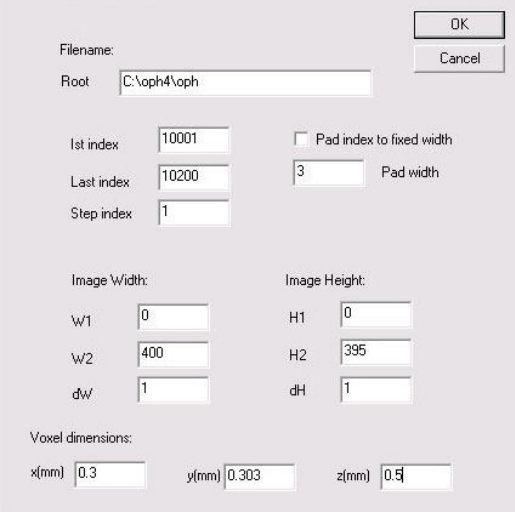

Figure A.4.1 – 3D scan load bitmap screen. The volume was scaled to the appropriate dimensions using the voxel dimension screen and dW and dH combination.

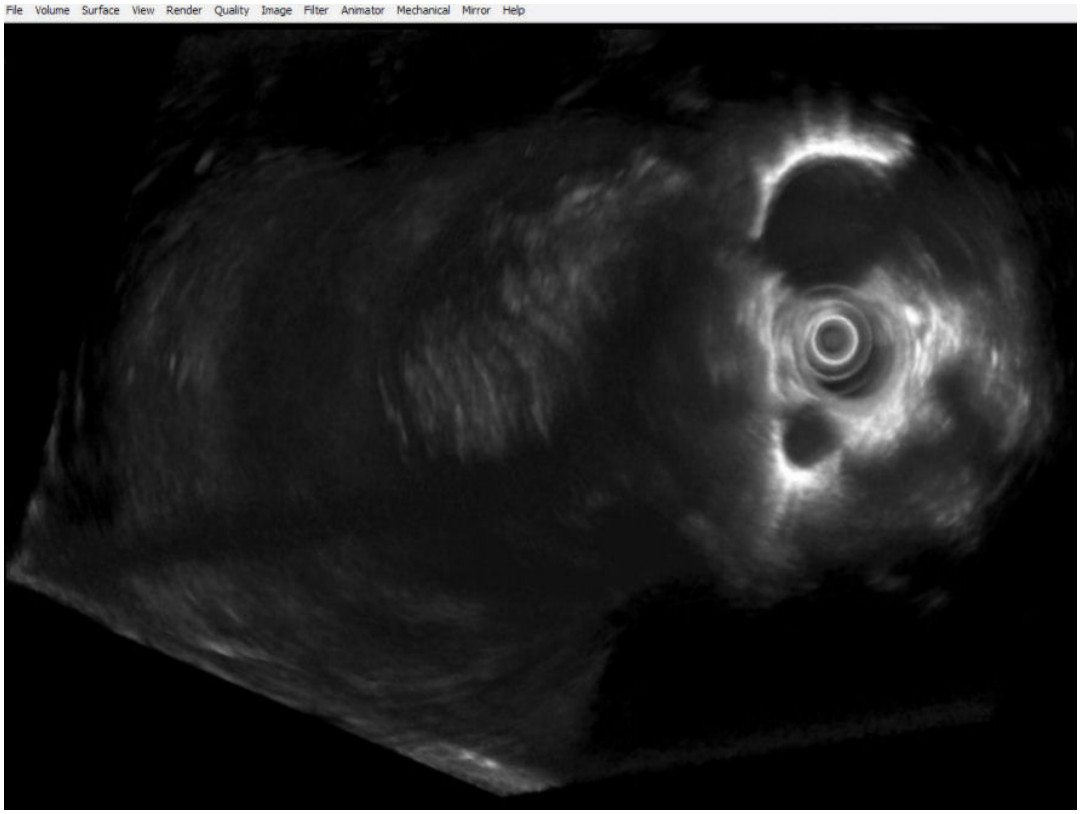

Figure A.4.2 – 3D scan window with an example clinical reconstructed volume. The volume could be modified and manipulated by changing brightness and opacity maps.

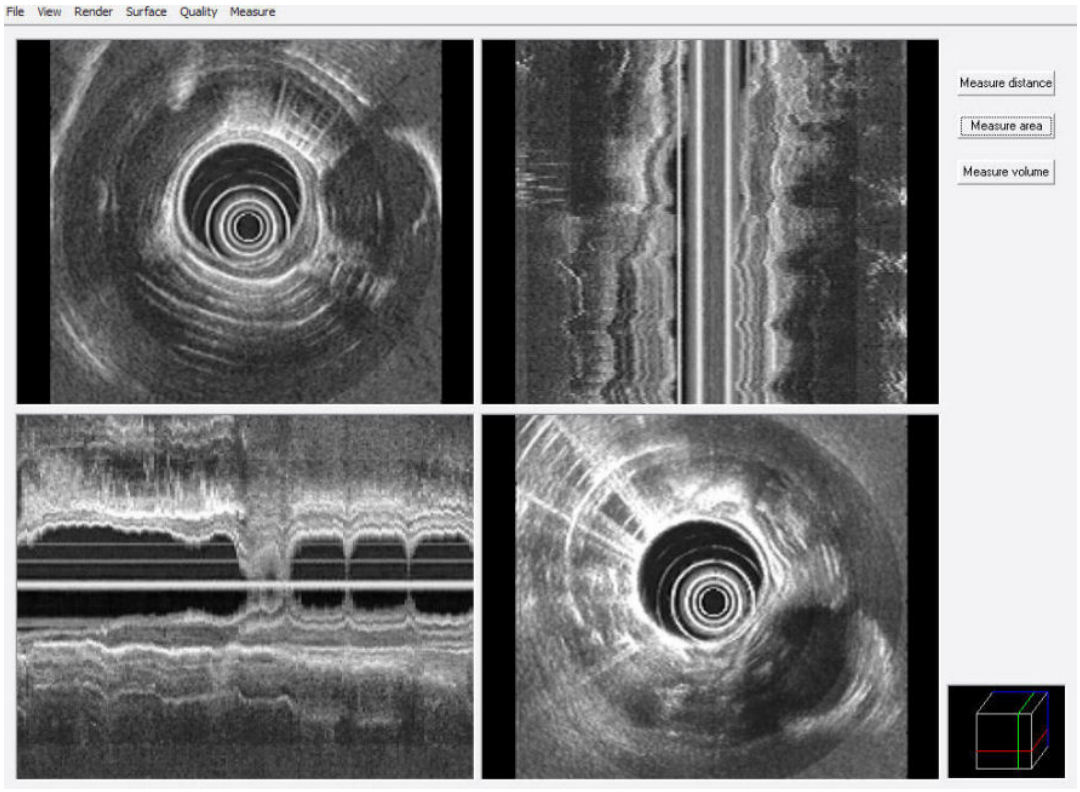

Figure A.4.3 – The ‘S view’ window with an example clinical reconstructed volume. This was the main window where the analysis and measurements were performed.

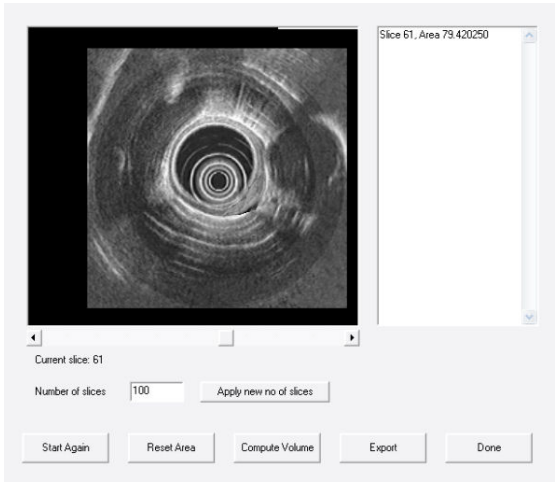

Figure A.4.4 – The ‘S view’ area and volume measurement window with an example clinical reconstructed volume.

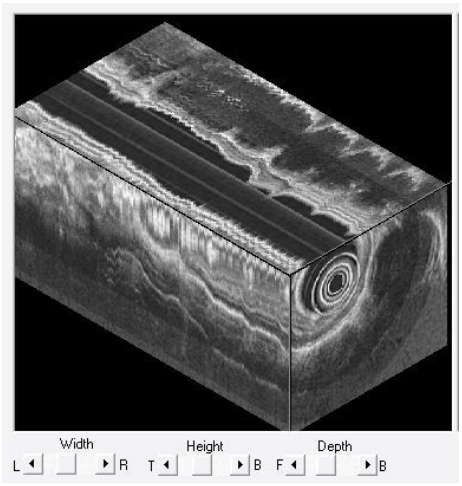

Figure A.4.5 – The ‘Box view’ window with an example clinical reconstructed volume. A user selectable 3D segment can be visualised by changing the dimensions of the wire frame.

A.4.2. - IC3D program

The main window of the IC3D program is shown in figure A.4.6a. Within the main window, it was possible to initiate separate segments of the IC3D application by pressing the relevant buttons. Pressing the 'capture data' button initiates the window shown in figure A.4.6b. The user selects the directory where the image stack is to be saved and then enters the patients initials within the 'Enter subject's initials' text box.

The program automatically initiates a count that allows for up to 9 acquisitions to be performed with the same initials. The subject's initials and count were concatenated to create a folder where the images would be saved. The capture was initiated by pressing the 'start capture' button and terminated by pressing the 'stop capture' button. During the capture, the position, and available space was displayed in real time. Individual images were captured with a file name made from the subject initials and an incrementing number (e.g. 10001).

A text file was created at the start of the acquisition, as an image was acquired; the comma delimited file was updated with the image filename, the X, Y and Z position and the time between captures. At the end of the capture a capture comments box was displayed summarising the total capture time, the number of images captured and capture rate. The captured image stack could be reviewed, frame by frame, using the 'replay data' window (figure A.4.6c). The user definable image capture parameters could be altered within the 'image setup' window (figure A.4.6d). Using the slider bars, it was possible to alter the size and position of the square that defined the image capture region. The arm status window, displayed in figure A.4.6e, was used to alter the unit dimensions of the positional arm from inches to centimetres and from radians to degrees.

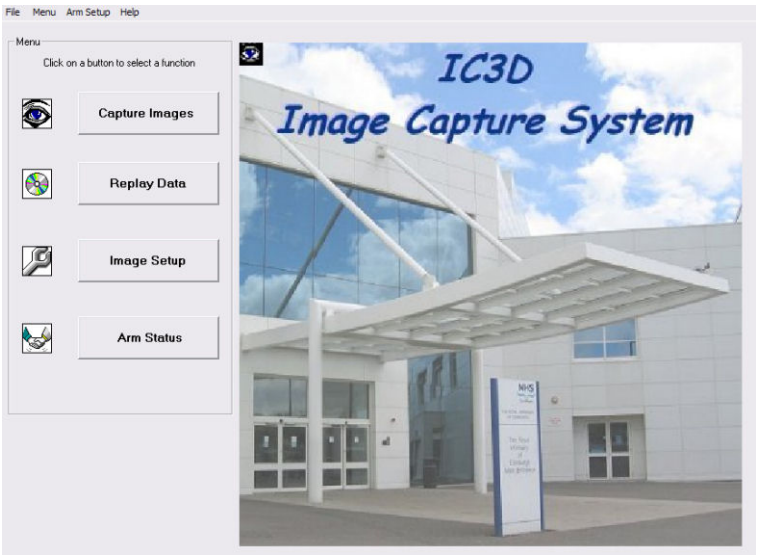

Figure A.4.6a – The main window and menu of the IC3D package.

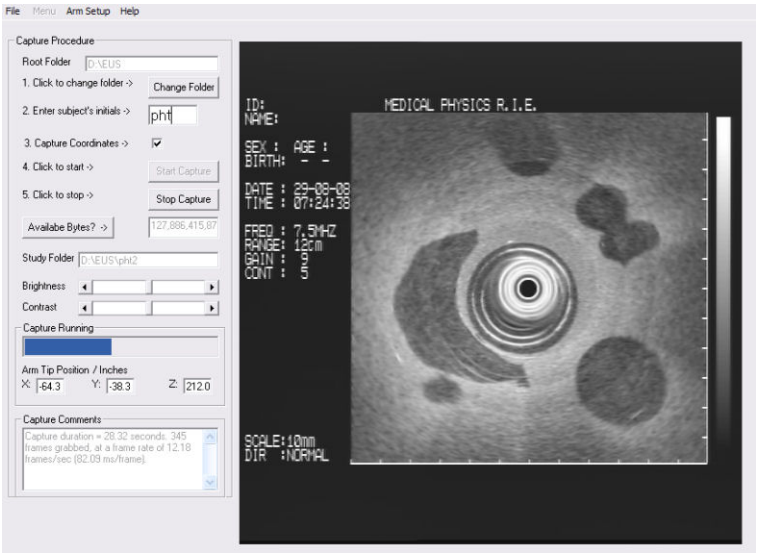

Figure A.4.6b – The image and positional capture window was used to capture a series of images and XYZ positional information simultaneously. An alternate full screen capture version was produced to operate with the Aloka system.

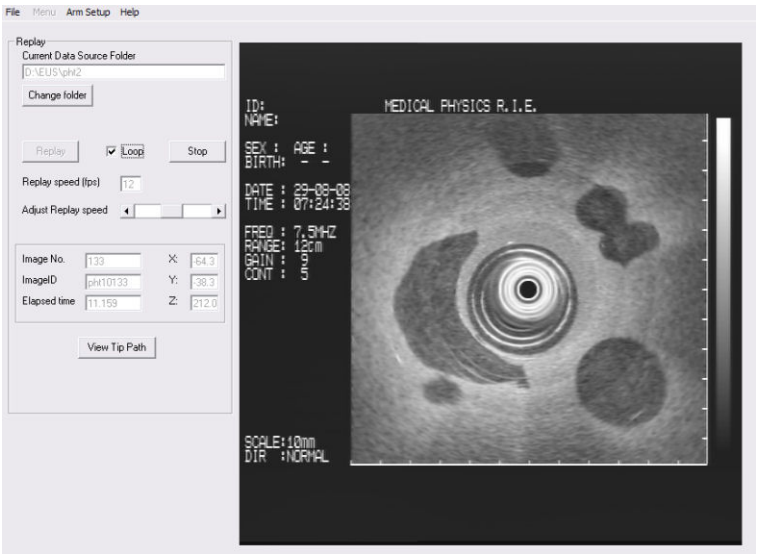

Figure A.4.6c – The replay window that enables the user to review the captured images.

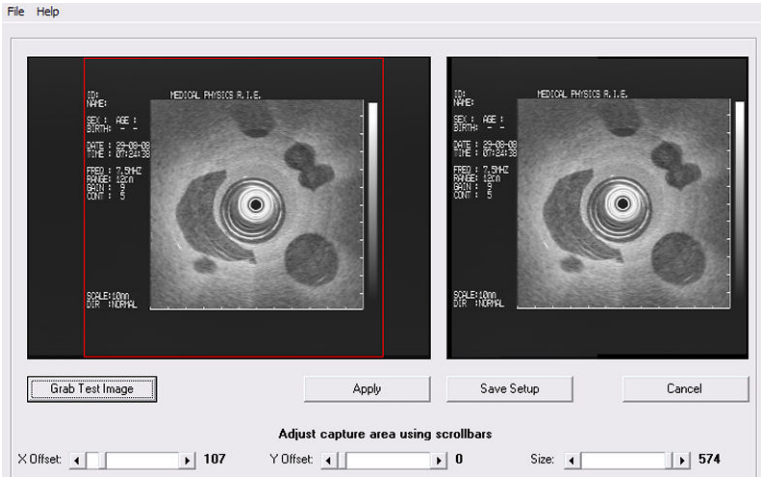

Figure A.4.6d – The image setup window used to select the image parameters for the capture of user defined areas.

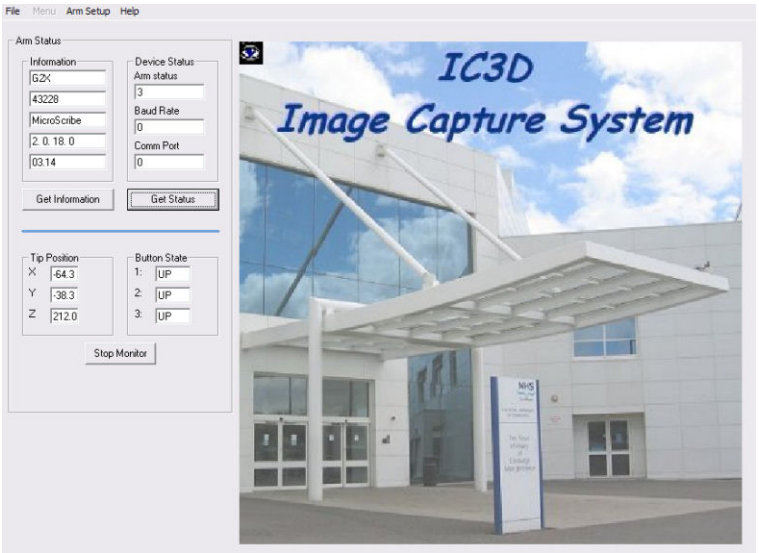

Figure A.4.6e – The arm status window, used to setup and test the communication to the digitising arm.

A.4.3. - 3D EUS Reconstruction & Analysis Toolbox GUIs

The EUS.m function shown in figure A.4.7.a was the main menu for the toolbox. This would allow for the initialisation of a number of different functions that would allow for the entry of the data, the reconstruction of the volume, different visualisation methods and analysis tools. The selection of the 'Enter EUS data' button activated the 'EUS_Startup' function and initiates the GUI shown in figure A.4.7.b.

The Matlab GUI builder was used to construct the EUS_Display.fig GUI and the basic control functions within the EUS_Display.m program. An example of the EUS_Display GUI is illustrated in figure A.4.7.c. This interactive GUI contained four different views the angle, coronal, sagittal and transverse planes of the volume. The first part of the display program was to load the volume data, calculation of a number of constants and scaling factors for the control tools, and extract the initial angle, coronal, sagittal and transverse slices from the volume. Control slider bars allowed the user to alter the visualised slice of the coronal, sagittal, transverse planes throughout the volume. The dashed lines on the angle, coronal, sagittal and transverse views showed the location of slices within the volume. As a slider was manipulated, the corresponding slice was calculated and updated within the appropriate plot window. The dashed lines displayed on all plot windows were updated when a movement of the slider bar occurred. The angle view was reconstructed from the volume data. Boundary conditions were determined and depended on the location of the coronal and sagittal planes and the angle of the selected cut. The angle plane was either shortened or elongated as the intersection point of the coronal and sagittal planes were changed. From these conditions, a recursive routine searched for corresponding pixels within the volume and generated a 180º angle plane from the intersection point. The angle was altered using a slider bar from 0 to 90º in one quadrant and by altering the angle direction it was possible to visualise any angle within a 360º circumference. It was possible to apply various image filters to the angle, coronal and sagittal planes to smooth and minimise artefacts created due to physiological changes within the anatomy during the acquisition phase, by using a number of different filtering algorithms. Scaled dimensional measurements could be performed on any of the available views using the 'imdistline.m' function. To record the any significant findings or measurements, a screen capture could be performed at any time.

Volume and area measurements were performed using the EUS_Display_Volume window shown in figure A.4.7.d. This interactive GUI contained a single plot window that displayed the transverse planes of the volume.

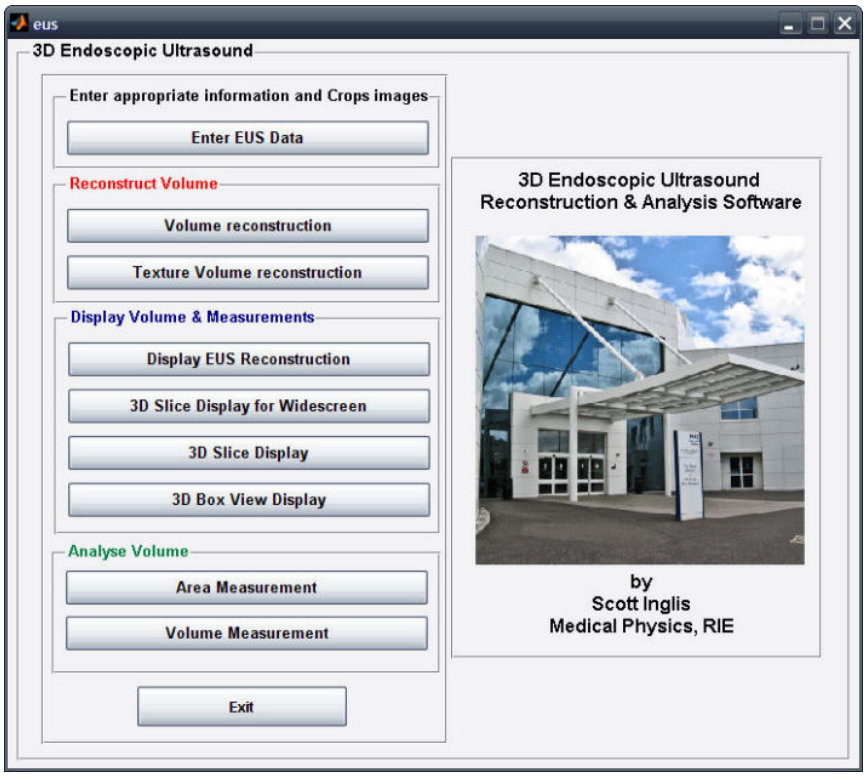

Figure A.4.7.a – 3D-EUS main menu selection window.

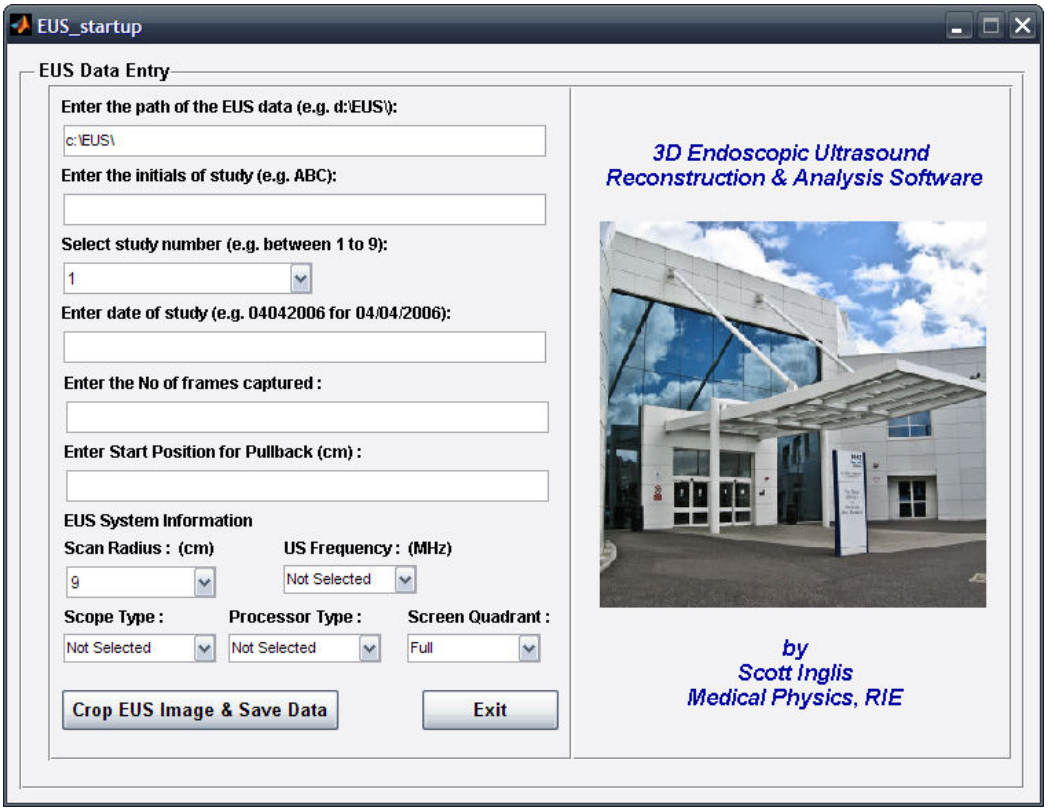

Figure A.4.7.b – 3D-EUS data entry window.

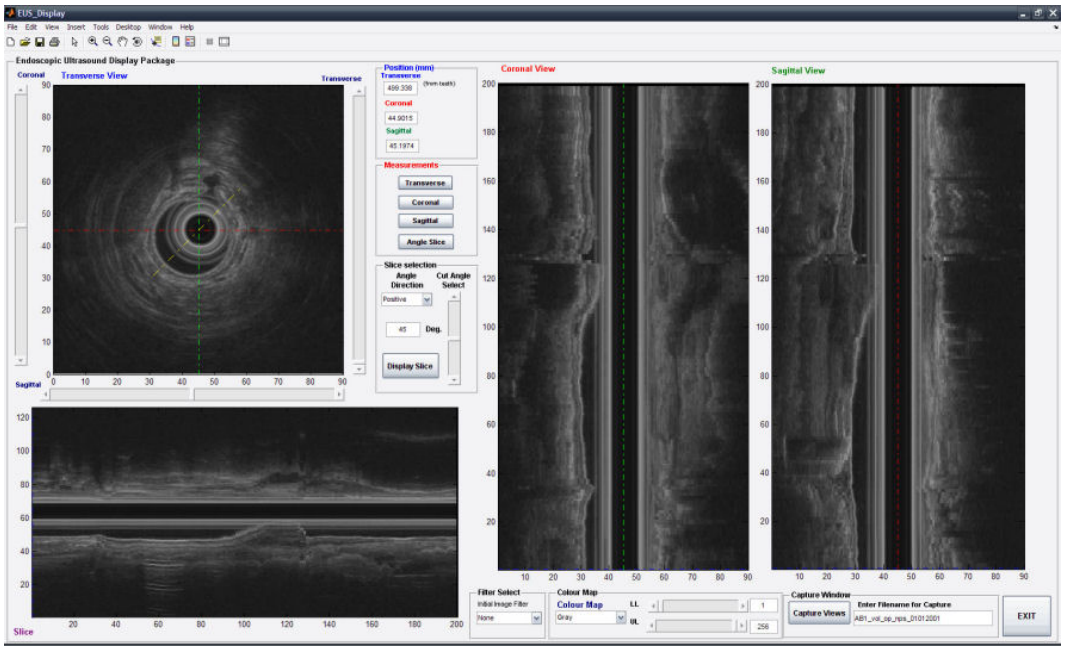

Figure A.4.7.c – 3D-EUS window used to visualise the transverse, coronal, sagittal and slice views.

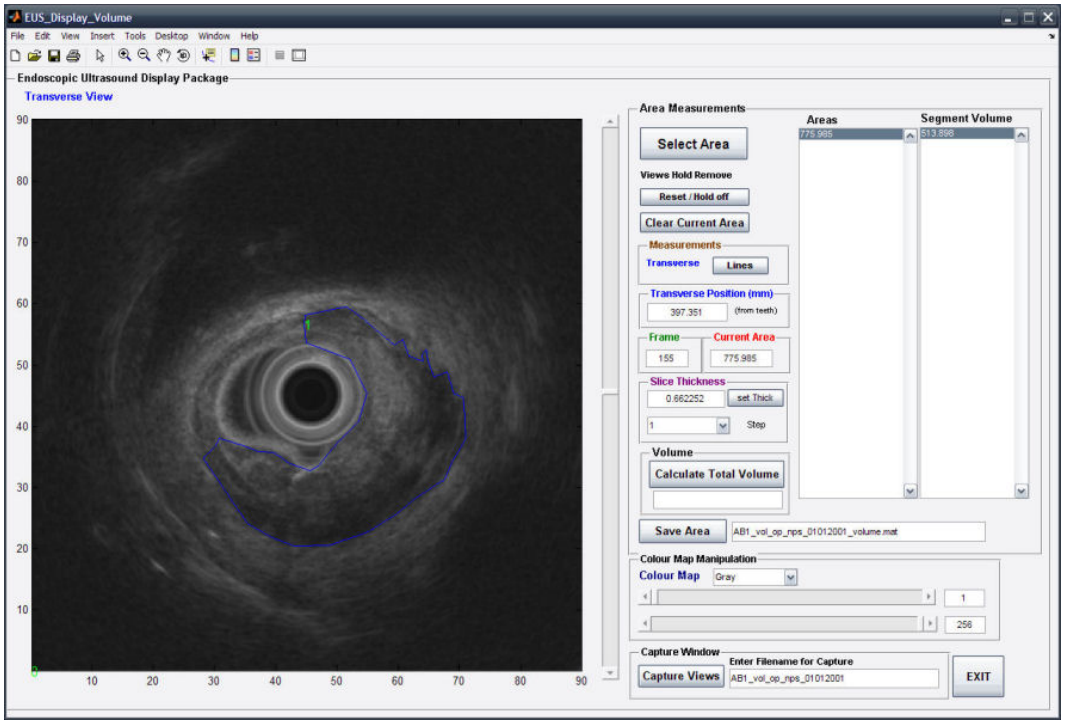

Figure A.4.7.d – 3D-EUS volume and area measurement screen.

Appendix 5. – Main Matlab programs used within the project

Chapter 2. Program used to analyse the Scanning acoustic macroscope data, to calculate attenuation and speed of sound.

A.5.1. SAM main program to enter and calculate data

```
clear;
close all;
% ---------------------------------------------------------
% Creates an GUI input dialog box to allow the user to enter
% the appropriate input parameters.
prompt = {
'Enter the reference file name without the extension(*.vol):',
'Enter the data file name without the extension(*.vol):',
'Enter the sampling frequency of ADC (MHz): ',
'Enter the thickness of the sample (cm):  ',
'Enter the reference speed of sound (m/s): ',
'Enter the attenuation/gain difference (dB): '
'Enter the probe frequency in MHz : ',
'Enter the size of image in the X direction : ',
'Enter the size of image in the Y direction : ',
'Enter the pixel size in mm : ';
'Enter the fast direction : ' };
title = 'Parameters for analysis of Ultrasound Acoustic properties';
lines = 1;
% ---------------------------------------------------------
% Default settings and parameters
def = {
'c:\samdata\',
'c:\samdata\',
'100'
'0.46'
'1485'
'0'
'7'
'16'
'16'
'1'
'x'};
answer = inputdlg(prompt, title, lines, def);
f = {'refname' 'dataname' 'samp_freq' 'thickness' 'ref_speed' 'gain' 'probe' 'X_sc' 'Y_sc' 'pixel_size'
'fast'};
s = cell2struct(answer, f, 1);
% ---------------------------------------------------------
% Checks and splits data obtained from input dialog box
% into relevant information for the software.
% If a question mark is placed in the box then the user
% is allowed to search for a file
if s.refname == '?'
 [refname2,refpath] = uigetfile('c:\attenuation_data\*.vol','Select reference file');
 s.refname=strcat(refpath,refname2);
end
if s.dataname == '?'
 [dataname2, datapath] = uigetfile('c:\attenuation_data\*.vol', 'Select data file');
 s.dataname = strcat(datapath,dataname2);
```

```
end
% ------------------------------------------------------
% Value of the sampling frequency in MHz
sampling_frequency = str2num(s.samp_freq);
sampling_frequency = sampling_frequency * 1000000;
%Value of the thinkness of the tissue sample
thick = str2num(s.thickness);
% Reference speed of sound (in water as default)
reference_speed = str2num(s.ref_speed);
reference_speed = reference_speed*100; % Convert to cm/s
% Value of the attenuation obtained from the acquisition program
atten = str2num(s.gain);
% Value of the frequency of the probe
probe_frequency = str2num(s.probe);
probe_frequency = probe_frequency*1000000;
% Value of the X and Y scan lines
X_scan = str2num(s.X_sc);
Y_scan = str2num(s.Y_sc);
pix_size = str2num(s.pixel_size);
fast_dir = (s.fast);
% ------------------------------------------------------
% Allows the user to enter the file name
% and assigns it to a .vol file extension
% and then opens the file ready for reading
filename_string_ref = [s.refname,'.vol'];
infile_ref = fopen(filename_string_ref,'r');
% Returns an error if the file is not found
if infile_ref == -1;
 error(['Cannot find the file: ',filename_ref,'.vol']);
end;
filename_string_data = [s.dataname,'.vol'];
infile_data = fopen(filename_string_data,'r');
% Returns an error if the file is not found
if infile_data == -1;
 error(['Cannot find the file: ',filename_data,'.vol']);
end;
% ------------------------------------------------------
% Rewinds the file to the start and then opens it
%fseek (infile_ref,1024,'bof');
%[header] = fread(infile_ref,5120,'char');
fseek(infile_ref,0,'bof');  % Rewinds pointer to start of file
[ref_data,count_ref] = fread(infile_ref,inf,'int8');    % Reads in file to end
ref_data = ref_data(20481:count_ref);   % Assigns data to variable and misses header data
% ------------------------------------------------------
% Works out and scales the data appropriately
% These three following sections of code are used to
% allign the data for measurement
% Section1
squared_ref_data = ref_data .* ref_data;
ave_ref_data = mean(ref_data(1:1000));
squared_ref_data = squared_ref_data - ave_ref_data;
max_ref_data = max(squared_ref_data);
scaled_ref_data = squared_ref_data/max_ref_data;
% ------------------------------------------------------
% Filters the data to create a logical mask
% to allign the data pulses
% Section2
```

```
filter_order = 3;
cutoff_freq = probe_frequency/2;
lowpass = cutoff_freq / (sampling_frequency / 2);
[B,A] = butter(filter_order, lowpass);
filtered_ref_data = filtfilt(B,A,scaled_ref_data);
mask_ref_data = filtered_ref_data > 0.05;
clear scaled_ref_data filtered_ref_data;
% ---------------------------------------------------------
% Obtains the number of peaks and points
% and creates an index for alligning the pulses
% Section3
count_peaks = 0;
for i = 1:length(mask_ref_data) - 1
 if     mask_ref_data(i) < mask_ref_data(i+1)
  count_peaks = count_peaks + 1;
  index(count_peaks,1) = i;
 end;
end;
clear cutoff_freq lowpass B A mask_ref_data squared_ref_data;
num_points = round(length(ref_data) / count_peaks);
start_position = round(0.25 * num_points);  % calculates the start position of the pulse
end_position = round(0.75 * num_points);        % calculates the end position of the pulse
count = 0;
for i = 2:length(index) - 2
 count = count + 1;
 split_ref_data(:,count) = ref_data(index(i) - start_position :(index(i) + end_position));
end;
cwd = pwd;
cd(tempdir);
pack
cd(cwd)
% ---------------------------------------------------------
% Rewinds the file to the start and then opens it
fseek(infile_data,0,'bof'); % Rewinds pointer to start of file
[data,count_data] = fread(infile_data,inf,'int8');  % Reads in file to end
data = data(20481:count_data);  % Assigns data to variable and misses header data
% Alligns the pulses and stores them into an array
% the data is setup so that it will store a pulse
% with 1/4 of the pulses proceeding the pulse and
% 3/4 of the pulses following the pulse.
count = 0;
for i = 2:length(index) - 2
 count = count + 1;
 split_data(:,count) = data(index(i) - start_position :(index(i) + end_position));
end;
% Calculates a 256 point fft for the split data
subplot(2,1,1); plot(split_ref_data);
grid; TITLE('Reference split data'); xlabel('Number of Points');
subplot(2,1,2); plot(split_data);
TITLE('Attenuated signal data split into arrays');
xlabel('Number of Points'); grid; zoom; pause
% ---------------------------------------------------------
% input dialog box
prompt = {
'Enter the start point of the window :',
'Enter the end point of the window :'};
title = 'Graph window';
```

```
lines = 1;
%-------------------------------------------------------
% Default settings and parameters

def = {
'70'
'250'};
answer = inputdlg(prompt, title, lines, def);
f = { 'start' 'end' };
s1 = cell2struct(answer, f, 1);
close all;
% Obtains the values of the start and end points of the window
start_point = str2num(s1.start);
end_point = str2num(s1.end);
start_position = round(0.25 * num_points) - start_point;
end_position = end_point - round(0.25 * num_points);
clear split_ref_data split_data;
count = 0;
for i = 1:length(index) - 2
 count = count + 1;
 split_ref_data(:,count) = ref_data(index(i) - start_position :(index(i) + end_position));
% stores each pulse into an array for furture manipulation
 split_data(:,count) = data(index(i) - start_position :(index(i) + end_position));
end;
clear ref_data data;
cwd = pwd;
cd(tempdir);
pack
cd(cwd)
% -------------------------------------------------------
% Function to calculate the attenuation due to a sample
[pwr_ref,pwr_data,att,attenuation,ave_attenuation,att_freq,ave_att_freq,ave_data_fft,ave_ref_fft,freq_
mhz] = sam_att_calc(index,split_ref_data,split_data,sampling_frequency,atten,thick);
cwd = pwd; cd(tempdir);
pack
cd(cwd)
% Function to calculate the speed of sound in a sample
 [sample_speed,ave_sample_speed,ave_speed_std]=sam_speed_calc(index, count_peaks,
split_ref_data, split_data, sampling_frequency, reference_speed, thick, probe_frequency);
cwd = pwd; cd(tempdir);
pack
cd(cwd)
% Creates image matrix for display later
% Function to construct the attenuation and speed images
 [rf_image,speed_image] =
sam_recon_images(pix_size,count_peaks,attenuation,X_scan,sample_speed);
cwd = pwd; cd(tempdir);
pack
cd(cwd)
% Clears all irrelevant data and variables
clear pwr data_fft count start_position end_position header;
clear data filtered_data mask_data lowpass filter_order;
clear squared_data scaled_data ref_data i maxdata A B;
clear ans count_data count_ref cutoff_freq ave_ref_data;
clear filtered_ref_data mask_ref_data scaled_ref_data;
clear squared_ref_data max_data max_ref_data ref_fft;
clear ave_data anwser def f infile_data infile_ref;
```

```
clear lines num_points prompt title thickness2 reference_speed;
clear atten filename_string_data filename_string_ref gain2;
clear speed ave_att count1 count2;
clear answer temp split_data split_ref_data s1 index_ref index_data;
clear filtered_split_ref_data filtered_split_data index temp1 temp2;
clear image i1 frequency zero_index1 zero_index2 start_point;
clear end_point fast_dir cwd count_peaks probe_frequency;
% ------------------------------------------------------
% Allows the user to save the data at the end of the calculation
out_name1 = s.dataname;
out_name2 = '-output';
out_name3 = '.mat';
out_name = strcat(out_name1,out_name2,out_name3);
[output2,outputpath] = uiputfile(out_name,'Save file name');
s.outputname=strcat(outputpath,output2);
output_string = [s.outputname];
%clear out_name out_name1 out_name2 out_name3 outputpath;
eval(['save ' output_string ]);
```

A.5.2. SAM function used to calculate the attenuation.

```
function
[pwr_ref,pwr_data,att,attenuation,ave_attenuation,att_freq,ave_att_freq,ave_data_fft,ave_ref_fft,freq_
mhz] = sam_att_calc(index,split_ref_data,split_data,sampling_frequency,atten,thick);
frequency = ((0 : 2048 - 1) * sampling_frequency / 2048)';
frequency = frequency(1:512);
freq_mhz = frequency/1000000;
 count = 0;
 for i = 1:length(index) - 2
 count = count + 1;
 ref_fft = fft(split_ref_data(:,count),2048);
 pwr =  ref_fft .* conj(ref_fft) / 2048;
 temp = abs(pwr);
 temp = temp(1:512);
 pwr_ref(:,count) = temp;
 max_pwr_ref(:,count) = max(temp);
 data_fft = fft(split_data(:,count),2048);
 pwr2 =  data_fft .* conj(data_fft) / 2048;
 temp2 = abs(pwr2);
 temp2 = temp2./(10^(atten/10));
 temp2 = temp2(1:512);
 pwr_data(:,count) = temp2;
% Elimnates all zeros from the FFT's and assigns a very small value to that point
 zero_index1 = find(pwr_ref == 0);
 zero_index2 = find(pwr_data == 0);
 pwr_ref(zero_index1) = 0.0000001;
 pwr_data(zero_index2) = 0.0000001;
% Calculates the Attenuation
 att(:,count) = (pwr_data(:,count) .\ pwr_ref(:,count));
 attenuation(:,count) = ((10/(2 * thick)) * log10(att(:,count)));
 att_freq(:,count) = ((attenuation(:,count)).\freq_mhz);
end;
clear frequency temp ref_fft pwr pwr2;clear temp2 ref_data data;clear pwr pwr2 ref_fft temp temp2;
max_ref_fft = max(max_pwr_ref);
pwr_ref = (pwr_ref / max_ref_fft)*100;
clear max_pwr_ref;
pwr_data = (pwr_data / max_ref_fft)*100;
```

```
clear max_ref_fft start_point end_point;
ave_ref_fft = mean(pwr_ref');
ave_ref_fft = mean(pwr_ref');
ave_data_fft = mean(pwr_data');
ave_att = mean(att');
ave_attenuation = ((10 / (2 * thick)) * log10(ave_att));
ave_att_freq = (ave_attenuation ./ freq_mhz');
ave_attenuation =ave_attenuation';
ave_att_freq =ave_att_freq';
ave_data_fft = ave_data_fft';
ave_ref_fft = ave_ref_fft';
clear max_ref_fft;
clear frequency temp ref_fft pwr pwr2;
clear index temp2 ref_data data;
clear pwr pwr2 ref_fft temp temp2;
% clear index split_ref_data split_data sampling_frequency atten thick;
```

A.5.3. SAM function used to calculate the Speed of Sound.

```
function [sample_speed,ave_sample_speed,ave_speed_std]=sam_speed_calc(index, count_peaks,
split_ref_data, split_data, sampling_frequency, reference_speed, thick, probe_frequency);
% Filters the data and calculates the indexes for the speed
% of sound calculations. This is done by obtaining the peak
% of the squared signal and then finding the corresponding
% point.
clear temp temp2;
filter_order = 3;
cutoff_freq = probe_frequency;
lowpass = cutoff_freq / (sampling_frequency / 2);
[B,A] = butter(filter_order, lowpass);
count = 0; count1 = 0; count2 = 0;
for i = 1:count_peaks - 2
 count = count + 1;
 temp = split_data(:,count) .* split_data(:,count);
 filtered_split_data(:,count) = filtfilt(B,A,temp);
 temp2 = split_ref_data(:,count) .* split_ref_data(:,count);
 filtered_split_ref_data(:,count) = filtfilt(B,A,temp2);
end;
clear temp temp2 count split_data split_ref_data;
% ------------------------------------------------------
for i = 1:count_peaks - 2
 count1 = count1 + 1;
 temp1 = filtered_split_ref_data(:,count1);
 max_ref_data = max(temp1);
 index_ref(:,count1) = find(temp1 == max_ref_data);
 count2 = count2 + 1;
 temp2 = filtered_split_data(:,count2);
 max_data = max(temp2);
 index_data(:,count2) = find(temp2 == max_data);
end;
index_ref = index_ref';
index_data = index_data';
clear temp temp2 max_data max_ref_data count1;
clear filtered_ref_data filtered_data;
% ------------------------------------------------------
% Calculation of the speed of sound
speed = (1 / reference_speed) - (((index_ref - index_data) / sampling_frequency) / (2 * thick));
```

```
sample_speed = (1 ./ speed) ./ 100;
ave_sample_speed = mean(sample_speed);
ave_sample_speed = ave_sample_speed';
ave_speed_std = std(sample_speed);
clear speed;
```

A.5.3. SAM function used to generate 3D attenuation image array.

The function used to generate a 3D image array of attenuation, depending on frequency and an image of speed within the material for display.

```
function [rf_image,speed_image] =
sam_recon_images(pix_size,count_peaks,attenuation,X_scan,sample_speed);
pix_size1 = pix_size / 2;
pix_size2 = pix_size;
pix = (round(1 / pix_size2 * X_scan));
index = 1:(pix):count_peaks - 1;
count = 0;
count1 = 0;
pix_size1 = pix_size / 2;
pix_size2 = pix_size;
pix = (round(1 / pix_size2 * X_scan));
index = 1:(pix):count_peaks - 1;
count = 0;
count1 = 0;
for i = 1:length(attenuation(:,1)) - 1
    count = count + 1;
    temp = attenuation(count,:)';
    count1 = 0;
    for i1 = 1:length(index) - 1
       count1 = count1 + 1;
       image(:,count1) = temp(index(i1):(index(i1 + 1)-1));
    end;
    image2 = flipud(image);
    rf_image(:,:,count) = image2;
 end;
 % Reconstructs the speed of sound image
count = 0;
for i1 = 1:length(index) - 1
   count = count + 1;
   speed_image2(:,count) = sample_speed(index(i1):(index(i1 + 1)-1));
end;
speed_image = flipud(speed_image2);
clear image count count1
```

A.5.4. Hydrophone analysis routine to calculate pressure wave and PSE.

Hydrophone analysis programs main components used within Chapter 3. Matlab program used to calculate the acoustic pressure plots and PSE for the hydrophone analysis.

```
clear
load ue260_mod.mat
close all
N=1000;
b=1:N;
Fs = 500000000;
Ts = 1/Fs;
count1 = 1;
count2 = 0;
frs = (b-1)/N*Fs;
frsa =frs(1:128);
ue260_5mhz_ax1 = (ue260_5mhz_ax/0.0465)/7.6;
ue260_75mhz_ax1 = (ue260_75mhz_ax/0.04775)/7.5;
ue260_10mhz_ax1 = (ue260_10mhz_ax/0.0485)/7.5;
for i1 = 1:15
        count1 = count1+1;
        count2 = count2+1;
        xa = ue260_5mhz_ax1(:,count1);
        xa1 = power(xa,2);
        ppi5(:,count2) = cumtrapz(xa1);
        Xa(:,count2) = fft(xa);
        pwra(:,count2) = Xa(:,count2).*conj(Xa(:,count2))/N;
        tmp = pwra(:,count2);
        pwrs5(:,count2) = tmp(1:128);
end
max_pwrs5 = max(pwrs5);
max_pwrs52 = max(max_pwrs5);
norm_pwrs5 = pwrs5./max_pwrs52;
figure
        plot(ue260_5mhz_ax(:,1),ue260_5mhz_ax1(:,5),'r');
        hold
        plot(ue260_5mhz_ax(:,1),ue260_5mhz_ax1(:,9),'b');
        plot(ue260_5mhz_ax(:,1),ue260_5mhz_ax1(:,13),'g');
        grid
        ylabel('Acoustic Pressure (MPa)');
        xlabel('Time (s)');
figure
        bar(frsa,norm_pwrs5(:,8))
        hold
        bar(frsa,norm_pwrs5(:,12),'g')
        bar(frsa,norm_pwrs5(:,4),'r')
grid
ylabel('Normalised Power Magnitude');
xlabel('Frequency (Hz)');
```

A.5.5. Hydrophone analysis routine to reconstruct lateral beam plots.

Chapter 4. Matlab program used to produce the beam plots from the lateral data acquired during the hydrophone measurements.

```
clear all
close all
load ue260_mod2.mat
r = length(generic_dist);
tm = max(lat_time1ms);
t_scale = (2*tm)/500;
temp_lata = (ue260_MI1_lat/0.04775)/7.5;
temp_lat = 0.0125+temp_lata;
x = 1:499;
% scaling to convert from Time to distance data.
rotation = 16; % Hz
time_rot = 1/rotation;
time_per_deg = time_rot/360;
trans_diameter = 10.7; % mm
radius = trans_diameter/2;
Circ = 2*pi*radius;
Dist_deg = Circ/360;
speed = Circ/time_rot;
time_per_point = 20e-6;
sam_rate = 1/time_per_point;
dist_per_point = speed * time_per_point;
ang_per_point = atand(dist_per_point / radius);
ang_per_point_half = atand(2*(dist_per_point) / radius);
plot_point = tand(ang_per_point_half)*(generic_dist + radius);
tot_plot_dist = (tand(ang_per_point_half)*(generic_dist + radius))*499;
tot_plot_dista = round(tot_plot_dist *100);
scale = tot_plot_dista/(min(tot_plot_dista));
num_point = round(scale * 499);
m12 = 2000; % or 2000 for the + radius points
m12a = max(num_point);
n12 = length(num_point);
dmax = max(tot_plot_dist);
d_scale = dmax / m12a;
strt_pt = round((m12 - num_point)/2);
strt_pta = strt_pt+(num_point-1);
 [bs,as] = butter(3,(4000/(sam_rate/2)));

clear a pos_lata pos_loca neg_lata neg_loca pos_lat_smth neg_lat_smth;
count = 0;
for i = 1: length(generic_dist)
   count = count+1;
   a = temp_lat(:,count);
   pos_lata, pos_loca] = findpeaks((a*1),'threshold', 0);
   pos_lat(:,count) = pos_lata *1;
   pos_loc(:,count) = pos_loca;
   neg_lata, neg_loca] = findpeaks((a*-1),'threshold', 0);
   neg_lat(:,count) = neg_lata * 1;
   neg_loc(:,count) = neg_loca;
   clear a pos_lata pos_loca neg_lata neg_loca;
end
```

```
s1 = pos_lat > 0.05;
pos_lat1 = pos_lat .*s1;
s2 = neg_lat >0.115;
neg_lat = neg_lat* -1;
neg_lat1 = neg_lat .* s2;
count = 0;
for i = 1: length(generic_dist)
        count = count+1;
        pos_lata, pos_loca] = findpeaks(pos_lat1(:,count));
        pos_y = interp1(pos_loca,pos_lata,x);
        pos_max = max(pos_loca);
        pos_min = min(pos_loca);
        neg_lata, neg_loca] = findpeaks((neg_lat1(:,count)*-1));
        neg_y = interp1(neg_loca, neg_lata,x);
        neg_max = max(neg_loca);
        neg_min = min(neg_loca);
        pos_lat_tmp = pos_lat1(:,count);
        pos_lat_tmp(pos_min:pos_max) = pos_y(pos_min:pos_max)';
        pos_lat_tmp2 = filter(bs,as,pos_lat_tmp);
        pos_lat_smth(:,count) = pos_lat_tmp2 *1;
        neg_lat_tmp = neg_lat1(:,count);
        neg_lat_tmp(neg_min:neg_max) = neg_y(neg_min:neg_max);
        neg_lat_tmp2 = filter(bs,as,neg_lat_tmp);
        neg_lat_smth(:,count) = neg_lat_tmp2 * 1;
        clear pos_lata pos_loca neg_lata neg_loca neg_lat_tmp pos_lat_tmp pos_y neg_y;
end
count = 0;
for ia = 1: length(generic_dist)
        count = count+1;
        tmpp = resample(pos_lat_smth(:,count),tot_plot_dista(count),tot_plot_dista(1));
        tmp2p = zeros(m12,1);
        tmp2p(strt_pt(count):strt_pta(count)) = tmpp(1:num_point(count));
        pos_array(:,count) = tmp2p;
        tmpn = resample(neg_lat_smth(:,count),tot_plot_dista(count),tot_plot_dista(1));
        tmp2n = zeros(m12,1);
        tmp2n(strt_pt(count):strt_pta(count)) = tmpn(1:num_point(count));
        neg_array(:,count) = tmp2n;
        clear tmpp tmp2p tmpn tmp2n;
end
d2 = 1:m12;
d12 = d_scale*d2;
t = 1:499;
t = t_scale*t;
figure
colormap(jet);
subplot(2,2,1)
surf(generic_dist,d12,pos_array,'FaceColor','interp','EdgeColor','none','FaceLighting','phong')
view([-90,90])
title('(i) Positive Wave - MI1')
ylabel('Distance (mm)');
xlabel('Hydrophone Position (mm)')
axis tight
subplot(2,2,2)
surf(generic_dist,d12,neg_array,'FaceColor','interp','EdgeColor','none','FaceLighting','phong')
view([-90,90])
title('(ii) Negative Wave - MI1')
ylabel('Distance (mm)');
```

```
xlabel('Hydrophone Position (mm)')
axis tight
subplot(2,2,3)
surf(generic_dist,d12,pos_array,'FaceColor','interp','EdgeColor','none','FaceLighting','phong')
view([180,0])
title('(iii) Peak Profile of Positive Wave - MI1')
zlabel('Acoustic Pressure (MPa)');
xlabel('Hydrophone Position (mm)')
axis tight
subplot(2,2,4)
surf(generic_dist,d12,neg_array,'FaceColor','interp','EdgeColor','none','FaceLighting','phong')
view([180,0])
title('(iv) Peak Profile of Negative Wave - MI1')
zlabel('Acoustic Pressure (MPa)');
xlabel('Hydrophone Position (mm)')
axis tight
```

A.5.6. 3D-EUS volume reconstruction and positional correction function.

Code used within Chapter 4. Program used to reconstruct the volume and positional information with the Mark 2 3D-EUS system.

```
function eus1_2
clear
close all
load EUS_settings.mat
button = questdlg('Do you want remove transducer artifact?');
button3 = strcmp('Yes', button);
button3 = strcmp('Yes', button);
button4 = strcmp('Cancel', button);
if (button3 == 1) & (button4 == 0)
   artrem = 'artifact_remove';
   mask2 = 'CM';
   ext = '.bmp';
   div = '\';
   masknamestr2 =
strcat(s.euspath,artrem,div,s.processor,div,s.scope,div,s.quadrant,s.frequency,s.eussysscale,mask2,ext)
;
   msk = imread(masknamestr2);
   msk = flipud(msk);
   msk = imcrop(msk,finalRect);
elseif (button3 == 0) & (button4 == 0)
   artrem = 'artifact_remove';
   mask2 = 'BLANK';
   ext = '.bmp';
   div = '\';
   masknamestr2 = strcat(s.euspath,artrem,div,mask2,ext);
   msk = imread(masknamestr2);
   msk = flipud(msk);
   msk = imcrop(msk,finalRect);
end
button = questdlg('Do you want to include Arm Positional Data?');
button1 = strcmp('Yes', button);
button1 = strcmp('Yes', button);
```

```
button2 = strcmp('Cancel', button);
if (button1 == 1) & (button2 == 0)
   ext = '.txt';
   div = '\';
   filenamestr = strcat(s.euspath,s.studyinit,s.studynum,div,s.studyinit,ext);
   [im_names, x3D, y3D, z3D, time3D] = textread(filenamestr, '%s %f %f %f %f', 'delimiter', ',');
   file2 = 10002;
   fileno2 = num2str(file2);
   ext = '.bmp';
   div = '\';
   filenamestr2 = strcat(s.euspath,s.studyinit,s.studynum,div,s.studyinit,fileno2,ext);
   clear fileno1 fileno2 lines x y %finalRect1 finalRect2;
   xx1 = x3D';
   xx = xx1-xx1(1);
   yy1 = y3D';
   yy = yy1-yy1(1);
   zz1 = z3D';
   zz = zz1-zz1(1);
   count = 0;
   index = 1:length(x3D);
      for i = 1:length(x3D) -1
         count  = count +1;
         i_X_Dif(count) = xx(count+1) - xx(count);
         i_Y_Dif(count) = yy(count+1) - yy(count);
         i_Z_Dif(count) = zz(count+1) - zz(count);
         i_dist(count) = sqrt((power(xx(count),2)+ power(yy(count),2)+ power(zz(count),2)));
      end;
   count = 0;
   index = 1:length(x3D);
   for i = 1:length(i_dist) -1
      count  = count +1;
      i_Difa(count) = i_dist(count+1) - i_dist(count);
   end;
   i_X_Dif';
   i_Y_Dif';
   i_Difa';
   i_dist';
   dist_t = cumsum(i_Difa);
   noframes = 500;
   i2 = imread(filenamestr2);
   i2 = flipud(i2);
   i2 = imcrop(i2,finalRect);
   x = size(i2,1);
   y = size(i2,2);
   vol = zeros(x, y, noframes);
   act_pull_dist = max(i_dist) - min(i_dist);
   sample_rate = act_pull_dist/noframes;
   i_dif = i_Difa';
   count = 0;
      for i = 1:length(i_dist) -1
         count  = count +1;
         image_ID(count) = i_dif(count)/sample_rate;
      end;
   image_ID2 = round(image_ID);
   imag = image_ID2 >= 1;
   ID = 1:length(image_ID2);
   Im_ID = imag.*ID;
```

```
pulldist=act_pull_dist/10;
vol_index =zeros(1,noframes);
count = 0;
count2 = 0;
   for i = 1:length(x3D) -2;
      count = count + 1;
      if imag(count) == 1
           samp_im = image_ID2(count);
         for i = 1 : samp_im
            count2 = count2 + 1;
            vol_index(count2) = Im_ID(count);
         end
      end
   end
count = 0;
   for i = 1:noframes - 2
     count = count + 1;
     file = 10000 + vol_index(count);
     fileno = num2str(file);
     filenamestr3 = srcat(s.euspath,s.studyinit,s.studynum,div,s.studyinit,fileno,ext);
     i2 = imread(filenamestr3);
     i2 = flipud(i2);
     i2 = imcrop(i2,finalRect);
     i3 = imsubtract(i2,msk);
     vol(:,:,count) = i3;
   end;
% Produces the scaling factors
scalingx = (finalRect(4))+1;
scalingy = (finalRect(3))+1;
scale = 1:scalingx;
x = scale * ((eusscale*10)/scalingx);
xs = (eusscale*10);
scale = 1:scalingy;
y = scale * ((eusscale*10)/scalingy);
ys = (eusscale*10);
zs = round(act_pull_dist);
zscale = 1:noframes;
z = zscale * ((zs)/noframes);
close all
clear xx yy zz i_X_Dif i_Y_Dif i_Z_Dif;
clear filenamestr fileno i i1 k title scalingx scalingy;
clear i2 i2a i1a file file1 file2 ext count scale;
clear  i2 filenamestr1 filenamestr2 filenamestr3 i3 i4;
x_size = size(vol,1);
y_size = size(vol,2);
z_size = size(vol,3);
ds_x = round((x_size / (eusscale*20)));
ds_y =  round((y_size / (eusscale*20)));
ds_z = round((z_size / (pulldist*10)));
[x_ds,y_ds,z_ds,vol_ds] = reducevolume(vol,[ds_x,ds_y,ds_z]);
clear filenamestr fileno i i1 k title scalingx scalingy;
clear i2 i2a i1a file file1 file2 ext count scale;
%pack
out_name1 = s.studyinit;
out_name1a = s.studynum;
out_name2 = '_vol_op_ps_';
out_name3 = s.studydate;
```

```
    out_name4 = '.mat';
    out_name = strcat(out_name1,out_name1a,out_name2,out_name3,out_name4);
    [output2,outputpath] = uiputfile(out_name,'Save file name');
    s.outputname=strcat(outputpath,output2);
    output_string = [s.outputname];
    clear out_name1 out_name1a out_name2 out_name3;
    eval(['save ' output_string ]);
elseif (button1 == 0) & (button2 == 0)
    prompt = {'Enter the Distance of the Endoscope Pullback in cm: '};
    title = '3D Endoscopic Ultrasound Pull Back Distance';
    lines = 1;
% ----------------------------------------------------
% Default settings and parameters
   % Default settings and parameters
    def = {''};
    answer = inputdlg(prompt, title, lines, def);
    f = {'pulldist'};
    r = cell2struct(answer, f, 1);
    clear prompt def f answer;
    pulldist = str2num(r.pulldist);
% Preload images 1 and 2 to create matrix
    file2 = 10002;
    fileno2 = num2str(file2);
    ext = '.bmp';
    div = '\';
    filenamestr2 = strcat(s.euspath,s.studyinit,s.studynum,div,s.studyinit,fileno2,ext);
% Crop the image to the desired region of interest.
    i2 = imread(filenamestr2);
    i2 = flipud(i2);
    i2 = imcrop(i2,finalRect);
    x = size(i2,1);
    y = size(i2,2);
    vol = zeros(x, y, noframes);
    clear  i2 filenamestr1 filenamestr2 i3 i4;
    clear fileno1 fileno2 lines x y %finalRect1 finalRect2;
% Loads the rest of the frames into the matrix
    count = 0;
    for i = 1:noframes - 2
       count = count + 1;
       file = 10000 + count;
       fileno = num2str(file);
       filenamestr = strcat(s.euspath,s.studyinit,s.studynum,div,s.studyinit,fileno,ext);
       i2 = imread(filenamestr);
       i2 = flipud(i2);
       i2 = imcrop(i2,finalRect);
            i3 = imsubtract(i2,msk);
       vol(:,:,count) = i3;
    end;
   % Produces the scaling factors
    scalingx = (finalRect(4))+1;
    scalingy = (finalRect(3))+1;
    scale = 1:scalingx;
    x = scale * ((eusscale*10)/scalingx);
    xs = (eusscale*10);
    scale = 1:scalingy;
    y = scale * ((eusscale*10)/scalingy);
    ys = (eusscale*10);
```

```
    zs = (pulldist*10);
    zscale = 1:noframes;
    z = zscale * ((pulldist*10)/noframes);
    x_size = size(vol,1);
    y_size = size(vol,2);
    z_size = size(vol,3);
    ds_x = round((x_size / (eusscale*20)));
    ds_y =  round((y_size / (eusscale*20)));
    ds_z = round((z_size / (pulldist*10)));
    [x_ds,y_ds,z_ds,vol_ds] = reducevolume(vol,[ds_x,ds_y,ds_z]);
    clear filenamestr fileno i i1 k title scalingx scalingy;
    clear i2 i2a i1a file file1 file2 ext count scale;
    %pack
    out_name1 = s.studyinit;
    out_name1a = s.studynum;
    out_name2 = '_vol_op_nps_';
    out_name3 = s.studydate;
    out_name4 = '.mat';
    out_name = strcat(out_name1,out_name1a,out_name2,out_name3,out_name4);
    [output2,outputpath] = uiputfile(out_name,'Save file name');
    s.outputname=strcat(outputpath,output2);
    output_string = [s.outputname];
    clear out_name1 out_name1a out_name2 out_name3;
    eval(['save ' output_string ]);
elseif(button1 == 0) & (button2 == 1)
    msgbox('Reconstruction Cancelled')
end
clear
close all
eus
```

Appendix 6. – Beam reconstructions from the GF-UE260 Scope

A.6.1. Beam reconstructions from the GF-UE260 at 5, 7.5 and 10MHz.

All plots were displayed as the positive (i) and negative (ii) lateral plots were displayed as distance against hydrophone position. The positive (iii) and negative (iv) profiles were displayed as hydrophone position (x) against signal amplitude (y).

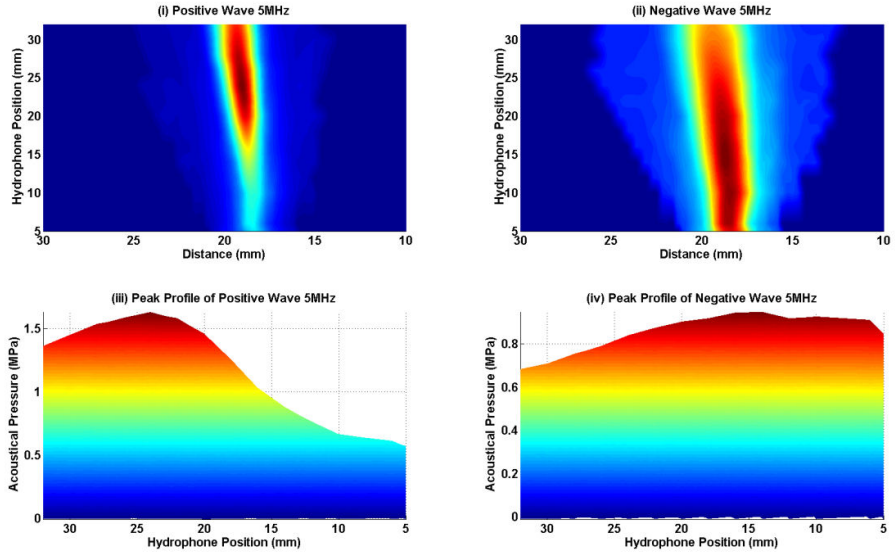

Figure A.6.1a – Plots of the hydrophone lateral measurements from the GF-UE260 echoendoscope at 5MHz.

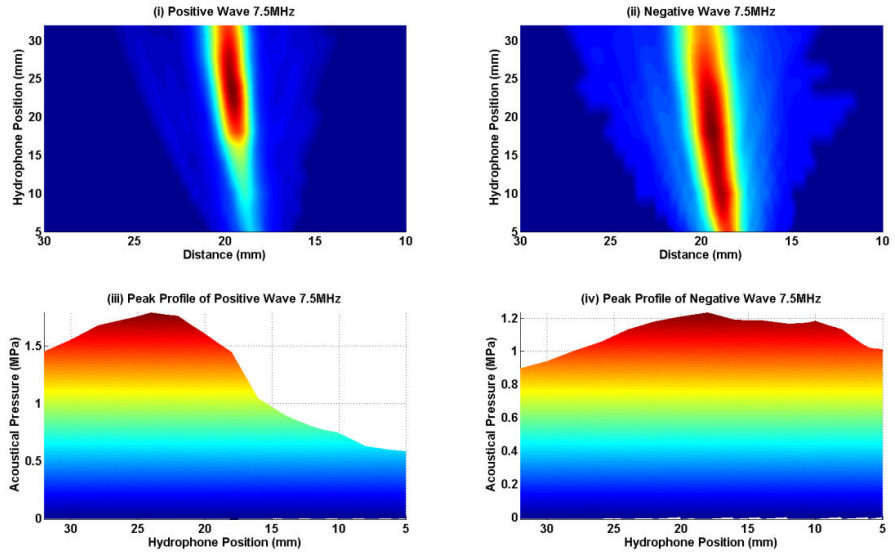

Figure A.6.1b – Plots of the hydrophone lateral measurements from the GF-UE260 echoendoscope at 7.5MHz.

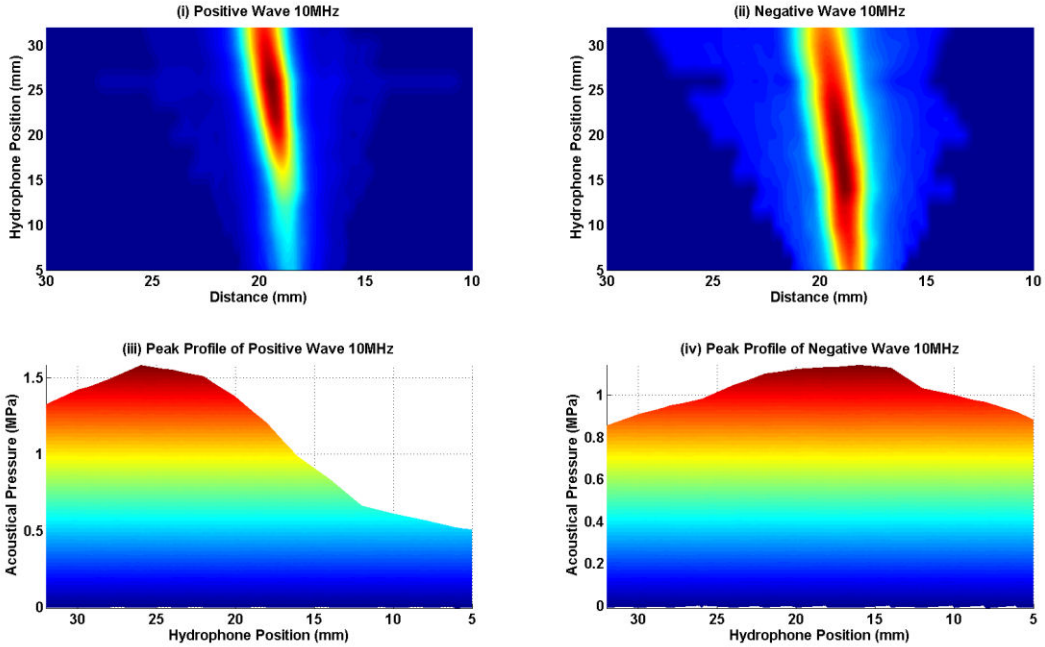

Figure A.6.1c – Plots of the hydrophone lateral measurements from the GF-UE260 echoendoscope at 10MHz.

A.6.2. Beam reconstructions from the GF-UE260 at varying focal depths.

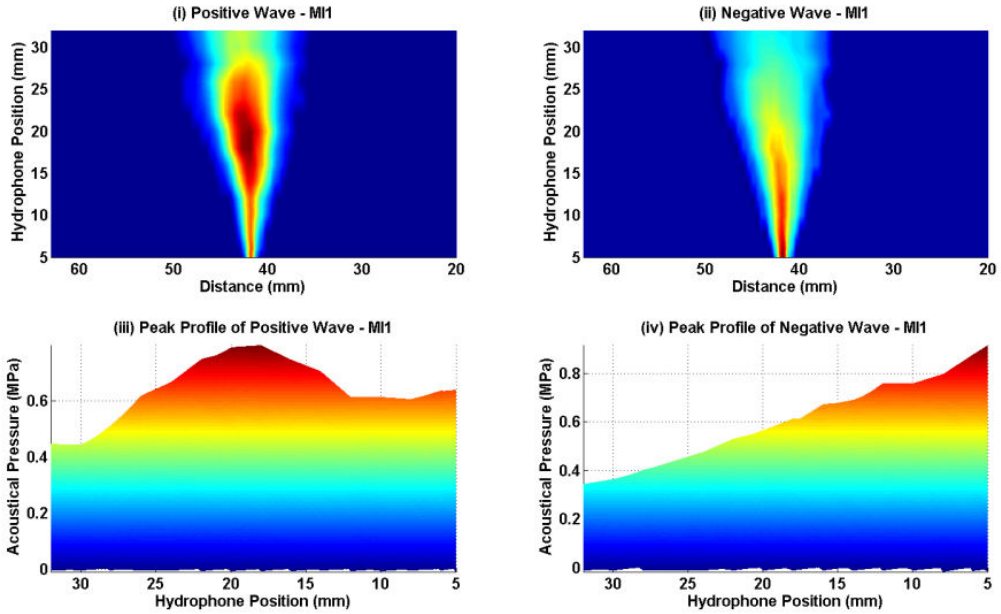

Figure A.6.2a – Plots of hydrophone lateral measurements from the GF-UE260 echoendoscope at 7.5MHz and 1st focal (F1) setting.

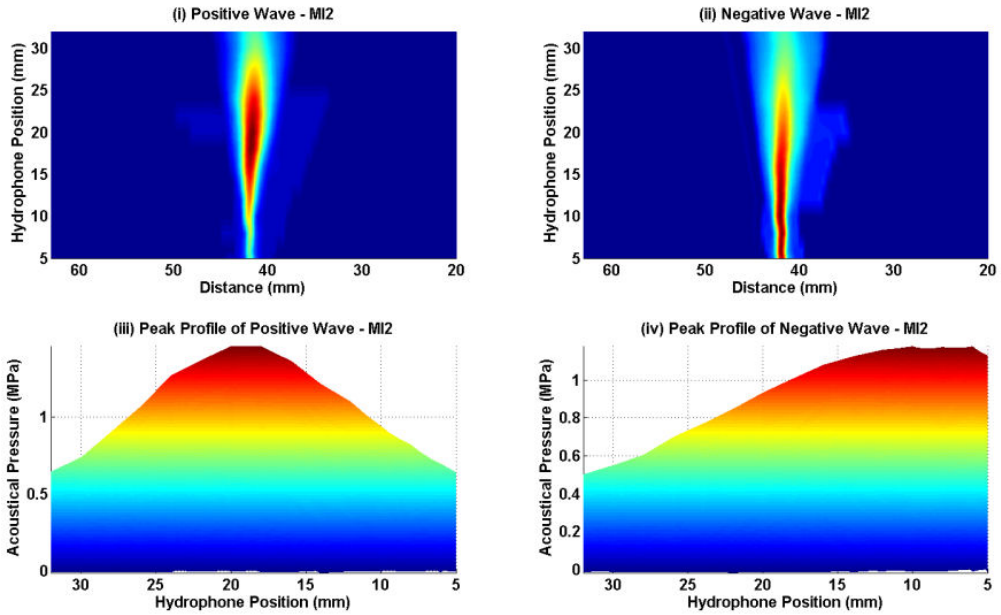

Figure A.6.2b – Plots of hydrophone lateral measurements from the GF-UE260 echoendoscope at 7.5MHz and 2nd focal (F2) setting.

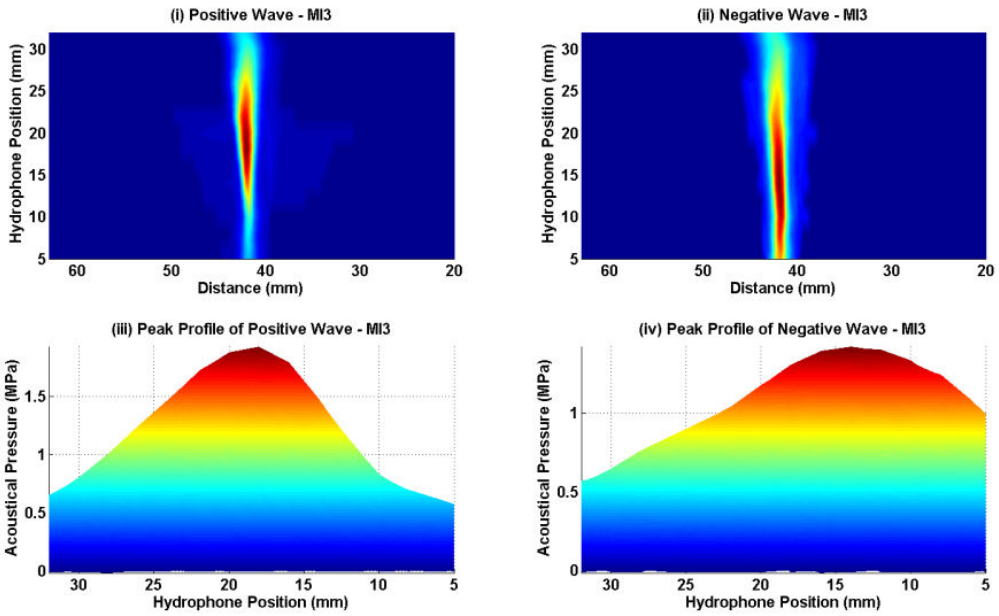

Figure A.6.2c – Plots of hydrophone lateral measurements from the GF-UE260 echoendoscope at 7.5MHz and 3rd focal (F3) setting.

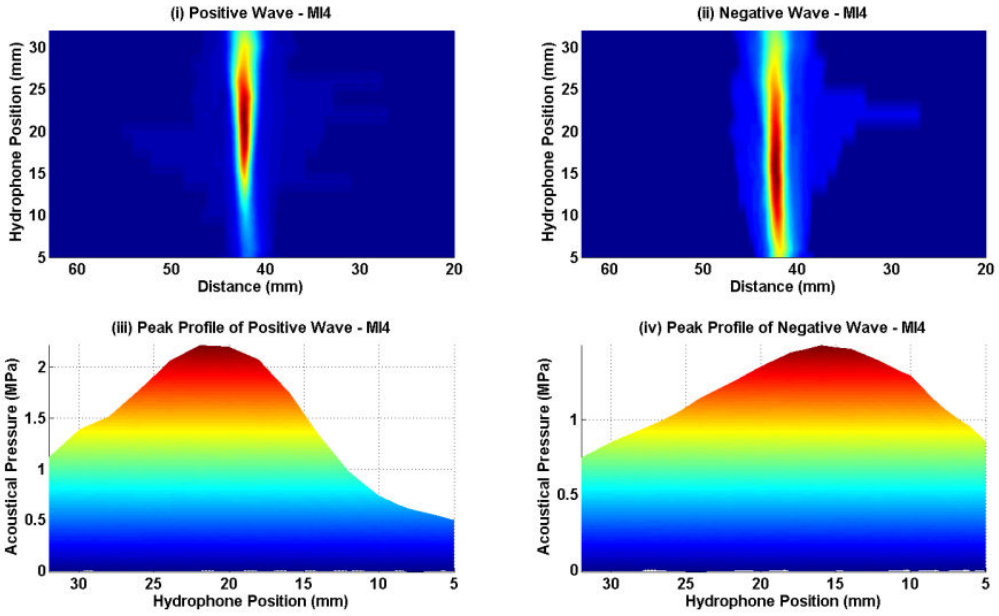

Figure A.6.2d – Plots of hydrophone lateral measurements from the GF-UE260 echoendoscope at 7.5MHz and 4th focal (F4) setting.

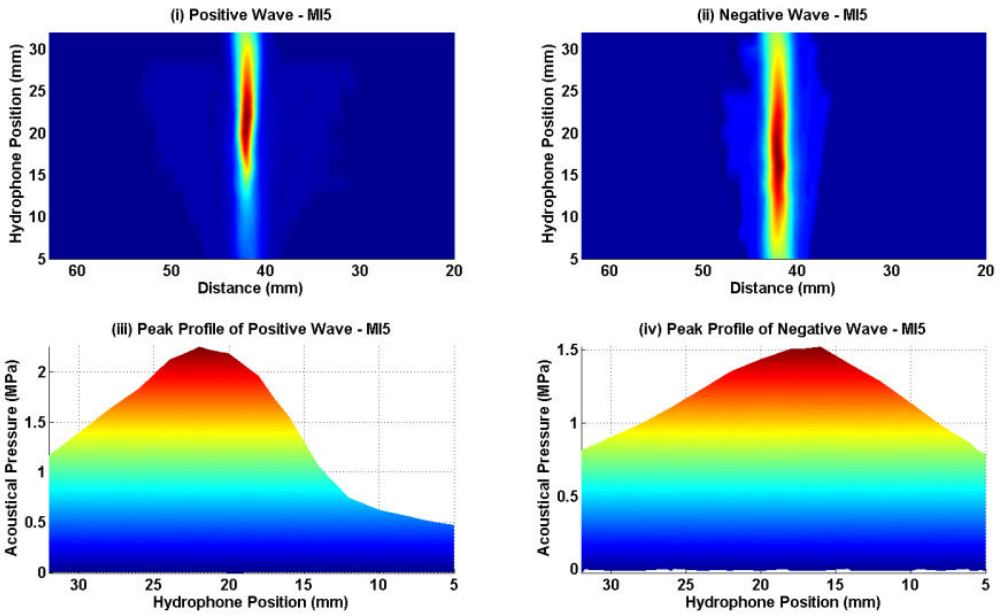

Figure A.6.2e – Plots of hydrophone lateral measurements from the GF-UE260 echoendoscope at 7.5MHz and 5th focal (F5) setting.

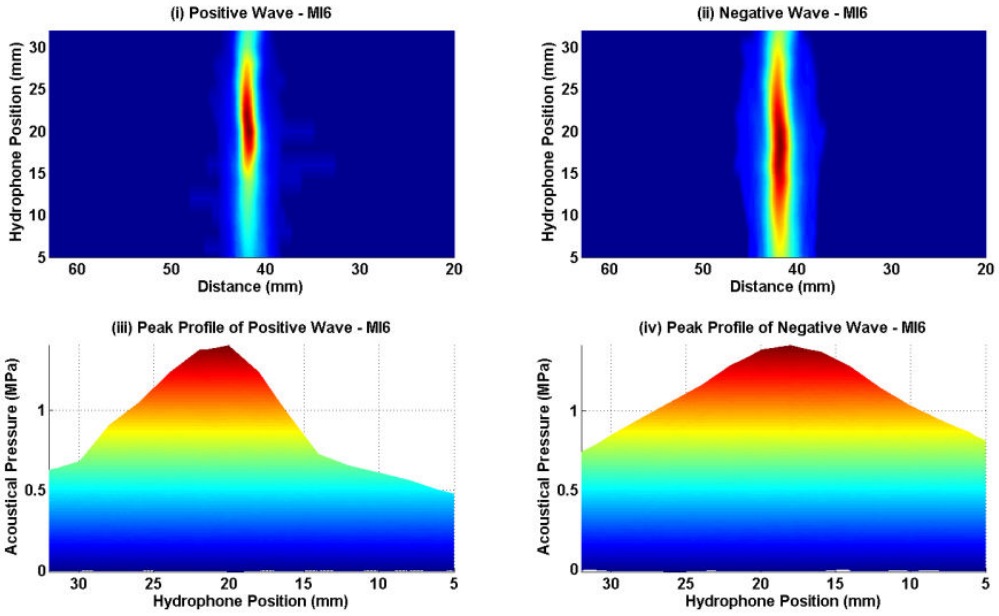

Figure A.6.2f – Plots of hydrophone lateral measurements from the GF-UE260 echoendoscope at 7.5MHz and 6th focal (F6) setting.

Appendix 7. - Patient results obtained during the studies.

The following results were tabulated and derived from the analysis of the conventional EUS examinations and the 3D-EUS volume reconstructions acquired from patients referred for EUS, to stage early and advanced upper GI cancer.

Table A.7.1 contained the results obtained from the retrospective study of the 16 patients diagnosed with T1 tumours and staged with the Royal Infirmary of Edinburgh between the years of 2002 and 2008. Tables A.7.2 and A.7.3 detail the results obtained from the 24 cases of advanced oesophageal cancer treated at the Royal Infirmary of Edinburgh between the years of 2002 and 2007.

Table A.7.1 – Tabulated results of the 16 patients studied from 2002 to 2008 including demographics, stage and treatment received. Location of Ca was either Oes - Oesophagus or OGJ - Oesophago-Gastric Junction. Treatment abbreviations were ER- Endoscopic Resection and RT - Radiotherapy.

Pat. No.	Age	Sex	Location of Ca	T (2D)	N (2D)	T (3D)	N (3D)	Location	Location (2D) (cm)	Location (3D) (mm)	OGJ Location (mm)	Treatment
1	74	F	Oes	T1	N1	T1	N1	Upper	23 - 27	240 - 278	33	ER
2	76	F	Oes	T1	N0	T1	N0	Mid	28 - 30	280 - 305	40	ER
3	82	M	Oes	T1		T1		Mid	30 - 33	295 - 330	38	RT
4	67	M	Oes - OGJ	T1	N0	T1	N0	Lower	38 - 39	370 - 380	40	Surgery
5	67	M	Oes - OGJ	T1	N0	T1	N0	Lower	38 - 39	375 - 395	39	Surgery
6	78	M	Oes - OGJ	T1	N1	T1	N1	Lower	35 - 40	277 - 330 & 360 - 395	40	ER
7	65	M	Oes - OGJ	T1	N	T1	N0	Lower	31 - 36	310 - 358	25	Surgery
8	56	F	Oes	T1	N0	T1	N0	Mid	28 - 30	280 - 310	39	Surgery
9	75	F	Oes	T2	N0	T1	N0	Mid	29 - 31	290 - 310	31	Surgery
10	47	M	Oes - OGJ	T1		T1		Lower	37 - 39	375 - 390	39	RT
11	81	F	Oes	T1	N0	T1	N0	Mid	26 - 28	255 - 282	40	RT
12	73	M	Oes	T1	N0	T1	N0	Mid	31 - 32	310 - 325	39	RT
13	77	M	Oes - OGJ	T1	N0	T1	N0	Lower	Lower	352 - 384		ER
14	61	M	Oes	T1	N1	T1	N1	Mid	32 - 34	285 - 362	40	Surgery
15	74	M	Oes - OGJ	T1	N0	T1	N0	Lower	42	410 - 420	42	ER
16	64	M	Oes	T1	N0	T1	N0	Mid	26 - 30	260 - 310	40	Surgery

Table A.7.2 – A list of the patients, date of procedure and how long these patients survived post surgery.

Patient	Date of EUS performed	Length of Survival from EUS exam as of 14 / 09/ 2007 (Months)
1	17/06/2003	22
2	20/02/2007	Alive as of 14/09/2007
3	01/04/2003	52
4	26/11/2002	6
5	30/07/2002	12
6	13/04/2004	38
7	16/05/2006	Alive as of 14/09/2007
8	21/06/2005	5
9	14/03/2006	7.5
10	10/05/2005	10
11	15/07/2003	3.5
12	31/01/2006	Alive as of 14/09/2007
13	02/11/2004	Alive as of 14/09/2007
14	15/11/2005	Alive as of 14/09/2007
15	21/02/2006	Alive as of 14/09/2007
16	11/07/2006	Alive as of 14/09/2007
17	22/06/2004	22.5
18	24/05/2005	Alive as of 14/09/2007
19	31/05/2005	1.5
20	01/03/2005	Alive as of 14/09/2007
21	27/07/2004	Alive as of 14/09/2007
22	24/09/2002	35
23	18/04/2006	Alive as of 14/09/2007
24	16/03/2004	16.5

Table A.7.3 - Demographics and results of the 24 cases of the advanced cancer staging and each case progressed to surgical resection, NACR - Neo-Adjuvant Chemotherapy and RT - Radiotherapy.

Pat	Standard EUS Stage		3D EUS Stage		Pathological Stage			% stage of Ca from 3D-EUS			Num. of Nodes		Delay of EUS to Path result	Pre-surgical treatment	Involved nodes from pathology	
	T	**N**	**T**	**N**	**T**	**N**	**M**	**T3**	**T2**	**T1**	**3D**	**2D**	**(mnths)**		**Mal.**	**Tot.**
1	T1	N0	T3	N0	T3	N1	Mx	53.7	3	43.3	1		2	NACR	3	32
2	T3	N1	T3	N1	T3	N1	Mx	79.2	16.9	3.9	18	1	2.5	NACR	3	31
3	T1	N0	?T2	N0	T3	N1	Mx	25.8	25.8	48.4	2		1.5	NACR	9	15
4	T2	N1	T3	N1	T3	N1	Mx	23.5	61.8	14.7	3		0.5	NACR	3	17
5	T2	N1	T3	N1	T3	N1	Mx	34.8	13	52.2	9		3	NACR	1	22
6	T2	N0	T3	N1	T3	N1	Mx	32	34	34	2		1.5	None	1	13
7	T2/3	N1	?T3	N1	T3	N1	Mx	52.4	32.8	14.8	7	2	2.5	NACR	2	10
8	T3	N1	T3	N1	T3	N1	Mx	47	27.7	25.3	5		2	NACR	11	11
9	T3	N1	T3	N1	T3	N1	Mx	62	21	17	11	7	2	NACR / RT	1	11
10	T3	N1	T3	N1	T3	N1	Mx	33	37	30	7		2.5	NACR	2	39
11	T3	Nx	T3	Nx	T3	N1	Mx	45.5	22.8	31.7	5		3	NACR	1	22
12	T3	N1	T3	N1	T3	N1	Mx	51.6	13.4	35	6	2	2.5	NACR	3	27
13	T3	N1	T3	N1	T3	N1	Mx	54	23.7	22.3	4		1.5	RT	5	36
14	T3	N1	T3	N1	T3	N1	Mx	32.2	40.2	27.6	14	6	0.5	None	1	19
15	T3	N1	T3	N1	T3	N1	Mx	8	15	77	6	2	1	NACR	6	24
16	T3	N0	T3	N1	T3	N1	Mx	69.5	14.3	16.2	6	3	2	None	2	31
17	T3	N1	T3	N1	T3	N1	Mx	55	37.5	7.5	4		0.5	NACR	1	44
18	T3	N1	T3	N1	T3	N1	Mx	8.1	25.9	66	9		2.5	None	14	20
19	T3	N1	T3	N1	T3	N1	Mx	28.4	26.3	45.3	8		1	NACR	1	20
20	T3	N1	T3	N1	T3	N1	Mx	30.7	34.7	34.6	5		2	NACR	1	35
21	T2	N1	T3	N1	T3	N1	Mx	34.5	29.8	35.7	7		0.5	None	4	18
22	T3	N1	T3	N1	T3	N1	Mx	86	14		7	3	0	None		
23	T3	N1	T3	N1	T3	N1	Mx	57.4	24.1	18.5	2	1	1	NACR		
24	T3	N1	T3	N1	T3	N1	M1a	49.2	6.6	44.2	4		2	NACR	3	34

Appendix 8. – TMM Stirrer Design

There was much debate from the users of the TMM manufacturing setup what would be the best design for a stirrer to be used in the manufacturing process. A significant problem that was faced in the 'cooking' of the TMM was loss of particles, due to inadequate stirring of large volumes. This was evident due to deposits of silicon carbide particles observed at the bottom of the mixing beaker. A number of modifications were performed on the initial stirrer which employed a coil at the base and a custom designed paddle arrangement to stir the middle of the material (figure A.8.a). The coil arrangement was effective during the initial manufacture of older phantoms and objects that were made from smaller volumes. However as the volume of TMM increased, the coil / paddle combination could not move material at the edges of the mixing beaker.

Figure A.8.b show a customised commercial stirrer. This consisted of a base stirrer with 4 fins downward facing to obtain movement at the bottom of the beaker. Then 4 fins were attached to the top of the base to provide movement in the middle segment of the beaker. Holes were drilled into the fins and base to reduce drag on the material and minimise the possibility of a vortex being produced. This design produced effective movement of the material. However, there were 'dead' areas where the SiC particles settled during the mixing process.

The third stirrer (figure A.8.c) was based on a helical design where theoretically the particles would be drawn from the bottom of the beaker and transported to the top of the material and then allowed to sink. The arrow on the diagram shows the movement of the material as the helical blades spiral up. However, there was significant particle settling at the base of the large central shaft of the stirrer.

The final stirrer (figure A.8.d) I designed was to try and eliminate a lot of the problems observed from the previous designs and remove the limitations of modifying commercial stirrers and obtaining reduced efficiency. A single large paddle design was chosen as it would minimise the 'dead' area created under a central shaft and obtain substantial movement of material throughout the beaker. The 'S' shape design was incorporated to try and 'scoop' particles off the bottom of the beaker at the leading edge of the paddle. The curved top of the leading edge provided a smoothing effect to the stirring process. The following edge of the paddle, top of the 'S', would draw the material down to the bottom of the beaker and obtain an even mix. The arrows on figure A.8.d show the movement of the material as the stirrer rotates in the beaker. Holes were drilled into the paddle to reduce drag and aid the mixing process. The single paddle stirrer was found to obtain efficient in mixing the material and left minimal to no particle residue at the bottom of the beaker. Care was taken to ensure that there was sufficient volume of material to minimise the possible production of a vortex at the top of the material.

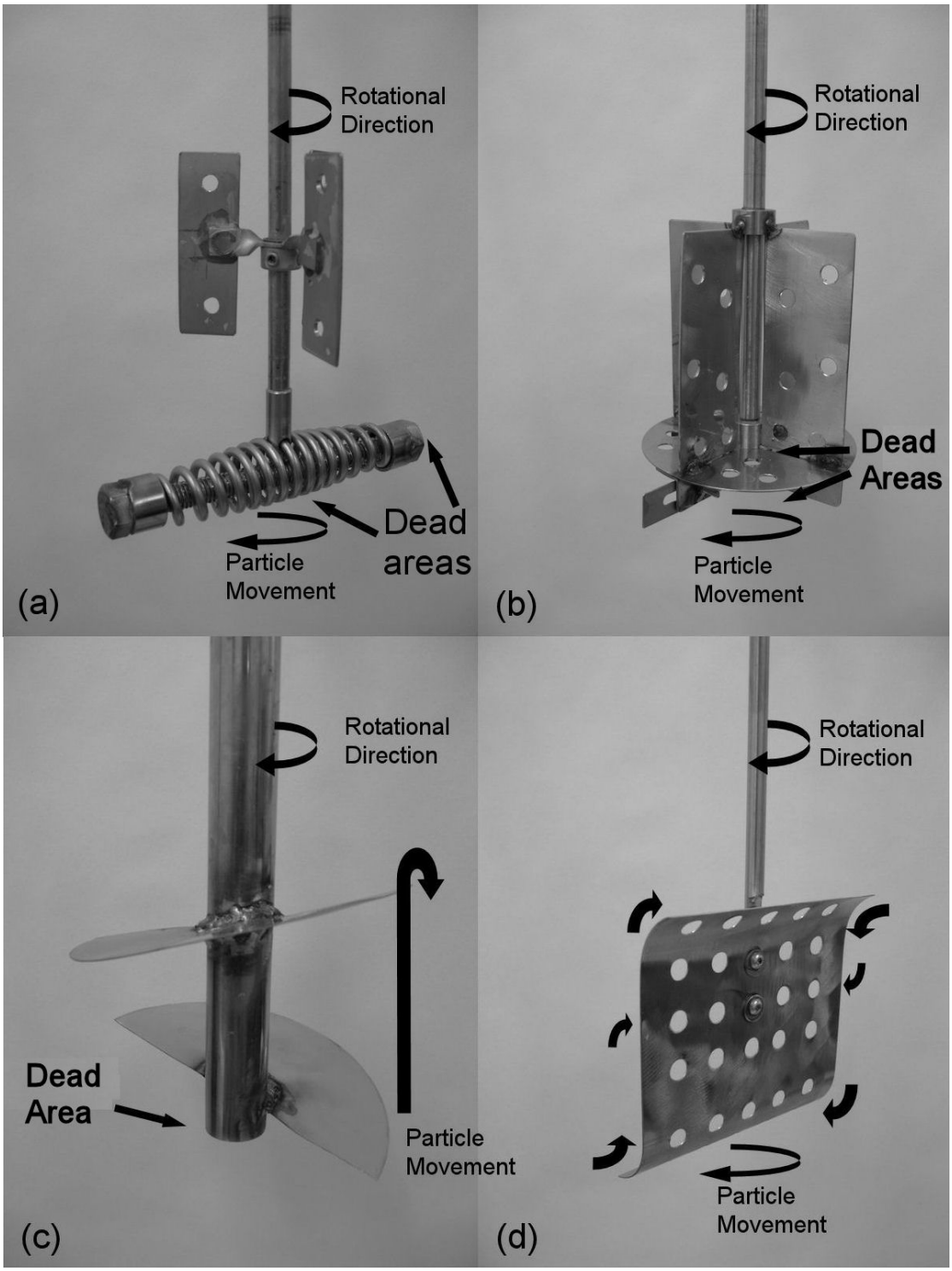

Figure A.8. - The evolution of the stirrer design. (a) A modified coil + paddle stirrer. (b) A paddle stirrer with additional fins at base to move the material at the bottom. (c) Helical style stirrer. (d) A modified 'S' shape paddle stirrer.

Appendix 9. – Published Material.

Published Papers

An anthropomorphic tissue-mimicking phantom of the oesophagus for endoscopic ultrasound
Inglis S., Ramnarine K. V., Plevris J. N., and McDicken W. N.;
Ultrasound in Medicine & Biology, Volume 32, Issue 2, February 2006, Pages 249-259

Published Abstracts

3D-EUS in the staging and accuracte localisation of early oesophageal cancer prior to treatment.
Inglis S., Paterson-Brown S., Patel D., and Plevris J.N.,
Endoscopy, Vol 38, P12 (WE10) 2006.

Value of 3D EUS in staging and detailed accuracte localisation of early oesophageal cancer prior to treatment.
Inglis S., Paterson-Brown S., Patel D., and Plevris J.N.,
GUT, Vol 55, (Suppl. 2), A58, 2006.

Could Cancer Staging And Tumour Measurements Be Improved Using 3d Endoscopic Ultrasonography?
Inglis S., Ramnarine K.V. and Plevris J.N.,
GUT, (Suppl. I) 52: A5. 2003

Comparison of 2D and 3D-EUS Diagnostic Capability on Specially Designed EUS Phantoms and Patients with Oesophageal Cancer.
Inglis S, Watson RJ, Ramnarine KV, Plevris JN.
Gastrointestinal Endoscopy 55 (5): W1486 Suppl. S147 APR 2002

A Comparison of the Measurement and Diagnostic Capabilities of 2D and 3D Endoscopic Ultrasound.
Inglis S.; Watson R.J.; Ramnarine K.V.; Christie D.; Plevris J.N.; McDicken W.N.
European J Ultrasound, Volume 15, Supplement 1, Pages 1-60, 2002

A Realistic Phantom of the Oesophagus for 3D Endoscopic Ultrasonography.
Inglis S, Ramnarine KV, Watson RJ and Plevris JN.
GUT 2001, (Suppl. I) 48: A97.

Ultrasound in Med. & Biol., Vol. 32, No. 2, pp. 249–259, 2006
Copyright © 2006 World Federation for Ultrasound in Medicine & Biology
Printed in the USA. All rights reserved
0301-5629/06/$–see front matter

ELSEVIER

doi:10.1016/j.ultrasmedbio.2005.10.005

● *Original Contribution*

AN ANTHROPOMORPHIC TISSUE-MIMICKING PHANTOM OF THE OESOPHAGUS FOR ENDOSCOPIC ULTRASOUND

SCOTT INGLIS,* KUMAR V. RAMNARINE,‡ JOHN N. PLEVRIS,† and W. NORMAN MCDICKEN§

*Medical Physics and †Centre for Liver and Digestive Disorders, NHS Lothian, University of Edinburgh, Royal Infirmary of Edinburgh, Edinburgh, UK; ‡Medical Physics, University Hospitals of Leicester NHS Trust, Leicester, UK; and §Medical Physics, University of Edinburgh, Edinburgh, UK

(*Received* 21 *July* 2005, *revised* 22 *September* 2005, *in final form* 6 *October* 2005)

Abstract—This study details the design and construct of an anthropomorphic phantom of the oesophagus suitable for use with endoscopic ultrasound (EUS) and 3-D volume measurements. The phantom was constructed using agar-based tissue-mimicking material (TMM) of different acoustical properties to simulate various anatomical and pathologic features. The acoustical properties were measured with a scanning acoustical macroscope. An Olympus GF-UM200 echo-endoscope and digital position measurement arm were used to scan the phantom at 7.5 and 12 MHz. Comparative dimensional measurements were performed on the phantom *via* 2-D and 3-D EUS. TMM attenuation varied between 0.1 and 0.5 dB/cm.MHz. Backscatter power, relative to normal TMM, was from 0 to −12.2 dB, with an average speed of sound of 1537 ± 1.9 m/s. Measurements of objects within the phantom by 2-D and 3-D EUS had mean errors of 8% and 2.2%, respectively. The construction of the anthropomorphic EUS phantom facilitated EUS training and research and development studies. (E-mail: s.inglis@ed.ac.uk) **© 2006 World Federation for Ultrasound in Medicine & Biology.**

Key Words: **Endoscopic ultrasound, Phantom, Three-dimensional, Anthropomorphic.**

INTRODUCTION

Endoscopic ultrasound (EUS) is a technique that combines endoscopy and ultrasonography. Currently, the main application of EUS in the upper gastrointestinal system is for assessment of benign and malignant lesions (Wakelin et al. 2002). Other applications include the study of the submucosal vasculature in relation to angiodysplasias of the stomach and study of oesophageal varices in patients with portal hypertension (Fusaroli and Caletti 2003; Irisawa et al. 2002, 1999). The standard diagnostic instrument for EUS uses a single rotating crystal that scans a 360° sector perpendicular to the long axis of the endoscope. Current developments in EUS technology have seen the production of the first solid-state multielement transducer radial echo-endoscope that is connected to a general purpose US scanner (Hitachi Medical, Tokyo, Japan). Unlike abdominal US, high frequencies are used (7.5 to 20 MHz) to provide improved resolution to visualise the anatomical layers of the gastrointestinal tract and lesions as small as 2 to 3 mm. However, this is achieved at the expense of reduced penetration depth (approximately 5 cm with the 7.5-MHz probe). The main disadvantage of conventional (2-D) EUS is that, although it is an established technique for staging upper GI malignancies, it is operator-dependent. It may provide adequate information on extent of tumor invasion, but it has reduced accuracy in the estimation of the length of the lesion. In the study of the structures around the oesophagus and stomach, the complexity of nearby structures, such as varices and collateral circulation, makes correct anatomical interpretation even more difficult.

US phantoms are used in US quality assurance programs to compare and evaluate system and transducer performance (Hoskins and Ramnarine 2000; Teirlinck et al. 1998). In addition to specific test objects, there is a growing need for realistic anthropomorphic phantoms for different US applications. These are required for teaching and training, machine calibration and assessment of new imaging modalities. Anthropomorphic phantoms have been developed to simulate features of the breast (Madsen et al. 1982b), abdomen (Madsen et al. 1980; Zagzebski et al. 1991)

Address correspondence to: Scott Inglis, Medical Physics, Royal Infirmary of Edinburgh, 51 Little France Crescent, Edinburgh EH16 4SA UK. E-mail: s.inglis@ed.ac.uk

and arteries (Ryan and Foster 1997; Brunette et al. 2001; Gatzoulis et al. 2003; Chu and Rutt 1997).

It is important that the various simulated tissue types in an anthropomorphic phantom have appropriate and well-characterised acoustical properties: speed of sound, frequency dependence of attenuation, backscatter and reflection. Data on the acoustical properties of different tissue types is scarce (Duck 1990) and published values differ because of a wide variety of factors concerned with measurement technique, tissue type (*e.g.*, muscle, skin, liver) and tissue preparation. International standards and professional bodies have made recommendations with regard to the acoustic properties of tissue-mimicking materials (TMM); speed of sound of 1540 m/s as assumed by US machines and attenuation coefficient of 0.3 to 0.7 dB/cm.MHz (AIUM Technical Standards Committee 1991; AIUM/NEMA 1992; IEC 1997) and 0.5 dB/cm.MHz (IEC 2001).

A variety of materials have been suggested and used in TMM phantoms and test objects. Many of the materials have poor or inappropriate acoustical properties, particularly with regard to frequency-dependence of attenuation and/or speed of sound. TMMs with good acoustical properties typically consist of appropriate scattering particles suspended in a water-based gelatin or agar material (Burlew 1980; Madsen et al. 1978; Madsen 1986; Zagzebski 1991; Ryan and Foster 1997; Ramnarine et al. 2001; Madsen et al 1982a; Bush and Hill 1983; Blechinger et al 1988). The use of cellulose scattering particles has been suggested (Rickey et al. 1995) and used to develop an intravascular artery phantom (Brunette et al. 2001) and flow phantom (Rickey et al. 1995; Poepping et al. 2002), although this TMM suffers from poor frequency-dependence of attenuation.

A well-characterised, agar-based tissue mimic with good acoustic properties was used to construct the phantom (Ramnarine et al. 2001). This paper describes the development, characterisation and application of an EUS phantom of the oesophagus, which is required for teaching, and research and development studies. The phantom construction technique could be modified to facilitate the construction of a quality assurance phantom.

METHODS

Phantom construction methodology

The agar-based tissue-mimicking material used to construct the phantom had the ingredients detailed in Table 1. The water, glycerol and benzalkonium chloride were mixed together in an appropriate container and placed within a heated water bath. Tap water was used as the water source and was degassed during the cooking process. A stirrer was used at all times to mix the tissue mimic. The stirring speed was initially set at between 50 and 70 rpm, but was altered to maintain good particle dispersion whilst avoiding the creation of air bubbles. At this point, the Al_2O_3 (0.3 μm and 3 μm) and SiC particles were mixed into the solution. The agar was slowly poured into the mixture, to ensure that it was completely dissolved and that no clumps formed. A suitable seal was placed over the top of the container to minimise evaporation. The water bath was heated to 96 °C ± 3 °C and, after this temperature was reached, it was maintained for 1 h, during the TMM cooking process. After 1 h, the mixture was cooled to 42 °C and then cast into a mould and left to set. For large batches, the tissue mimic was placed in a refrigerator for rapid cooling to minimise particle settling.

Different percentage combinations of the Al_2O_3 (3 and 0.3 μm) and SiC (400 grain) particles were used to alter the acoustic attenuation and scattering properties of the materials (from no scatterer particles, 0%, to the % concentration of scatterer particles in the original, or normal, TMM, 100%). The % particle concentrations chosen to characterise the effects on the acoustical properties of the tissue-mimicking materials were 0, 5, 10, 15, 20, 30, 40, 50, 60, 75 and 100% of the Al_2O_3 (3 and 0.3 μm) and SiC (400 grain) particles. From the characterised acoustic properties of attenuation and backscatter, specific values were chosen to construct the various

Table 1. Ingredients of the agar-based tissue-mimicking material

Ingredient	% Weight concentration	Order code and manufacturer/distributor details
Water	82.97	
Glycerol 99% (pure)	11.21	(G7757) Sigma-Aldrich Company Ltd. The Old Brickyard, New Road, Gillingham, Dorset, UK.
Merck Agar–Agar technical (111925)	3	(53648 5K) VWR International Ltd. Hunter Boulevard, Magna Park, Lutterworth, Leics, UK.
3 μm Al_2O_3 powder	0.95	Logitech Ltd. Erskine Road, Old Kilpatrick, Glasgow, Scotland.
0.3 μm Al_2O_3 powder	0.88	
400 grain SiC powder	0.53	
10% solution of Benzalkonium chloride	0.46	(09621) (50% solution, diluted in-house to 10%) Sigma-Aldrich Company Ltd.

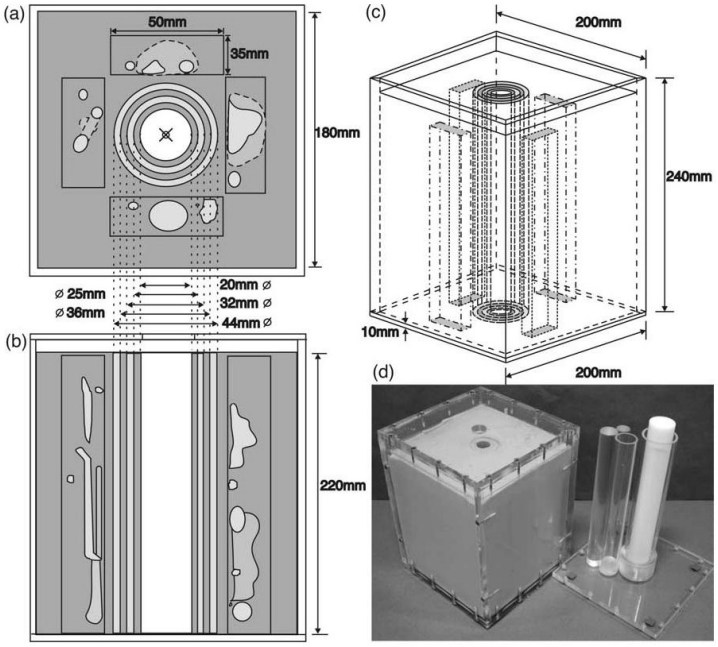

Fig. 1. Engineering drawing of the construction of the phantom and picture of manufactured phantom and mould. (a) Transverse view of the phantom, (b) coronal view through the phantom, (c) 3-D engineering view of construction of phantom, and (d) the constructed phantom and mould.

layers of the phantom and embedded objects. Modeling plasticine or clay was used to construct custom anatomical shapes to mimic the aorta, tumors, cysts, vascular structures and lymph nodes. A layer of latex was applied to the surface of the modeled objects to seal the plasticine, or clay, and allowed to dry for 24 h. The objects were positioned within four cubic moulds and then filled with normal TMM. After cooling, the objects were carefully removed and the resultant TMM block stored in water/glycerol/benzalkonium chloride mix. Four different TMMs, at 0, 10, 20 and 40% particle concentrations, were then manufactured and carefully poured into the cavities within the TMM block. For complex structures, where different objects came into contact, one of the latex-covered objects would be placed and the cavity filled with the appropriate TMM. After the TMM solidified, the latex-covered object was removed and that cavity filled with a different TMM. Four scenario blocks were manufactured with different anatomical features. The mould used to produce the "oesophageal" layers of the phantom consisted of a plastic tube and a series of receding-diameter plastic rods. The tube and largest rod were placed together to produce a layer of 2-mm thickness. The TMM was poured and allowed to solidify; the rod was then removed and a second rod inserted into the mould. This procedure was repeated to produce four different layers with different acoustical properties and varying thicknesses. After the "wall" layers and the four scenarios were manufactured, the phantom was assembled and filled with original TMM material. Figure 1a to c illustrates the construction of the phantom *via* an engineering drawing, where the shapes shown embedded within the phantom are examples only. Figure 1d is an example of the mould, phantom and embedded shapes. The object dimensions were recorded using the Microscribe G2X positional digitizing arm (Immersion Corporation, San Jose, CA, USA).

Acoustical measurement methodology

The acoustical properties were measured using a personal computer (PC)-based scanning acoustical macroscope (SAMa) (Ultrasonic Sciences Limited, Fleet, UK). The system was computer-controlled (hardware, stepping motors, data acquisition and analysis). The basic SAMa hardware consisted of a master system controller analog to digital input/output board allowing software control of the system, a 20-MHz pulser receiver and an 8-bit 100-MHz analog to digital converter. The transducer was attached to an x-y raster scan rig and consisted of computer-controlled dual stepper motors with at-

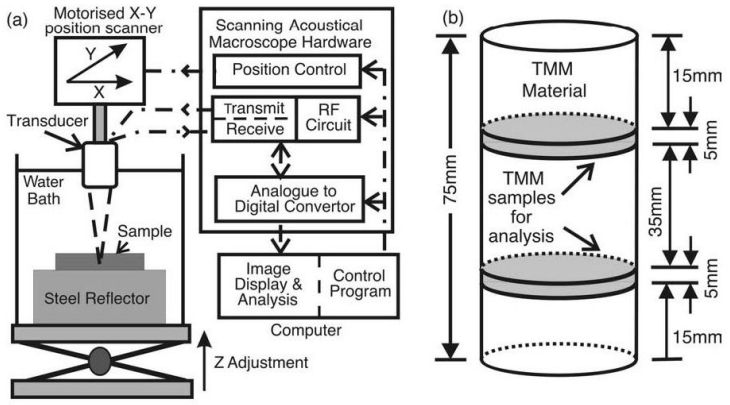

Fig. 2. (a) Block diagram of the SAMa and acoustical measurement setup, (b) Diagram detailing positional setup for sample extraction from each of the manufactured TMMs, for acoustical analysis.

tached screw shafts. This controlled the position of the transducer and enabled a scan area of the sample to be defined. The acoustical properties were measured using the pulse echo substitution technique, in which the reference echo signal from a 20-mm thick plane steel reflector was compared with the signal after insertion of the sample in the water path (see Fig. 2a). The steel reflector was positioned at the transducer focus point for the attenuation and speed of sound measurements. For the backscatter measurements, the focus was altered to just below the surface of the sample and the reference signal was obtained from the original (100%) TMM. A wideband, 7-MHz center frequency focused transducer was used as a transmitter and receiver and was aligned perpendicularly to the plane reflector. The transducer had a diameter of 1.4 cm, a focal length of 5.4 cm and a −6-dB beam width of 1 mm at the focus. The active element of the transducer was a concave single crystal, with a focal length defined by the distance from the transducer face to the axial pressure maximum. The water bath was filled with tap water and left for four hours to ensure no bubbles generated by the filling process were present and that the temperature of the water had stabilised to room temperature (nominally 20 ± 0.4 °C). Boiled water was also used within the water bath and allowed to cool before proceeding with the acoustical measurements.

Samples of each of the manufactured materials were cut, using a bench microtome and sectioning razor, into 25-mm diameter × 5-mm thick cylinders and each of the acoustical properties (attenuation, backscatter and speed of sound) was measured using the scanning acoustical macroscope (SAMa). Two samples were cut at different depths from the same batch of material, as per Fig. 2b. To perform the acoustical measurements, the test sample was placed into the water bath for approximately 2 to 3 min. During this time diffusion of the glycerol was assumed to be negligible and, when the measurement was completed, the sample was stored in water/glycerol/benzalkonium chloride mix, at room temperature, to maintain the material hydration and properties. The error in the thickness from cutting the TMM, measured using a micrometer, was at a maximum of 5%, but was normally 2%.

The attenuation and speed of sound measurements consisted of a reference data set of the echo signal from only water and the steel reflector, and a sample data set, consisting of the echo signal from the steel reflector with the sample placed just above the reflector. Water was used as the reference medium. For backscatter power measurements, a 5 μs gated RF signal at the transducer focal point was acquired from just below the sample surface. This avoided interference caused by the reflection from the TMM sample surface and minimised sample attenuation affecting the backscatter power measurement. The backscatter power was calculated from the difference of the fast Fourier transform from the reference TMM material (100% particle scatterer particles) and the manufactured materials at the transducer centre frequency of 7 MHz and expressed in dB relative to the steel reflector.

The transducer performed a raster scan over the sample of tissue-mimicking material with a set scan size and step-size. At each step, the reflected radiofrequency (RF) signal from the steel reflector was digitized at a sampling rate of 100 MHz and stored. Custom-designed analysis software developed using Matlab™ (The Mathworks Inc, Natick, MA, USA) was used to calculate the acoustical properties from the raw RF data and display an image of attenuation, speed of sound and backscatter

power at specified frequencies of the FFT. The mean results were obtained by analyzing the RF signals received from a 16 × 16 mm sample area, with 256 RF signal pairs. The attenuation was calculated from the log difference between the FFT of the sample spectrum and the reference spectrum, using eqn (1).

$$\alpha(x, y, f) = -\frac{10}{2d} \log_{10} \frac{I(x, y, f)}{I_o(x, y, f)} \quad (1)$$

Where d was the sample thickness, $I(x, y, f)$ was the power spectrum intensity at frequency f and position x, y through the sample, $I_o(x, y, f)$ was the power spectrum intensity at position x, y and frequency f of the reference signal with no sample in the path. The calculation was performed on each of the 256 RF signals.

The random uncertainty from repeat measurements of the attenuation was better than ± 0.03 dB over the frequency range 3 to 10 MHz. Contributions to the error in attenuation measurements may arise from a large number of sources (Bamber 1986). These include errors because of sample thickness measurement, reflection, diffraction, nonlinear propagation, alignment and temperature. Estimated systematic uncertainty caused by equipment was < 0.2 dB (*e.g.*, noise, transducer stability, calibration errors, variation of pulse generator output). The estimated systematic uncertainty detailed in homogeneous samples was < 1 dB (*e.g.*, temperature, sample thickness, reflection, nonlinear propagation). Measurements of attenuation were validated using standard silicon oil reference cells supplied by the UK National Physical Laboratory (NPL, Teddington, UK) (Zeqiri 1989). The stated value for attenuation of the 5-mm reference cell, measured with a 7-MHz wideband transducer, was 9.7 dB, at 21.5 °C. The attenuation was within 5% of the NPL measurements. It is estimated that the overall uncertainty in attenuation measurement was ± 5%. Nonlinear propagation of the RF pulse becomes apparent at high acoustic pressures with the progressive distortion of the pulse, and occurred with the generation of higher frequency harmonics. This had been estimated to be less than 2% of the maximum acoustic pressure of the pulse-restricted nonlinear loss of the fundamental. To minimise the nonlinear propagation a lower power excitation pulse was applied to the SAMa system transducer crystal.

The speed of sound in the material was calculated from the difference between the time taken for the RF pulse to travel to and from the plane reflector with and without the sample in the path using eqn (2):

$$\frac{1}{c_s} = \frac{1}{c_w} - \frac{\Delta T}{2d}, \quad (2)$$

where c_s was the speed of sound through the sample, c_w was the speed of sound in water (speed of sound in water is 1481 m/s at nominally 20 ± 0.4 °C), ΔT is the time-shift and d was the thickness of the sample. A total of 256 RF signals were stored and analysed.

The random uncertainty in the measurement of speed of sound was assessed from repeat measurements from a reference water path scan. The random uncertainty was ± 0.2 m/s. The estimated systematic uncertainty was ± 0.15% in the measurement of the speed of sound. This depends on the contributions from the uncertainty in the measurement of the thickness of the sample, the uncertainty in measurement of the difference between the time of arrival of the reference pulse and the pulse through the sample and the uncertainty in the speed of sound in the reference medium of water. Examples of the estimated systematic uncertainties were temperature, water speed accuracy, alignment, digitization, noise, time base accuracy and sample thickness. Measurements of speed of sound were validated using liquid reference cells (5,10 and 15 mm thickness) containing Dow Corning 710 silicon fluid supplied by the UK National Physical Laboratory (Zeqiri 1991). The NPL stated values for speed of sound within the 5-mm reference cell at 7 MHz was 1378 m/s, measured at 21.5 °C. It was estimated that the overall uncertainty in speed of sound measurement was ± 0.15%.

It must be noted that, because of the lack of a national standard backscatter reference cell, and the wide differences across laboratories in the measurement of backscatter, it was not possible to characterise the uncertainties involved with the backscatter measurements.

Phantom scanning methodology

A clinical study to investigate the endoscopist's ability to accurately estimate the length of a mimicked cancer lesion within the phantom using conventional (2-D) EUS and compare it with 3-D EUS, was performed to visualise and validate the phantom. An Olympus EU-M30 processor and the GF-UM20 and 200 echo-endoscopes were used to scan the phantom at 7.5 and 12 MHz. The echo-endoscope was introduced into the central core of the phantom. The endoscopists performed two independent examinations of the phantom, mimicking a normal diagnostic patient procedure. When the endoscopist identified an object, the dimensions were measured using the tools provided by the EU-M30 US processing unit and the position and dimensional measurements were recorded. Five distinct objects were chosen, with different shape and dimensions characteristics, to compare the endoscopic and 3D-EUS measurements.

Figure 3 illustrates the 3D-EUS measurement and acquisition setup. The echo-endoscope was positioned at the base of the central core of the phantom and then

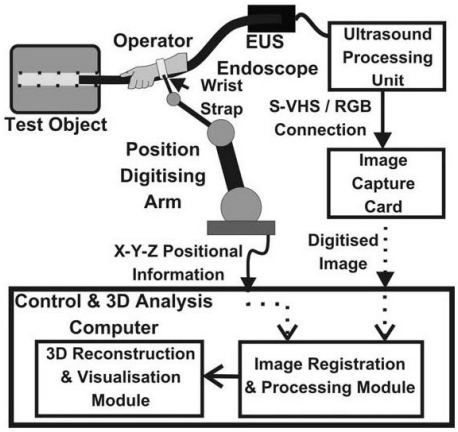

Fig. 3. Block diagram of the 3-D acquisition and measurement setup.

withdrawn at a relatively constant rate as the images were captured at 12.5 frames/second (fps), using the Meteor II image acquisition card (Matrox Electronic Systems Ltd, Dorval, QU, Canada).

The positional information was captured using a Microscribe G2X positional digitizing arm. The tip of the digitizing arm was attached to the back of the endoscopist's hand that controlled the withdrawal of the echo-endoscope, using a custom-designed strap and holder. The endoscopist maintained a fixed position upon the endoscope's insertion tube and then withdrew the scope from the phantom. Positional data were acquired simultaneously with EUS images, over the entire length of the phantom (22 cm).

The 3-D data sets were acquired from the custom 3-D anthropomorphic tissue-mimicking EUS phantom. Volumes were reconstructed from the series of parallel B-mode images and the positional information. A comparison was made between the dimensions obtained during the scan and those obtained from the 3-D reconstruction and analysis software.

RESULTS

A total of 11 different particle concentration TMM samples were manufactured and the acoustical properties (attenuation, speed of sound and backscatter power) were measured. The TMM samples of different particulate concentrations had attenuation coefficients which varied between 0.12 to 0.5 dB/cm.MHz, backscatter power between 0 and −12.2 dB relative to 100% of scatterer particle concentration (or "standard" TMM) and an average speed of sound of 1537 ± 1.9 m/s (mean ± 1 SD). Table 2 summarizes the averages of the acoustical properties of attenuation, backscatter power (both at 7.5 MHz) and the average speed of sound of the material. The acoustical properties of attenuation and backscatter at 7.5 MHz were displayed because this is the frequency most common to all existing echo-endoscopes. The gradient was obtained from the calculated equation of the line of linear best fit to the attenuation data, for each particle concentration, between 4 and 18 MHz.

A graph showing the relationship of the average attenuation coefficient ($n = 2$) plotted as a function of the frequency for the eleven TMM particulate concentration samples is shown in Fig. 4. The graph displays the attenuation coefficient as a function of frequency, vs. frequency and indicates the frequency-dependence of the attenuation for each of the materials. To obtain the gradient of the attenuation, a line of best fit ($Y = mX + c$), where m is the gradient of the line, was applied to each of the plots of attenuation (dB/cm.MHz) of each particle concentration. Table 2 illustrates that the gradient decreased as the particle concentration increased. The reduction in gradient of the linear line of best fit with increased particle concentration illustrates the reduction of the frequency-dependence of the attenuation.

Single attenuation readings were taken at 7.5 MHz, 10 MHz and 12 MHz. The frequencies were chosen because they correspond to the implemented frequencies of the transducers in most diagnostic and therapeutic EUS systems. Figure 5 illustrates the linear relationship between averaged attenuation and particle concentration over the set frequencies. The mean attenuation was obtained by averaging the calculated attenuation at chosen frequencies of the two samples taken at different depths

Table 2. Summary of the properties obtained from the scanning acoustical macroscope

Particle concentration (%)	Average attenuation, dB/cm.MHz, or dB/cm	Average backscatter power (dB)	Average speed of sound (m/s)	Gradient
100	0.501 (3.79)	0	1538.1	4×10^{-6}
75	0.420 (3.10)	−1.05	1538.3	0.0003
60	0.376 (2.83)	−1.85	1534.4	0.0006
50	0.337 (2.53)	−2.8	1536	0.0015
40	0.294 (2.20)	−3.75	1535	0.0025
30	0.264 (1.98)	−5.07	1535	0.0032
20	0.228 (1.73)	−6.85	1535.3	0.0036
15	0.202 (1.50)	−8.35	1536.5	0.0045
10	0.173 (1.30)	−9.55	1536.5	0.0047
5	0.159 (1.17)	−10.6	1538.2	0.0054
0	0.124 (0.93)	−11.85	1540.4	0.0055

The attenuation and backscatter were displayed as an average at a frequency of 7.5 MHz on the attenuation plot (Fig. 6), of two mean values calculated from the 16 × 16 mm sample scan. The speed of sound was the mean value, calculated same scan dimensions. The gradient was obtained from the linear line of best fit of each of the plotted attenuation data (Fig. 6).

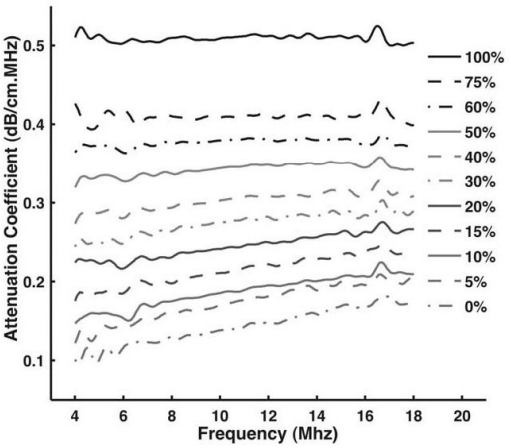

Fig. 4. The average attenuation coefficient of the extracted sample (n = 2), plotted as a function of the frequency for a range of TMM particulate concentrations. The x-axis is frequency of the calculated FFT (MHz) and y-axis is the attenuation calculated as a function of frequency (dB/cm · MHz).

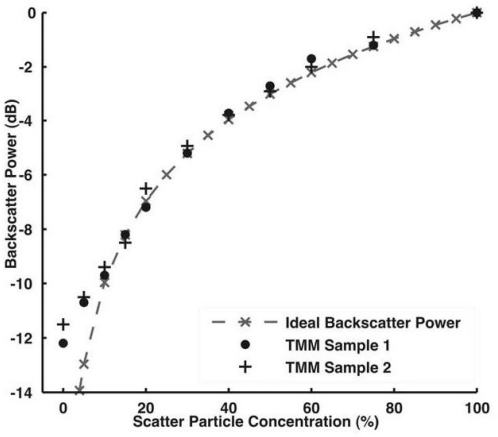

Fig. 6. The backscatter power relative to 100% particle concentration of the standard TMM measured at 7.5 MHz. The particle concentration was plotted as a function of the backscatter power. The x-axis is scatterer particle concentration (%) and y-axis is the backscatter power (dB).

(35 mm separation) (n = 6). The graph is displayed as an average of the two samples at three different frequencies to enable the selection of a particle concentration for a set attenuation over the operating frequency range of the EUS system (7.5 to 12 MHz). The error bars are ± 2 SDs from the mean. The plot illustrates that the attenuation has a linear trend between 0.15 and 0.5 dB/cm.MHz with increasing scatterer particle concentration.

Figure 6 shows the logarithmic relationship between the backscatter power with increasing particle concentration at 7.5 MHz from two samples of the same material (as per Fig. 1b). Reducing scatterer concentration by 50% and 75% reduced backscatter power by 50% (−3 dB) and 75% (−6 dB). Between 100% and 10%, the results show good agreement with the ideal logarithmic trend of the backscatter power.

In our pilot study, repeated dimensional measurements were performed on the phantom shown in Fig. 7 by two experienced endoscopists. It was found that the endoscopists had a maximum error in the x-y plane of 5% and average of 3% (example of transverse view is Fig. 7e). The 2-D measurements performed by the endoscopists, in the z plane, produced an average error of 8% with a maximum error of 23%. Identical measurements in the z-plane performed on the 3-D data set (illustrated in Fig. 7a to d), obtained an average error of 2.2% and a maximum of 3.7%. Table 3 details the average and maximum percentage errors obtained from the endoscope measurements and duplicate measurements on the volume reconstructed phantom.

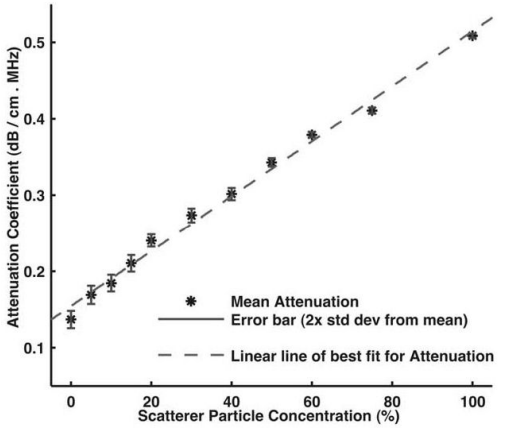

Fig. 5. The mean attenuation against the particle concentration obtained from measurements of two samples at frequencies of 7.5, 10 and 12 MHz of the FFT. Error bars indicate ± 2 SDs. The x-axis is scatter particle concentration (%) and y-axis is the attenuation calculated as a function of frequency (dB/cm · MHz).

DISCUSSION

In this study, we have demonstrated that it was possible to design and construct a complex acoustical phantom. In addition, by varying the scatterer particle concentration, a wide range of materials with different

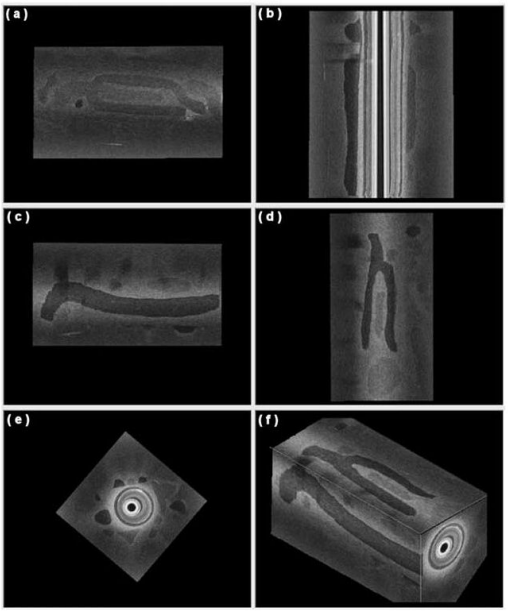

Fig. 7. 3-D reconstruction of acoustical phantom used to assess accuracy of the measurements performed by endoscopists and reproducibility and accuracy of volume measurements within the phantom. (a), (c) and (b), (d) are the coronal and sagittal views, respectively, at different levels, (e) is the transverse view, and (f) is the 3-D perspective view of the volume.

attenuation and backscatter properties could be manufactured without compromising the speed of sound. The technique used in the manufacture of the phantom could be used to construct a wide number of anatomical and pathologic scenarios and for different tasks (*e.g.*, simplified structures for quality assessment purposes).

This study concentrated upon the results of acoustic properties for TMM mixtures with decreasing concentrations of scattering and attenuating particles compared with the standard 100% TMM formulation. Each of the ingredients was found to contribute to specific acoustical properties of the TMM. The water, glycerol and agar produced the speed of sound of 1540 m/s; the Al_2O_3 (0.3 and 3 μm) contributed predominately to the value of the attenuation coefficient. A combination of Al_2O_3 (0.3 and 3 μm) and SiC particles produced the value of the backscatter power. The SiC particles were used to increase the speckle effect and backscatter of the TMM to produce a similar US speckle to liver. The particles were used to normalize the attenuation coefficient over a wide range of frequencies at 100% concentration.

Using the TMM manufacturing described technique, it was possible to generate a tissue-mimicking material with the desired properties, detailed in IEC (2001) standard 61685. It was found that altering the concentration of the particles changed the attenuation coefficient and backscatter power, but maintained the speed of sound. It was decided to simplify and minimize the number of materials manufactured, and that the concentrations of Al_2O_3 and SiC would be kept the same. The attenuation coefficient detailed in Fig. 4 showed that decreasing the particle concentration from 100% decreased the attenuation, but also increased the gradient of the plot over the range of frequency. This was attributed to the increasing influence of the frequency response of the agar (0%) as the particle concentration reduced. The gradient varied from 4×10^{-6} (100%) to 0.0055 (0%), indicating that increasing the Al_2O_3 and SiC particle concentration corrected for the gradient obtained from agar alone and minimized the frequency-dependence of the attenuation coefficient over the range of frequencies (in this case 4 to 18 MHz).

The average values of attenuation, at 7.5, 10 and 12 MHz, were singled out to investigate the relationship with increasing particle concentration. The values were averaged, obtaining the mean and SD over that frequency range. It can be seen from Fig. 5 that there is a linear

Table 3. Summary of the dimensional measurements obtained from the scanning of the EUS phantom

	Endoscopist 1		Endoscopist 2		3-D EUS	
Object	Average error (%)	Maximum error (%)	Average error (%)	Maximum error (%)	Average error (%)	Maximum error (%)
1	15	23	8	8	1.85	2.3
2	11	11	5	11	1.3	1.5
3	3	8	7	7	3.1	3.5
4	11	19	6	10	1.65	1.8
5	4	11	10	18	3.3	3.7

The average error was obtained from two independent examinations of the phantom or reconstructed volume. Max error is the maximum error obtained from a single measurement obtained from the individual objects.

relationship between the attenuation coefficient and particle concentration. The error bars indicate that, at higher particle concentrations, the attenuation was consistent over the frequency range. However, as the particle attenuation reduced below 50%, the effects of agar upon the gradient become noticeable.

With the chosen TMM mixture, it was found that there was a set minimum value for attenuation and backscatter that could not be exceeded. By reducing the concentration of the agar, it was possible to further reduce the attenuation coefficient and backscatter power. However, this compromised the speed of sound and mechanical strength of the material. An alternative agar or gelatin could also be used to lower backscatter power, but this would also alter the acoustical and physical properties. This would be required if it was necessary to simulate fluid-filled cysts and other similar pathology.

The ideal backscatter trend (Fig. 6) was plotted with the results obtained from the backscatter measurements. At particle concentrations lower than 10%, the scatter effects of the agar contributed to the backscatter power and caused the results to deviate from the ideal trend. In practice, changing the scatterer concentration between 10% and 50% resulted in the greatest change in the B-mode images of object echolucency because of the log compression of the displayed grey-scale image. The backscatter measurements required the averaging of the data from each point of the raster scan for both the reference (100%) and the data. The small reflection obtained from the surface of the material, and resultant spectrum of the signal through the material, was very small. The signal-to-noise ratio of the RF data for the backscatter measurements was a maximum of 3:1 on single measurements for the high particle concentration materials. At the lower particle concentrations, the signal could be masked within the noise. The backscatter measurement technique used with the SAMa system was not optimal.

Using graphs in Figs. 5 and 6, it was possible to design and manufacture a number of different materials for the phantom with known acoustical properties and to determine the required particle concentration to obtain the desired attenuation or backscatter power. Testing of the manufactured materials ensured that the mixture and manufacturing processes were consistent. The maximum deviation from the expected attenuation and backscatter values was less than 10% at the lower concentrations of scatterer particles (0%–15%).

During the initial phases of the research into the phantom, brighter (more hyperechoic) objects than the 100% mixture were also assessed. To obtain an increasingly hyperechoic object, it required 4 times the normal amounts of SiC added to the mixture to produce a noticeably brighter object than normal (100%) TMM. The resultant material was highly attenuating and produced marked shadowing behind the object. Adding more scatterer particles, (2 and 3 times relative to the 100% mixture), did not result in a significant change in the apparent brightness of the material under EUS. Hyperechoic tissue characteristic is predominately associated with benign lesions or tumors of the third layer; examples include calcified nodes, lipoma and carcinoid tumors. However, using EUS, the majority of the pathologic structures investigated were observed to be increasingly hypoechoic compared with normal tissue. To obtain hyperechoic acoustical characteristics, it would have been necessary to investigate different materials.

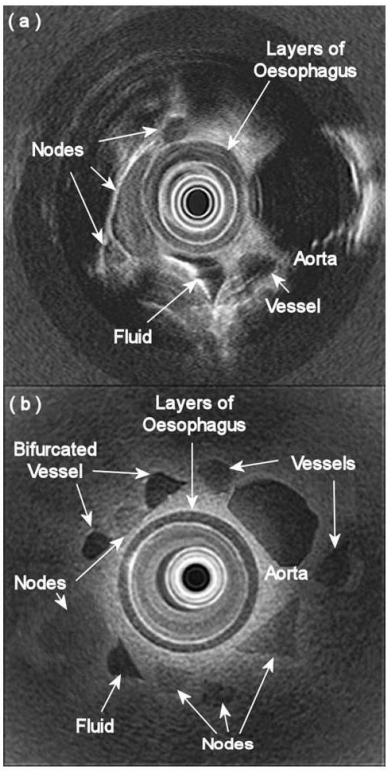

Fig. 8. Examples of (a) oesophageal cancer invasion and (b) EUS image of the five-layer phantom.

The phantom was constructed from the agar-based tissue-mimicking materials. Examples of the images acquired during patient scans and the images obtained from the phantom are displayed in Fig. 8. The phantom was designed to mimic the general and simplified anatomy of the oesophagus (wall layers of oesophagus, aorta and vessels) and pathologic and diseased structures of the oesophagus (malignant and benign looking nodes, tumor

and thickening). The structures that were embedded into the phantom were manufactured to be measurable in three dimensions (x, y and z directions) with finite start and end points. It was observed from the images of the phantom that there was minimal interface reflection caused by either perpendicular wall reflection or trapped air bubbles.

Within the phantom, a cancerous lesion was mimicked either as a break in the layer or as a thickened layer, with a reduced number of layers within the phantom, or as a large object close to the outer layer of the central core of the phantom. Other pathologic structures, including invading tumour, were constructed from complex shapes of varying sizes. These were constructed from various concentrations of scatterer particles (10%–50%). Nodes were represented by dark, echolucent spheres of various sizes (malignant looking) (0%–20%) or different shapes (benign nodes) of various concentrations of scatterer particles (20%–50%). Vessels and the aorta were manufactured from tubes of agar-only TMM, and embedded in various orientations. The simplicity or complexity of the contents was varied depending upon the application of the phantom (*e.g.*, a quality assessment phantom had less anatomy-mimicking structures).

In the clinical study to test the endoscopist's ability to accurately estimate the length of a mimicked cancer lesion within the phantom using conventional (2-D) EUS and compare it with 3-D EUS, it was found that 3-D EUS reduced the average error in the z dimension from 8% to 2.2%. The main advantage of 3-D EUS was that it minimised the errors observed during single measurements. The maximum z measurement error obtained upon a single object was 23%, with conventional 2-D EUS, and was reduced to 3.7% using 3-D EUS. It was also felt that 3-D EUS was able to increase diagnostic information by allowing the user to observe an object in 3-D and provide accurate volume estimation for planning chemoradiotherapy and accurate xyz measurements to facilitate tumor surgery.

CONCLUSIONS

This study has shown that it is possible to manufacture a complex phantom that can mimic the broad spectrum of the anatomy and pathology occurring within the region of the oesophagus, with good acoustical properties. The flexibility of the manufacturing technique ensured that a phantom could be constructed for tailored applications, including EUS research and development, teaching, quality assessment and performance/acceptance testing. The wide range of acoustical properties of the TMM meant that it was possible to manufacture a large number of materials to simulate the US characteristics of different tissues, while maintaining the required constant speed of sound. Varying the particle concentration allowed the attenuation coefficient and the backscatter power to be tailored to mimic different pathologic scenarios. In future studies, the investigation of the TMM textures (speckle) may lead to further improvement in the US imaging quality of the phantom.

In conclusion, we have demonstrated that the phantom can be used effectively in the development and validation of the 3-D EUS technique. 3-D EUS was able to improve the accuracy and reproducibility of dimensional measurements of the simulated cancerous lesions. It was found, by using the phantom, that the main error during endoscopy was the estimation of length of an embedded object. It is, therefore, likely that *in vivo* EUS cannot estimate tumor length as accurately as previously thought. Anthropomorphic tissue-mimicking phantoms are of important value in research and development, and training of endoscopists, in the field of EUS.

Acknowledgements—This work was supported by NHS Lothian, Research and Development Office.

REFERENCES

AIUM (American Institute of Ultrasound in Medicine). AIUM Technical Standards Committee 1990, Standard methods for measuring performance of pulse-echo ultrasound imaging equipment. Laurel: AIUM, 1991.

AIUM/NEMA (American Institute of Ultrasound in Medicine/National Electrical Manufacturers Association). Standard for real time display of thermal and mechanical indices of diagnostic ultrasound equipment. Laurel, MD: AIUM, 1992.

Bamber JC. Attenuation and absorption, In: Hill CR, ed. Physical principles of medical ultrasonics. Chichester, UK. Ellis Horwood Ltd, 1986.

Blechinger JC, Madsen EL, Frank GR. Tissue mimicking gelatine-agar gels for use in magnetic resonance imaging phantoms. Med Phys 1988;15:629–636.

Brunette J, Mongrain R, Cloutier G, et al. A novel realistic three-layer phantom for intravascular ultrasound imaging. Int J Cardiac Imaging 2001;17(5):371–381.

Burlew MM, Madsen EL, Zagzebski JA, Banjavic RA, Sum SW. A new ultrasound tissue-equivalent material. Radiology 1980;134: 517–520.

Bush NL, Hill CR. Gelatine-alginate complex gel: A new acoustically tissue-equivalent material. Ultrasound Med Biol 1983;9:479–484.

Chu KC, Rutt BK. Polyvinyl alcohol cryogel: An ideal phantom material for MR studies of arterial flow and elasticity. Magn Reson Med 1997;37:314–319.

Duck FA. Physical properties of tissue. A comprehensive reference book. London: Academic Press, 1990.

Fusaroli P, Caletti G. Endoscopic ultrasonography. Endoscopy 2003; 35(2):127–135.

Gatzoulis L, Ramnarine KV, Pye SD, et al. Doppler colour flow imaging and flow quantification with a novel forward-viewing intravascular ultrasound system. Ultrasound Med Biol 2003;29(1): 53–64.

Hoskins PR, Ramnarine KV. Doppler test devices. In: Evans DH, McDicken WN, eds. Doppler ultrasound: Principles, instrumentation and signal processing. 2nd ed. Chichester, UK: Wiley, 2000: 382–404.

IEC (International Electrotechnical Commission). Ultrasonics flow measurement systems—flow test object. Standard 61685. London: IEC, 2001.

IEC (International Electrotechnical Commission). Ultrasonics—Real-time pulse-echo systems. Guide for test procedures to determine performance specifications. Standard 61390. London: IEC, 1997.

Irisawa A, Obara K, Sato Y, et al. EUS analysis of collateral veins inside and outside the oesophageal wall in portal hypertension. Gastroint Endosc 1999;50(3):374–380.

Irisawa A, Shibukawa G, Obara K, et al. Collateral vessels around the oesophageal wall in patients with portal hypertension: Comparison of EUS imaging and microscopic findings at autopsy. Gastroint Endosc 2002;56(2):249–253.

Madsen EL. Ultrasonically soft tissue mimicking materials and phantoms. In: Greenleaf JF, ed. Tissue characterisation with ultrasound. Methods. Vol. 1. Boca Raton, FL: CRC Press, 1986:165–181.

Madsen EL, Zagzebski JA, Ghilardi-Netto T. An anthropomorphic torso section phantom for ultrasonic imaging. Med Phys 1980;7(1): 43–50.

Madsen EL, Zagzebski JA, Banjavie RA, Jutila RE. Tissue mimicking materials for ultrasound phantoms. Med Phys 1978;5:391–394.

Madsen EL, Zagzebski JA, Frank GR. Oil-in-gelatine dispersions for use as ultrasonically tissue mimicking materials. Ultrasound Med Biol 1982a;8:277–287.

Madsen EL, Zagzebski JA, Frank GR. An anthropomorphic ultrasound breast phantom containing intermediate-sized scatterers. Ultrasound Med Biol 1982b;8(4):381–392.

Poepping TL, Nikolov HN, Rankin RN, Lee M, Holdsworth DW. An *in vitro* system for Doppler ultrasound flow studies in the stenosed carotid artery bifurcation. Ultrasound Med Biol 2002;28(4): 495–506.

Ramnarines KV, Anderson T, Hoskins PR. Construction and geometric stability of physiological flow rate wall-less stenosis phantoms. Ultrasound Med Biol 2001;27(2):245–250.

Rickey DW, Picot PA, Christopher DA, Fenster A. A wall-less phantom for Doppler ultrasound studies. Ultrasound Med Biol 1995;21: 1163–1176.

Ryan LK, Foster FS. Tissue equivalent vessel phantoms for intravascular ultrasound. Ultrasound Med Biol 1997;23(2):261–273.

Teirlinck CJP, Bezemer RA, Kollmann C, et al. Development of an example flow test object and comparison of five of these test objects, constructed in various laboratories. Ultrasonics 1998;36: 653–660.

Wakelin SJ, Deans C, Crofts TJ, et al. A comparison of computerised tomography, laparoscopic ultrasound and endoscopic ultrasound in the preoperative staging of oesophago-gastric carcinoma. Eur J Radiol 2002;41(2):161–167.

Zagzebski JA, Madsen EL, Frank GR. A teaching phantom for sonographers. J Clin Ultrasound 1991;19(1):27–38.

Zeqiri B. Reference liquid for ultrasonic attenuation. Ultrasonics 1989; 27:314–315.

Zeqiri B. UK interlaboratory comparison of ultrasonic attenuation and velocity measurements—A preliminary report. Proc Inst Acoust 1991;13(Part 2):137–142.